Bright and Dusty Regions of Mars: New Insights from Experiments and Orbital Color Imaging

Inaugural dissertation
Of the Faculty of Science
University of Bern

A dissertation presented

by

ADOMAS VALANTINAS

From Lithuania

Supervisor of the doctoral thesis:
Prof. Dr. Nicolas Thomas

University of Bern

Bright and Dusty Regions of Mars: New Insights from Experiments and Orbital Color Imaging

Inaugural dissertation
Of the Faculty of Science
University of Bern

A dissertation presented

by

ADOMAS VALANTINAS

From Lithuania

Supervisor of the doctoral thesis:
Prof. Dr. Nicolas Thomas
University of Bern

Accepted by the Faculty of Science

Bern, 2022-11-28

The Dean:
Prof. Dr. Marco Herwegh

Acknowledgments

This work could not have been completed without the contribution of several people during the last four years. First, I wish to thank my supervisor Prof. Dr. Nicolas Thomas for giving me the opportunity to shift my research focus from lunar to Mars geology. I highly appreciate the scientific independence that I was given since day one, which allowed me to explore the many mysteries that Mars has to offer.

I also thank the entire Planetary Imaging Group (PIG) here in Bern. The patience and willingness of Dr. Antoine Pommerol to share his knowledge of laboratory instrumentation were of immense help throughout the experimental work. The engineers Miguel Almeida and Dr. Matthew Read imparted invaluable comments on spacecraft operations and planning. Dr. Patricio Becerra provided scientific support and guidance during the early stages of this work, for which I am very grateful.

I would also like to thank Prof. Dr. Vincent Chevrier who lent me his superb iron oxide sample collection. Without these samples, a large part of this work would not have been possible. Dr. Norbert Schorghofer and his input on thermal modeling were vital in completing the second part of this project. I also thank Prof. Dr. Alfred McEwen who shared several insightful comments that improved this work. I am highly thankful for the enthusiasm of Prof. Dr. Pete Schultz that inspired me to strive for an academic career. May I one day be like you!

Finally, I would like to thank my family and friends. My parents Rytis and Snaiguolė allowed me to pursue my dreams for as far as I can remember. I am fortunate to have the support

of my brother Mykolas and my friend Deividas. I owe much to the good spirits of my girlfriend Toma, who also helped to proofread parts of this work.

Table of contents

Chapter 1:

INTRODUCTION

This PhD thesis contributes to the investigation of the origin of Mars dust and analyzes dynamic processes in Mars bright, dusty regions. To understand the nature of the active phenomena and the spectral characteristics of Martian dust this work employs a combination of orbital observations and laboratory bi-directional reflectance measurements of ferric iron oxide powders. Orbital observations are mostly derived from the Colour and Stereo Surface Imaging System (CaSSIS; Thomas et al., 2017) on board the ESA's ExoMars Trace Gas Orbiter (TGO), which present novel multispectral data that is exploited here for high precision photometry. The orbital observations are complemented by laboratory measurements using the PHysikalisches Institut Radiometric Experiment-2 (PHIRE-2; Pommerol et al., 2011) and the Mobile Hyperspectral Imaging System (MoHIS; Pommerol et al., 2015) at the University of Bern. The use of the CaSSIS orbital data is at the core of each chapter of this thesis.

Chapter 2 analyzes the observations of active geomorphologic features known as slope streaks in the dusty regions of Mars. Substantial differences in their surface structures were determined using CaSSIS multi-angular observations. To study the particle size effects on the reflectance of slope streaks we employed PHIRE-2 measurements of sieved size fractions of Mars Global Simulant (MGS-1; Cannon et al., 2019) and the Hapke (2012) reflectance model. It was determined that a decrease in brightness can be caused by a decrease in particle size. This chapter was published in the *Planetary and Space Science* journal (Valantinas et al., 2021).

Chapter 3 presents the discovery of tropical frost on Martian volcanoes, which is significant because frost was not observed in these latitudes before. These observations of dusty, high altitude and low thermal inertia areas provide a deeper understanding of the current Mars climate. The high signal-to-noise ratio (SNR) and the capability of CaSSIS to image any given

point at various local times allows sharp imaging of processes never observed before. We intend to submit this chapter to *Geophysical Research Letters.*

Chapter 4 focuses on preliminary analyses of the photometry of Mars bright and dusty regions. The comparison of CaSSIS color data and laboratory PHIRE-2 measurements of various iron oxide powders revealed that ferrihydrite is the dominant mineral phase present in Martian dust. This finding indicates cold and icy conditions on Mars and limited liquid water activity in the latest geologic epoch. Additionally, using CaSSIS multi-angular data, phase curves for Martian dust deposits are derived. We intend to submit this work to a high-impact journal.

Appendix A presents additional work published in the journal *Geology*. It was partly conducted at the University Bern but is not directly related to the PhD thesis topic. Valantinas & Schultz (2020) report the discovery of an active tectonic system of wrinkle ridges on the nearside of the Moon. This finding is important because for decades the Moon was considered a geologically "dead" body. Lithospheric stresses under the active wrinkle ridge systems may be sources of deep moonquakes, which might be detected by future geophysical missions foreseen by NASA (Haviland et al., 2022).

Appendix B includes additional results that are not shown in Chapter 4. This comprises phase curves and phase curve color ratios of selected ferric iron oxides.

Motivation

1. Origin of Mars color

Astronomers have observed the reddish Mars in the night sky for millennia. Since Mars is clearly visible to the naked eye one could have wondered: What makes Mars appear red? Why is Mars

not blue or green like the Earth? Was Mars always red? If not, what made it red? Answering these questions may provide fundamental insights about the planet. The first attempts to answer these questions started with the invention of the telescope, which allowed observers such as Christiaan Huygens to see bright and dark regions that divide Mars (see Fig. 1, end of this section). The amount of observed surface detail grew with the development of larger telescopes in the following centuries.

However, the first major breakthroughs in understanding the nature of Mars color were achieved when methods of reflectance spectroscopy were applied to telescopic and laboratory observations. A reflectance spectrum is a measurement of the fraction of reflected light from a given surface as a function of wavelength. Direct compositional and mineralogical information can be acquired about the material from the absorption bands within its spectrum. By modeling the spectra of various materials in the laboratory and comparing them to the ground-based observations of Mars, Adams & McCord (1969) inferred that Mars bright regions are composed of fine oxidized ferric iron particles and that dark regions are more mafic in composition (i.e. basaltic in origin). The spectrum of Mars bright regions at visible wavelengths contains a steep red slope, which is attributed to the strong absorptions from electronic transitions in the blue to UV by surface materials containing oxidized Fe(III) (McCord et al., 1977; Singer et al., 1979). The same studies showed that low albedo regions contain broad absorption features near 1 and 2 μm resulting from unoxidized surface constituents containing ferrous Fe(II). This was later confirmed by the observations of Bell et al. (1990, 1997) and Mustard et al. (1993).

In the early telescopic data, bright, dusty regions resembled palagonized volcanic glass because of the lack of iron silicate absorptions (Soderblom & Wenner, 1978; Evans and Adams,

1980; Singer 1982). Palagonites are an assemblage of a complex group of materials (e.g. plagioclase feldspar, olivine, pyroxene, glass) that have been altered by weathering processes such as hydration and oxidation. Laboratory investigations by Morris et al. (1989) showed that the steep red slope and the ~0.85 μm absorption band could be attributed to the pigmentary form of synthetically produced nanophase (<20 nm) hematite particles that are within the volume of spectrally neutral materials such as dust, rocks and coatings. An in-depth laboratory analysis of Hawaiian palagonitic tephra found that the bright dust color arises from nanophase particles of hematite (anhydrous) or a mixture of hematite and ferrihydrite (hydrated) that is imbedded in a noncrystalline, hydrated aluminosilicate matrix (Morris et al., 1993). The distinction between ferrihydrite and hematite could not be made because both materials were X-ray amorphous, meaning they did not produce well-defined diffraction lines using X-ray diffraction (XRD) methods. Interestingly, the mineral hematite is crystalline but hematite particles of <20 nm in size do not scatter X-rays coherently and behave as an amorphous material (Morris et al., 1989). Ferrihydrite, on the other hand, naturally occurs only as fine-grained nanomaterial on Earth and has poor crystallinity (Schwertmann & Fischer, 1973). Note that, in planetary context, the term "nanophase ferric oxide" applies to any nano-scale Fe^{3+}-rich weathering product such as ferrihydrite, superparamagnetic hematite, maghemite, goethite, akaganeite, hisingerite, schwertmannite and lepidocrocite (Morris et al., 1993, 2019) (see Table 1 for chemical formulas). The term was implied to be generic because the hydration state of the Martian particles was not known and there may be a series of poorly crystalline ferric nanomaterials that fit the Mars visible spectrum and are X-ray amorphous (Morris et al., 2000).

Telescopic observations in the short wavelength infrared (SWIR) revealed a strong 3-μm absorption band in the Mars spectrum (Moroz, 1964; Sinton, 1967; Houck et al., 1973). Later spacecraft observations from NASA's Mariner 6&7 (Pimentel et al., 1974) and the Soviet Phobos-2 (Murchie et al., 1993) spectrometers revealed that both dark and bright regions contain adsorbed or molecularly-bound H_2O. Murchie et al. (2000) concluded that the 3-micron band is the strongest for bright regions and the same but weaker band for dark regions is due to a thin coating of bright ferric dust. Murchie et al. (1993) suggested that different chemical alteration histories and/or mixtures of ferric minerals other than hematite caused the spectral heterogeneities between bright regions of Arabia and Tharsis. Based on data from Observatoire pour la Minéralogie, l'Eau, les Glaces et l'Activité (OMEGA) experiment onboard ESA's Mars Express spacecraft in the 1-2.5 micron range, Bibring et al. (2006) argued that bright regions are strictly anhydrous and composed of nanocrystalline hematite or maghemite particles. Later re-evaluation of the OMEGA data within the 3 micron range revealed that bright, dusty regions have larger water absorption band depths relative to less dusty equatorial terrains (Jouglet et al., 2007; Milliken et al., 2007). This was attributed to either adsorbed water on grain surfaces due to large surface to volume ratio of the dust particles (e.g. Zent & Quinn, 1997) or H_2O bound in hydrated minerals. Audouard et al. (2014), using ten years' worth of OMEGA data, showed that the 3-micron band accounts for tightly bound H_2O and/or hydroxyl groups in the mineral structure of the surface materials in Mars bright regions. NASA's Compact Reconnaissance Imaging Spectrometer for Mars (CRISM; Murchie et al., 2007) onboard the Mars Reconnaissance Orbiter (MRO) also indicated a deep absorption in the dust spectrum centered at 3 μm (Murchie et al., 2019). Finally, laboratory reflectance investigations of the Martian

meteorite NWA 7533 (also known as the "Black Beauty") also revealed the 3-μm hydration band, which was attributed to OH- rather than H_2O-bearing phase (Beck et al., 2015).

The magnetic experiments on NASA's Viking landers showed that the soil contains 1-7% of a strongly magnetic component (Hargraves et al. 1977). Magnetic phases such as magnetites, maghemites, feroxyhytes and a paramagnetic nanophase hematite were put forward to explain the data (Hargraves et al., 1977; Burns, 1980; Posey-Dowty et al., 1986; Morris et al., 1989). Maghemite was also favored to explain the reactivity of the Martian soil during the Viking's gas exchange experiment (Oyama et al., 1978). The Mars Pathfinder mission identified that the dust was composed of composite particles containing a few percent of a magnetic phase such as maghemite (Madsen et al., 1999). The Mars Exploration Rovers (MER) carried a set of magnet arrays that were able to identify two different populations of dust: one that was weakly magnetic and bright in color, and the other that was strongly magnetic and dark in color (Madsen et al., 2009). It was found that the former is enriched in elements Si, S, Ca and K and the latter in Fe, Ti, and Cr. Another study using MER magnetic data (Goetz et al., 2005), identified olivine and magnetite (possibly titanomagnetite) mixed with reddish ferric oxides in the Mars dust, which suggested a primarily of basaltic origin with some degree of alteration. Additionally, the analysis of soils in Gusev crater and Meridiani Planum using several MER instruments indicated a mixture of igneous (e.g. pyroxenes, plagioclase, olivine) and alteration materials (e.g. nanophase oxides, amorphous silica), which suggested that these products are derived from fundamentally different processes, and alteration pathways (McSween et al., 2010). Data collected by the MIMOSII Mössbauer instrument (MB) revealed the existence of coarse-grained hematite and goethite in discrete mineralogical assemblages as well as the ubiquitous presence of nanophase

ferric oxides in the dust (Morris et al., 2006). A caveat here is that MER data alone (MB, Mini-TES, Pancam) cannot distinguish between the various ferric nanophase materials that may be present in Mars dust (Soderblom & Bell, 2008). Ming et al. (2008) argued that nanophase materials could be any of the already mentioned ferric oxides (see Table 1) and additionally hydronium jarosite or iddingsite. The hydration state of the possible ferric minerals in the Mars dust could not be determined but it was reported that the Fe concentration is positively correlated with S+Cl abundances, which suggested that dust is a chemical alteration product (Yen et al., 2005; Morris et al., 2006; Ming et al., 2008). Morris & Klingelhöfer (2008) concluded that the form of nanophase oxide materials on Mars is highly sensitive to the local conditions and processes, which raises the possibility that perhaps their formation is uncommon or absent on Earth.

NASA's Mars Science Laboratory (MSL) rover provided several key chemistry and mineralogy measurements of Martian soils and dust. The Chemistry and Mineralogy (CheMin) XRD instrument, analyzed the inactive aeolian materials (soil + dust) at the "Rocknest" site, which revealed that ~95% of the crystalline component is composed of primary igneous materials (plagioclase, forsterite, pyroxenes) and only a few secondary minerals were identified (anhydrite ~0.9± 0.2 wt%, magnetite 1.8 ± 0.3 wt% , hematite 1.0 ± 0.1 wt%) (Bish et al., 2013). 27 to 45 wt% of the bulk "Rocknest" soil was attributed to X-ray amorphous materials (Bish et al., 2013; Blake et al., 2013). The amorphous mineralogy of CheMin could be constrained by bulk chemistry measurements of dust using the Alpha Particle X-ray Spectrometer (APXS) and Chemistry and Camera (ChemCam) laser induced breakdown-spectrometer, which revealed that the amorphous component is enriched in SO_3, Cl and Fe relative to the Mars soil (Berger et al.,

2016; Lasue et al., 2018). The X-ray amorphous fraction of the "Rocknest" sample was also enriched in the same elements, which suggested by inference that ferric oxide dust dominates the X-ray amorphous part of the inactive soils (Achilles et al., 2017). The SAM (Sample Analysis at Mars) instrument, which is a chromatograph and a quadrupole mass spectrometer, documented several volatile species (H_2O, SO_2, CO_2 & O_2) when the "Rocknest" soil was heated up to ~835 °C (Leshin et al., 2013). This suggested that H_2O is bound to the amorphous component because CheMin did not detect any hydrated/clay minerals (Leshin et al., 2013). ChemCam also showed that the widespread hydrogen signal in the fine grain fraction of soils and dust does not vary diurnally, which suggests that hydrogen is strongly bound to the host materials and may account for the hydrated amorphous component (Meslin et al., 2013).

The elusive ferric iron oxide mineral (or minerals) present in the Mars dust probably represents an alteration product from Fe(II)-bearing silicate materials of the Mars crust. Since the formation of ferric oxides is sensitive to thermal, aqueous and pH histories, the mineralogical phases of dust can provide information about the ancient climate of Mars, which is a major goal of current Mars research. It is likely that for the past billions of years Mars was a cold, arid planet (Wordsworth et al., 2021), which narrows down the list of plausible ferric iron phases that can retain metastability during such conditions. Finding this phase (or phases) is the goal of Chapter 4, that can provide additional constraints on the past habitability of Mars.

2. Dynamic phenomena in Mars bright, dusty regions

Decades of spacecraft and telescopic observations of Mars have shown both small and large regional dust events, as well as planet-encircling dust storms (e.g. Zurek, 1982; Sánchez-Lavega

et al., 2019). After such events, the bright and dark regions may exhibit regional changes in albedo, due to removal or deposition of bright dust (Christensen, 1988; Geissler, 2005; Szwast et al., 2006; Wellington & Bell, 2020). Because dust storms originate during summer in the southern midlatitudes it was proposed that there is a net transport and accumulation of dust from southern (dark) to northern (bright) regions (Zurek & Martin, 1993). Roughly 2.9 x 10^{12} kg/yr of dust is exchanged between the surface and atmosphere according to Pollack et al. (1979) estimates. Atmospheric models of past obliquity cycles predict preferential deposition of dust over high topography regions such as Tharsis or Arabia but fail to produce peak accumulation in low elevation areas such as Elysium or Amazonis (Newman et al., 2005). It is unclear if dusty regions are sources of dust or simply locations where dust accumulates over large timescales. Recent investigations of Ojha et al. (2018) showed that most of Martian dust may have been eroded from the equatorial Medusa Fossae region, which would result in an equivalent 2-12 m global layer. Based on crater size measurements Mangold et al. (2009) concluded that Arabia is mantled by more than 20 m of dust. Keszthelyi et al. (2008) using HiRISE images estimated that at least 4 m thick layer of dust covers the Tharsis volcanoes. Using radar and thermal inertia measurements, Christensen (1986) calculated that bright regions are covered by up to 2 m of dust.

The bright, dusty regions exhibit unusually low thermal inertia values of <100 J m^{-2} K^{-1} $sec^{-1/2}$ (Christensen et al., 2001). During the Martian night, they cool to extremely low temperatures (~130 K) because of the low density and the small particle size of their surface fines (Putzig & Mellon, 2007). Individual dust particle size was estimated to be <5 microns (Christensen, 1986; Lemmon et al., 2004). Using Mars Climate Sounder (MCS) data from

onboard NASA's MRO, the dust was proposed to serve as favorable nucleation cores for CO_2 frost condensation (Piqueux et al., 2016). The diurnal variability of temperature in these equatorial regions lead to the conclusion that the CO_2 frost is thermodynamically stable only during the night and, perhaps, up to an hour after sunrise (Piqueux et al., 2016). Because CO_2 frost sublimation/condensation is most efficient on steep east-facing slopes, it was hypothesized that disturbed dust particles could trigger large avalanches of granular material (Piqueux et al., 2016). Interestingly, bright, dusty regions are known to host peculiar features known as slope streaks (Schorghofer et al., 2007), making this idea plausible.

The origin of slope streaks has been debated since early Viking orbiter observations in the early 1980s. First hypotheses argued that slope streaks are debris weathered from dark pyroclastic materials (Morris, 1982) or stains from liquid brines (Ferguson & Lucchitta, 1984). Later studies based on an analog of terrestrial dry, loose snow avalanches proposed the dust avalanche model (Sullivan et al., 2001) but the liquid brine model was still discussed on the basis of the fluid-like morphology (Miyamoto et al., 2004), equatorial noon temperatures (~275 K) (Schorghofer et al., 2002) and unique dust properties that provide insulation from desiccation (Kreslavsky & Head, 2009). However, the dust avalanche model was particularly convincing because slope streak formation did not appear to be correlated with seasons (Schorghofer & King, 2011). The subsequent discovery of season-dependent Recurring Slope Lineae (RSL; McEwen et al., 2011) somewhat precluded further discussion on the origin slope streaks and the dust avalanche model has become the current paradigm.

Several key observations are difficult to explain by the dust avalanche model. Particularly in Arabia Terra, slope streaks appear as dark or bright markings on dusty slopes. This dichotomy

was originally proposed to be a result of different particle sizes of the excavated substrate material (Sullivan et al., 2001). This implies that both dark and bright slope streaks can form. In contrast, the absence of newly-formed bright slope streaks lead Schorghofer et al. (2007) to postulate that bright streaks are old dark streaks. A rare type of streaks that appear bright at the apex but dark at the distal ends further fueled the controversy, leading some studies to propose viewing angle effects (Baratoux et al., 2006). In Chapter 2 using CaSSIS color data, I show that transitioning streaks are real and are more abundant than previously thought. Using complementary images of other orbiters, I also present evidence that some dark streaks brighten over decadal timescales. Furthermore, it will be shown that the use of multi-angular data provides an opportunity to study the surface structural differences between the dark and bright slope streaks.

The discovery of CO_2 frost in dusty regions such as Arabia or Tharsis would provide supporting evidence for the dry origin of slope streaks. However, most spacecraft are in Sun-synchronous orbits (i.e. pass over a given point at the same local time) and light-reflecting instruments cannot observe during the night, therefore, the direct detection of frost is particularly challenging (Lange et al., 2022). According to the dust avalanche model, ~90% of the moving mass is lofted into the atmosphere (Sullivan et al., 2001), which, taken together with the CO_2 frost sublimation hypothesis (Piqueux et al., 2016), argues that morning images acquired in dusty regions should reveal not only pervasive frost deposits but also large km-scale billowing dust clouds. Until recently such reliable imaging campaigns were not possible. In Chapter 3, I show that the CaSSIS experiment can consistently discern and identify the presence/absence of early morning CO_2 frost.

3. CaSSIS applications and uses

Mars surface has been imaged by a plethora of orbiting imagers including Mariner 9 (Leighton et al., 1969), Viking (Flinn, 1977), Mars Orbiter Camera (MOC; Malin & Edgett, 2001), The High Resolution Stereo Camera (HRSC; Neukum & Jaumann, 2004), High Resolution Imaging Experiment (HiRISE; McEwen et al., 2007), Context camera (CTX; Malin et al., 2007) and CRISM (technically a spectrometer but it includes VIS capabilities). However, novel data acquired by CaSSIS provide the following advantages over previous missions. First, the non-sun-synchronous orbit of TGO allows observing a given point at a variety of local times (with a repeat every ~30 days), which consequently allows observations of diurnal processes and photometric studies of phase angle-dependent phenomena. CaSSIS multi-angular observations then can be compared with the data acquired by laboratory spectrogoniometry instruments that mimic CaSSIS observation geometries. Chapters 2 & 4 make use of this latter opportunity and compare orbital CaSSIS observations with laboratory PHIRE-2 and MoHIS measurements. Second, the superior SNR and absolute calibration (within 3%) of CaSSIS (Pommerol et al., 2022; Thomas et al., 2022) offers reliable spectroscopic and photometric investigations of the Martian surface. It is the first Mars camera to achieve such precision and photometric stability.

Additionally, CaSSIS offers large color coverage (~8 x 50 km), high spatial resolution (4.5 m/pixel) and precise spectroscopy in four broadband filters (BLU = 497 nm, PAN = 677 nm, RED = 830 nm, NIR = 940 nm). The position of RED and NIR filters provide an opportunity to study the absorptions near 860 nm of Mars bright regions (e.g. Bell et al. 1990). In comparison to other recent missions, CaSSIS color coverage is ~x6 that of HiRISE and the HiRISE detector already shows signs of aging (McEwen et al., 2022). Lastly, since April 2022, CRISM is no

longer operational, which leaves CaSSIS as the only state-of-the-art instrument capable of providing reliable spectral information, at least until the end of the 2020s.

References

Achilles, C. N., Downs, R. T., Ming, D. W., Rampe, E. B., Morris, R. V., Treiman, A. H., et al. (2017). Mineralogy of an active eolian sediment from the Namib dune, Gale crater, Mars. *Journal of Geophysical Research: Planets*, *122*(11), 2344–2361. https://doi.org/10.1002/2017JE005262

Adams, J. B., & McCord, T. B. (1969). Mars: Interpretation of spectral reflectivity of light and dark regions. *Journal of Geophysical Research (1896-1977), 74*(20), 4851–4856. https://doi.org/https://doi.org/10.1029/JB074i020p04851

Audouard, J., Poulet, F., Vincendon, M., Milliken, R. E., Jouglet, D., Bibring, J.-P., et al. (2014). Water in the Martian regolith from OMEGA/Mars Express. *Journal of Geophysical Research: Planets*, *119*(8), 1969–1989. https://doi.org/https://doi.org/10.1002/2014JE004649

Baratoux, D., Mangold, N., Forget, F., Cord, A., Pinet, P., Daydou, Y., et al. (2006). The role of the wind-transported dust in slope streaks activity: Evidence from the HRSC data. *Icarus*, *183*(1), 30–45. https://doi.org/https://doi.org/10.1016/j.icarus.2006.01.023

Beck, P., Pommerol, A., Zanda, B., Remusat, L., Lorand, J. P., Göpel, C., et al. (2015). A Noachian source region for the “Black Beauty” meteorite, and a source lithology for Mars surface hydrated dust? *Earth and Planetary Science Letters*, *427*, 104–111. https://doi.org/https://doi.org/10.1016/j.epsl.2015.06.033

Bell III, J. F., McCord, T. B., & Owensby, P. D. (1990). Observational evidence of crystalline iron oxides on Mars. *Journal of Geophysical Research: Solid Earth*, *95*(B9), 14447–14461. https://doi.org/https://doi.org/10.1029/JB095iB09p14447

Bell III, J. F., Wolff, M. J., James, P. B., Clancy, R. T., Lee, S. W., & Martin, L. J. (1997). Mars surface mineralogy from Hubble Space Telescope imaging during 1994–1995: Observations, calibration, and initial results. *Journal of Geophysical Research: Planets*, *102*(E4), 9109–9123. https://doi.org/https://doi.org/10.1029/96JE03990

Berger, J. A., Schmidt, M. E., Gellert, R., Campbell, J. L., King, P. L., Flemming, R. L., et al. (2016). A global Mars dust composition refined by the Alpha-Particle X-ray Spectrometer in Gale Crater. *Geophysical Research Letters*, *43*(1), 67–75. https://doi.org/10.1002/2015GL066675

Bibring, J. P., Langevin, Y., Mustard, J. F., Poulet, F., Arvidson, R., Gendrin, A., et al. (2006). Global mineralogical and aqueous Mars history derived from OMEGA/Mars express data. *Science*, *312*(5772), 400–404. https://doi.org/10.1126/science.1122659

Bish, D. L., Blake, D. F., Vaniman, D. T., Chipera, S. J., Morris, R. V, Ming, D. W., et al. (2013). X-ray Diffraction Results from Mars Science Laboratory: Mineralogy of Rocknest at Gale Crater. *Science*, *341*(6153), 1238932. https://doi.org/10.1126/science.1238932

Blake, D. F., Morris, R. V, Kocurek, G., Morrison, S. M., Downs, R. T., Bish, D., et al. (2013). Curiosity at Gale Crater, Mars: Characterization and Analysis of the Rocknest Sand Shadow. *Science*, *341*(6153). https://doi.org/https://doi.org/10.1126/science.1239505

Burns, R. G. (1980). Does feroxyhyte occur on the surface of Mars? *Nature*, *285*(5767), 647. https://doi.org/10.1038/285647a0

Cannon, K. M., Britt, D. T., Smith, T. M., Fritsche, R. F., & Batcheldor, D. (2019). Mars global simulant MGS-1: A Rocknest-based open standard for basaltic martian regolith simulants. *Icarus*, *317*, 470–478. https://doi.org/https://doi.org/10.1016/j.icarus.2018.08.019

Christensen, P. R. (1986). Regional dust deposits on Mars: Physical properties, age, and history. *Journal of Geophysical Research: Solid Earth*, *91*(B3), 3533–3545. https://doi.org/10.1029/jb091ib03p03533

Christensen, P. R. (1988). Global albedo variations on Mars: Implications for active aeolian transport, deposition, and erosion. *Journal of Geophysical Research: Solid Earth*, *93*(B7), 7611–7624. https://doi.org/https://doi.org/10.1029/JB093iB07p07611

Christensen, P. R., Bandfield, J. L., Hamilton, V. E., Ruff, S. W., Kieffer, H. H., Titus, T. N., et al. (2001). Mars Global Surveyor Thermal Emission Spectrometer experiment: Investigation description and surface science results. *Journal of Geophysical Research: Planets*, *106*(E10), 23823–23871. https://doi.org/https://doi.org/10.1029/2000JE001370

Ferguson, H. M., & Lucchitta, B. K. (1984). Dark streaks on talus slopes, Mars., 188–190.

Flinn, E. ~A. (1977). Scientific results of the Viking Project. *JGR*, *82*.

Geissler, P. E. (2005). Three decades of Martian surface changes. *Journal of Geophysical Research: Planets*, *110*(2), 1–23. https://doi.org/10.1029/2004JE002345

Goetz, W., Bertelsen, P., Binau, C. S., Gunnlaugsson, H. P., Hviid, S. F., Kinch, K. M., et al. (2005). Indication of drier periods on Mars from the chemistry and mineralogy of atmospheric dust. *Nature*, *436*(7047), 62–65. https://doi.org/10.1038/nature03807

Hapke, B. (2012). *Theory of Reflectance and Emittance Spectroscopy* (2nd ed.). Cambridge University Press. https://doi.org/https://doi.org/10.1017/CBO9781139025683

Hargraves, R. B., Collinson, D. W., Arvidson, R. E., & Spitzer, C. R. (1977). The Viking Magnetic Properties Experiment: Primary mission results. *Journal of Geophysical Research (1896-1977)*, *82*(28), 4547–4558. https://doi.org/https://doi.org/10.1029/JS082i028p04547

Haviland, H. F., Weber, R. C., Neal, C. R., Lognonné, P., Garcia, R. F., Schmerr, N., et al. (2022). The Lunar Geophysical Network Landing Sites Science Rationale. *The Planetary Science Journal*, *3*(2), 40. https://doi.org/10.3847/psj/ac0f82

Leighton, R. B., Horowitz, N. H., Murray, B. C., Sharp, R. P., Herriman, A. H., Young, A. T., et al. (1969). Mariner 6 and 7 Television Pictures: Preliminary Analysis. *Science*, *166*(3901), 49–67. Retrieved from http://www.jstor.org/stable/1727733

Houck, J. R., Pollack, J. B., Sagan, C., Schaack, D., & Decker, J. A. (1973). High altitude infrared spectroscopic evidence for bound water on Mars. *Icarus*, *18*(3), 470–480. https://doi.org/https://doi.org/10.1016/0019-1035(73)90156-5

Jouglet, D., Poulet, F., Milliken, R. E., Mustard, J. F., Bibring, J. P., Langevin, Y., et al. (2007). Hydration state of the Martian surface as seen by Mars Express OMEGA: 1. Analysis of the 3 μm hydration feature. *Journal of Geophysical Research: Planets*, *112*(8), 1–20. https://doi.org/10.1029/2006JE002846

Keszthelyi, L., Jaeger, W., McEwen, A., Tornabene, L., Beyer, R. A., Dundas, C., & Milazzo, M. (2008). High resolution imaging science experiment (HiRISE) images of volcanic terrains from the first 6 months of the Mars reconnaissance orbiter primary science phase. *Journal of Geophysical Research: Planets*, *113*(4), 1–25. https://doi.org/10.1029/2007JE002968

Kreslavsky, M. A., & Head, J. W. (2009). Slope streaks on Mars: A new “wet” mechanism.

Icarus, *201*(2), 517–527. https://doi.org/https://doi.org/10.1016/j.icarus.2009.01.026

Lange, L., Piqueux, S., & Edwards, C. S. (2022). Gardening of the Martian Regolith by Diurnal CO2 Frost and the Formation of Slope Streaks. *Journal of Geophysical Research: Planets*, *127*(4), e2021JE006988.

Lasue, J., Cousin, A., Meslin, P. Y., Mangold, N., Wiens, R. C., Berger, G., et al. (2018). Martian Eolian Dust Probed by ChemCam. *Geophysical Research Letters*, *45*(20), 10,968-10,977. https://doi.org/10.1029/2018GL079210

Lemmon, M. T., Wolff, M. J., Smith, M. D., Clancy, R. T., Banfield, D., Landis, G. A., et al. (2004). Atmospheric Imaging Results from the Mars Exploration Rovers: Spirit and Opportunity. *Science*, *306*(5702), 1753–1756. https://doi.org/10.1126/science.1104474

Leshin, L. A., Mahaffy, P. R., Webster, C. R., Cabane, M., Coll, P., Conrad, P. G., et al. (2013). Volatile, Isotope, and Organic Analysis of Martian Fines with the Mars Curiosity Rover. *Science*, *341*(6153), 1238937. https://doi.org/10.1126/science.1238937

Madsen, M. B., Hviid, S. F., Gunnlaugsson, H. P., Knudsen, J. M., Goetz, W., Pedersen, C. T., et al. (1999). The magnetic properties experiments on Mars Pathfinder. *Journal of Geophysical Research: Planets*, *104*(E4), 8761–8779. https://doi.org/https://doi.org/10.1029/1998JE900006

Madsen, M. B., Goetz, W., Bertelsen, P., Binau, C. S., Folkmann, F., Gunnlaugsson, H. P., et al. (2009). Overview of the magnetic properties experiments on the Mars Exploration Rovers. *Journal of Geophysical Research: Planets*, *114*(E6). https://doi.org/https://doi.org/10.1029/2008JE003098

Malin, M. C., & Edgett, K. S. (2001). Mars Global Surveyor Mars Orbiter Camera:

Interplanetary cruise through primary mission. *Journal of Geophysical Research: Planets*, *106*(E10), 23429–23570. https://doi.org/https://doi.org/10.1029/2000JE001455

Malin, M. C., Bell III, J. F., Cantor, B. A., Caplinger, M. A., Calvin, W. M., Clancy, R. T., et al. (2007). Context Camera Investigation on board the Mars Reconnaissance Orbiter. *Journal of Geophysical Research: Planets*, *112*(E5). https://doi.org/https://doi.org/10.1029/2006JE002808

Mangold, N., Ansan, V., Masson, P., & Vincendon, C. (2009). Estimate of aeolian dust thickness in Arabia Terra, Mars: implications of a thick mantle (> 20 m) for hydrogen detection. *Géomorphologie : Relief, Processus, Environnement*, *15*(1), 23–32. https://doi.org/10.4000/geomorphologie.7472

McCord, T. B., Huguenin, R. L., Mink, D., & Pieters, C. (1977). Spectral reflectance of Martian areas during the 1973 opposition: Photoelectric filter photometry 0.33-1.10 μm. *Icarus*, *31*(1), 25–39. https://doi.org/10.1016/0019-1035(77)90069-0

McEwen, A. S., Eliason, E. M., Bergstrom, J. W., Bridges, N. T., Hansen, C. J., Delamere, W. A., et al. (2007). Mars Reconnaissance Orbiter's High Resolution Imaging Science Experiment (HiRISE). *Journal of Geophysical Research: Planets*, *112*(E5). https://doi.org/https://doi.org/10.1029/2005JE002605

McEwen, A. S., Ojha, L., Dundas, C. M., Mattson, S. S., Byrne, S., Wray, J. J., et al. (2011). Seasonal Flows on Warm Martian Slopes. *Science*, *333*, 740–743. https://doi.org/https://doi.org/10.1126/science.1204816

McSween, H. Y., McGlynn, I. O., & Rogers, A. D. (2010). Determining the modal mineralogy of Martian soils. *Journal of Geophysical Research: Planets*, *115*(12), 1–10.

https://doi.org/10.1029/2010JE003582

Meslin, P.-Y., Gasnault, O., Forni, O., Schröder, S., Cousin, A., Berger, G., et al. (2013). Soil Diversity and Hydration at Gale Crater , Mars. *Science*, *341*(September), 1–9. Retrieved from http://science.sciencemag.org/content/sci/341/6153/1238670.full.pdf

Milliken, R. E., Mustard, J. F., Poulet, F., Jouglet, D., Bibring, J. P., Gondet, B., & Langevin, Y. (2007). Hydration state of the Martian surface as seen by Mars Express OMEGA: 2. H2O content of the surface. *Journal of Geophysical Research: Planets*, *112*(8), 1–15. https://doi.org/10.1029/2006JE002853

Ming, D. W., Morris, R. V., Clark, B. C. (2008). The Martian Surface. In J. Bell (Ed.), *Aqueous alteration on Mars* (pp. 519–540). Cambridge University Press. https://doi.org/10.1017/cbo9780511536076

Miyamoto, H., Dohm, J. M., Beyer, R. A., & Baker, V. R. (2004). Fluid dynamical implications of anastomosing slope streaks on Mars. *Journal of Geophysical Research: Planets*, *109*(E6). https://doi.org/https://doi.org/10.1029/2003JE002234

Moroz, V. I. (1964). The Infrared Spectrum of Mars (λ1.1 - 4.1μ). *Soviet Astronomy*, *8*, 273. Retrieved from https://ui.adsabs.harvard.edu/abs/1964SvA.....8..273M

Morris, E. C. (1982). Aureole deposits of the Martian volcano Olympus Mons. *Journal of Geophysical Research: Solid Earth*, *87*(B2), 1164–1178. https://doi.org/https://doi.org/10.1029/JB087iB02p01164

Morris, R. V., & Klingelhöfer, G. (2008). Iron mineralogy and aqueous alteration on Mars from the MER Mossbauer spectrometers. In J. Bell (Ed.), *The Martian Surface* (pp. 339–366). Cambridge University Press. https://doi.org/10.1017/CBO9780511536076

Morris, R. V., Agresti, D. G., Lauer, H. V., Newcomb, J. A., Shelfer, T. D., & Murali, A. V. (1989). Evidence for pigmentary hematite on Mars based on optical, magnetic, and Mossbauer studies of superparamagnetic (Nanocrystalline) hematite. *Journal of Geophysical Research*, *94*(B3), 2760–2778. https://doi.org/10.1029/JB094iB03p02760

Morris, R. V., Golden, D. C., Bell, J. F., Lauer, H. V, & Adams, J. B. (1993). Pigmenting agents in martian soils: Inferences from spectral, Mössbauer, and magnetic properties of nanophase and other iron oxides in Hawaiian palagonitic soil PN-9. *Geochimica et Cosmochimica Acta*, *57*(19), 4597–4609. https://doi.org/https://doi.org/10.1016/0016-7037(93)90185-Y

Morris, R. V., Golden, D. C., Bell, J. F., Shelfer, T. D., Scheinost, A. C., Hinman, N. W., et al. (2000). Mineralogy, composition, and alteration of Mars Pathfinder rocks and soils: Evidence from multispectral, elemental, and magnetic data on terrestrial analogue, SNC meteorite, and Pathfinder samples. *Journal of Geophysical Research: Planets*, *105*(E1), 1757–1817. https://doi.org/10.1029/1999JE001059

Morris, R. V., Klingelhöfer, G., Schröder, C., Rodionov, D. S., Yen, A., Ming, D. W., et al. (2006). Mössbauer mineralogy of rock, soil, and dust at Meridiani Planum, Mars: Opportunity's journey across sulfate-rich outcrop, basaltic sand and dust, and hematite lag deposits. *Journal of Geophysical Research: Planets*, *111*(E12). https://doi.org/https://doi.org/10.1029/2006JE002791

Morris, R. V., Schröder, C., Klingelhöfer, G., & Agresti, D. G. (2019). Mössbauer Spectroscopy at Gusev Crater and Meridiani Planum: Iron Mineralogy, Oxidation State, and Alteration on Mars. In J. F. Bell III, J. L. Bishop, & J. E. Moersch (Eds.), *Remote Compositional Analysis: Techniques for Understanding Spectroscopy, Mineralogy, and Geochemistry of*

Planetary Surfaces (pp. 538–554). Cambridge: Cambridge University Press. https://doi.org/DOI: 10.1017/9781316888872.029

Murchie, S., Mustard, J., Bishop, J., Head, J., Pieters, C., & Erard, S. (1993). Spatial Variations in the Spectral Properties of Bright Regions on Mars. *Icarus*, *105*(2), 454–468. https://doi.org/https://doi.org/10.1006/icar.1993.1141

Murchie, S., Kirkland, L., Erard, S., Mustard, J., & Robinson, M. (2000). Near-Infrared Spectral Variations of Martian Surface Materials from ISM Imaging Spectrometer Data. *Icarus*, *147*(2), 444–471. https://doi.org/https://doi.org/10.1006/icar.2000.6446

Murchie, S. L., Bibring, J.-P., Arvidson, R. E., Bishop, J. L., Carter, J., Ehlmann, B. L., et al. (2019). Visible to Short-Wave Infrared Spectral Analyses of Mars from Orbit Using CRISM and OMEGA. In J. F. Bell III, J. L. Bishop, & J. E. Moersch (Eds.), *Remote Compositional Analysis: Techniques for Understanding Spectroscopy, Mineralogy, and Geochemistry of Planetary Surfaces* (pp. 453–483). Cambridge: Cambridge University Press. https://doi.org/DOI: 10.1017/9781316888872.025

Murchie, S, Arvidson, R., Bedini, P., Beisser, K., Bibring, J.-P., Bishop, J., et al. (2007). Compact Reconnaissance Imaging Spectrometer for Mars (CRISM) on Mars Reconnaissance Orbiter (MRO). *Journal of Geophysical Research: Planets*, *112*(E5). https://doi.org/https://doi.org/10.1029/2006JE002682

Mustard, J. F., Erard, S., Bibring, J.-P., Head, J. W., Hurtrez, S., Langevin, Y., et al. (1993). The surface of Syrtis Major: Composition of the volcanic substrate and mixing with altered dust and soil. *Journal of Geophysical Research: Planets*, *98*(E2), 3387–3400. https://doi.org/https://doi.org/10.1029/92JE02682

Neukum, G., & Jaumann, R. (2004). HRSC: The high resolution stereo camera of Mars Express. In *Mars Express: The Scientific Payload* (Vol. 1240, pp. 17–35).

Newman, C. E., Lewis, S. R., & Read, P. L. (2005). The atmospheric circulation and dust activity in different orbital epochs on Mars. *Icarus*, *174*(1), 135–160. https://doi.org/10.1016/j.icarus.2004.10.023

Ojha, L., Lewis, K., Karunatillake, S., & Schmidt, M. (2018). The Medusae Fossae Formation as the single largest source of dust on Mars. *Nature Communications*, *9*(1), 2867. https://doi.org/10.1038/s41467-018-05291-5

Oyama, V. I., Berdahl, B. J., Woeller, F., & Lehwalt, M. (1978). The chemical activities of the Viking biology experiments and the arguments for the presence of superoxides, peroxides, γ-fe2o3 and carbon suboxide polymer in the Martian soil. In R. B. T.-L. S. and S. R. Holmquist (Ed.) (pp. 3–8). Pergamon. https://doi.org/https://doi.org/10.1016/B978-0-08-022022-2.50005-8

Pimentel, G. C., Forney, P. B., & Herr, K. C. (1974). Evidence about hydrate and solid water in the Martian surface from the 1969 Mariner Infrared Spectrometer. *Journal of Geophysical Research (1896-1977)*, *79*(11), 1623–1634. https://doi.org/https://doi.org/10.1029/JB079i011p01623

Piqueux, S., Kleinböhl, A., Hayne, P. O., Heavens, N. G., Kass, D. M., McCleese, D. J., et al. (2016). Discovery of a widespread low-latitude diurnal CO2 frost cycle on Mars. *Journal of Geophysical Research: Planets*, *121*(7), 1174–1189.

Pollack, J. B., Colburn, D. S., Flasar, F. M., Kahn, R., Carlston, C. E., & Pidek, D. (1979). Properties and effects of dust particles suspended in the Martian atmosphere. *Journal of*

Geophysical Research: Solid Earth, *84*(B6), 2929–2945. https://doi.org/https://doi.org/10.1029/JB084iB06p02929

Pommerol, A., Thomas, N., Affolter, M., Portyankina, G., Jost, B., Seiferlin, K., & Aye, K.-M. (2011). Photometry and bulk physical properties of Solar System surfaces icy analogs: The Planetary Ice Laboratory at University of Bern. *Planetary and Space Science*, *59*(13), 1601–1612. https://doi.org/https://doi.org/10.1016/j.pss.2011.07.009

Pommerol, A., Jost, B., Poch, O., El-Maarry, M. R., Vuitel, B., & Thomas, N. (2015). The SCITEAS experiment: Optical characterizations of sublimating icy planetary analogues. *Planetary and Space Science*, *109–110*, 106–122. https://doi.org/https://doi.org/10.1016/j.pss.2015.02.004

Pommerol, A., Thomas, N., Almeida, M., Read, M., Becerra, P., Cesar, C., et al. (2022). In-flight radiometric calibration of the ExoMars TGO Colour and Stereo Surface Imaging System. *Planetary and Space Science*, 105580. https://doi.org/https://doi.org/10.1016/j.pss.2022.105580

Posey-Dowty, J., Moskowitz, B., Crerar, D., Hargraves, R., Tanenbaum, L., & Dowty, E. (1986). Iron oxide and hydroxide precipitation from ferrous solutions and its relevance to Martian surface mineralogy. *Icarus*, *66*(1), 105–116. https://doi.org/https://doi.org/10.1016/0019-1035(86)90010-2

Putzig, N. E., & Mellon, M. T. (2007). Apparent thermal inertia and the surface heterogeneity of Mars. *Icarus*, *191*(1), 68–94. https://doi.org/10.1016/j.icarus.2007.05.013

Sánchez-Lavega, A., del Río-Gaztelurrutia, T., Hernández-Bernal, J., & Delcroix, M. (2019). The Onset and Growth of the 2018 Martian Global Dust Storm. *Geophysical Research*

Letters, *46*(11), 6101–6108. https://doi.org/https://doi.org/10.1029/2019GL083207

Schorghofer, N., & King, C. M. (2011). Sporadic formation of slope streaks on Mars. *Icarus*, *216*(1), 159–168. https://doi.org/https://doi.org/10.1016/j.icarus.2011.08.028

Schorghofer, N., Aharonson, O., & Khatiwala, S. (2002). Slope streaks on Mars: Correlations with surface properties and the potential role of water. *Geophysical Research Letters*, *29*(23), 41–44. https://doi.org/https://doi.org/10.1029/2002GL015889

Schorghofer, N., Aharonson, O., Gerstell, M. F., & Tatsumi, L. (2007). Three decades of slope streak activity on Mars. *Icarus*, *191*(1), 132–140. https://doi.org/https://doi.org/10.1016/j.icarus.2007.04.026

Schwertmann, U., & Fischer, W. R. (1973). Natural "amorphous" ferric hydroxide. *Geoderma*, *10*(3), 237–247. https://doi.org/https://doi.org/10.1016/0016-7061(73)90066-9

Singer, R. B., McCord, T. B., Clark, R. N., Adams, J. B., & Huguenin, R. L. (1979). Mars surface composition from reflectance spectroscopy: a summary. *Journal of Geophysical Research*, *84*(B14), 8415–8426. https://doi.org/10.1029/JB084iB14p08415

Sinton, W. M. (1967). On the composition of martian surface materials. *Icarus*, *6*(1), 222–228. https://doi.org/https://doi.org/10.1016/0019-1035(67)90018-8

Soderblom, L. A., & Bell, J. (2008). Exploration of the Martian surface: 1992–2007. In J. Bell (Ed.), *The Martian Surface* (pp. 3–19). Cambridge University Press. https://doi.org/10.1017/CBO9780511536076

Sullivan, R., Thomas, P., Veverka, J., Malin, M., & Edgett, K. S. (2001). Mass movement slope streaks imaged by the Mars Orbiter Camera. *Journal of Geophysical Research: Planets*, *106*(E10), 23607–23633. https://doi.org/https://doi.org/10.1029/2000je001296

Szwast, M. A., Richardson, M. I., & Vasavada, A. R. (2006). Surface dust redistribution on Mars as observed by the Mars Global Surveyor and Viking orbiters. *Journal of Geophysical Research: Planets*, *111*(E11). https://doi.org/https://doi.org/10.1029/2005JE002485

Thomas, N., Cremonese, G., Ziethe, R., Gerber, M., Brändli, M., Bruno, G., et al. (2017). The Colour and Stereo Surface Imaging System (CaSSIS) for the ExoMars Trace Gas Orbiter. *Space Science Reviews*, *212*(3), 1897–1944. https://doi.org/10.1007/s11214-017-0421-1

Thomas, N., Pommerol, A., Almeida, M., Read, M., Cremonese, G., Simioni, E., et al. (2022). Absolute calibration of the Colour and Stereo Surface Imaging System (CaSSIS). *Planetary and Space Science*, *211*, 105394. https://doi.org/https://doi.org/10.1016/j.pss.2021.105394

Valantinas, A., & Schultz, P. H. (2020). The origin of neotectonics on the lunar nearside. *Geology*, *48*(7). https://doi.org/10.1130/G47202.1

Valantinas, A., Becerra, P., Pommerol, A., Tornabene, L. L., Affolter, L., Cremonese, G., et al. (2021). CaSSIS Color and multi-angular observations of martian slope streaks. *Planetary and Space Science*, *209*(November), 105373. https://doi.org/10.1016/j.pss.2021.105373

Wellington, D. F., & Bell, J. F. (2020). Patterns of surface albedo changes from Mars Reconnaissance Orbiter Mars Color Imager (MARCI) observations. *Icarus*, *349*(October 2018). https://doi.org/10.1016/j.icarus.2020.113766

Wordsworth, R., Knoll, A. H., Hurowitz, J., Baum, M., Ehlmann, B. L., Head, J. W., & Steakley, K. (2021). A coupled model of episodic warming, oxidation and geochemical transitions on early Mars. *Nature Geoscience*, *14*(3), 127–132. https://doi.org/10.1038/s41561-021-00701-8

Yen, A. S., Gellert, R., Schröder, C., Morris, R. V., Bell, J. F., Knudson, A. T., et al. (2005). An

integrated view of the chemistry and mineralogy of martian soils. *Nature*, *436*(7047), 49–54. https://doi.org/10.1038/nature03637

Zent, A. P., & Quinn, R. C. (1997). Measurement of H2O adsorption under Mars-like conditions: Effects of adsorbent heterogeneity. *Journal of Geophysical Research: Planets*, *102*(E4), 9085–9095. https://doi.org/https://doi.org/10.1029/96JE03420

Zurek, R. W. (1982). Martian great dust storms: An update. *Icarus*, *50*(2), 288–310. https://doi.org/https://doi.org/10.1016/0019-1035(82)90127-0

Zurek, R. W., & Martin, L. J. (1993). Interannual variability of planet-encircling dust storms on Mars. *Journal of Geophysical Research: Planets*, *98*(E2), 3247–3259. https://doi.org/https://doi.org/10.1029/92JE02936

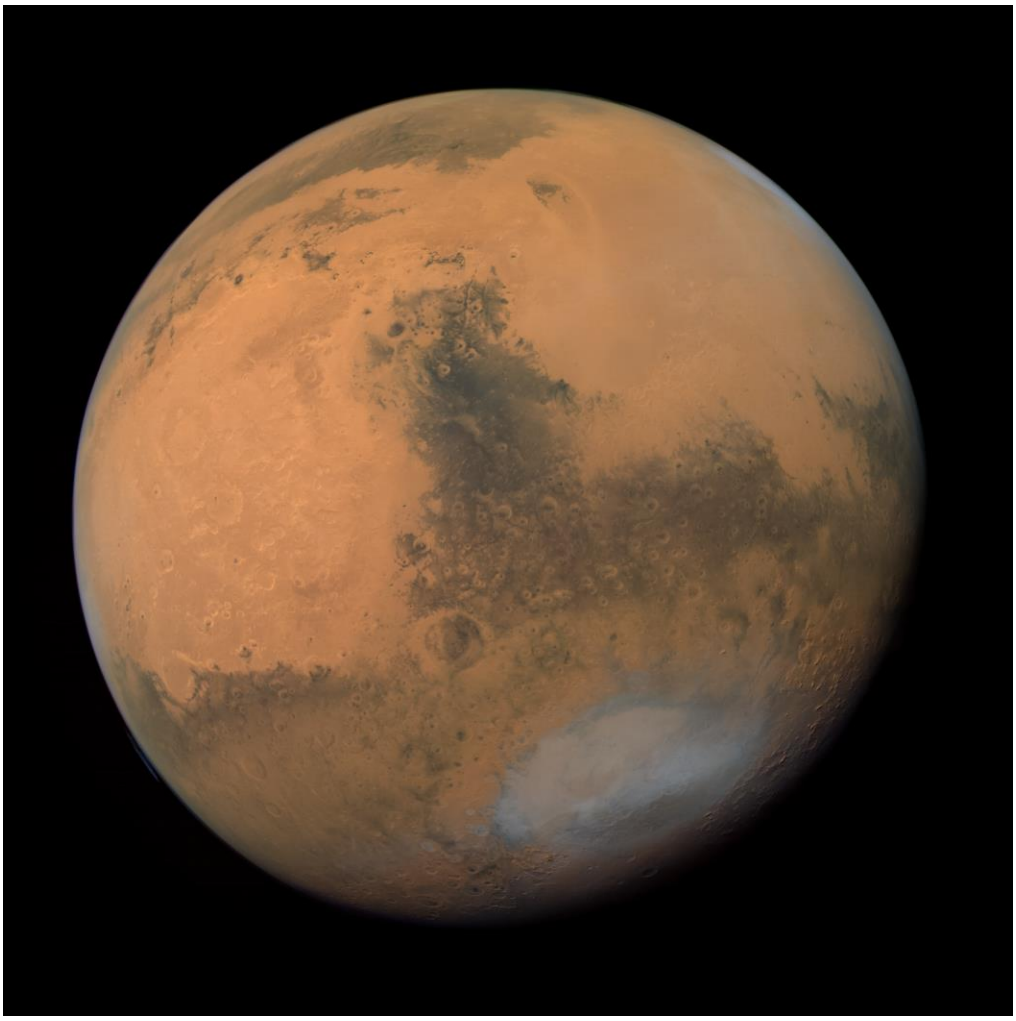

Figure 1. The dark region of Syrtis Major divides the bright regions of Arabia Terra and Elysium Planitia in this image. The clouds or fogs near the terminator are in Hellas basin. Emirates eXploration Imager (EXI) color composite image (filters f635, f546 and f437). Credit: CU/LASP EMM/EXI ITF/Kevin M. Gill.

Table 1. Examples of ferric iron oxide minerals detected on Mars.

Mineral	Chemical formula	Crystallinity	Group	Detected on Mars?
Hematite	α-$Fe^{3+}_2O_3$	high	Iron oxide	✓
Ferrihydrite	$5Fe^{3+}_2O_3 \cdot 9H_2O$	low	Iron oxyhydroxide	-
Maghemite	γ- $Fe^{3+}_2O_3$	high	Iron oxide	-
Magnetite	$Fe^{2+}Fe^{3+}_2O_4$	high	Iron oxide	✓
Goethite	α-$Fe^{3+}O(OH)$	high	Iron oxyhydroxide	✓
Lepidocrocite	γ-$Fe^{3+}O(OH)$	high	Iron oxyhydroxide	-
Feroxyhyte	δ'-$Fe^{3+}O(OH)$	high	Iron oxyhydroxide	-
Schwertmannite	$Fe^{3+}_8O_8(OH)_6(SO_4) \cdot n H_2O$	low	Iron-oxy hydroxysulphate	-
Hydronium jarosite	$(H_3O)Fe^{3+}_3(SO_4)_2(OH)_6$	high	Iron-oxy hydroxysulphate	Jarosite only
Akaganeite	β-$Fe^{3+}O(OH)$	high	Iron oxyhydroxide	✓
Hisingerite	$Fe^{3+}_2Si_2O_5(OH)_4 \cdot 2 H_2O$	low	Iron phyllosilicate	-
Iddingsite	$MgFe^{3+}_2Si_3O_{10} \cdot 4(H_2O)$	Not a mineral	Mixture	-

Chapter 2:

CASSIS COLOR AND MULTI-ANGULAR OBSERVATIONS OF MARTIAN SLOPE STREAKS

A.Valantinas[1], P. Becerra[1], A. Pommerol[1], L.L. Tornabene[2], L. Affolter[1], G. Cremonese[3], E. Hauber[4], A.S. McEwen[5], G. Munaretto[3], M. Pajola[3], A. Parkes Bowen[6], M.R. Patel[7], V.G. Rangarajan[2], N. Schorghofer[8] and N. Thomas[1]

[1]Physikalisches Institut, Universität Bern, Sidlerstrasse 5, 3012 Bern, Switzerland.
[2]Institute for Earth & Space Exploration, Western University, London, Canada.
[3]Osservatorio Astronomico di Padova, INAF, Padova, Italy.
[4]DLR, Institut für Planetenforschung, Berlin, Germany.
[5]Lunar and Planetary Lab, University of Arizona, Tucson, USA.
[6]Space Research Centre, University of Leicester, Leicester, UK.
[7]Open University, Milton-Keynes, UK.
[8]Planetary Science Institute, Tucson, USA.

Published in:

Planetary and Space Science

1 November 2021

Abstract

Slope streaks are albedo features that form frequently on equatorial Martian slopes. Most slope streaks are dark relative to surrounding terrains, a minor fraction is bright, and there are rare transitioning streaks that exhibit a contrast reversal partway downslope. Their formation mechanisms and physical surface properties are not well understood. New observations acquired by the Colour and Stereo Surface Imaging System (CaSSIS) on board ESA's ExoMars Trace Gas Orbiter (TGO) provide insights into slope streaks' surface microstructure, roughness and particle size ranges. Using multiple phase angle observations, we show that dark slope streaks are substantially rougher and possibly more porous than their bright counterparts, which are likely composed of more compact regolith. Color data acquired in the four wavelength bands suggest that dark streaks are spectrally similar to bright streaks but are composed of larger particles. The comparison of our orbital results to the laboratory measurements of Martian regolith analogs indicates that particles within dark slope streaks may be up to a factor of four larger than the granular material of the surrounding terrains. At one study site in Arabia Terra, using complementary imagery from other orbiters, we identify a case where dark slope streaks turned fully bright in a twenty-year period. These and CaSSIS observations suggest that bright slope streaks are old dark slope streaks, likely formed by deposition of dust or decomposition of surface aggregates into smaller particles.

1 Introduction

The surface of contemporary Mars hosts a variety of active geologic processes (Dundas et al., 2021). Linear and fan-shaped albedo features, known as dark slope streaks, were discovered in Viking orbiter images of the Olympus Mons aureole (Morris, 1982). Knowledge about their global extent and formation mechanism was considerably expanded using the Mars Global Surveyor (MGS) Mars Orbiter Camera (MOC; Malin and Edgett 2001) datasets (Sullivan et al., 2001; Schorghofer et al., 2007). Very high image resolution (~0.3 m/px) analysis studies based on the Mars Reconnaissance Orbiter (MRO) High Resolution Imaging Experiment (HiRISE; McEwen et al. 2007) revealed further information about slope streak morphology and aeolian surface evolution (e.g. Chuang et al., 2010). Slope streaks are found in equatorial, high albedo and low thermal inertia regions that are covered by a fine surface particle layer (Ruff and Christensen, 2002). Within the forty years of orbital observations of slope streaks several hypotheses have been raised to explain their origin. Initially proposed to be debris weathered from dark pyroclastic materials (Morris, 1982), a dry model where avalanching surface dust exposes a deeper, darker, and presumably less oxidized Martian substrate was subsequently suggested (Williams, 1991; Sullivan et al., 2001; Dundas, 2020). The latter model was supported by low-sun illumination HiRISE observations, which showed that a surface layer is removed, at least in large slope streaks (Phillips et al., 2007; Chuang et al., 2007). Conversely, several properties of slope streaks have been proposed as evidence for fluid-related formation mechanisms. Slope streak ability to initiate well below the angle of repose (Brusnikin et al., 2016) and exhibit bifurcating morphology (Miyamoto et al., 2004), the presence of a fine particle layer that slows desiccation (Ferguson and Lucchitta, 1984) and allows capillarity (Kreslavsky

and Head, 2009); and the regional detection of chloride-rich chemistry (Bhardwaj et al., 2017) have all been inferred to support fluid formation models.

Slope streaks are known to be darker than their surrounding material by ~10% (Sullivan et al.,2001). The various contrast states of slope streak darkness suggested that a time-dependent fading mechanism likely related to dust deposition is occurring (Aharonson et al., 2003). Some streaks have been observed to fade on timescales of four decades (Bergonio et al., 2013) and generally persist longer than the seasonal occurrences of dust devil tracks (Balme et al., 2003). While slope streaks have been observed to form sporadically (Schorghofer and King, 2011), seasonal formation has also been recently indicated (Heyer et al., 2019).

On Mars, a peculiar type of slope streaks that are brighter than their surroundings by up to 2% are known to exist (Sullivan et al., 2001). Bright streaks might appear on the same slope as dark streaks, and remain visible under varying lighting geometry conditions (Schorghofer et al., 2007). Initially it was proposed that bright streaks form in a thinner particle layer (Sullivan et al., 2001). However, the absence of newly formed bright slope streaks suggested that bright slope steaks are simply old dark slope streaks (Schorghofer et al., 2007). A rare transitioning case in which slope streak brightness contrast reverses partway downslope was observed and suggested to be either an angular unconformity (Sullivan et al., 2001) or viewing angle effect (Baratoux et al., 2006).

Using hyperspectral images from the Compact Reconnaissance Imaging Spectrometer for Mars (CRISM; Murchie et al. 2007) and HiRISE color photometry, Mushkin et al. (2010) found that slope streaks are spectrally featureless at the visible and near-infrared wavelengths. They concluded that dark slope streaks appear dark not due to an exposure of the pre-existing

substrate, as suggested by the avalanching dust model (Sullivan et al., 2001), but due to soil enrichment of low-albedo ferric oxides and amalgamation of nanophase FeOx grains into larger particles. They argued that slope streak surfaces are dry, but a short-lived liquid phase was needed to explain the particle agglomeration. Although no spectral hydration signatures were found in a subsequent study (Amador et al., 2016).

Little is known about the rare transitioning and bright slope streaks. In this paper, we investigate the properties and plausible origin of these much rarer surface features. First, to find out the extent of bright slope streak distributions and also to locate previously undiscovered transitioning slope streaks, we implemented a grid mapping approach of Arabia Terra using MRO's Context Camera images (CTX; Malin et al. 2007). We then investigated the photometric parameters of these streaks, such as particle size, roughness and surface texture, through multi-angular observations of all three types of slope streaks (i.e. dark, bright and transitioning; Fig. 1). For this purpose we primarily use images taken by the Colour and Stereo Surface Imaging System (CaSSIS; Thomas et al. 2017) onboard the ExoMars Trace Gas Orbiter (TGO), which is able to acquire such multi-angular data due to the non-sun-synchronous orbit of TGO. To investigate particle size effects, we compared our CaSSIS observations with the spectral reflectance of the Mars Global Simulant (MGS-1) soil (Cannon et al., 2019), measured with the PHIRE-2 (PHysikalisches Institut Reflectance Experiment - 2) radio-goniometer (Pommerol et al., 2011) and the Mobile Hyperspectral Imaging System (MoHIS; Pommerol et al. 2015). In addition, we used a reflectance model (Hapke, 2012) to analyze the effects of particle size on the regolith albedo. When higher resolution or a time dependent analysis were found to be necessary

(and were available), we complemented the CaSSIS observations with images acquired by HiRISE and MOC.

2 Methods and Data

2.1 Mapping of bright slope streaks in Arabia Terra

Based on MOC observations, it was shown that bright slope streaks are more common in Arabia Terra and are much rarer in other geologic regions where dark slope streaks are abundant (Schorghofer et al., 2007). To map the complete regional distributions of bright slope streaks in Arabia Terra we used a normalized global CTX mosaic, which has been recently released by Dickson et al. (2018). It provides an excellent opportunity for large scale surveys of geologic features that are larger than 10 meters in size. MRO's CTX acquires panchromatic (500-750 nm) images at 5-6 m/px in resolution, and with image swaths of 30 km x ≥40 km, it has imaged >97% of the Martian surface. We selected a 30° x 40° bounding box in Arabia Terra (Fig. 1) and employed a qualitative grid-mapping method (Ramsdale et al., 2017). This region of interest was divided into ~16,000 hexagonal facets 20 km in diameter. 20 km size hexagons were determined to be the most optimal for rapid large scale studies. Each hexagon was assigned a category: 1) no data available, 2) bright slope streaks absent 3) bright slope streaks present. To qualify for the third category at least one bright slope streak had to be present in a hexagon. In addition, to date, only one case of transitioning slope streak had been observed (Sullivan et al., 2001; Baratoux et al., 2006, also see Fig. 1D). Thus, we also use our mapping efforts to search for more transitioning slope streaks in Arabia Terra.

2.2 CaSSIS photometry

Given TGO's non-Sun-synchronous orbit, CaSSIS can monitor surface changes at varying local solar times (LST), several times per Martian season. We made use of this capability by acquiring multi-angular observations of several selected slope streak sites in our study (see Table 1). This allows us to investigate plausible phase-angle-dependent effects, which are closely associated with surface parameters such as particle size, porosity and/or roughness (Fernando et al., 2016). CaSSIS observations are generally acquired in at least two of the four possible color bands (BLU 497 nm, PAN 677 nm, RED 835 nm and NIR 940 nm; Roloff et al. 2017; Perry et al. 2021 this issue). The observations we use in this paper were primarily taken in all four CaSSIS filters. We display them here as NPB (NIR, PAN, BLU) or RPB (RED, PAN, BLU) linearly stretched false color composite products (Perry et al. 2021, this issue). This allows us to investigate possible compositional differences between dark, bright and transitioning slope streaks.

We selected 25 sites in Arabia Terra that contained dark, bright and transitioning slope streaks for the photometric analysis study. Additionally, we include one site in Tharsis, one in Labeatis Fossae and two in Amazonis Planitia (see Table 1 for details). Out of a total of 29 sites, 14 include transitioning slope streaks that had previously never been imaged. The three types of slope streaks observed in our study (see Fig. 1 for examples) are defined as follows: (1) dark slope streaks are entirely darker than their surroundings, i.e. the whole streak, from apex to terminus has a lower apparent brightness in images then the surrounding terrain; (2) bright streaks are entirely brighter than their surroundings from apex to terminus; (3) transitioning streaks are brighter than the surroundings at the apex, but the contrast reverses partway downslope, i.e. the terminus of a transitioning streak is darker than its surroundings. We

measured the I/F values of the apexes and termini of selected slope streaks (I/F = detected radiance (I) divided by the solar irradiance at zero incidence (F), such that I/F = 1 for a normally illuminated, perfectly diffuse reflector). To do this, we calculated the mean I/F values of regions-of-interest (ROIs), typically 30-100 pixels in size. The ROI I/F averages (numerator) for each CaSSIS band were then divided by respective I/F values for similar ROIs of the surrounding surface (denominator), which results in ratioed reflectance spectra. Such relative photometry methods are well established (e.g. Daubar et al., 2016; Schaefer et al., 2019; Munaretto et al., 2020, 2021), and afford the advantage of cancelling out the reflectance dependence at the condition that both ROIs selected have the same local slope and aspect. Ratioed reflectance spectra also partially cancel out atmospheric attenuation effects. However, light scattered by the Martian atmosphere is an additive, not a multiplicative term. Also, scattered light is dependent on: 1) wavelength (greater at low BLU than long NIR wavelengths), 2) phase angle (atmospheric column is larger for larger phase angles) and 3) optical opacity (r) values. While a detailed and quantitative study of these effects is left for future work, we use atmospheric opacity values to qualitatively assess the potential impact of atmospheric effects on the surface reflectance.

A quantitative assessment of the atmospheric conditions in each CaSSIS observation was made using the climatological assimilation of dust opacities derived from the Mars Climate Sounder (MCS) instrument (McCleese et al., 2007). The assimilated MCS column dust optical depths provide a global-scale reanalysis of the atmospheric dust loading during a period of the CaSSIS observations, with a grid point spacing of approximately 200 km. The assimilation is an extension of the Open access to Mars Assimilated Remote Soundings (OpenMARS) dataset (Holmes et al., 2020), a publicly available global record of Martian weather from 1999 onward.

The image execution times and location of each CaSSIS image were then used to extract the dust opacity at visible wavelengths, which gives a dust optical depth value to accompany each CaSSIS image. While this approximation provides a means to evaluate whether a CaSSIS image is suitable for color and multispectral analysis, we note that the assimilation is rather coarse in resolution (~200 km x 200 km). Thus, a particular opacity estimate may not reflect the conditions under which a particular CaSSIS image (generally less than 10 x 50 km on average) was taken, and is only used as a proxy for a more accurate estimation of dust opacity.

2.3 Laboratory measurements

Precise, image-based photometric analyses of the Martian surface are often complicated by differences in illumination and observation geometries among images, varying amounts of scattering by aerosols and clouds in the atmosphere, or the limited signal-to-noise ratio of the data. Such studies are therefore ideally complemented by measurements of the reflectance of analogues in the laboratory and physical modelling of light scattering. Physical modelling allows us to vary all relevant parameters independently within a wide parameter space, in order to investigate their influence and understand the physical causes behind photometric behaviors. On the other hand, experimenting with actual analogue soil samples allows us to consider some of the complexity encountered on real planetary surfaces (including possible correlations between the parameters), and can provide ground truth for the interpretation of remote-sensing data. Here, we use both approaches in a complementary way.

For decades, JSC Mars-1, a natural weathered volcanic ash from Hawaii (Allen et al., 1998), has been the most widely used Martian soil analogue. It has been used to study on Earth

various properties expected to be similar to those of the Martian surface material. JSC Mars-1 is not distributed anymore, however and a replacement is desirable. The CLASS Exolith Lab, located at the University of Central Florida, has undertaken the development of suitable analogous materials for the surfaces of various Solar System objects. There the analogue material is produced by mixing a series of individual mineral and phase components based on our knowledge to date of the compositional characteristics of soils (Cannon et al., 2019). In particular, their Mars Global simulant (MGS-1) was designed to mimic the chemical and mineralogical compositions of soil from the Rocknest site, which was analysed by Curiosity (Blake et al., 2013) and considered the best characterised Martian soil to date. Note however that the composition of this soil sample is nearly indistinguishable from that of other in-situ soil samples, which is what makes it suitable as a global soil simulant that can be used in a variety of contexts. The overall composition of the sample is basaltic, but it also contains hydrated silica, ferrihydrite and magnesium sulfate to simulate the amorphous fraction of the Rocknest sample, which itself consists mainly of basaltic glass with amorphous or poorly crystalline components derived from Martian dust.

To prepare our MGS-1 sample for analysis, we baked it at 333 K for 24 hours and then dry-sieved it using a sonic separator (VariSifter™ from Advantech Manufacturing, Inc.) to retrieve the different size fractions we investigated (Fig. 2). Note that because of the way the initial sample was produced (i.e., mixing several components with different particle size distributions and resistance to crushing), dry-sieving the bulk sample almost certainly results in some mechanical fractionation of minerals/phases between the different particle size fractions. However, such fractionation is also expected on Mars, where the bimodal distribution of particle

sizes corresponds to a mineralogical distinction between fine dust particles rich in iron oxides and coarser sand-sized particles derived from local mechanical alteration of the basaltic crust. Based on this assumption, we use the smallest particle size ranges of sieved MGS-1 samples to serve as an analog for the surface fine grains found in slope streak rich equatorial regions. However, such analog samples should be used with caution since the dust grains present in bright and low thermal inertia regions of Arabia Terra are not well constrained and have not been studied in detail by any lander.

The resulting size-sorted samples were then characterized using different techniques, including visible (VIS) Bidirectional Reflectance Distribution Function (BRDF), and visible and near-infrared (VIS-NIR) hyperspectral imaging. To experimentally test phase angle effects on reflectance behavior of sieved MGS-1 samples, we used the PHIRE-2 radio-goniometer. PHIRE-2 is designed to measure the visible bidirectional reflectance of surface samples over a wide range of geometries and under cold (240 K) to ambient (295K) conditions (Pommerol et al., 2011). Two mobile arms rotate around the samples within a hemisphere to illuminate the sample and measure the scattered radiance within a wavelength range restricted by one of six bandpass filters (with centers at 450, 550, 650, 750, 905 and 1064 nm and with Full width at Half Maximum bandpasses of 70 nm for VIS wavelengths and 30 nm for NIR wavelengths). The measurements are automated to produce dense sets of reflectance data, which can then be interpolated and integrated to estimate the hemispherical albedo of the sample or other photometric quantities, or fit by photometric models. The reflectance data are radiometrically calibrated by comparing the measurements of the sample to measurements of a plate of Spectralon™ (Labsphere) that has well-known reflectance properties.

For each particle size fraction of MGS-1 we also acquire high resolution spectra using The Mobile Hyperspectral Imaging System (MoHIS). MoHIS was constructed from the setup previously used to acquire hyperspectral images of samples in the Simulation Chamber for Imaging the Temporal Evolution of Analogue Samples (SCITEAS; Pommerol et al. 2015). MoHIS consists of two cameras, one sensitive in the VIS range (0.4 – 1.0 μm) and the other in the NIR (0.9 – 2.4 μm), and a monochromatic illumination system, allowing acquisitions of hyperspectral images of the samples (Pommerol et al., 2015). The hyperspectral cubes are produced by illuminating the sample with monochromatic light, and then acquiring an image with one of the two cameras before shifting the wavelength slightly and repeating the procedure. We acquire these measurements with high spectral resolution (6.5 to 13 nm), and a spectral sampling such that there is overlap between adjacent bands (6 to 15 nm), mimicking datasets acquired by orbital instruments such as OMEGA or CRISM. From the hyperspectral cubes, averaged spectra over user-defined regions of interest (ROI) can be calculated and exported. As with PHIRE-2, the radiometric calibration of the MoHIS data consists of a normalization to the measured reflectance of a Spectralon™ plate after subtraction of a dark signal (see Pommerol et al., 2015; Yoldi et al., 2021) and correction of minor absorption by the Spectralon beyond 2 μm using manufacturer data.

2.4 Reflectance modeling

To complement orbital observations and laboratory measurements in this work, we used the Hapke spectral reflectance model (Hapke, 2012) (for methodology see the Appendix section). Our goal was to investigate the effects of different particle sizes of Martian dust on the spectral

reflectance that would be observed by orbital imagers. Our implementation of the model primarily follows the approach of Becerra et al. (2015), which is itself based on those of Roush (1994) and Warell and Davidsson (2010), and neglects atmospheric extinction and scattering. The model simulates the reflectance spectra of a uniform dusty surface on Mars for a user-given mean particle size with a 1 nm spectral sampling between 300 and 4000 nm. The complex indices of refraction (optical constants) of the simulated dust are obtained from the CRISM/OMEGA measurements of Wolff et al. (2009). In order to simulate instrument observations, the 1 nm model spectra are convolved with the instrument bandpasses. Convolving the raw modeled spectra with the CaSSIS band-pass coefficients (Thomas et al., 2017) results in simulated CaSSIS I/F values for each grain size selected. The same convolution procedure was also used to convolve the MoHIS measurements to CaSSIS I/F, outputting laboratory-based simulations of CaSSIS observations of the MGS-1 simulant.

3 Results

3.1 Mapping of bright slope streaks in Arabia Terra

The results of our grid mapping campaign are shown in Fig. 3. The region of interest is roughly 2000 km x 2000 km in size and covers most of Arabia Terra where bright slope streaks exist. An initial observation at this scale suggests that bright slope streaks are very common in Arabia Terra. The distribution of bright slope streaks in our study area is not homogeneous, i.e. the density of the streaks increases towards the center of the map. We note that an HRSC-MOLA slope mosaic does not suggest steep slopes in these regions. Moreover, the crater size-frequency distributions do not appear to be correlated with the increased density of bright slope streaks,

although some bright streaks are observed around the rims of large craters. At smaller local scales not resolvable by this map, streaks are primarily found around small craters, channels and hills. An OMEGA nanophase ferric iron oxide abundance map (300 m/px to 5 km/px) (Ody et al., 2012) and TES dust cover index map (3.5 km/px) (Ruff and Christensen, 2002) indicate evenly distributed dust in this region. The bright slope streak distributions are likely correlated with regions where dark slope streaks are less active, i.e. regions with few fresh dark streaks contain many old bright slope streaks (see also Schorghofer et al., 2007). Alternatively, there could be a regional thicker settled dust layer in the center of Arabia. However, the apparent lack of bright streaks in other regions than Arabia may suggest different surface fines particle size distribution and/or composition.

3.2 Observation of a brightening slope streak

A time-dependent slope streak contrast reversal that would provide clues about the relationship between dark and bright streaks, has not yet been reported. Here, we have captured such a contrast reversal of several slope streaks at one site in our study region within Arabia Terra (site S15; Fig. 4). This site was first observed at high resolution by MOC, on 2001-04-16, and the streaks visible in this MOC image appear dark, although slight brightening at the apexes can already be observed. On 2019-12-27, CaSSIS observed this site again, with a slightly different Sun-azimuth direction (incidence: 56.5°) as the original MOC observation (incidence: 35.6°). The streaks in this CaSSIS image appear almost completely bright.

Finally, the same location was observed recently by HiRISE on 2020-10-04, which confirmed the observation in the CaSSIS image, i.e. that such streaks are indeed brighter than

their surroundings. These three observations by MOC, CaSSIS and HiRISE suggest an apex-to-bottom brightening process. To rule out possible photometric effects, i.e. the prospect that streaks appear brighter under high phase angle illumination, we present multi-angular observations that show on the contrary that streaks brighten with decreasing phase angle (see subsection 3.4).

3.3 Slope streak color observations

Based on photometric measurements of 34 dark, 25 bright and 19 transitioning streaks from all our study sites, we calculated ratioed reflectance spectra in each CaSSIS band (Fig. 5). Averages were based only on images that were identified by the atmospheric model to have $r<1$ (see Table 1). Where more than one observation was available for a given site, only the one with the best atmospheric conditions was included in the average. In total 29 CaSSIS images were used for the calculation of ratioed reflectance averages. For each streak we included one measurement at the apex and one at the terminus, which revealed that on average all 3 types of streaks are brighter at the apex and darker at the terminus. Dark streaks are on average darker than their surroundings by ~6% and bright streaks are brighter by ~2%. The darkest streak was found to be 12% darker and the brightest streak 4% brighter than the surroundings. The largest difference between apex and terminus measurements can be seen in transitioning slope streak spectra, for which the apex is brighter than the terminus by about 3%. We also observed that both transitioning streak termini and both sections of dark slope streaks exhibit a characteristic "kink" upwards from PAN to BLU wavelengths. CRISM spectral ratios of dark slope streaks exhibited the same spectral

kink at <500 nm (Mushkin et al., 2010). Lastly, bright streaks and the apex of transitioning streaks instead display a roughly flat spectrum, indicative of no difference in particle size.

3.4 Slope streak multi-angular observations

Phase angle dependent phenomena related to particulate materials are known to occur on Mars. For example, dark sand deposits in Juventae Chasma appeared brighter than their surrounding in high phase angle images, thereby suggesting that it is comprised of strongly forward-scattering material (Geissler, 1992; Johnson et al., 2008). To investigate how the reflectance of bright and transitioning slope streaks varies with phase angle, we imaged site S1 (Fig. 6) under three different illumination geometries. This site includes a transitioning streak and several bright slope streaks. There is a faded bright streak at NW position from the transitioning streak T1, which has almost completely faded into the background (Fig. 6D white arrow). We performed multi-angular photometric measurements on T1 and B1 to understand how ratioed reflectance varies with phase angle. Fig. 6 reveals that differences in brightness of the B1a and B1b sections are phase-angle-dependent. Both apex and terminus measurements show an increase in brightness by 3% in the low phase angle observation (24.3°). T1a also exhibits a similar brightening under low phase. The spectrum of T1b does not exhibit a large dependence on phase angle but the characteristic "kink" from PAN to BLU was observed as in Fig. 5. Optical opacity estimates indicated that r is 1.523 for the observation shown in Fig. 6B. However, the actual atmospheric conditions for this image appear to be better than those derived from the climatology data.

At site S16 (Fig. 7), which is located in the center of a large crater in Arabia Terra, we acquired three low phase angle observations (12.3°, 19.6° and 37.7°). We analyzed the termini section of two bright streaks (B1 and B2), two dark streaks (D1 and D2) and one transitioning (T1) streak to further quantify changes in brightness. Only the termini parts were selected since they were close to homogeneous dusty areas on a comparable slope (yellowish tone material as seen in the CaSSIS NPB products). The steeper slopes of these outcrops are likely composed of different material and/or dust than the floor unit of this crater. In site S16 we also observed transitioning streaks that are not bright at the apex even in low phase angle observations (see Fig. 7B black arrow). Only surface texture observable in high resolution HiRISE images reveal that the apex is part of the same streak (ID: ESP_060342_1985). A similar type of streak can be also observed in site S21 (Table 1). Fig. 7D shows that several surface details are not visible without high signal-to-noise ratio and good atmospheric conditions. These data points are therefore not included in the photometric analysis.

The results in Fig. 7 show a slight brightening with decreasing phase angle of the two (B1 and B2) bright slope streaks by 1%. However, there is not much difference between the measurements at 12.3° and 19.6°. We again observe here a similar featureless brightening as in Fig. 6. Dark streaks (D1 and D2) also show a sharp ratio decrease by 3% in the BLU, which is even stronger under the lowest phase angle acquisition. The terminus part of T1 presents a flatter spectrum, than that in D1 and D2, but the kink from BLU to PAN is still recognizable within about 2%. The last plot in Fig. 7 features the ratio of the termini parts of transitioning (T2) and bright (B3) slope streak. The T2/B3 ratio at 19.6° phase is lower than at 37.7° phase likely because the bright streak terminus (denominator) brightened more than the dark streak terminus

(numerator). Also, it illustrates that the spectral ratio between dark and bright streak is comparable in shape to that of dark slope streak and surrounding dust (i.e. the same kink in D1, D2 and T1 plots).

We summarize our CaSSIS multi-angular results for bright and dark slope streaks in Fig. 8. This plot, in the CaSSIS PAN band (677 nm), is based on measurements of all sites from Table 1 that include two or more images and have at least one under 20° phase. Each site on the plot is a separate curve composed of either individual images and/or stereo observations. Dark slope streaks, in comparison to bright ones, exhibit a steeper phase slope and in some cases brighten by up to ~7% (site S24, 7.5 to 46.2° phase). Bright streaks show a slight (up to 1%) brightening with decreasing phase and in some cases even no brightening at all (see nearly flat spectra of site S7, 19.6 to 56.7° phase). A difference in reflectance can also be observed between stereo pairs (data points marked as stars), where the lower phase observation always includes larger ratioed reflectance value. Since CaSSIS stereo pairs are acquired roughly within 40 s, the atmospheric column in both images should be the same, therefore the observed signal is due to the light scattering properties of the surface. Fig. 8 illustrates that with decreasing phase angle dark streaks brighten more, relative to the surrounding terrain, than do the bright streaks. Also, based on this plot, we do not observe the hypothesized slope streak contrast reversal inferred from observations of Earth snow avalanches (Baratoux et al., 2006). Additionally, we have investigated the other three CaSSIS filters but did not observe a considerable wavelength dependence. However, in the BLU filter dark streaks exhibited slightly bluer ratioed reflectance values (shifted upwards in the y-axis) but retained the same slope and phase dependence. This conclusion generally agrees with multi-angular observations of OMEGA and CRISM

(Vincendon, 2013) that indicated that Mars' surface phase function behavior is independent of wavelength, at least for some surface materials.

3.5 Laboratory measurements and comparison to CaSSIS data

The results of multi-angular measurements using the PHIRE-2 radio-goniometer for six grain size fractions of MGS-1 (at wavelengths 450, 650 and 905 nm) are shown in Fig. 9, together with their reflectance spectra for the same grain size fractions acquired by MoHIS. From multi-angular data we can observe that for all particle phase curves, reflectance starts to increase as the phase angles approach low values. The latter behavior is expected for particulate materials and is characterized by an exponential increase in reflectance towards 0° phase. This phenomena is known as the opposition surge effect and is composed of two components: 1) the shadow hiding effect due to decreasing shadows between the particles as opposition is approached (Hapke, 1984; Shkuratov et al., 1994; Shkuratov and Helfenstein, 2001), and 2) the coherent backscattering due to constructive interference of photons at very small phase angles (Muinonen, 1994; Muinonen et al., 2010). Depending on the material, the coherent backscattering peak can be very narrow (~<2°), whereas the shadow hiding peak is relatively broad (~<20°) (e.g. Helfenstein et al., 1997). Therefore, since most of our CaSSIS data are above the phase angle range where coherent backscattering occurs, it is likely that our observations in Fig. 8 illustrate the increased backscattering due to shadow hiding effects.

To test our hypothesis that slope streaks are composed of larger particles than the surrounding dusty terrains, we calculated the ratio of selected CaSSIS-convolved spectra of the large particles (numerator) to that of MGS-1 with smaller mean particles (denominator). Three

selected laboratory ratios for different particle size ranges are shown in Fig. 10. On the same plot we compare these ratioed laboratory spectra with CaSSIS ratioed reflectance spectra of dark and bright streaks from Fig. 5. We were able to replicate the shape of the dark slope streak spectral ratio using laboratory MGS-1 20-10 and 10-0 μm, 45-20 and 10-0 μm, and 45-20 and 20-10 μm spectral ratios. The characteristic "kink" visible from PAN to BLU band for dark slope streaks resembles the shape of all three MGS-1 ratios at the same wavelength. However, laboratory spectra exhibit a more enhanced and deeper spectral ratio. This could be due to the fact that particles within slope streaks have much broader size distributions than fractions isolated in the lab. We cannot exclude that the PAN to BLU feature of dark slope streak spectra is diminished by atmospheric effects and therefore is more pronounced in the lab spectral ratios. We also cannot rule out the possibility that this feature contains a compositional component (Viviano-Beck et al., 2014).

3.6 Reflectance modeling

The Hapke-modeled reflectance of different particle size fractions of Martian dust are shown in Fig. 11. Our modeling suggests that only a narrow particle size range of relatively small mean grain sizes can reproduce the different reflectance behavior at wavelengths below 500 nm. Indeed, only for mean particle sizes below 20 μm, the spectra diverge from a flat curve with a value of 0.03 Lambert albedo at these wavelengths. This conclusion partially supports our laboratory findings that the only size fractions capable of producing these effects are relatively small particles. Also, the shape of the spectrum of the smallest particle size range and its albedo value generally agrees with the results of Martian dust analog studies (Wells et al., 1984).

4 Discussion

CaSSIS color spectral ratios of dark, bright and transitioning slope streaks suggest a genetic relationship between these three populations. For example, the average ratioed reflectance plot shown in Fig. 5 indicates that the spectra of the dark slope streaks are similar to that of the termini spectra of the transitioning streaks. The spectra of bright streaks also appear to have a similar flat shape to that of the apex of the transitioning streak. This implies that some streaks may form as dark, then enter a transitioning phase, and finally become completely bright. Furthermore, based on Fig. 5, dark slope streak apexes are fainter than their termini, which might indicate a top-to-bottom fading process. In support of the aforementioned evidences, MOC, CaSSIS and HiRISE consecutive observations (Fig. 4) of the site S15 identified a complete dark to bright slope streak reversal. This observation, combined with the CaSSIS spectral evidence, supports the hypothesis that bright streaks may be purely old dark slope streaks (Schorghofer et al., 2007).

Dust deposition might play a role, not only in the fading of slope streaks (Aharonson et al., 2003), but also in their time-dependent brightening. We present a conceptual model, primarily based on dust deposition on pre-existing surface microtexture and its temporal compaction (see Model 1, Fig. 12). Although there are documented cases of slope streaks which contain discernible meter-scale topography, e.g. longitudinal ridges (Chuang et al., 2007; Beyer et al., 2008) and linear mounds (Phillips et al., 2007), in all of our analyzed sites we did not observe albedo contrast dependency on topography. Meter-scale topographic features were observed for both dark, bright and faded streaks alike (e.g. HiRISE ID: ESP_066514_2050).

Therefore, we must assume that slope streak photometric darkening/brightening is due to the changes in the surface cm-mm scale
microstructure (« HiRISE resolution). Model 1 describes a scenario where as the streak forms, it exposes a deeper and darker substrate. Such a substrate would be composed of larger particles than the nearby dusty terrains. Alternatively, a larger particle layer could be achieved due to particle sorting (Kleinhans, 2004), since in granular materials large particles are observed to move to least shear strain zones (Bagnold, 1954). The decrease in reflectance may also be due to the increase in porosity and microscopic roughness (Shepard and Helfenstein, 2007). With time, dust would settle on the rough slope streak surface, creating an optically opaque coating and effectively erasing the spectral signature described earlier (i.e. "kink" from PAN to BLU). Perhaps due to particle settling and/or surface properties that allow compaction of dust (Herkenhoff et al., 2004), slope streak reversal in contrast could be achieved. Given enough time, even more dust would settle and fully bury the intricate microstructure. From a spectral perspective, such a surface would be indistinguishable from the nearby terrains. Note that in this model the settled amount of dust is insufficient in erasing macroscopic topography, which may remain intact after the initial avalanche flow.

Although conceptually viable, the described dustfall model, would need to be very slow (on the order of decades) to be consistent with known slope streak brightening/fading rates (Bergonio et al. 2013, also Fig. 4). On Mars most surface features are suggested to fade from atmospheric dust settling relatively quickly. Global changes in surface albedo and therefore dust deposition are known to be modulated seasonally (Szwast et al., 2006). The formation of mesoscale windstreaks was shown to be enhanced during seasons of increased local dust storm

activity (Thomas et al., 2003). On a much smaller scale, dust devil tracks, which are formed via dust deflation by moving dust devils, also usually fade within a Martian season (Malin and Edgett, 2001; Balme et al., 2003). Deposition of perhaps a few microns of airfall dust was suggested to be enough to cause dust devil track disappearance (Malin and Edgett, 2001). Also, some dust devils tracks were shown to completely disappear right after global dust storms (Greeley et al., 2010). Interestingly, in case of slope streaks in Lycus Sulci, it appeared that the dust storm in 2001 did not cause them to fade away (Bergonio et al., 2013).

Secondly, Recurring Slope Lineae (RSL) found on equatorial slopes are known to fade seasonally (McEwen et al., 2011; Stillman et al., 2017; Vincendon et al., 2019). Their occurrence on steep slopes around the angle of repose for granular material suggested that RSL may be flows of sand, which remove a thin coating of dust (Dundas, 2020). Schaefer et al. (2019) proposed that one of the key differences between the fading mechanisms of RSL and slope streaks is their occurrence in two distinctly different albedo regimes. RSL are found in host terrains of albedo <0.1 and slope streaks in that of ~0.3 (McEwen et al., 2014). Since low albedo terrains brighten more easily by even small amounts of dust fallout (Wells et al., 1984), Schaefer et al. (2019) suggested that it takes more time for slope streaks to fade from dust deposition. However, it has been noted that dust devil tracks found within the same location as slope streaks, still faded within a few martian seasons, while slope streaks did not appear to be affected (Schorghofer and King, 2011). Paradoxically, high albedo regions like Arabia, which are known to be dusty (Ruff and Christensen, 2002; Szwast et al., 2006) should naturally experience higher dustfall rates, consequently making slope streaks more susceptible to fading by atmospheric dust fallout.

Slope streaks represent a unique type of albedo features that persist for decades on the martian surface. Perhaps the atmospheric dust settling process plays only a minor role and merely provides the raw materials for soil cohesion during the slope streak formation. Therefore, it is conceivable that another mechanism is responsible for slope streak fading and/or brightening. In Fig. 12 we present Model 2 that evokes temporal surface evolution from other factors unrelated to dust fallout. In this model, the assumption that slope streaks expose a darker substrate is also not required. This is evoked in order to be consistent with the observations where boulder tracks on the same slopes as dark streaks do not expose a darker substrate (Mushkin et al., 2010) and the lack of scars in some new streaks (Kreslavsky and Head, 2009). Instead, the flow as it moves downslope consumes and effectively enlarges surficial particles sizes by either: 1) cementation and electrostatic cohesion by weakly bound van der Waals forces (Bridges et al., 2010; Vaughan et al., 2010) or 2) a diagenetic process, which increases the grain sizes of pre-existing iron oxide materials by agglomeration (Mushkin et al., 2010). Cohesion of dust likely due to electrostatic charging has been documented by the Spirit rover (Herkenhoff et al., 2006) and also happens in the martian atmosphere (Harrison et al., 2016). In case of diagenesis, Mushkin et al. (2010) argued that FeOx grains not only increase the volume scattering, but also create mm-cm scale roughness within the slope streak surfaces. Regardless of the exact process responsible for particle enlargement, the resultant surface would likely be very porous and rough. At least for materials made of mixed silica sand, thermal conductivity tends to decrease with high porosity and low proportion of fine particles (Ahn and Jung, 2017). Interestingly, Schorghofer et al. (2007) using THEMIS day IR data observed a dark streak that is warmer than nearby slopes and suggested that this is due to a decrease in thermal conductivity.

The next stage of Model 2 illustrates a scenario, where with time, the fragile large grain agglomerates would start to break down, perhaps due to external erosion or the wear-off of interparticle forces. As the particle effective size decreases the albedo of such surface would start to increase. Once all uppermost particles have decomposed, the new layer would likely be more compact than the surrounding slightly more porous terrains. Perhaps once this stage is reached, dust deposition may be able to effectively mask the new small particles and erase the bright streak spectral signatures. The proposed soil degradation process could potentially lead to a scar formation (Gerstell et al., 2004; Kreslavsky and Head, 2009) if the initial agglomerated particle layer is thick enough. Lastly, the observed top-to-bottom brightening process might be controlled by slope because larger aggregates are not as stable on sloping surfaces and are more exposed to wind (Sullivan et al., 2008).

Conclusions

Based on CaSSIS spectral and multi-angular evidence from ~30 sites, and temporal observations of one location that exhibited a contrast reversal, we show that slope streaks undergo changes in albedo after their formation. Fresh slope streaks are composed of larger particles, contain a rougher and more porous surface layer, and appear ~10% darker than the surrounding terrains. Within decades, a substantial proportion of slope streaks in Arabia Terra likely experiences regolith compaction and a reduction of the upper surface layer in effective particle size. Eventually this process results in streaks, which are brighter by up to 4% than the surrounding particulate materials. Ultimately even these bright slope streaks fade out and lose their spectral

signatures. In this case, meter scale topography observable only in high-res imagery would be reminiscent of the old slope streak.

Our global mapping of bright slope streaks revealed that these features are very common in the Arabia Terra region. Although remote sensing observations by other missions suggest that Tharsis and Arabia regions are covered by comparable albedo, it is plausible that the rarity of bright slope streaks in other regions than Arabia may be an indicator of variable dust thickness, dust deposition rates and/or cohesive soil properties on Mars.

Laboratory measurements of sieved Mars simulant samples of particle size fractions from <10 to 40 μm yielded reflectance ratios comparable to those observed by CaSSIS for dark and bright slope streaks. It suggests that particles found within and outside of slope streaks are perhaps different by several factors in size. Hapke reflectance modeling of palagonite dust indicated that the largest albedo increase occurs for the smallest particle size ranges (<10 μm grain size).

We have shown that slope streak surfaces are non-Lambertian (i.e. scatter light non uniformly with phase angle) and are susceptible to shadow hiding opposition effects. If low tau atmospheric conditions are available, optical phenomena can be observed on the Martian surface using CaSSIS. Since CaSSIS is able to image under extremely low phase angle illumination (<5°) perhaps coherent backscattering opposition effect can also be investigated for martian particulate materials. The observations of these optical phenomena will be analyzed within future work.

Acknowledgements

The authors thank Mikhail Kreslavsky and one anonymous reviewer for constructive comments, and Angelo Pio Rossi for editorial handling. CaSSIS is a project of the University of Bern and funded through the Swiss Space Office via ESA's PRODEX programme. The instrument hardware development was also supported by the Italian Space Agency (ASI) (ASI-INAF agreement no. 2020-17-HH.O), INAF/Astronomical Observatory of Padova, and the Space Research Center (CSK) in Warsaw. Support from SGF (Budapest), the University of Arizona (Lunar and Planetary Lab.) and NASA are also gratefully acknowledged. Operations support from the UK Space Agency under grant ST/R003025/1 is also acknowledged. LLT wishes to personally acknowledge funding and support from the Canadian Space Agency (CSA) through their Planetary and Astronomy Missions Co-Investigator programme (19PACOI07) and the Canadian NSERC Discovery Grant programme (RGPIN 2020-06418).

References

Aharonson, O., Schorghofer, N., and Gerstell, M. F. (2003). Slope streak formation and dust deposition rates on Mars. *Journal of Geophysical Research: Planets*, 108(E12). https://doi.org/10.1029/2003JE002123.

Ahn, J. and Jung, J. (2017). Effects of Fine Particles on Thermal Conductivity of Mixed Silica Sands. *Applied Sciences*, 7(7). https://doi.org/10.3390/app7070650.

Allen, C. C., Jager, K. M., Morris, R. V., Lindstrom, D. J., Lindstrom, M. M., and Lock- wood, J. P. (1998). JSC Mars-1: A Martian Soil Simulant. *Space 98*, pages 469–

476. https://doi.org/10.1061/40339(206)54.

Amador, E. S., Mushkin, A., and Gillespie, A. (2016). Spectral characteristics of dark slope streaks on Mars: a global survey with CRISM (abstract # 2696). 47th Lunar and Planetary Science Conference.

Bagnold, R. A. (1954). Experiments on a gravity-free dispersion of large solid spheres in a Newtonian fluid under shear. *Proceedings of the Royal Society of London. Series A. Mathematical and Physical Sciences*, 225(1160):49–63. https://doi.org/10.1098/rspa.1954.0186.

Balme, M. R., Whelley, P. L., and Greeley, R. (2003). Mars: Dust devil track survey in Argyre Planitia and Hellas Basin. *Journal of Geophysical Research: Planets*, 108(E8). https://doi.org/10.1029/2003JE002096.

Baratoux, D., Mangold, N., Forget, F., Cord, A., Pinet, P., Daydou, Y., Jehl, A., Masson, P., Neukum, G., and The HRSC CO-Investigator Team (2006). The role of the wind-transported dust in slope streaks activity: Evidence from the HRSC data. *Icarus*, 183(1):30 – 45. https://doi.org/10.1016/j.icarus.2006.01.023.

Becerra, P., Byrne, S., and Brown, A. J. (2015). Transient bright "halos" on the South Polar Residual Cap of Mars: Implications for mass-balance. *Icarus*, 251:211–225. https://doi.org/10.1016/j.icarus.2014.04.050.

Bergonio, J. R., Rottas, K. M., and Schorghofer, N. (2013). Properties of martian slope streak populations. *Icarus*, 225(1):194 – 199.

https://doi.org/10.1016/j.icarus.2013.03.023.

Beyer, R. A., Chuang, F. C., Thomson, B. J., Milazzo, M. P., and Wray, J. (2008). Martian Slope Streak Brightening Mechanisms (abstract # 2538). 39th Lunar and Planetary Science Conference.

Bhardwaj, A., Sam, L., Martín-Torres, F. J., Zorzano, M.-P., and Fonseca, R. M. (2017). Martian slope streaks as plausible indicators of transient water activity. *Scientific Reports*, 7(1). https://doi.org/10.1038/s41598-017-07453-9.

Blake, D. F., Morris, R. V., Kocurek, G., Morrison, S. M., Downs, R. T., Bish, D., Ming, D. W., Edgett, K. S., Rubin, D., Goetz, W., Madsen, M. B., Sullivan, R., Gellert, R., Campbell, I., Treiman, A. H., McLennan, S. M., Yen, A. S., Grotzinger, J., Vaniman, D. T., Chipera, S. J., Achilles, C. N., Rampe, E. B., Sumner, D., Meslin, P.-Y., Maurice, S., Forni, O., Gasnault, O., Fisk, M., Schmidt, M., Mahaffy, P., Leshin, L. A., Glavin, D., Steele, A., Freissinet, C., Navarro-González, R., Yingst, R. A., Kah, L. C., Bridges, N., Lewis, K. W., Bristow, T. F., Farmer, J. D., Crisp, J. A., Stolper, E. M., Des Marais, D. J., Sarrazin, P., et al. (2013). Curiosity at Gale Crater, Mars: Characterization and Analysis of the Rocknest Sand Shadow. *Science*, 341(6153).

Bridges, N., Banks, M., Beyer, R., Chuang, F., Noe Dobrea, E., Herkenhoff, K., Keszthelyi, L., Fishbaugh, K., McEwen, A., Michaels, T., Thomson, B., and Wray, J. (2010). Aeolian bedforms, yardangs, and indurated surfaces in the Tharsis Montes as seen by the HiRISE Camera: Evidence for dust aggregates. *Icarus*, 205(1):165–182. https://doi.org/10.1016/j.icarus.2009.05.017.

Brusnikin, E. S., Kreslavsky, M. A., Zubarev, A. E., Patratiy, V. D., Krasilnikov, S. S., Head, J. W., and Karachevtseva, I. P. (2016). Topographic measurements of slope streaks on Mars. *Icarus*, 278:52 – 61. https://doi.org/10.1016/j.icarus.2016.06.005.

Cannon, K. M., Britt, D. T., Smith, T. M., Fritsche, R. F., and Batcheldor, D. (2019). Mars global simulant MGS-1: A Rocknest-based open standard for basaltic martian regolith simulants. *Icarus*, 317:470–478. https://doi.org/10.1016/j.icarus.2018.08.019.

Chuang, F. C., Beyer, R. A., and Bridges, N. T. (2010). Modification of martian slope streaks by eolian processes. *Icarus*, 205(1):154 – 164. https://doi.org/10.1016/j.icarus.2009.07.035.

Chuang, F. C., Beyer, R. A., McEwen, A. S., and Thomson, B. J. (2007). Hirise observations of slope streaks on Mars. *Geophysical Research Letters*, 34(20). https://doi.org/10.1029/2007GL031111.

Daubar, I., Dundas, C., Byrne, S., Geissler, P., Bart, G., McEwen, A., Russell, P., Chojnacki, M., and Golombek, M. (2016). Changes in blast zone albedo patterns around new martian impact craters. *Icarus*, 267:86 – 105. https://doi.org/10.1016/j.icarus.2015.11.032.

Dickson, J. L., Kerber, L. A., Fassett, C. I., and Ehlmann, B. L. (2018). A Global, Blended CTX Mosaic of Mars with Vectorized Seam Mapping: A New Mosaicking Pipeline Using Principles of Non-Destructive Image Editing. (abstract # 2480. 49th Lunar and Planetary Science Conference.

Dundas, C. M. (2020). An aeolian grainflow model for Martian Recurring Slope Lineae.

Icarus, 343:113681. https://doi.org/10.1016/j.icarus.2020.113681.

Dundas, C. M. (2020). Geomorphological evidence for a dry dust avalanche origin of slope streaks on Mars. *Nature Geoscience*, 13(7):473–476. https://doi.org/10.1038/s41561-020-0598-x.

Dundas, C. M., Becerra, P., Byrne, S., Chojnacki, M., Daubar, I. J., Diniega, S., Hansen, C. J., Herkenhoff, K. E., Landis, M. E., McEwen, A. S., Portyankina, G., and Valantinas, A. (2021). Active Mars: A Dynamic World. *Journal of Geophysical Research: Planets*, 126(8):e2021JE006876. https://doi.org/10.1029/2021JE006876.

Ferguson, H. M. and Lucchitta, B. K. (1984). Dark streaks on talus slopes, Mars. pages 188–190. NASA Tech. Memo., NASA TM-86246.

Fernando, J., Schmidt, F., and Douté, S. (2016). Martian surface microtexture from orbital CRISM multi-angular observations: A new perspective for the characterization of the geological processes. *Planetary and Space Science*, 128:30–51.

Geissler, P. E. (1992). *Spectrophotometric mapping of Coprates quadrangle, Mars*. The University of Arizona. PhD Thesis.

Gerstell, M. F., Aharonson, O., and Schorghofer, N. (2004). A distinct class of avalanche scars on mars. *Icarus*, 168(1):122–130.

Greeley, R., Waller, D. A., Cabrol, N. A., Landis, G. A., Lemmon, M. T., Neakrase, L. D. V., Pendleton Hoffer, M., Thompson, S. D., and Whelley, P. L. (2010). Gusev Crater, Mars: Observations of three dust devil seasons. *Journal of Geophysical Research: Planets*,

115(E7). https://doi.org/10.1029/2010JE003608.

Hapke, B. (1984). Bidirectional reflectance spectroscopy 3. Correction for macroscopic roughness. *Icarus*, 59(1):41–59. https://doi.org/10.1016/0019-1035(84)90054-X.

Hapke, B. (2012). *Theory of Reflectance and Emittance Spectroscopy*. Cambridge University Press, 2nd edition.

Harrison, R. G., Barth, E., Esposito, F., Merrison, J., Montmessin, F., Aplin, K. L., Borlina, C., Berthelier, J. J., Déprez, G., Farrell, W. M., Houghton, I. M. P., Renno, N. O., Nicoll,

K. A., Tripathi, S. N., and Zimmerman, M. (2016). Applications of Electrified Dust and Dust Devil Electrodynamics to Martian Atmospheric Electricity. *Space Sci. Rev.*, 203:299–345. https://doi.org/10.1007/s11214-016-0241-8.

Helfenstein, P., Veverka, J., and Hillier, J. (1997). The Lunar Opposition Effect: A Test of Alternative Models. *Icarus*, 128(1):2–14. https://doi.org/10.1006/icar.1997.5726.

Herkenhoff, K. E., Squyres, S. W., Anderson, R., Archinal, B. A., Arvidson, R. E., Barrett, J. M., Becker, K. J., Bell III, J. F., Budney, C., Cabrol, N. A., Chapman, M. G., Cook, D., Ehlmann, B. L., Farmer, J., Franklin, B., Gaddis, L. R., Galuszka, D. M., Garcia, P. A., Hare, T. M., Howington-Kraus, E., Johnson, J. R., Johnson, S., Kinch, K., Kirk, R. L., Lee, E. M., Leff, C., Lemmon, M., Madsen, M. B., Maki, J. N., Mullins, K. F., Redding, B. L., Richter, L., Rosiek, M. R., Sims, M. H., Soderblom, L. A., Spanovich, N., Springer, R., Sucharski, R. M., Sucharski, T., Sullivan, R., Torson, J. M., and Yen, A. (2006). Overview of

the microscopic imager investigation during spirit's first 450 sols in gusev crater. *Journal of Geophysical Research: Planets*, 111(E2). https://doi.org/10.1029/2005JE002574.

Herkenhoff, K. E., Squyres, S. W., Arvidson, R., Bass, D. S., Bell, J. F., Bertelsen, P., Cabrol, N. A., Gaddis, L., Hayes, A. G., Hviid, S. F., Johnson, J. R., Kinch, K. M., Madsen, M. B., Maki, J. N., McLennan, S. M., McSween, H. Y., Rice, J. W., Sims, M., Smith, P. H., Soderblom, L. A., Spanovich, N., Sullivan, R., and Wang, A. (2004). Textures of the Soils and Rocks at Gusev Crater from Spirit's Microscopic Imager. *Science*, 305(5685):824–826. https://doi.org/10.1126/science.3050824.

Heyer, T., Kreslavsky, M., Hiesinger, H., Reiss, D., Bernhardt, H., and Jaumann, R. (2019). Seasonal formation rates of martian slope streaks. *Icarus*, 323:76 – 86. https://doi.org/10.1016/j.icarus.2019.01.010 Holmes, J. A., Lewis, S. R., and Patel, M. R. (2020). OpenMars: A global record of martian weather from 1999 to 2015. *Planetary and Space Science*, 188:104962. https://doi.org/10.1016/j.pss.2020.104962.

Johnson, J. R., Bell, J. F., Geissler, P., Grundy, W. M., Guinness, E. A., Pinet, P. C., and Soderblom, J. (2008). Physical properties of the Martian surface from spectrophotometric observations. In Bell, J., editor, *The Martian Surface: Composition, Mineralogy and Physical Properties*, Cambridge Planetary Science, page 428–450. Cambridge University Press. https://doi.org/10.1017/CBO9780511536076.020.

Kleinhans, M. (2004). Sorting in grain flows at the lee side of dunes. *Earth-Science Reviews*, 65(1):75–102. https://doi.org/10.1016/S0012-8252(03)00081-3.

Kreslavsky, M. A. and Head, J. W. (2009). Slope streaks on Mars: A new "wet" mechanism. *Icarus*, 201(2):517 – 527. https://doi.org/10.1016/j.icarus.2009.01.026.

Malin, M. C., Bell III, J. F., Cantor, B. A., Caplinger, M. A., Calvin, W. M., Clancy, R. T., Edgett, K. S., Edwards, L., Haberle, R. M., James, P. B., Lee, S. W., Ravine, M. A., Thomas, P. C., and Wolff, M. J. (2007). Context Camera Investigation on board the Mars Reconnaissance Orbiter. *Journal of Geophysical Research: Planets*, 112(E5). https://doi.org/10.1029/2006JE002808.

Malin, M. C. and Edgett, K. S. (2001). Mars Global Surveyor Mars Orbiter Camera: Interplanetary cruise through primary mission. *Journal of Geophysical Research: Planets*, 106(E10):23429– 23570. https://doi.org/10.1029/2000JE001455.

McCleese, D. J., Schofield, J. T., Taylor, F. W., Calcutt, S. B., Foote, M. C., Kass, D. M., Leovy, C. B., Paige, D. A., Read, P. L., and Zurek, R. W. (2007). Mars climate sounder: An investigation of thermal and water vapor structure, dust and condensate distributions in the atmosphere, and energy balance of the polar regions. *Journal of Geophysical Research: Planets*, 112(E5). https://doi.org/10.1029/2006JE002790.

McEwen, A. S., Dundas, C. M., Mattson, S. S., Toigo, A. D., Ojha, L., Wray, J. J., Chojnacki, M., Byrne, S., Murchie, S. L., and Thomas, N. (2014). Recurring slope lineae in equatorial regions of Mars. *Nature Geoscience*, 7(1):53–58. https://doi.org/10.1038/ngeo2014.

McEwen, A. S., Eliason, E. M., Bergstrom, J. W., Bridges, N. T., Hansen, C. J., Delamere, W. A., Grant, J. A., Gulick, V. C., Herkenhoff, K. E., Keszthelyi, L., Kirk, R. L., Mellon, M. T.,

Squyres, S. W., Thomas, N., and Weitz, C. M. (2007). Mars reconnaissance orbiter's high resolution imaging science experiment (hirise). *Journal of Geophysical Research: Planets*, 112(E5). https://doi.org/10.1029/2005JE002605.

McEwen, A. S., Ojha, L., Dundas, C. M., Mattson, S. S., Byrne, S., Wray, J. J., Cull, S. C., Murchie, S. L., Thomas, N., and Gulick, V. C. (2011). Seasonal Flows on Warm Martian Slopes. *Science*, 333:740–743. https://doi.org/10.1126/science.1204816.

Miyamoto, H., Dohm, J. M., Beyer, R. A., and Baker, V. R. (2004). Fluid dynamical implications of anastomosing slope streaks on Mars. *Journal of Geophysical Research: Planets*, 109(E6). https://doi.org/10.1029/2003JE002234.

Morris, E. C. (1982). Aureole deposits of the Martian volcano Olympus Mons. *Journal of Geophysical Research: Solid Earth*, 87(B2):1164–1178. https://doi.org/10.1029/JB087iB02p01164.

Muinonen, K. (1994). Coherent Backscattering by Solar System Dust Particles. *Symposium - International Astronomical Union*, 160:271–296. https://doi.org/10.1017/S0074180900046593.

Muinonen, K., Tyynelä, J., Zubko, E., and Videen, G. (2010). Coherent backscattering in planetary regoliths. In Kokhanovsky, A. A., editor, *Light Scattering Reviews 5: Single Light Scattering and Radiative Transfer*, pages 477–518. Springer Berlin Heidelberg, Berlin, Heidelberg. https://doi.org/10.1007/978-3-642-10336-0_11.

Munaretto, G., Pajola, M., Cremonese, G., Re, C., Lucchetti, A., Simioni, E., Mcewen, A.,

Pommerol, A., Becerra, P., Conway, S., Thomas, N., and Massironi, D. M. (2020). Implications for the origin and evolution of Martian Recurring Slope Lineae at Hale crater from CaSSIS observations. *Planetary and Space Science*, 187:104947. https://doi.org/10.1016/j.pss.2020.104947.

Munaretto, G., Pajola, M., Lucchetti, A., Re, C., Cremonese, G., Simioni, E., Cambianica, P., and Thomas, N. (2021). Topographic correction of HiRISE and CaSSIS images: Validation and application to color observations of Martian albedo features. *Planetary and Space Science*, 200:105198. https://doi.org/10.1016/j.pss.2021.105198.

Murchie, S., Arvidson, R., Bedini, P., Beisser, K., Bibring, J.-P., Bishop, J., Boldt, J., Cavender, P., Choo, T., Clancy, R. T., Darlington, E. H., Des Marais, D., Espiritu, R., Fort, D., Green, R., Guinness, E., Hayes, J., Hash, C., Heffernan, K., Hemmler, J., Heyler, G., Humm, D., Hutcheson, J., Izenberg, N., Lee, R., Lees, J., Lohr, D., Malaret, E., Martin, T., McGovern, J. A., McGuire, P., Morris, R., Mustard, J., Pelkey, S., Rhodes, E., Robinson, M., Roush, T., Schaefer, E., Seagrave, G., Seelos, F., Silverglate, P., Slavney, S., Smith, M., Shyong, W.-J., Strohbehn, K., Taylor, H., Thompson, P., Tossman, B., Wirzburger, M., and Wolff, M. (2007). Compact Reconnaissance Imaging Spectrometer for Mars (CRISM) on Mars Reconnaissance Orbiter (MRO). *Journal of Geophysical Research: Planets*, 112(E5). https://doi.org/10.1029/2006JE002682.

Mushkin, A., Gillespie, A. R., Montgomery, D. R., Schreiber, B. C., and Arvidson, R. E. (2010). Spectral constraints on the composition of low-albedo slope streaks in the Olympus Mons Aureole. *Geophysical Research Letters*, 37(22).

https://doi.org/10.1029/2010GL044535.

Ody, A., Poulet, F., Langevin, Y., Bibring, J.-P., Bellucci, G., Altieri, F., Gondet, B., Vincendon, M., Carter, J., and Manaud, N. (2012). Global maps of anhydrous minerals at the surface of Mars from OMEGA/MEx. *Journal of Geophysical Research: Planets*, 117(E11). https://doi.org/10.1029/2012JE004117.

Perry, J. E., Heyd, R., Read, M., Tornabene, L. L., Sutton, S., Byrne, S., Thomas, N., Fennema, A., McEwen, A., and Berry, K. (2021). Geometric Processing of TGO CaSSIS Observations. *Planetary and Space Science*.

Phillips, C. B., Burr, D. M., and Beyer, R. A. (2007). Mass movement within a slope streak on Mars. *Geophysical Research Letters*, 34(21). https://doi.org/10.1029/2007GL031577.

Pommerol, A., Jost, B., Poch, O., El-Maarry, M., Vuitel, B., and Thomas, N. (2015). The SCITEAS experiment: Optical characterizations of sublimating icy planetary analogues. *Planetary and Space Science*, 109-110:106–122. https://doi.org/10.1016/j.pss.2015.02.004.

Pommerol, A., Thomas, N., Affolter, M., Portyankina, G., Jost, B., Seiferlin, K., and Aye, K.-M. (2011). Photometry and bulk physical properties of Solar System surfaces icy analogs: The Planetary Ice Laboratory at University of Bern. *Planetary and Space Science*, 59(13):1601–1612. https://doi.org/10.1016/j.pss.2011.07.009.

Ramsdale, J. D., Balme, M. R., Conway, S. J., Gallagher, C., van Gasselt, S. A., Hauber, E., Orgel, C., Séjourné, A., Skinner, J. A., Costard, F., Johnsson, A., Losiak, A., Reiss, D.,

Swirad, Z. M., Kereszturi, A., Smith, I. B., and Platz, T. (2017). Grid-based mapping: A method for rapidly determining the spatial distributions of small features over very large areas. *Planetary and Space Science*, 140:49 – 61. https://doi.org/10.1016/j.pss.2017.04.002.

Roloff, V., Pommerol, A., Gambicorti, L., et al. (2017). On-Ground Performance and Calibration of the ExoMars Trace Gas Orbiter CaSSIS Imager. *Space Sci Rev*, 212:1871–1896. https://doi.org/10.1007/s11214-017-0404-2.

Roush, T. L. (1994). Charon: More than Water Ice? *Icarus*, 108(2):243–254. https://doi.org/10.1006/icar.1994.1059.

Ruff, S. W. and Christensen, P. R. (2002). Bright and dark regions on Mars: Particle size and mineralogical characteristics based on Thermal Emission Spectrometer data. *Journal of Geophysical Research: Planets*, 107(E12). https://doi.org/10.1029/2001JE001580.

Schaefer, E., McEwen, A., and Sutton, S. (2019). A case study of recurring slope lineae (RSL) at Tivat crater: Implications for RSL origins. *Icarus*, 317:621 – 648. https://doi.org/10.1016/j.icarus.2018.07.014.

Schorghofer, N., Aharonson, O., Gerstell, M., and Tatsumi, L. (2007). Three decades of slope streak activity on Mars. *Icarus*, 191(1):132 – 140. https://doi.org/10.1016/j.icarus.2007.04.026.

Schorghofer, N. and King, C. M. (2011). Sporadic formation of slope streaks on Mars.

Icarus, 216(1):159 – 168. https://doi.org/10.1016/j.icarus.2011.08.028.

Shepard, M. K. and Helfenstein, P. (2007). A test of the Hapke photometric model. *Journal of Geophysical Research: Planets*, 112(E3). https://doi.org/10.1029/2005JE002625.

Shkuratov, Y. G. and Helfenstein, P. (2001). The Opposition Effect and the Quasi-fractal Structure of Regolith: I. Theory. *Icarus*, 152(1):96–116. https://doi.org/10.1006/icar.2001.6630.

Shkuratov, Y. G., Starukhina, L. V., Kreslavsky, M. A., Opanasenko, N. V., Stankevich, D. G., and Shevchenko, V. G. (1994). Principle of Undulatory Invariance in Photometry of Atmosphereless Celestial Bodies. *Icarus*, 109(1):168–190. https://doi.org/10.1006/icar.1994.1084.

Stillman, D. E., Michaels, T. I., and Grimm, R. E. (2017). Characteristics of the numerous and widespread recurring slope lineae (rsl) in valles marineris, mars. *Icarus*, 285:195–210. https://doi.org/10.1016/j.icarus.2016.10.02.

Sullivan, R., Arvidson, R., Bell III, J. F., Gellert, R., Golombek, M., Greeley, R., Herkenhoff, K., John- son, J., Thompson, S., Whelley, P., and Wray, J. (2008). Wind-driven particle mobility on Mars: In- sights from Mars Exploration Rover observations at "El Dorado" and surroundings at Gusev Crater. *Journal of Geophysical Research: Planets*, 113(E6). https://doi.org/10.1029/2008JE003101.

Sullivan, R., Thomas, P., Veverka, J., Malin, M., and Edgett, K. S. (2001). Mass movement slope streaks imaged by the Mars Orbiter Camera. *Journal of Geophysical Research:*

Planets, 106(E10):23607–23633. https://doi.org/10.1029/2000je001296.

Szwast, M. A., Richardson, M. I., and Vasavada, A. R. (2006). Surface dust redistribution on Mars as observed by the Mars Global Surveyor and Viking orbiters. *Journal of Geophysical Research: Planets*, 111(E11). https://doi.org/10.1029/2005JE002485.

Thomas, N., Cremonese, G., Ziethe, R., et al. (2017). The Colour and Stereo Surface Imaging System (CaSSIS) for the ExoMars Trace Gas Orbiter. *Space Sci Rev*, 212:1897–1944. https://doi.org/10.1007/s11214-017-0421-1.

Thomas, P. C., Gierasch, P., Sullivan, R., Miller, D. S., Alvarez del Castillo, E., Cantor, B., and Mellon, M. T. (2003). Mesoscale linear streaks on Mars: environments of dust entrainment. *Icarus*, 162(2):242–258. https://doi.org/10.1016/S0019-1035(03)00028-9.

Vaughan, A. F., Johnson, J. R., Herkenhoff, K. E., Sullivan, R., Landis, G. A., Goetz, W., and Madsen, M. B. (2010). Pancam and Microscopic Imager observations of dust on the Spirit Rover: cleaning events, spectral properties, and aggregates. *Mars J.*, 5:129–145. https://doi.org/10.1555/mars.2010.0005.

Vincendon, M. (2013). Mars surface phase function constrained by orbital observations. *Planetary and Space Science*, 76:87–95. https://doi.org/10.1016/j.pss.2012.12.005.

Vincendon, M., Pilorget, C., Carter, J., and Stcherbinine, A. (2019). Observational evidence for a dry dust-wind origin of Mars seasonal dark flows. *Icarus*, 325:115–127. https://doi.org/10.1016/j.icarus.2019.02.024.

Viviano-Beck, C. E., Seelos, F. P., Murchie, S. L., Kahn, E. G., Seelos, K. D., Taylor, H. W., Taylor, K., Ehlmann, B. L., Wiseman, S. M., Mustard, J. F., and Morgan, M. F. (2014). Revised CRISM spectral parameters and summary products based on the currently detected mineral diversity on Mars. *Journal of Geophysical Research: Planets,* 119(6):1403–1431. https://doi.org/10.1002/2014JE004627.

Warell, J. and Davidsson, B. (2010). A Hapke model implementation for compositional analysis of VNIR spectra of Mercury. *Icarus,* 209(1):164–178. https://doi.org/10.1016/j.icarus.2009.11.037.

Wells, E., Veverka, J., and Thomas, P. (1984). Mars: Experimental study of albedo changes caused by dust fallout. *Icarus,* 58(3):331–338. https://doi.org/10.1016/0019-1035(84)90079-4.

Williams, S. H. (1991). Dark Talus Streaks on Mars are Similar to Aeolian Dark Streaks (abstract # 1509). 22nd Lunar and Planetary Science Conference.

Wolff, M. J., Smith, M. D., Clancy, R. T., Arvidson, R., Kahre, M., Seelos IV, F., Murchie, S., and Savijärvi, H. (2009). Wavelength dependence of dust aerosol single scattering albedo as observed by the Compact Reconnaissance Imaging Spectrometer. Journal of Geophysical Research: Planets, 114(E2). https://doi.org/10.1029/2009JE003350.

Yoldi, Z., Pommerol, A., Poch, O., and Thomas, N. (2021). Reflectance study of ice and Mars soil simulant associations – I. H2O ice. Icarus, 358:114169. https://doi.org/10.1016/j.icarus.2020.114169.

Table 1. Coordinates, IDs, streak category, CaSSIS IDs, atmospheric opacity values, phase angle and date for slope streak sites analyzed in this study.

Long (°E)	Lat (°)	ID	type of streaks	CaSSIS IDs	tau (τ)	phase angle (°)	date, UTC
31.91	27.26	S1	transitioning, bright	MY35_009479_155_0 MY35_013296_153_0 MY35_013582_153_0	0.34 0.48 1.52	24.3 84.3 53.2	2020-01-07T23:04:24.860 2020-11-15T11:55:46.597 2020-12-08T21:56:26.811
28.49	11.15	S2	transitioning	MY35_009616_169_0	0.22	9.7	2020-01-19T04:22:24.392
30.62	24.22	S3	bright, dark	MY35_009678_156_0	0.22	33.5	2020-01-24T06:08:13.632
28.94	23.03	S4	transitioning, dark, bright	MY35_008591_024_0 MY35_009417_160_0 MY35_009504_159_0 MY35_013154_026_0	0.13 0.21 0.21 0.37	83.0 36.5 21.3 70.2	2019-10-27T05:19:48.389 2020-01-02T21:15:40.619 2020-01-10T00:13:29.957 2020-11-03T20:10:45.992
38.22	11.74	S5	bright	MY35_010095_012_0	0.19	55.0	2020-02-27T08:48:07.250
35.82	13.38	S6	dark, bright	MY35_010685_170_0	0.47	73.6	2020-04-15T17:05:19.745
38.15	8.81	S7	transitioning, bright, dark	MY35_009653_172_0 MY35_013079_009_0	0.18 0.52	19.6 56.7	2020-01-22T05:05:49.535 2020-10-28T16:42:57.676
43.86	8.34	S8	transitioning, dark, bright	MY35_010244_008_0 MY35_011823_010_0	0.26 1.15	13.6 56.5	2020-03-10T13:35:08.952 2020-07-17T20:31:11.423
22.61	25.82	S9	dark, bright	MY35_008410_160_0	0.22	53.7	2019-10-12T10:23:11.700
38.76	13.51	S10	transitioning, dark	MY35_012152_169_0	0.77	50.4	2020-08-13T19:54:47.793
44.76	5.91	S11	transitioning, dark	MY35_012127_175_0	0.82	48.3	2020-08-11T18:49:48.689
16.93	6.03	S12	transitioning	MY35_009517_177_0 MY35_010133_006_0 MY35_010636_177_0	0.14 0.33 0.28	28.4 44.2 81.4	2020-01-11T01:52:12.008 2020-03-01T11:26:41.507 2020-04-11T16:50:19.535
257.86	26.01	S13	transitioning, dark	MY35_010187_027_0 MY35_010274_026_0	0.24 0.22	32.2 17.0	2020-03-05T21:40:30.724 2020-03-13T00:38:22.073
37.16	19.56	S14	dark, bright	MY35_009367_163_0 MY35_009454_163_0	0.18 0.16	53.3 37.8	2019-12-29T19:01:25.425 2020-01-05T21:59:21.763
40.06	24.62	S15	Transitioning, bright	MY35_009342_158_0 MY35_009429_158_0 MY35_010381_028_0 MY36_015024_154_0 MY36_016143_156_0	0.13 0.10 0.28 0.14 0.05	55.0 40.0 31.1 34.9 45.8	2019-12-27T17:52:05.328 2020-01-03T20:49:56.666 2020-03-21T18:54:44.502 2021-04-05T23:39:44.468 2021-07-06T14:38:36.754
48.90	18.30	S16	transitioning, dark, bright	MY34_005562_162_0 MY36_014887_165_0 MY36_014974_161_0 MY36_016466_161_0	0.79 0.03 0.11 0.07	37.7 12.3 19.6 32.9	2019-02-21T07:08:41.063 2021-03-25T18:29:27.025 2021-04-01T21:26:35.254 2021-08-02T01:24:03.246
41.23	11.38	S17	bright, dark, transitioning	MY35_010747_172_0	0.37	56.4	2020-04-20T18:56:10.000
41.66	10.41	S18	dark, bright	MY35_007017_173_0 MY35_011207_170_0 MY35_011848_013_0	0.38 0.42 0.91	45.6 71.6 73.0	2019-06-20T09:02:44.452 2020-05-28T10:52:56.892 2020-07-19T21:39:46.529
26.66	2.69	S19	transitioning, bright	MY35_007030_182_0 MY35_010257_002_0	0.28 0.21	49.1 15.2	2019-06-21T10:38:07.499 2020-03-11T15:06:01.004
30.90	6.60	S20	dark, bright	MY34_002312_006_2 MY34_003804_006_2	0.29 0.46	41.8 52.8	2018-05-31T06:57:02.000 2018-09-30T09:24:06.645
28.50	23.42	S21	transitioning, dark	MY35_010083_024_0	0.33	57.8	2020-02-26T09:17:14.203
33.98	20.88	S22	transitioning, bright	MY35_012930_021_0	0.61	50.5	2020-10-16T11:58:49.048
23.38	13.20	S23	dark	MY35_013179_016_0	0.44	76.2	2020-11-05T21:15:07.097
214.93	15.23	S24	dark	MY36_014844_167_0 MY36_014931_166_0	0.18 0.10	21.8 7.5	2021-03-22T06:00:29.909 2021-03-29T08:58:22.071

				MY36_015485_014_0	0.03	46.2	2021-05-13T16:49:17.575
39.60	9.19	S25	dark	MY35_010269_009_0	0.17	11.9	2020-03-12T14:43:04.053
				MY36_015049_170_0	0.19	28.0	2021-04-08T00:52:43.664
				MY36_015777_009_1	0.14	42.3	2021-06-06T14:36:11.960
				MY36_015777_009_2	0.14	30.7	2021-06-06T14:36:59.960
282.91	27.49	S26	dark	MY35_006735_152_0	0.27	32.2	2019-05-28T06:59:41.418
188.25	7.56	S27	dark	MY36_014932_173_0	0.16	13.9	2021-03-29T10:58:59.075
				MY36_015019_173_0	0.08	18.6	2021-04-05T13:56:03.446
37.79	11.24	S28	dark, bright	MY36_014875_169_0	0.06	19.1	2021-03-24T18:56:58.832
				MY36_014962_169_0	0.02	13.2	2021-03-31T21:54:02.203
				MY36_016454_169_1	0.04	28.5	2021-08-01T01:51:35.195
				MY36_016454_169_2	0.04	34.9	2021-08-01T01:52:22.195
21.64	12.64	S29	dark, bright	MY36_014975_168_0	0.04	9.1	2021-04-01T23:26:24.259
				MY36_016467_168_1	0.04	35.9	2021-08-02T03:23:57.251
				MY36_016467_168_2	0.04	40.6	2021-08-02T03:24:45.251

Figures

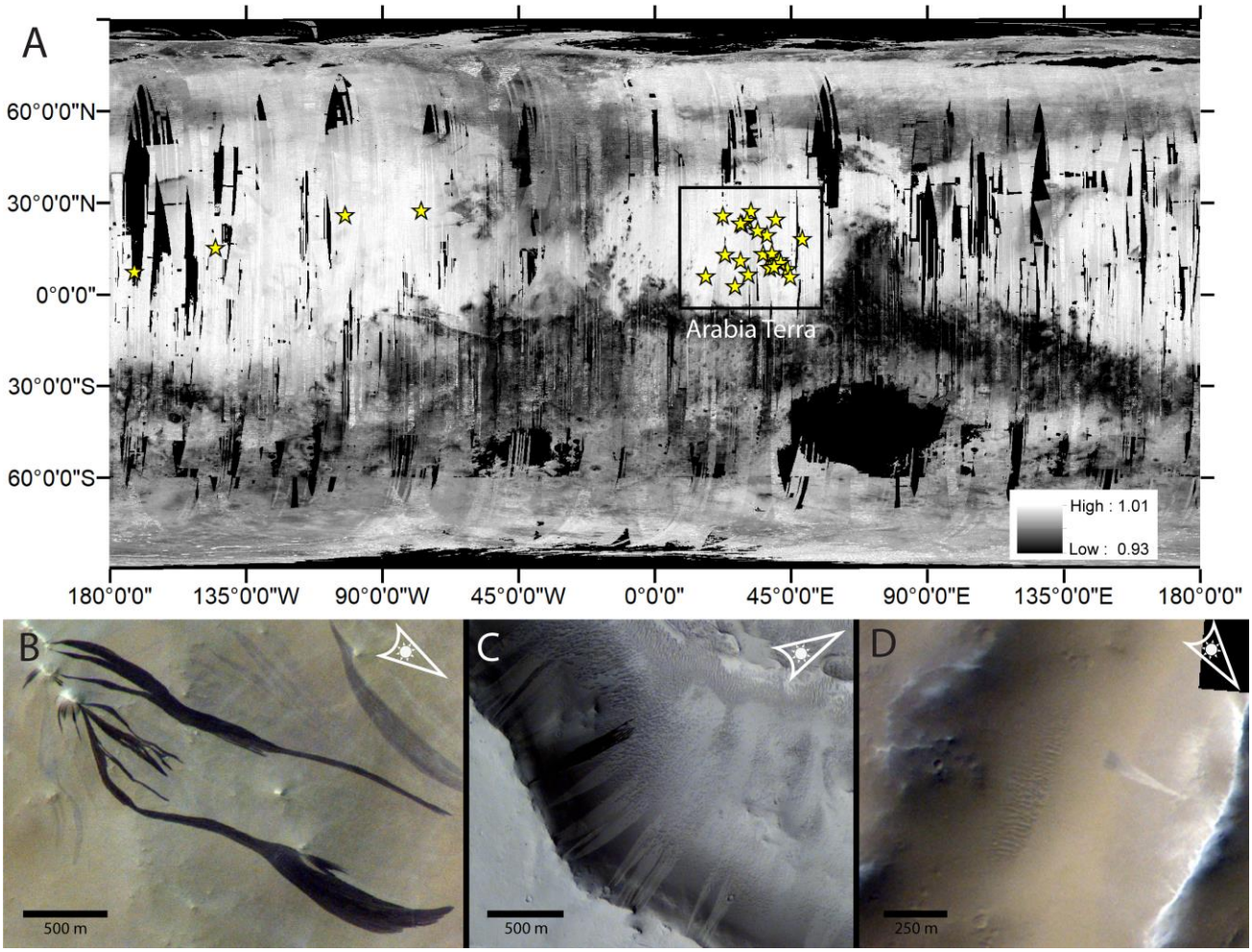

Figure 1: A) OMEGA derived nanophase ferric oxide spectral parameter map (Ody et al., 2012) overlain with locations studied in this work (yellow stars). Regions of ferric oxide parameter larger than 1 are generally dusty, low in thermal inertia and dominated by fine particles. Regions shaded in black correspond to an absence of data. B) Relatively fresh dark slope streaks on a crater wall in Arabia Terra (site S25). These streaks are observed to flow around obstacles and sustain bifurcating morphology. C) Bright slope streaks on a shadowed slope of a channel in Arabia Terra (S20). The fresher dark slope streak in the middle of the image is capping an older

bright streak. D) Transitioning slope streak on a slope of an irregular depression in Arabia Terra (S12). The fan-shaped streak exhibits a contrast reversal partway downslope and was first observed by Sullivan et al. (2001). CaSSIS IDs in respective order: MY35_010269_009_0_RPB, MY34_002312_006_2_RPB and MY35_009517_177_0_NPB. Sun illumination shown in the top right corner of each image. North is up in all panels.

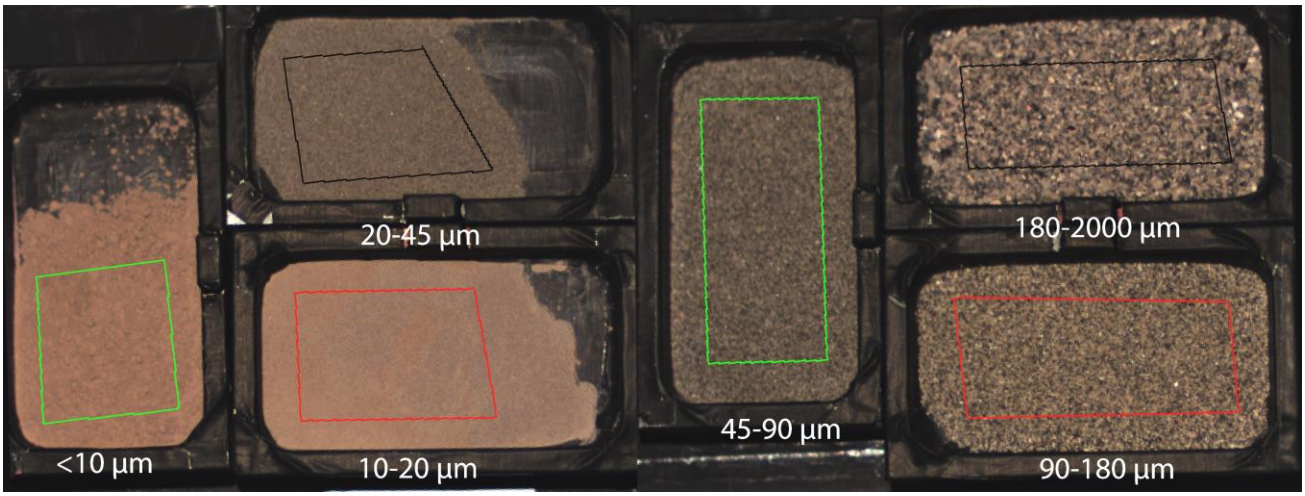

Figure 2: Spectral image of sieved MGS-1 sub-samples of different size fractions in measurement containers. Colored bounding boxes represent the regions of interest (ROI) that were used for the spectral measurements.

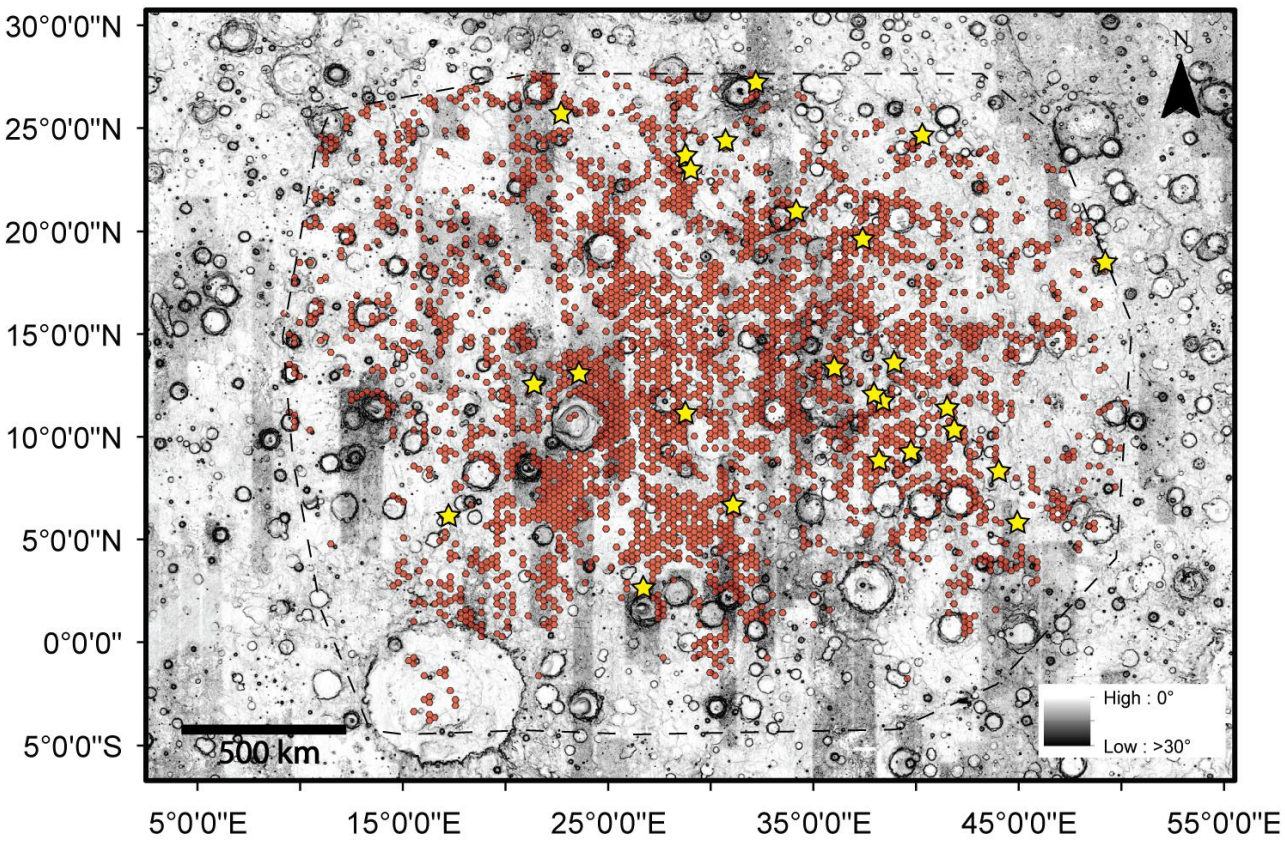

Figure 3: Bright slope streak distribution in Arabia Terra (red hexagons) based on mapping with a global 5 m/px CTX mosaic (Dickson et al., 2018). Each shaded hexagon (20 km in size) indicates at least one bright slope streak present in that area (see Ramsdale et al. (2017) for grid-mapping methodology). Yellow stars indicate locations of CaSSIS multi-angular color photometry. The basemap is HRSC-MOLA slope mosaic (200 m/px).

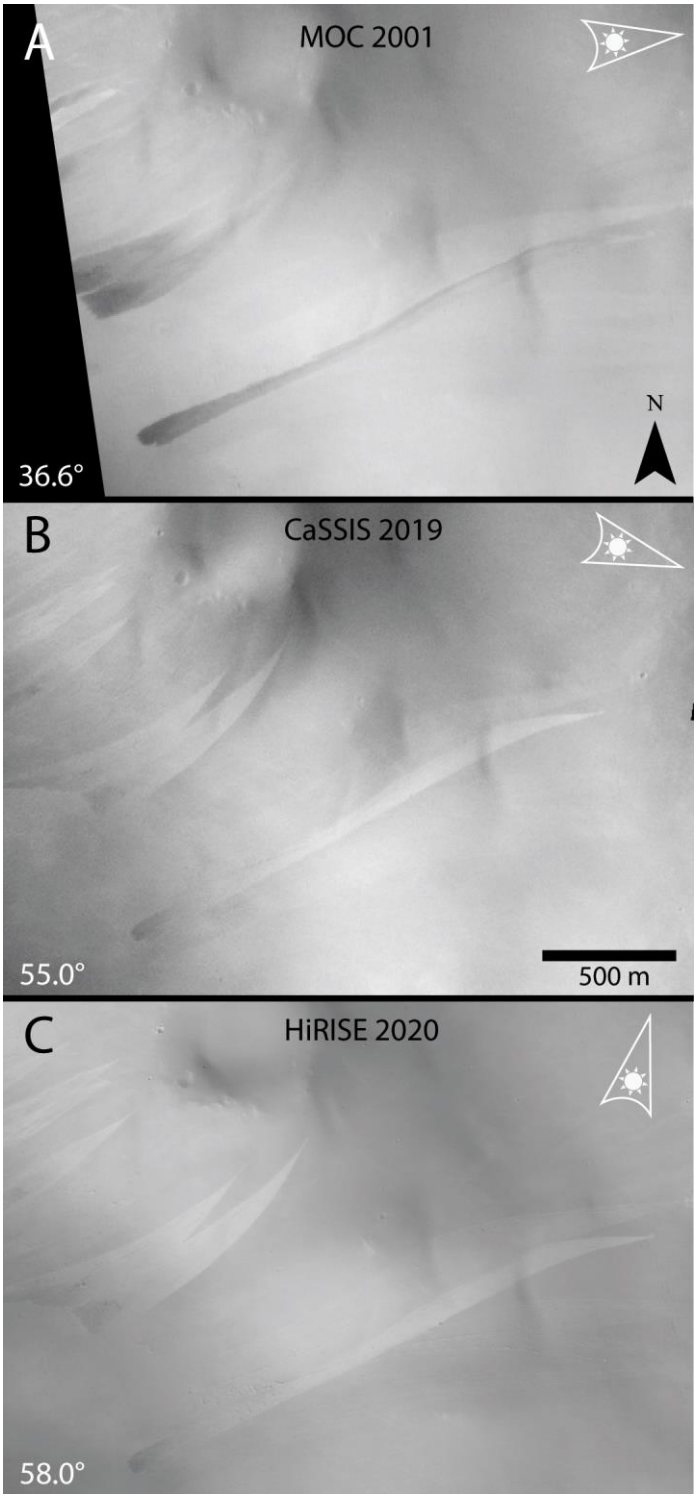

Figure 4: Time-lapse image sequence of slope streaks, exhibiting a contrast transition from dark into bright relative to the surrounding terrain. (A) MOC observation E0301436 taken on 2001-

04-16. (B) CaSSIS PAN image MY35_009342_158_0 taken on 2019-12-27. (C) HiRISE RED image ESP_066514_2050 taken on 2020-10-04. The phase angles are shown at the bottom left of each panel. Sun illumination direction shown in the top right of each image.

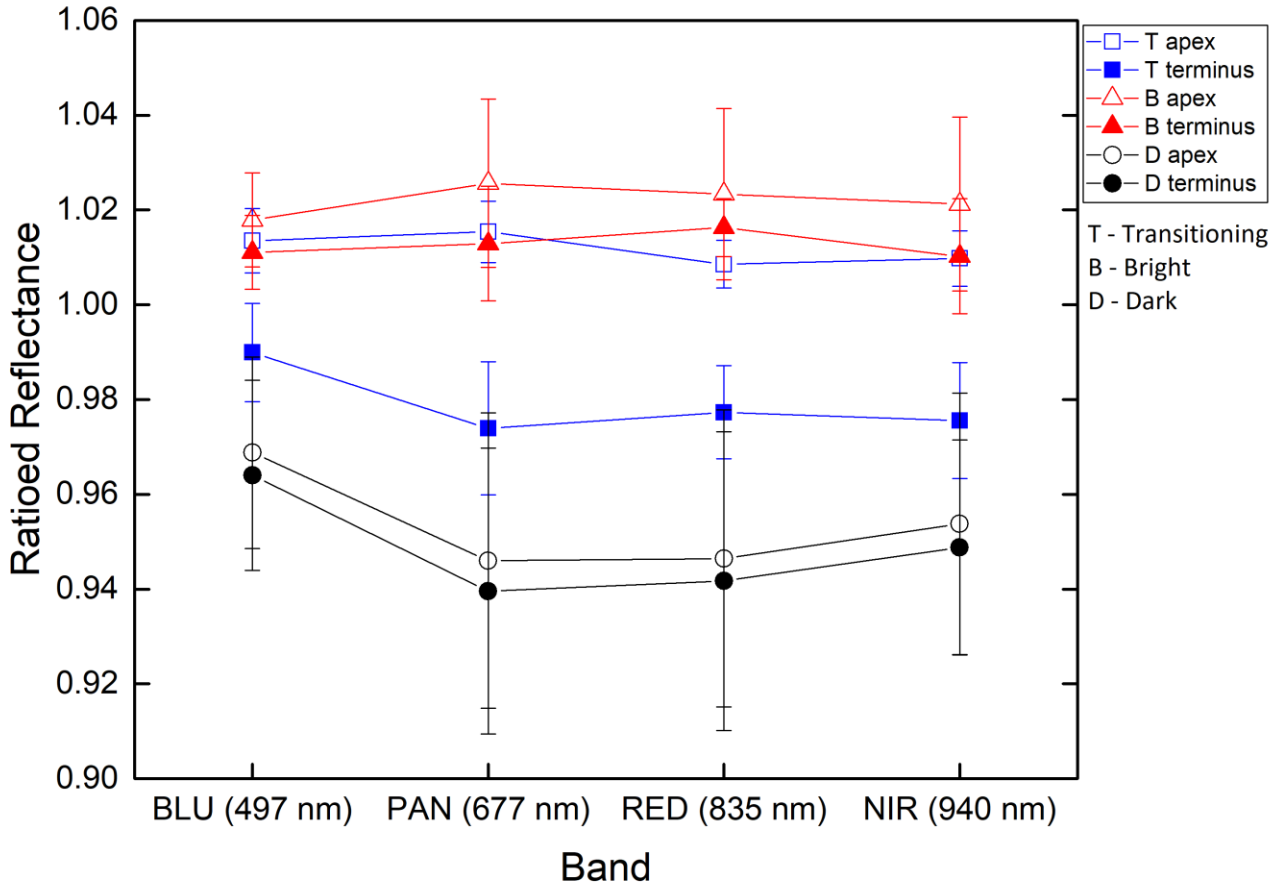

Figure 5: Average ratioed reflectance plot in the four color bands of CaSSIS (BLU, PAN, RED and NIR) for 34 dark, 25 bright and 19 transitioning slope streaks analyzed in this work. The bright streak and transitioning streak apex section spectra exhibit a featureless brightening. For

both sections of dark streaks and transitioning streaks terminus part, the measurements show a decrease from the BLU (497 nm) to PAN (677 nm) ratioed values. Errors bars are 1 sigma and suggest that a large variety of slope streak contrast states exist.

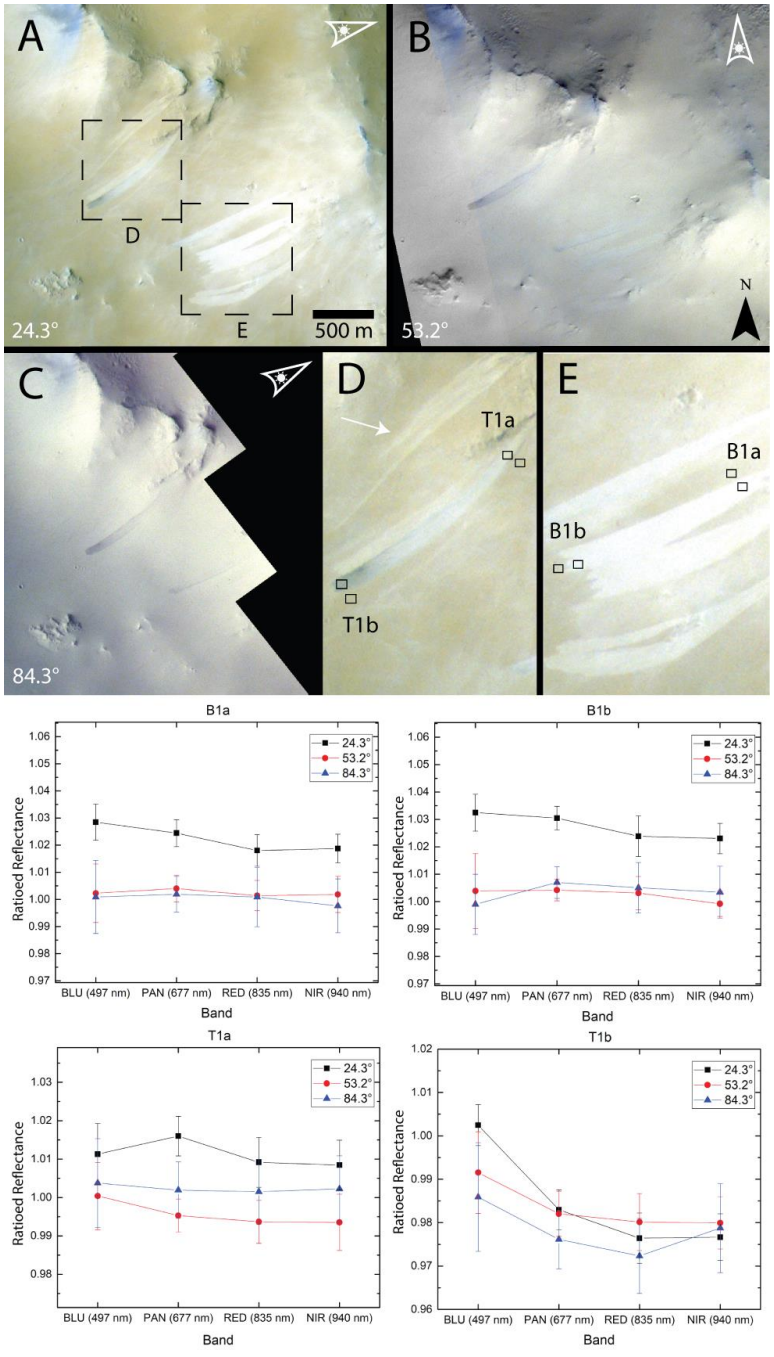

Figure 6: (A-C) CaSSIS multi-angular observations of site S1 (31.91E, 27.26N), which features a transitioning streak and many bright streaks. (D-E) ROI close ups selected for relative photometry on the transitioning streak (T1a and T1b) and on a bright streak (B1a and B1b).

Although the third observation (C) was acquired in low light conditions, the SNR is high enough to obtain reliable photometric measurements. CaSSIS multi-angular ratioed reflectance plots for the apex (B1a) and terminus (B1b) of one bright slope streak and the same measurement for a transitioning slope streak (T1a and T1b respectively). A general brightening with phase is observed for all slope streaks. Bright slope streaks show a featureless brightening in all 4 CaSSIS bands. The terminus part of transitioning streak (T1b) show a sharp decrease in ratio at the BLU band (497 nm). Phase angles are shown on the bottom left (A-C).

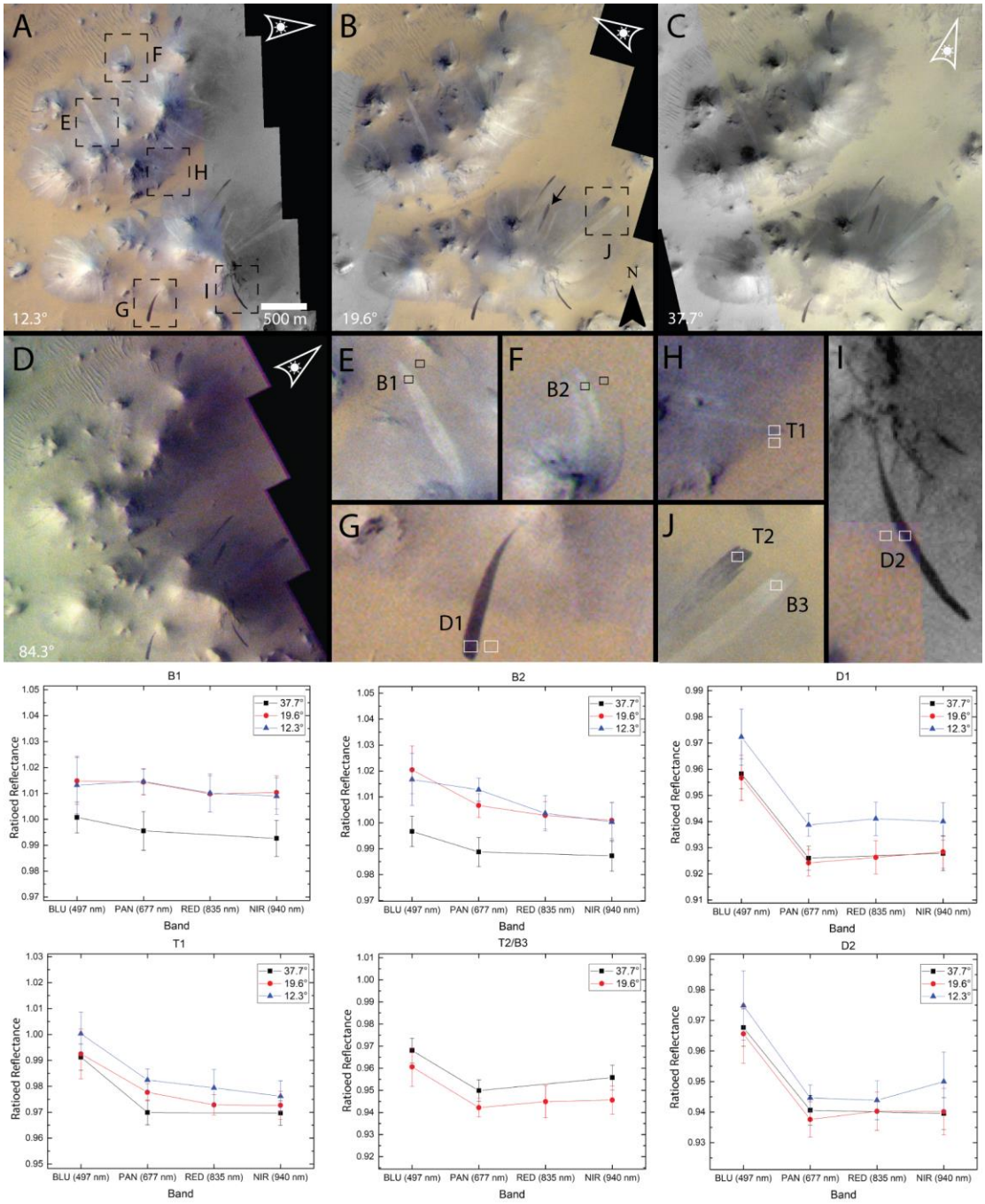

Figure 7: (A-D) CaSSIS multi-angular observations of various slope streaks for site S16. (E-I) ROI close ups selected for relative photometry (B1, B2, T1, D1 and D2). No photometric analysis was performed on (D), it is only shown here to display the importance of high SNR and

good atmospheric conditions in identifying slope streaks. CaSSIS multi-angular ratioed reflectance plots for the terminus of bright (B1 and B2), dark (D1 and D2) and transitioning (T1) streaks at site S16. Ratio plot (T2/B3) of transitioning talus (T2) and bright talus (B3) streak also provided. A general brightening with decreasing phase is observed on all slope streaks. The dark streaks (D1 and D2) and the transitioning streak (T1) show a sharp decrease in ratio at the CaSSIS BLU band (497 nm). A similar effect can be seen in transitioning (T2) and bright streak (B3) termini ratio plot (T2/B3). Phase angles are shown on the bottom left (A-D).

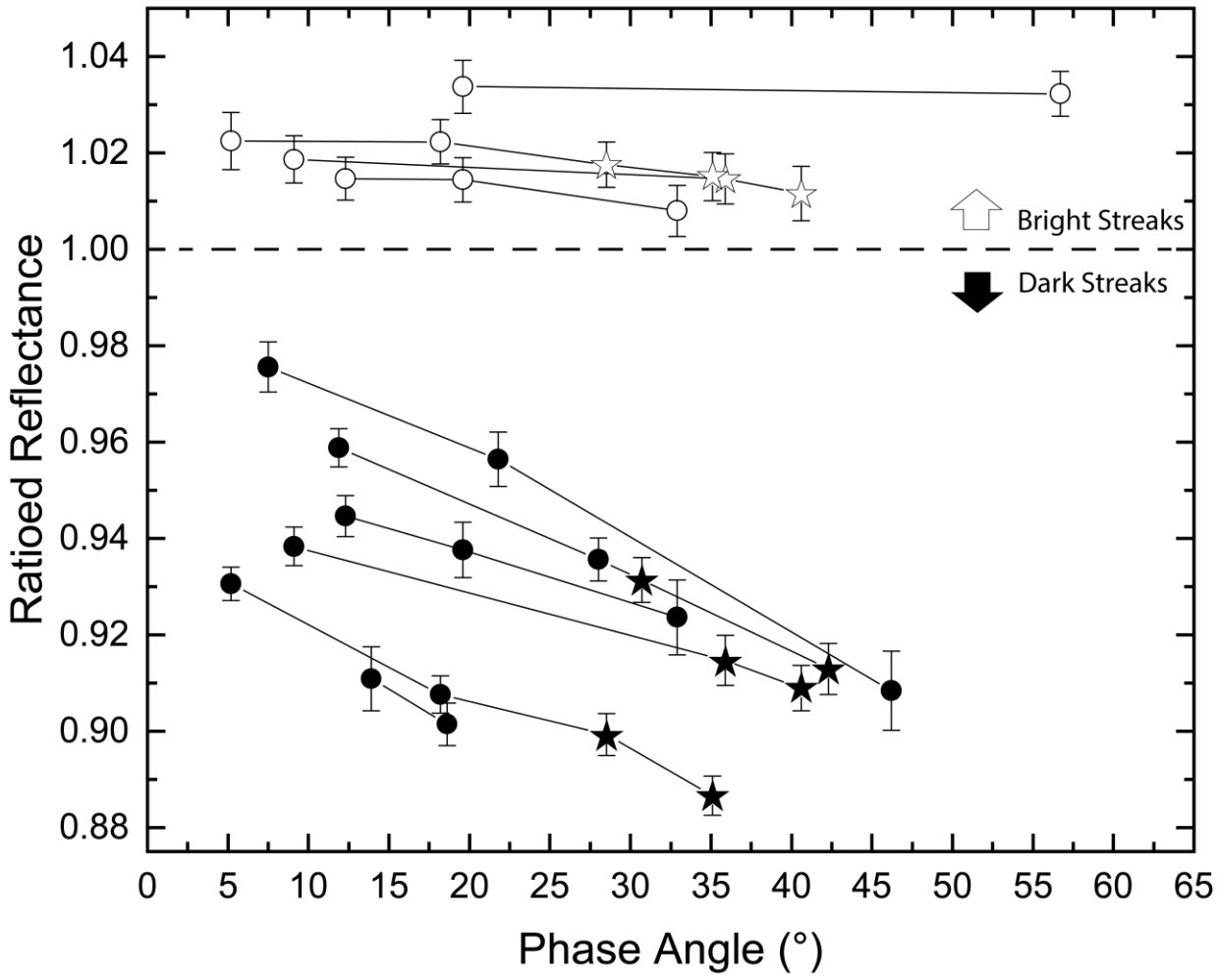

Figure 8: Multi-angular ratioed reflectance plot in the CaSSIS PAN (677 nm) band, for dark (black dots) and bright (white dots) slope streaks observed in this study. Each set of lines is a different site composed of either individual images (dots) and/or stereo observations (stars). A steep linear phase angle dependency is observed for dark slope streaks likely due to interparticle shadow hiding opposition effect. It suggests that slope streak surfaces are more porous and rough relative to the surrounding terrains. Bright streaks exhibit either no change in brightness or a slight brightening in a few cases, which may indicate that their surfaces are more compact relative to the surrounding materials.

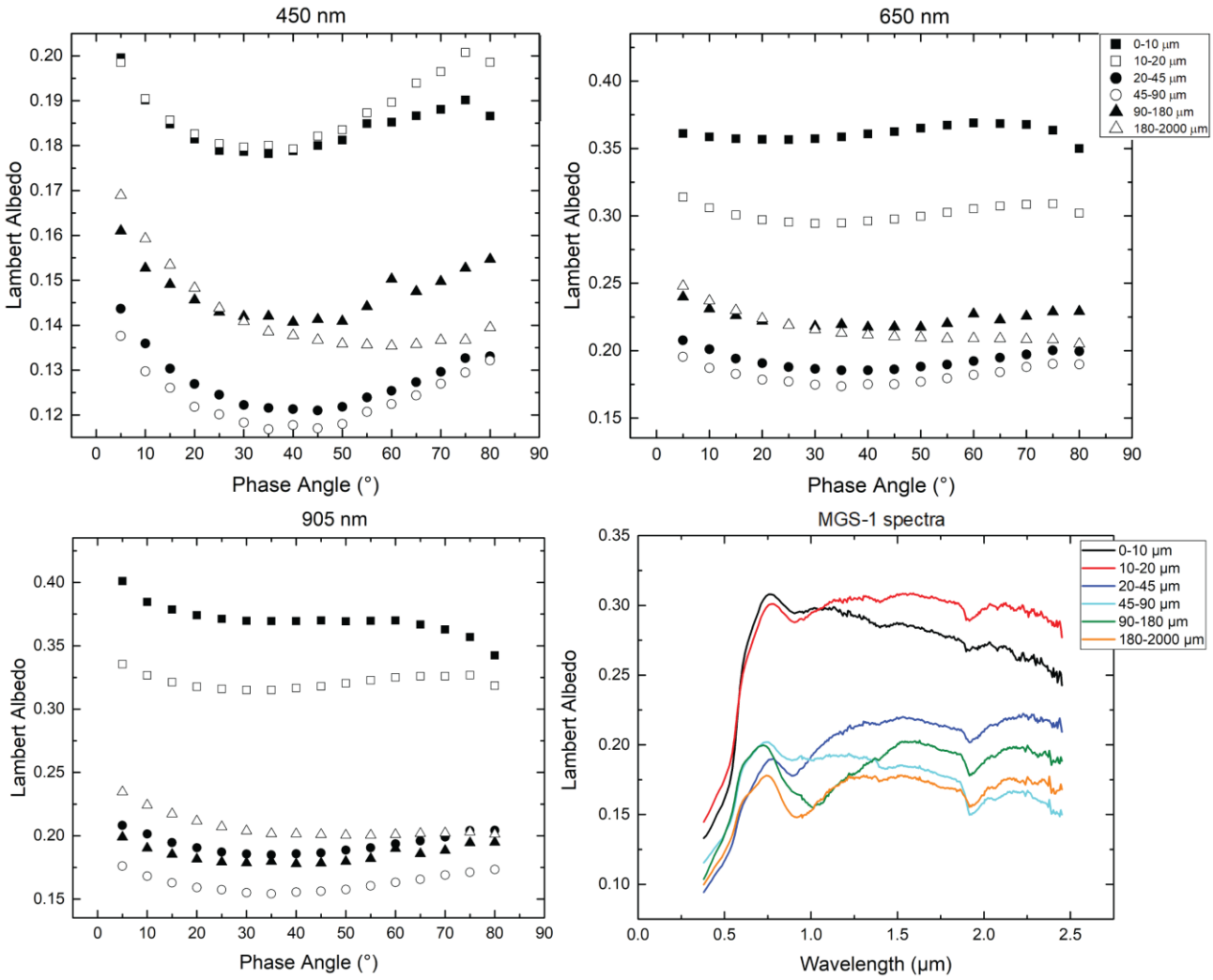

Figure 9: PHIRE-2 goniometer measurements for all MGS-1 size fractions at three different wavelengths (450, 650 and 905 nm). All grain fractions exhibit increased reflectance as phase angles approach 0° , likely due to the broad backscatterring peak of the shadow hiding effect. The fourth plot features MoHIS acquired spectra for different particle size fractions of MGS-1 sample. The smallest particles exhibit the largest albedo. Spectral range is from 0.38 μm to 2.45μm. Observation geometry for PHIRE-2 measurements: i = 0° , e = g.

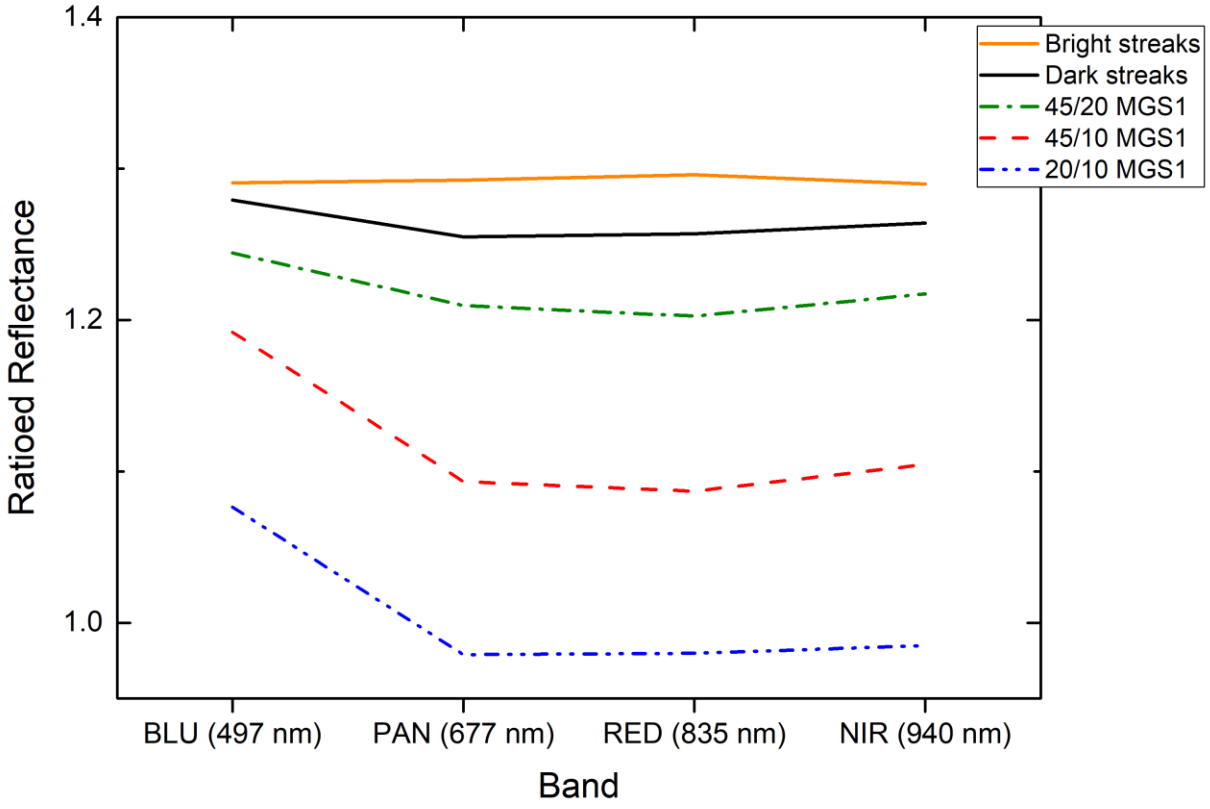

Figure 10: Ratioed reflectance averages for bright (orange solid line) and dark slope streaks (black solid line), and MoHIS spectrometer MGS-1 CaSSIS convolved spectral ratios for selected particle size fractions. A similar ratio feature can be observed from PAN to BLU for both lab and CaSSIS dark slope streak spectra, which indicates a possible particle size effect. Slope streak spectra taken from Fig. 5. Y axis offset for clarity.

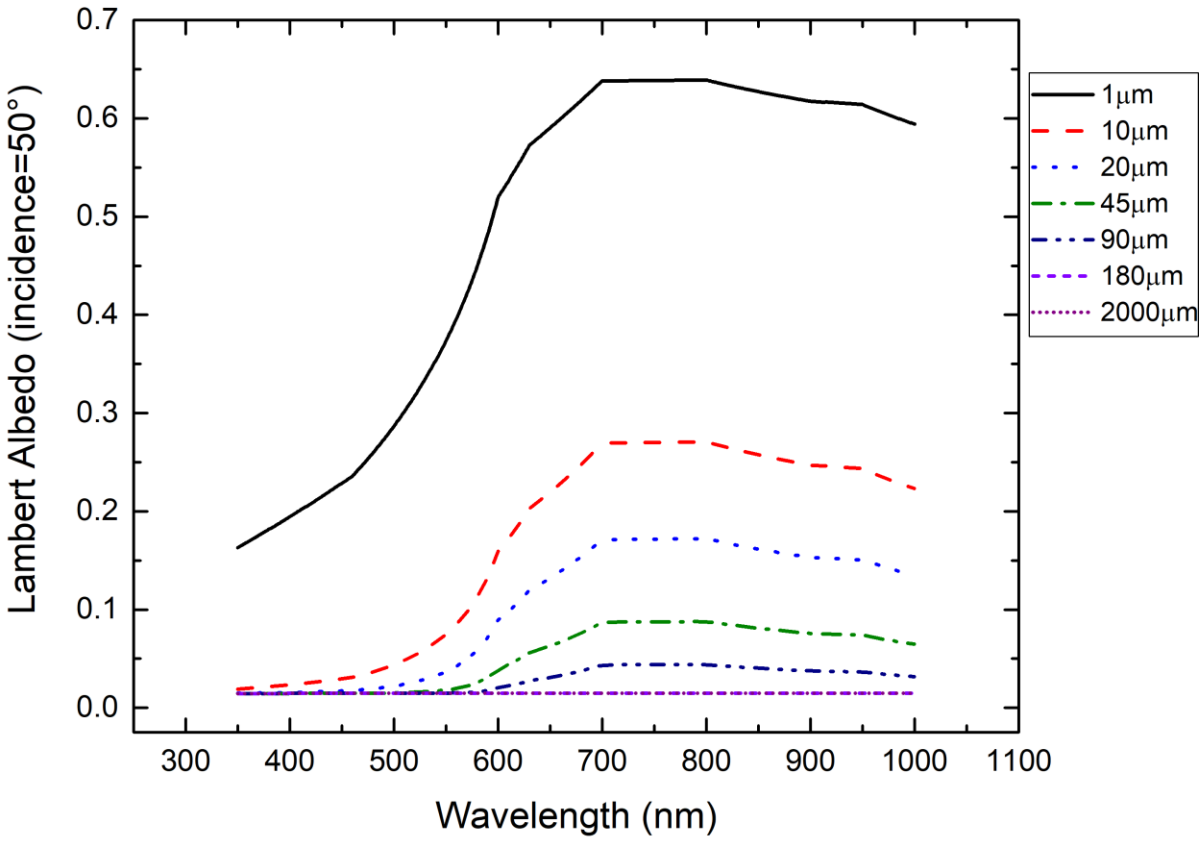

Figure 11: Modeled Lambert albedo reflectance curves for different grain sizes. The model was run for particle size fractions similar to those analyzed in the lab. The plot illustrates that the smallest particles <10 μm exhibit the largest increase in albedo. The incidence angle was set to equal 50° in order to analyze the reflectance dependence on particle size, unrelated to opposition surge phenomena. Based on optical constants derived from CRISM/OMEGA measurements (Wolff et al., 2009).

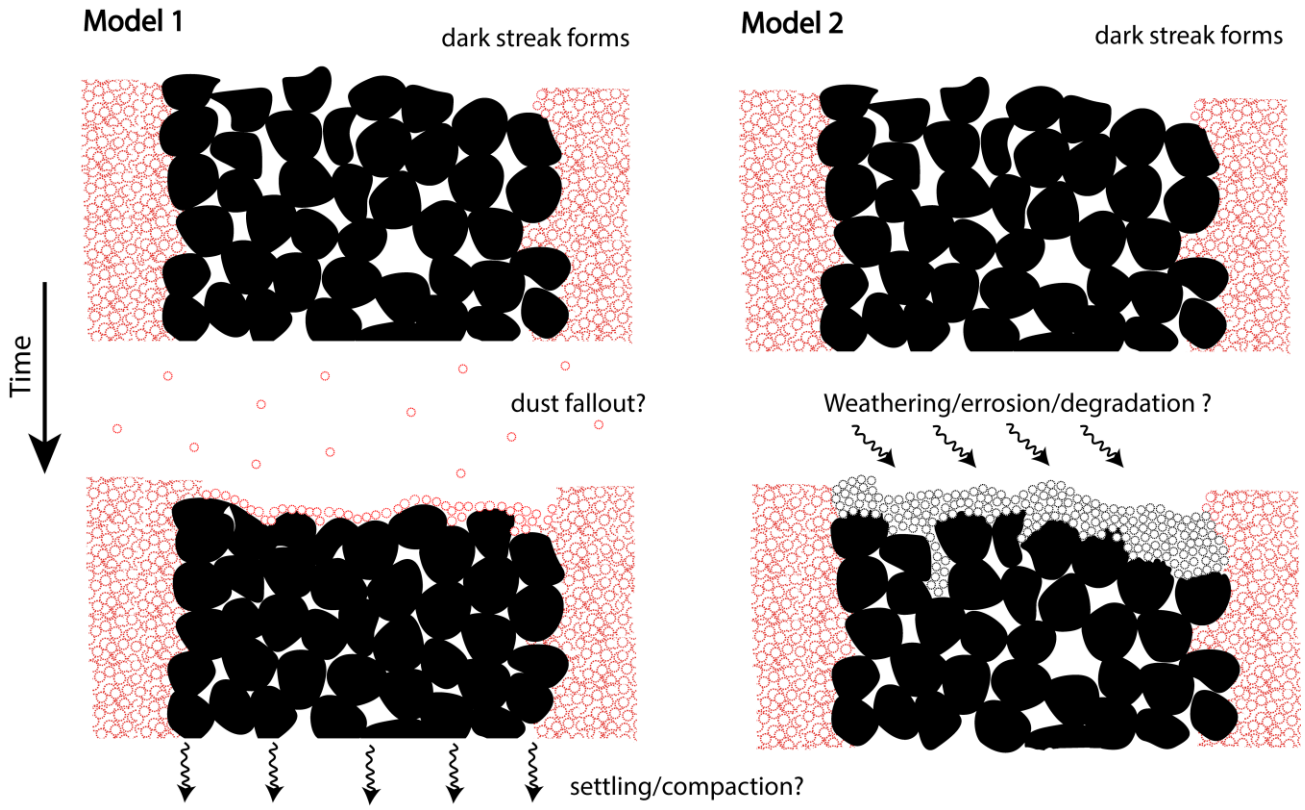

Figure 12: Surface profile view for two types of slope streak brightening models. Conceptual model of dust fallout (Model 1) and the brightening by decomposition of surface agglomerates (Model 2). In Model 1 the slope streak brightening is achieved by deposition of dust and compaction of the rough larger particle layer. Likely several decades are needed for the dark slope streak to become completely brighter than the surrounding terrains. Model 2 illustrates a case where, with time, the fragile large grain agglomerates break down, perhaps due to external weathering or the wear-off of interparticle forces. In this schematic, the color of the grains is only symbolic and particle sizes are not to scale.

Appendix: Hapke Reflectance Model

In our implementation of the Hapke reflectance model we primarily follow the work of Becerra et al., (2015). This version of the model simulated the reflective properties of intimate mixtures of Martian ices and dust. Our model was modified to include only one part in the mixture (dust). By varying the size of the individual particles, the model can output only the particle size effects of dust on albedo. The reflected light from planetary surfaces can be described by the bidirectional-reflectance distribution function (BRDF), as given by Hapke (2012) (eq. 10.2):

$$BRDF(i,e,g) = K\left(\frac{w}{4\pi}\right)\left(\frac{1}{\mu_0+\mu}\right)\{[1+B(g)]P(g) + H(\mu_0)H(\mu) - 1\} \quad (1)$$

where *w* is the average single scattering albedo of a particle, and depends on composition and grain size, μ_0 is the cosine of the incidence angle *i*, and μ is the cosine of the emission angle *e*. *B(g)* represents the opposition surge, which in our case is zero, because we modeled surfaces under moderate illumination conditions (incidence = 50º). *K* is the porosity coefficient, which is set to equal to 1. Since we assume isotropic scattering, the phase function *P(g)* is also 1. The volume average single scattering albedo of a mixed medium can be described by the fractional mass of each component (eq. 10.46; Hapke, 2012):

$$w = \frac{\left(\sum_j^n \frac{M_j Q_{S_j}}{\rho_j D_j}\right)}{\left(\sum_j^n \frac{M_j Q_{E_j}}{\rho_j D_j}\right)} \quad (2)$$

where M_j, ρ_j, D_j are the mass fraction, solid density, and diameter of the *j*th particle respectively. However, in our case the superscript *n*, which is the total number of components in the mixture is set to 1 because dust is the only modeled component. Note that in the original Hapke model, subscript *j* may refer to either shape, composition or size of the particle. In our case, it describes the size of the particle. The extinction efficiency for the *j*th particle is described by the parameter

Q_{Ej}, which is set to 1. This assumption only applies for particles that are much larger than the wavelength of light. Furthermore, Q_{Sj} is the scattering efficiency of the *j*th particle (eq. 6.20; Hapke, 2012):

$$Q_s = S_e + (1 - S_e)\frac{(1 - S_i)\Theta}{1 - S_i\Theta} \tag{3}$$

Where S_e and S_i are the external and internal reflection coefficients (eq. 5.36; Hapke, 2012):

$$S_e = \frac{1}{2}\left(\left|R_{\parallel}\right|^2 + |R_{\perp}|^2\right) \tag{4}$$

Integrating S_e over all angles gives S_i (internal reflection is excluded). The Fresnel reflectivities for parallel and perpendicular polarized light are defined by $R_{\parallel}$ and $R_{\perp}$ respectively. In Hapke (2012) they are given by eq. 4.44-4.49:

$$|R_{\perp}|^2 = \frac{\left(\cos\left(\frac{g}{2}\right) - u\right)^2 + v^2}{\left(\cos\left(\frac{g}{2}\right) + u\right)^2 + v^2} \tag{5a}$$

$$\left|R_{\parallel}\right|^2 = \frac{\left((\mathrm{n}^2 - \mathrm{k}^2)\cos\left(\frac{g}{2}\right) - u\right)^2 + (2nk\cos\left(\frac{g}{2}\right) - v)^2}{\left((\mathrm{n}^2 - \mathrm{k}^2)\cos\left(\frac{g}{2}\right) + u\right)^2 + (2nk\cos\left(\frac{g}{2}\right) + v)^2} \tag{5b}$$

where

$$u = \sqrt{\frac{1}{2}\left(n^2 - k^2 - \sin\left(\frac{g}{2}\right) + \sqrt{\left(\left(n^2 - k^2 - \sin\left(\frac{g}{2}\right)\right)^2 + 4n^2k^2\right)}\right)} \tag{6a}$$

and

$$v = \sqrt{\frac{1}{2}\left(-(n^2 - k^2 - \sin(\frac{g}{2})) + \sqrt{\left(\left(n^2 - k^2 - \sin\left(\frac{g}{2}\right)\right)^2 + 4n^2k^2\right)}\right)} \tag{6b}$$

n and *k* are the real and imaginary parts of the complex index of refraction for each component. The specific numeric values of n and k for martian dust were taken from Wolf et al., (2009).

To describe the internal scattering between the particles we use the internal transmission factor Θ relation (eq. 6.30; Hapke, 2012):

$$\Theta = \frac{r_1 + \exp(-\langle D\rangle\sqrt{\alpha(\alpha+s)})}{1 + r_1\exp(-\langle D\rangle\sqrt{\alpha(\alpha+s)})} \quad (7)$$

where r_1 is given by (6.27; Hapke, 2012):

$$r_1 = \frac{(1-\sqrt{\alpha/(\alpha+s)})}{(1+\sqrt{\alpha/(\alpha+s)})} \quad (8)$$

$\langle D\rangle$ is the mean photon path length and can be expressed by the grain diameter D and the real part of complex index of refraction n (eq. 5.55; Hapke, 2012):

$$\langle D\rangle = \frac{2}{3}\left(n^2 - \frac{\sqrt{n^2-1}}{n}\right)D \quad (9)$$

whereas α is the absorption coefficient, which is given by the light dispersion relation (eq. 2.95b; Hapke, 2012):

$$\alpha = \frac{4\pi k}{\lambda} \quad (10)$$

where λ is the incident light wavelength and k the imaginary index of refraction.

In eq, (8) s is the volume scattering coefficient, which is assumed to be 10^{-17} because of minimal internal scattering (Roush, 1994).

Finally, in eq. (1), $H(\mu_0)$ and $H(\mu)$ are Chandrasekhar's (1960) H-functions, defined by:

$$H(x) = \frac{1}{1-(1-\gamma)x\left[r_0+\left(1-\left(\frac{r_0}{2}\right)-r_0x\right)\ln\left(\frac{1+x}{x}\right)\right]} \quad (11)$$

where the albedo factor (eq. 7.21b; Hapke, 2012) is: $\gamma = \sqrt{1-w}$, and the diffusive reflectance (eq. 8.25; Hapke, 2012): $r_0 = \frac{1-\gamma}{1+\gamma}$.

The modeled bidirectional reflectance is then multiplied by π (assuming isotropic scattering), and divided by the cosine of the incidence angle (μ_0), which results in Lambert Albedo. We neglect atmospheric extinction and scattering in the calculation of the albedo values and output them for all wavelengths from 0.35 to 1 μm, at a resolution of 1 nm.

References

Becerra, P., Byrne, S., and Brown, A. J. (2015). Transient bright "halos" on the South Polar Residual Cap of Mars: Implications for mass-balance. Icarus, 251:211–225. https://doi.org/10.1016/j.icarus.2014.04.050.

Chandrasekhar, S., 1960. Radiative Transfer. New York: Dover. doi:10.1029/2005JE002531.

Hapke, B., 2012. Theory of Reflectance and Emittance Spectroscopy, Second Edition. Cambridge University Press.

Roush, T., 1994. Charon: more than water ice? Icarus 108, 243–254. Souchon, A. L., Pinet, Wavelength dependence of dust aerosol single scattering albedo as observed by the Compact Reconnaissance Imaging Spectrometer. Journal of Geophysical Research 114, E00D04, doi:10.1029/2009JE003350.

Chapter 3:

TROPICAL FROST ON MARTIAN VOLCANOES

A. Valantinas[1], N. Thomas[1], A. Pommerol[1], V. Bickel[1], M. Almeida[1], N. Schorghofer[2] and C. Re[3].

[1]Physikalisches Institut, Universität Bern, Sidlerstrasse 5, 3012 Bern, Switzerland.

[2]Planetary Science Institute, Tucson, USA.

[3]INAF-Astronomical Observatory Padova, Padova, Italy.

In preparation

Introduction

Close-up observations of frozen volatile species such as H_2O and CO_2 in the Mars polar caps were first conducted during the Mariner and Viking orbiter eras (Neugebauer et al., 1971; Farmer et al., 1976). The seasonal polar caps were observed to expand and contract each year to ~60° latitude in both hemispheres (James et al., 1992; Kieffer et al., 2000). Viking Lander 2 documented thin layers of water frost outside of polar caps (~48°N) during the Martian winter (Svitek & Murray, 1990). Norbert Schorghofer & Edgett (2006) using Mars Orbiter Camera (MOC) showed that seasonal frost in the southern hemisphere can be found to as low as 24°S on poleward-facing slopes. Observations of the Observatoire pour la Minéralogie, l'Eau, les Glaces, et l'Activité (OMEGA) spectrometer showed that seasonal water frost can be found up to 15°S and 15°N on shadowed slopes (Carrozzo et al., 2009). Using Compact Reconnaissance Imaging Spectrometer (CRISM) and OMEGA observations Vincendon, Mustard, et al. (2010) showed that seasonal CO_2 frost forms as low as 24°S on pole-facing slopes in the southern hemisphere. Using the same dataset Vincendon, Forget, et al. (2010) observed seasonal deposits of water ice that reach 13°S but are restricted to latitudes higher than 32°N.

Extremely small amounts of H_2O frost were observed to condense on calibration targets of the Opportunity rover at even equatorial latitudes ~2°S (Landis, 2007). Cushing & Titus (2008) used Thermal Emission Spectrometer (TES) 2 AM surface temperatures and thermal modeling to show that CO2 frost should form on Arsia Mons caldera (~9°S) every night throughout the year. Using 3 AM measurements of atmospherically corrected surface temperature of Mars Climate Sounder (MCS) and thermal modeling, Piqueux et al. (2016) suggested that most of equatorial, low thermal inertia regions undergo CO_2 frost condensation at night and may retain frost up to 1 hour after sunrise. More recently, Lange et al. (2022)

investigated THEMIS early morning data in the low thermal inertia regions (including Martian volcano calderas) but did not find evidence for early morning CO_2 frost.

Here, we analyze new early morning observations of low thermal inertia regions from the Colour and Stereo Surface Imaging System (CaSSIS; Thomas et al., 2017) onboard the ESA's Trace Gas Orbiter (TGO). TGO's non-Sun-synchronous orbit and CaSSIS high signal-to-noise (SNR) are particularly favorable for the detection of early morning phenomena. Our observations provide evidence for early morning frost in the tropics but only on high altitude Martian volcano calderas. Because at visible wavelengths it is difficult to distinguish between H_2O and CO_2 frost we use the Mars Subsurface Ice Model (MSIM; Schorghofer, 2022) to derive local temperatures and frost thicknesses at the sites imaged by CaSSIS. H_2O and CO_2 frosts can remain stable in different temperature regimes, therefore knowing the local thermal conditions may provide insights into the nature and composition of the frosts.

Methods

1. CaSSIS frost observations

We surveyed ~4,200 CaSSIS images (acquired up to 2022-02-05) with illumination geometries of 50 – 90° incidence within dusty, low thermal inertia regions (60° N – 30° S). These images consisted of early and late local solar times (LST). Analysis and comparison in these two local time regimes may help the distinction between early morning and late afternoon phenomena. During the survey, it was noticed that most CaSSIS images acquired at extremely high solar incidence angles of 85 – 90° contain color and calibration artifacts due to the decrease in signal-to-noise ratio (SNR) and/or an increase in aerosol contribution from the atmosphere (Pommerol et al., 2022). Therefore, after being surveyed the images with color artifacts were labeled as ambiguous and were not used for further analysis.

Frost identification relied upon the use of CaSSIS NPB (NIR = 940, PAN = 670, BLU = 497 nm) and RGB (PAN and BLU only) products. These filter configurations allow a convenient separation between frosty and frost-free terrains. In CaSSIS color products frosty areas appear bluish, and/or whitish, and sometimes are bright only in the BLU filter. As shown by previous studies (Carrozzo et al., 2009; Vincendon, Forget, et al., 2010) frost deposits are usually correlated with topography (prefer poleward slopping terrains). Therefore if both conditions were met (color & topographic correlation) it was considered a strong indication of surface frost. As a final procedure, each of these candidate detections was then analyzed using spectral profile measurements in the Environment for Visualizing Images (ENVI). This procedure extracts the pixel reflectance values between two selected points in each filter. The profile values were then normalized by a mean reflectance value of a nearby frost-free, relatively flat region of interest (ROI). If the frost deposits were brighter in the BLU filter than the surrounding frost-free terrains by at least 3% (within CaSSIS absolute uncertainty; Thomas et al., 2022), then such images were flagged as positive frost detections. Such survey yielded many frosty sites (not shown here) at latitudes ~40° N and ~30° S. However, because these latitude bands are dominated by known seasonal frost deposits (Carrozzo et al., 2009; Vincendon, Forget, et al., 2010; Vincendon, Mustard, et al., 2010) and we do not have a robust method to distinguish between seasonal and diurnal frost, we further narrowed down our filtering criteria. The final frost detections analyzed here were restricted to equatorial ~20° N to ~10° S latitudes (outside of the seasonal midlatitude regions). In the following sections, only equatorial sites that included visible evidence of frost are considered.

To demonstrate cases where frost deposits correlate with topography we used CaSSIS and Context camera (CTX) Digital Elevation Models (DEMs). CaSSIS DEMs were produced by

a pipeline developed at the University of Padova (Simioni et al., 2021; Re et al., 2022). The CaSSIS images that did not have respective CaSSIS DEMs were orthorectified over CTX DEMs using QGIS. CTX DEMs were produced using the NASA Ames stereo pipeline (Beyer et al., 2018).

2. Thermal modeling

Surface temperatures are modeled by solving the one-dimensional heat equation with a semi-implicit numerical model and the surface energy balance includes the latent heat of CO_2 frost. At each site, temperatures are evolved over 10 Mars years with 144 time steps per sol, and surface temperatures from the last Mars year are used for this study. The vertical grid consists of 80 points and at least 6 are within the diurnal skin depth, so diurnal and seasonal temperature cycles are resolved. Besides the site-specific input parameters (latitude, albedo, and thermal inertia) assumed parameters are a CO_2 albedo of 0.65 (Kieffer et al., 1977) and an infrared emissivity of 1. The atmospheric pressure varies throughout the year. This Mars thermal model is part of the MSIM program collection and has been used in several previous studies (e.g. Schorghofer & Edgett, 2006) and technical details are described in the online program repository (Schorghofer, 2022).

For sites with a non-negligible slope, the change in solar incidence angles and terrain shadowing (delayed sunrise or early sunset) are taken into account. In addition, the land area within the field of view emits infrared radiation onto the sloped surface (terrain irradiance). The terrain irradiance is estimated based on a second thermal model run for a horizontal surface, with its thermal emission added to the surface energy balance on the slope. The thermal model for

planar slopes has also been used in previous studies, e.g., in Schorghofer & Edgett (2006) for the modeling of seasonal CO_2 frost at low-latitude sites.

The extinction, absorption, and scattering in the Martian atmosphere are evaluated with a simple parametrization. The long-wavelength sky irradiance at the 520 Pascal level is assumed to be 4% of the noon-time insolation, as in Kieffer et al. (1977), and this fraction is scaled (reduced) exponentially based on the elevation of the site. Many of the study sites considered here are at extremely high elevation (above the 10.8 km scale-height of the atmosphere) and simultaneously have extremely low thermal inertia, so night-time temperatures can be very low and are highly sensitive to atmospheric model parameters, because long-wavelength sky irradiance prevents the surface temperature from falling even further. The night-time temperatures are also likely sensitive to the method used to determine the thermal inertia. However, the sky irradiance plays a minor role at daytime, when the frost observations were made. The extent of diurnal CO_2 at night is sensitive to the choice of model parameters, whereas the surface temperatures near the H_2O frost point temperature can be considered a robust prediction of the model.

3. Boulder size measurements

In order to investigate a potential effect of the diurnal frost cycle on the overall geomorphology and landscape evolution we studied the shape of mass-wasted boulders across 6 sites of interest. Here, we compare the sizes of boulders on volcanoes with frost as determined by CaSSIS (two sites in Olympus Mons and one in Arsia Mons) and on volcanoes where frost has not been detected (Tharsis Mons, Jovis Tholus, and Ulysses Tholus). Because frost accumulates preferentially on poleward facing slopes on Mars (Khuller et al., 2021), we only focused here on

N-facing and S-facing slopes. This might reveal if there are considerable differences in boulder sizes due to frost weathering (Hales & Roering, 2007).

We used 8 map-projected HiRISE images in QGIS to determine the three principal dimensions of each identified boulder. The first dimension is defined as the longest distance between two points on the boulder as visible from orbit. Similarly, the second dimension is defined as the diameter of the boulder orthogonal to the first dimension. Lastly, the third dimension is defined as the height of the boulder as estimated using shadow length and solar incidence angle. In total, we identified and measured 63 boulders across the six sites. All derived measurements were plotted on ternary diagrams (per Sneed & Folk, 1958) using the Tri-Plot software by Graham & Midgley (2000). These diagrams relate the three principal dimensions of each boulder, visualizing its overall shape as well as similarities and differences within and across the studied sites.

Results

1. CaSSIS observations of frost

Equatorial frost was detected only on extremely high altitude volcano calderas. Figure 1A shows one such case on Arsia Mons where frost is ubiquitous on the caldera floor and caldera rim. A correlation between frost deposits and topography is also observed. For example, frost can be seen on the shadowed slopes of craters (see the four largest craters on the caldera plains) but is absent on well-illuminated steep slopes. Since the CaSSIS image shown here is ~40 x 10 km in size and the frost is ubiquitous, it is likely that a layer of frost covered the whole Arsia Mons caldera (~100 km in diameter, Fig. 1C) at the time of the image acquisition.

We detected in total 7 instances of frost on Olympus, Ascraeus and Arsia Mons (Fig. 2). The frost is detected only at high altitudes (above 15 km in elevation). Additionally, the frost

deposits on Arsia Mons (Fig. 3) are observed only in the early Martian morning and during southern winter solstice (Ls = ~90°). We acquired three additional observations of Arsia Mons caldera in the warm Martian season and at three different LSTs (early morning, afternoon and late afternoon). These images do not appear to reveal frosts (Fig. 3 B-D). To prove that the frost is only brighter in the CaSSIS BLU filter we extracted a spectral profile, which shows that frosty surfaces are bluer by up to ~20% (Fig. 3E). For example, notice the increase in the BLU reflectance towards the less illuminated part of the crater floor as the reflectance in NIR and PAN decreases (e.g. pixel #100). The decrease of the reflectance in NIR and PAN is due to increased shadowing relative to the reflectance of the ROI used in the spectral ratioing step (Fig. 4E). The point where spectral profiles of each filter intersect, at pixel # ~75 (Fig. 3E) is equal to the reflectance ratio of 1, since this is the location of the frost-free ROI used in the reflectance ratio (Fig. 4E). The general trend that frost is only brighter in the BLU filter can also be observed in individual linearly stretched CaSSIS filter images (Fig. 4, A-C).

Figure 5A shows the global distribution of CaSSIS observations of the five tallest volcanoes on Mars. To illustrate that the positive frost detections correlate with L_s, LST and altitude we plotted all CaSSIS observations of Arsia, Ascraeus and Olympus Mons in Figures 5B-D. The three detections in Arsia Mons fall within autumn (Ls = 0-90°) and winter (Ls = 90-180°) seasons in the southern hemisphere. However, the autumn observation (at ~45° Ls) only shows frost on slopped terrains where temperatures in shadows are low enough for frost to condense. The single positive detection in Ascraeus also showed residual frost on slopped terrains. The detections in Olympus fall within northern winter (Ls = 270-360°) and early spring (Ls = 0-45°). Per chance, the early spring frost observations of Ascraeus (MY36_015228_168_0_NPB) and Olympus (MY36_015229_160_0_NPB) were taken within

the same Martian sol (orbit # 15,228 and 15,229) and roughly 1.5 h after sunrise (LST of 07:06 and 06:58 respectively). Careful inspection revealed that, although these observations were taken at similar LSTs, frost on Olympus was more pervasive than on Ascraeus. This might be because the Olympus observation was taken at a higher altitude and more northerly latitude, therefore colder temperatures could have prevented frost from sublimating.

In addition to Pavonis Mons negative detections, we do not observe frost on Elysium Mons (see Fig. 6). We cannot exclude the lack of appropriate observations in Elysium (early morning, high altitude and cold season) as the primary reason of non-detections. Collectively CaSSIS observations suggest that the frost cycle over Martian volcanoes is highly ephemeral. Extremely high altitudes above 15 km, cold seasons and early morning hours are required for successful detection of frost.

2. Thermal modeling: CO_2 frost?

In addition to the thermal model results of MSIM (Schorghofer, 2022), we include here KRC (Kieffer, 2013) and Mars Climate Database (MCD; Millour et al. 2018) results for comparison (Figure 8). The MSIM noon peak temperatures match with the temperatures extracted from the MCD. In contrast, the MCD does not predict any CO_2 frost at Arsia Mons at the time of CaSSIS observation (Fig. 2A) because surface night temperatures are above the frost point of CO_2 (>150 K). However, the MCD predicts a very thin layer (~0.3 microns) of H_2O frost at ~8 AM (not shown here). The H_2O frost point at an elevation of 16.4 km is about 190 K (see Schorghofer, 2020) and at the time of CaSSIS observation at 8AM surface temperatures reach ~204 K. Therefore, it is questionable if water frost can remain stable for such extended amount of time.

Both KRC and MSIM predict CO_2 frost over Arsia Mons, which is indicated by very low nighttime temperatures. The complete sublimation of frost is represented by a sharp increase in

temperatures at ~9 AM (Fig. 8B). However, the CO_2 frost point at this altitude (~16.4 km) is around 138 K and only the MSIM predicts such cold temperatures during the night on Arsia Mons. This is in contrast to temperatures of ~145 K indicated by the KRC. Both of these models use the same set of input parameters (albedo, thermal inertia, altitude, Ls and slope). The CO_2 frost point was calculated using Clapeyron's law from James et al. (1992) and assuming 30% lower atmospheric pressure (1.07 millibar) due to seasonal decrease in the southern winter. The CO_2 condensation temperature ranges from ~130 K on top of Olympus Mons to >153 K in Hellas basin (Piqueux et al., 2016). In any case, both models predict that CO_2 frost has completely sublimated at ~9 AM and from this perspective are in good agreement.

In addition, we model the CO_2 frost thickness (Fig. 9) present at the time of the acquisition of the CaSSIS image shown in Figure 2A. At 8 AM, the frost layer is about 185 microns. The maximum frost thickness of ~336 microns is reached just around sunrise and afterwards it continues sublimating until ~8:45 AM. At that point, the surface is free of frost and the underlying fine, low thermal inertia dust layer rapidly heats up.

3. Boulder sizes

Boulder size measurements on volcanoes with frost revealed that there are no considerable differences between N- and S-facing slopes on Olympus Mons (Fig. 7). The boulder size measurements are clustered around the compact and bladed (CB) category on both Olympus Mons S-facing slopes and SE-facing slopes on Arsia Mons. This suggests that boulder sizes are similar irrespective of slope orientation and geologic location. The sizes in frost-free sites of Jovis and Ulysses Tholus are similar on SE- and NW-facing slopes (centered towards the CB group). Compared to the boulder populations on respective slope orientations in frost-containing sites of Olympus Mons and Arsia Mons, boulder sizes are nearly identical. The boulder shapes

on Tharsis Tholus S-facing slopes appear to be plated (P) and the discrepancy here might imply differences in the bedrock properties unrelated to frost weathering.

Although the dataset of boulder size measurements is not statistically large, there seems to be little evidence for thermal stress and weathering. This is somewhat unsurprising because boulder cracking by expansion of water ice should be more efficient on Earth than on Mars. On Mars, atmospheric pressures are below the triple point of water and therefore the effects of a liquid phase are not involved. Therefore, frost weathering on Mars likely plays a minor role in landscape evolution.

Discussion

The absence of morning CO_2 frost in the equatorial regions except the tallest Martian volcanoes requires an explanation. The diurnal temperatures atop Arsia Mons vary by a factor of 2 (see Fig. 8) partly due to the very low atmospheric pressure (~1 millibar) and low thermal inertia (~30 J m^{-2} K^{-1} $sec^{-1/2}$) of the surface dust. Such surface conditions are quite extreme if compared to other Martian terrains (Cushing & Titus, 2008). The global diurnal CO_2 frost cycle presented by Piqueux et al. (2016) predicts up to 350 μm layer of CO_2 on the flanks of volcanoes, parts of northern Tharsis and Arabia, and in Daedalia Planum. Piqueux et al., (2016) argued that after the atmospheric correction many MCS observations were at or below the CO_2 frost point temperature (up to 9 K colder than uncorrected ones) and suggested that the lack of similar corrections in other studies precluded the detections of widespread CO_2 frost (Schorghofer & Edgett, 2006; Cushing & Titus, 2008; Vincendon, Mustard, et al., 2010). Although we do not have an independent way to test this, CaSSIS non-detections of frost place strong regional constraints. CO_2 frost is only identified on the volcano calderas during the morning of cold seasons and sublimates up to 2.5 h after sunrise. This agrees with our thermal modeling results,

which predict temperatures within CO_2 frost point up until ~9 AM on Arsia Mons. To explain the nondetections of frost in early morning THEMIS images Lange et al. (2022) proposed a "dirty" CO_2 ice model, which predicts CO_2 frost forming within the pores of the dusty regolith. They argued that such a non-homogenous layer (tens to hundreds of microns thick) would be unidentifiable in the visible images. However, CaSSIS clearly observes CO_2 frost on Arsia and other Martian volcanoes where temperatures are very low during the night but does not observe global morning deposits in other locations proposed by Piqueux et al. (2016). Therefore, if present in other locations, such frost deposits should be detectable in CaSSIS color images. Although, there is a slight bias in the CaSSIS database against images of 85 – 90° incidence, the superior SNR-in comparison to other imagers-is one reason for early morning detections. It is unclear what is the minimum layer of frost that CaSSIS can detect but previous studies showed that well calibrated spectrometers such as CRISM and OMEGA are sensitive to deposits a few microns thick (Vincendon, Forget, et al., 2010).

The discrepancy described above might be explained by thermal modeling considerations. The nighttime temperatures depend very much on model assumptions, whereas temperatures above say 200 K much less so. The assumption of reduced atmospheric absorption in the infrared wavelengths leads to colder nights. While reduced extinction and scattering in the atmosphere may be appropriate for high elevation, denser atmosphere at lower elevations would lead to warmer nighttime temperatures. This would result in decreased CO_2 frost thicknesses and earlier disappearance of frost during the early morning. Thermal inertia also plays a major role in the calculations of nighttime temperatures. Cushing & Titus (2008; Fig. 3) showed that modeled temperatures (based on KRC) are higher than TES-observed brightness temperatures of Arsia Mons caldera, which suggested temperature dependent thermal conductivity (i.e. variable

thermal inertia). Therefore, models that use simplified assumptions on thermal inertia may overpredict or underpredict local surface temperatures.

To test the hypothesis that the presence of CO_2 frost on the volcano calderas may interact with the surface geology, we acquired and reviewed several HiRISE observations. It has been shown that the caldera floor hosts meter-scale reticulate bedforms (Bridges et al., 2010). Although these indurated dust structures are present in locations where we observe frost, they are also found in regions where CO_2 frost is not observed to form, such as on the volcano flanks and surrounding Tharsis plains. In selected HiRISE images, we searched but were not able to find any correlation between reticulate textures and frost deposits. This likely suggests that aeolian processes and cementation agents other than frost control the formation of these features.

The dust layer capping the Tharsis volcanoes may be several meters thick (Keszthelyi et al., 2008). Such amounts of dust in combination with strong winds over the caldera (Rafkin et al., 2002) and plentiful steep slopes around the caldera rim should result in favorable environment for mass wasting phenomenon known as slope streaks (Sullivan et al., 2001). Moreover, Piqueux et al. (2016) and Lange et al. (2022) proposed that the diurnal CO_2 frost condensation/sublimation process may cause slope instabilities and trigger slope streak formation. After the inspection of CTX images we did not observe any slope streaks in locations where CaSSIS detected frost (on Arsia, Pavonis, Ascraeus, Olympus and Elysium calderas) nor on nearby slopes. Conversely, in regions with abundant slope streaks such as Arabia Terra, a CaSSIS-lead study did not find evidence for early morning frosts (Valantinas et al., 2021). Taken together, the dry formation model of slope streaks (Sullivan et al., 2001) and the CO_2 sublimation as the triggering mechanism (Piqueux et al., 2016) predict a process that would result in billowing dust clouds in the early Martian morning. It is estimated that there might be

~800,000 slope streaks on Mars (Aharonson et al., 2003) and that the average formation rate is around 4.7%/slope streak/Mars year (Bergonio et al., 2013). Morphologic measurements showed that up to 50,000 m^3 of dust may be removed from the dusty slopes during slope streak formation (Phillips et al., 2007) and modeling indicated that >90% of the sliding mass gets lofted into the atmosphere (Sullivan et al., 2001). Assuming the aforementioned parameters and that the dust density on the surface of Mars is similar to the density of the atmospheric dust, which is about 2,500 kg/m^3 (Forget & Montabone, 2017), we estimate that slope streaks should supply the atmosphere with ~4.2 x 10^{12} kg/yr of dust. This is an order of magnitude larger than estimates of the entire mass of a 1977 global dust storm (Martin, 1995). Such unrealistically large amounts of dust kicked up by active slope streaks would be detectable in early morning images of the surface. It has been shown that active phenomena can be identified in the visible images. For example, HiRISE has discovered hectometer-scale clouds of avalanching frost-dust on polar scarps (Russell et al., 2008) and similar dust clouds on polar dunes (Hansen et al., 2011). Although such polar avalanches and slope streaks are likely unrelated geologic phenomena, this example illustrates that in theory active processes can be observed via remote sensing. Unfortunately, CaSSIS has not observed any dust activity in the equatorial slope streak sites to date. In conclusion, the lack of positive correlation between frost deposits and slope streaks in dusty, low thermal inertia regions (~30% of the planet's surface) suggests that the origin of slope streaks is still poorly understood.

Conclusions

In this study, we reported the discovery of ephemeral early morning CO_2 frost on Martian volcanoes. Because of the unique thermal conditions atop these structures, frost may remain stable and detectable for a few hours after sunrise. After careful investigation of the local

geology, we conclude that the condensation and sublimation of the CO_2 frost in the equatorial regions is purely an atmospheric phenomenon. Our study also highlights the need for future missions that can exploit non-Sun-synchronous orbits and distinguish between surface CO_2 and H_2O frost. The presence of frost at tropical latitudes perhaps echoes of past climatic conditions in which frozen volatiles extended towards the low latitudes (Titus et al., 2017).

Acknowledgements

CaSSIS is a project of the University of Bern and funded through the Swiss Space Office via ESA's PRODEX programme. The instrument hardware development was also supported by the Italian Space Agency (ASI) (ASI-INAF agreement no. 2020-17-HH.O), INAF/Astronomical Observatory of Padova, and the Space Research Center (CSK) in Warsaw. Support from SGF (Budapest), the University of Arizona (Lunar and Planetary Lab.) and NASA are also gratefully acknowledged. Operations support from the UK Space Agency under grant ST/R003025/1 is also acknowledged.

References

Aharonson, O., Schorghofer, N., & Gerstell, M. F. (2003). Slope streak formation and dust deposition rates on Mars. *Journal of Geophysical Research: Planets*, *108*(E12). https://doi.org/https://doi.org/10.1029/2003JE002123

Bergonio, J. R., Rottas, K. M., & Schorghofer, N. (2013). Properties of martian slope streak populations. *Icarus*, *225*(1), 194–199.

https://doi.org/https://doi.org/10.1016/j.icarus.2013.03.023

Beyer, R. A., Alexandrov, O., & McMichael, S. (2018). The Ames Stereo Pipeline: NASA's Open Source Software for Deriving and Processing Terrain Data. *Earth and Space Science*, *5*(9), 537–548. https://doi.org/https://doi.org/10.1029/2018EA000409

Bridges, N. T., Banks, M. E., Beyer, R. A., Chuang, F. C., Noe Dobrea, E. Z., Herkenhoff, K. E., et al. (2010). Aeolian bedforms, yardangs, and indurated surfaces in the Tharsis Montes as seen by the HiRISE Camera: Evidence for dust aggregates. *Icarus*, *205*(1), 165–182. https://doi.org/https://doi.org/10.1016/j.icarus.2009.05.017

Carrozzo, F. G., Bellucci, G., Altieri, F., D'Aversa, E., & Bibring, J.-P. (2009). Mapping of water frost and ice at low latitudes on Mars. *Icarus*, *203*(2), 406–420.

Christensen, P. R., Bandfield, J. L., Hamilton, V. E., Ruff, S. W., Kieffer, H. H., Titus, T. N., et al. (2001). Mars Global Surveyor Thermal Emission Spectrometer experiment: Investigation description and surface science results. *Journal of Geophysical Research: Planets*, *106*(E10), 23823–23871. https://doi.org/https://doi.org/10.1029/2000JE001370

Cushing, G. E., & Titus, T. N. (2008). MGS-TES thermal inertia study of the Arsia Mons Caldera. *Journal of Geophysical Research: Planets*, *113*(E6).

Farmer, C. B., Davies, D. W., & LaPorte, D. D. (1976). Mars: Northern Summer Ice Cap—Water Vapor Observations from Viking 2. *Science*, *194*(4271), 1339–1341. https://doi.org/10.1126/science.194.4271.1339

Forget, F., & Montabone, L. (2017). Atmospheric Dust on Mars: A Review. *47th International Conference on Environmental Systems*, (July), 1–13. Retrieved from http://www-

mars.lmd.jussieu.fr

Graham, D. J., & Midgley, N. G. (2000). Graphical representation of particle shape using triangular diagrams: an Excel spreadsheet method. *Earth Surface Processes and Landforms*, *25*(13), 1473–1477. https://doi.org/https://doi.org/10.1002/1096-9837(200012)25:13<1473::AID-ESP158>3.0.CO;2-C

Hales, T. C., & Roering, J. J. (2007). Climatic controls on frost cracking and implications for the evolution of bedrock landscapes. *Journal of Geophysical Research: Earth Surface*, *112*(F2). https://doi.org/https://doi.org/10.1029/2006JF000616

Hansen, C. J., Bourke, M., Bridges, N. T., Byrne, S., Colon, C., Diniega, S., et al. (2011). Seasonal Erosion and Restoration of Mars' Northern Polar Dunes. *Science*, *331*(6017), 575–578. https://doi.org/10.1126/science.1197636

James, P. B., Kieffer, H. H., & Paige, D. A. (1992). The seasonal cycle of carbon dioxide on Mars. In *Mars* (pp. 934–968). AA(University of Toledo, Ohio), AB(USGS, Flagstaff, AZ), AC(University of California, Los Angeles). Retrieved from https://ui.adsabs.harvard.edu/abs/1992mars.book..934J

Khuller, A. R., Christensen, P. R., Harrison, T. N., & Diniega, S. (2021). The Distribution of Frosts on Mars: Links to Present-Day Gully Activity. *Journal of Geophysical Research: Planets*, *126*(3), e2020JE006577.

Kieffer, H. H. (2013). Thermal model for analysis of Mars infrared mapping. *Journal of Geophysical Research: Planets*, *118*(3), 451–470. https://doi.org/https://doi.org/10.1029/2012JE004164

Kieffer, H. H., Martin, T. Z., Peterfreund, A. R., Jakosky, B. M., Miner, E. D., & Palluconi, F. D. (1977). Thermal and albedo mapping of Mars during the Viking primary mission. *Journal of Geophysical Research (1896-1977), 82*(28), 4249–4291. https://doi.org/https://doi.org/10.1029/JS082i028p04249

Kieffer, H. H., Titus, T. N., Mullins, K. F., & Christensen, P. R. (2000). Mars south polar spring and summer behavior observed by TES: Seasonal cap evolution controlled by frost grain size. *Journal of Geophysical Research: Planets*, *105*(E4), 9653–9699. https://doi.org/https://doi.org/10.1029/1999JE001136

Landis, G. A. (2007). Observation of frost at the equator of Mars by the Opportunity rover. *38th Annual Lunar and Planetary Science Conference*, abstract 2433. Retrieved from http://adsabs.harvard.edu/abs/2007LPI....38.2423L

Lange, L., Piqueux, S., & Edwards, C. S. (2022). Gardening of the Martian Regolith by Diurnal CO2 Frost and the Formation of Slope Streaks. *Journal of Geophysical Research: Planets*, *127*(4), e2021JE006988.

Mangan, T. P., Salzmann, C. G., Plane, J. M. C., & Murray, B. J. (2017). CO2 ice structure and density under Martian atmospheric conditions. *Icarus*, *294*, 201–208. https://doi.org/https://doi.org/10.1016/j.icarus.2017.03.012

Martin, T. Z. (1995). Mass of dust in the Martian atmosphere. *Journal of Geophysical Research: Planets*, *100*(E4), 7509–7512. https://doi.org/https://doi.org/10.1029/95JE00414

Millour, E., Forget, F., Spiga, A., Vals, M., Zakharov, V., Montabone, L., et al. (2018). The Mars Climate Database (version 5.3). In *From Mars Express to ExoMars* (p. 68). AA(Laboratoire de Meteorologie Dynamique, Paris). Retrieved from

https://ui.adsabs.harvard.edu/abs/2018fmee.confE..68M

Neugebauer, G., Münch, G., Kieffer, H., Chase Jr., S. C., & Miner, E. (1971). Mariner 1969 Infrared Radiometer Results: Temperatures and Thermal Properties of the Martian Surface. *The Astronomical Journal, 76*, 719. https://doi.org/10.1086/111189

Phillips, C. B., Burr, D. M., & Beyer, R. A. (2007). Mass movement within a slope streak on Mars. *Geophysical Research Letters*, *34*(21). https://doi.org/https://doi.org/10.1029/2007GL031577

Piqueux, S., Kleinböhl, A., Hayne, P. O., Heavens, N. G., Kass, D. M., McCleese, D. J., et al. (2016). Discovery of a widespread low-latitude diurnal CO2 frost cycle on Mars. *Journal of Geophysical Research: Planets*, *121*(7), 1174–1189.

Pommerol, A., Thomas, N., Almeida, M., Read, M., Becerra, P., Cesar, C., et al. (2022). In-flight radiometric calibration of the ExoMars TGO Colour and Stereo Surface Imaging System. *Planetary and Space Science*, 105580. https://doi.org/https://doi.org/10.1016/j.pss.2022.105580

Re, C., Fennema, A., Simioni, E., Sutton, S., Mège, D., Gwinner, K., et al. (2022). CaSSIS-based stereo products for Mars after three years in orbit. *Planetary and Space Science*, *219*, 105515. https://doi.org/https://doi.org/10.1016/j.pss.2022.105515

Russell, P., Thomas, N., Byrne, S., Herkenhoff, K., Fishbaugh, K., Bridges, N., et al. (2008). Seasonally active frost-dust avalanches on a north polar scarp of Mars captured by HiRISE. *Geophysical Research Letters*, *35*(23). https://doi.org/https://doi.org/10.1029/2008GL035790

Schorghofer, N. (2022). Mars Subsurface Ice Model (MSIM) Program Collection (v1.2.0). Retrieved from https://github.com/nschorgh/MSIM https://doi.org/10.5281/zenodo.6499709

Schorghofer, Norbert. (2020). Mars: Quantitative Evaluation of Crocus Melting behind Boulders. *The Astrophysical Journal*, *890*(1), 49. https://doi.org/https://doi.org/10.3847/1538-4357/ab612f

Schorghofer, Norbert, & Edgett, K. S. (2006). Seasonal surface frost at low latitudes on Mars. *Icarus*, *180*(2), 321–334. https://doi.org/https://doi.org/10.1016/j.icarus.2005.08.022

Simioni, E., Re, C., Mudric, T., Cremonese, G., Tulyakov, S., Petrella, A., et al. (2021). 3DPD: A photogrammetric pipeline for a PUSH frame stereo cameras. *Planetary and Space Science*, *198*, 105165. https://doi.org/https://doi.org/10.1016/j.pss.2021.105165

Sneed, E. D., & Folk, R. L. (1958). Pebbles in the Lower Colorado River, Texas a Study in Particle Morphogenesis. *The Journal of Geology*, *66*(2), 114–150. Retrieved from http://www.jstor.org/stable/30058239

Sullivan, R., Thomas, P., Veverka, J., Malin, M., & Edgett, K. S. (2001). Mass movement slope streaks imaged by the Mars Orbiter Camera. *Journal of Geophysical Research: Planets*, *106*(E10), 23607–23633. https://doi.org/https://doi.org/10.1029/2000je001296

Svitek, T., & Murray, B. (1990). Winter frost at Viking Lander 2 site. *Journal of Geophysical Research: Solid Earth*, *95*(B2), 1495–1510. https://doi.org/https://doi.org/10.1029/JB095iB02p01495

Thomas, N., Cremonese, G., Ziethe, R., Gerber, M., Brändli, M., Bruno, G., et al. (2017). The Colour and Stereo Surface Imaging System (CaSSIS) for the ExoMars Trace Gas Orbiter.

Space Science Reviews, *212*(3), 1897–1944. https://doi.org/10.1007/s11214-017-0421-1

Thomas, N., Pommerol, A., Almeida, M., Read, M., Cremonese, G., Simioni, E., et al. (2022). Absolute calibration of the Colour and Stereo Surface Imaging System (CaSSIS). *Planetary and Space Science*, *211*, 105394. https://doi.org/https://doi.org/10.1016/j.pss.2021.105394

Titus, T. N., Byrne, S., Colaprete, A., Forget, F., Michaels, T. I., & Prettyman, T. H. (2017). The CO2 Cycle. In F. Forget, M. D. Smith, R. T. Clancy, R. W. Zurek, & R. M. Haberle (Eds.), *The Atmosphere and Climate of Mars* (pp. 374–404). Cambridge: Cambridge University Press. https://doi.org/DOI: 10.1017/9781139060172.012

Valantinas, A., Becerra, P., Pommerol, A., Tornabene, L. L., Affolter, L., Cremonese, G., et al. (2021). CaSSIS Color and multi-angular observations of martian slope streaks. *Planetary and Space Science*, *209*(November), 105373. https://doi.org/10.1016/j.pss.2021.105373

Vincendon, M., Mustard, J., Forget, F., Kreslavsky, M., Spiga, A., Murchie, S., & Bibring, J.-P. (2010). Near-tropical subsurface ice on Mars. *Geophysical Research Letters*, *37*(1). https://doi.org/https://doi.org/10.1029/2009GL041426

Vincendon, M., Forget, F., & Mustard, J. (2010). Water ice at low to midlatitudes on Mars. *Journal of Geophysical Research: Planets*, *115*(E10).

Figures

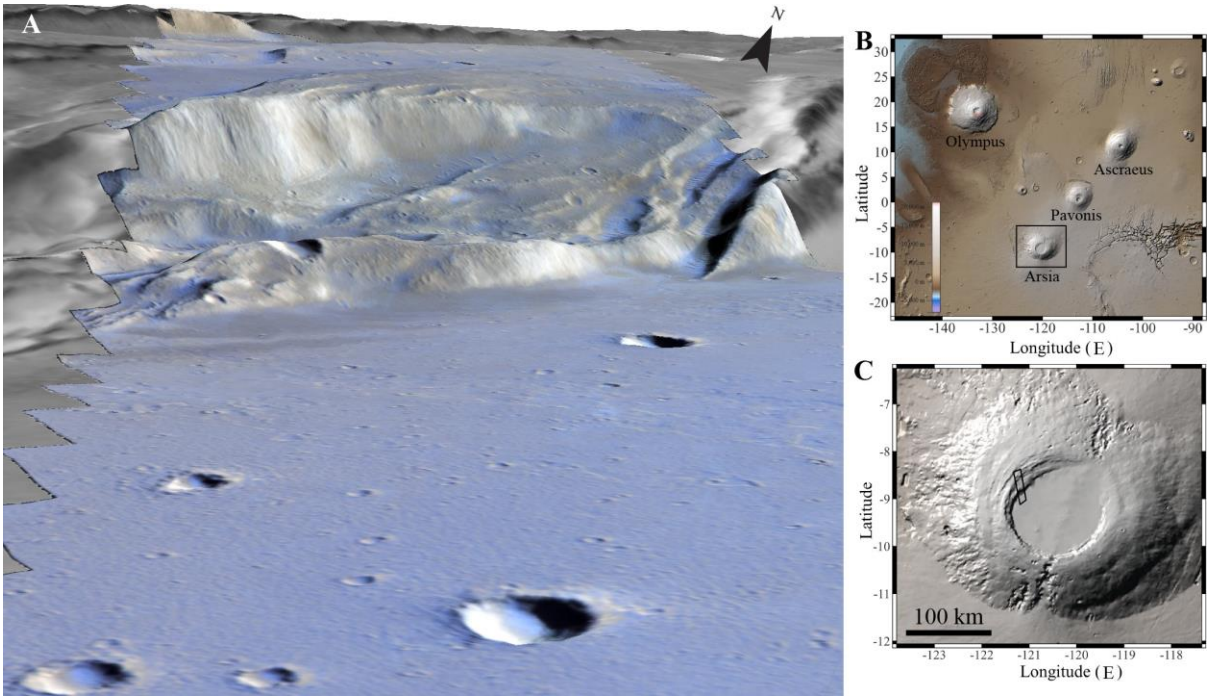

Figure 1. Frosty Arsia Mons caldera. Frost is observed on the caldera plains, small crater floors and behind topographic obstacles but is absent on well-illuminated steep slopes (A). Spatial context of Tharsis volcanoes (B) and a close up of Arsia Mons (C). CaSSIS image footprint is shown in black in (C). The CaSSIS color image MY35_008465_192_0_NPB was orthorectified and draped over the CTX digital elevation model (A). Vertical exaggeration is x10. The topographic map is MOLA color hillshade 64 ppd (B-C). The CaSSIS image is available online at https://cassis.halimede.unibe.ch/observations.

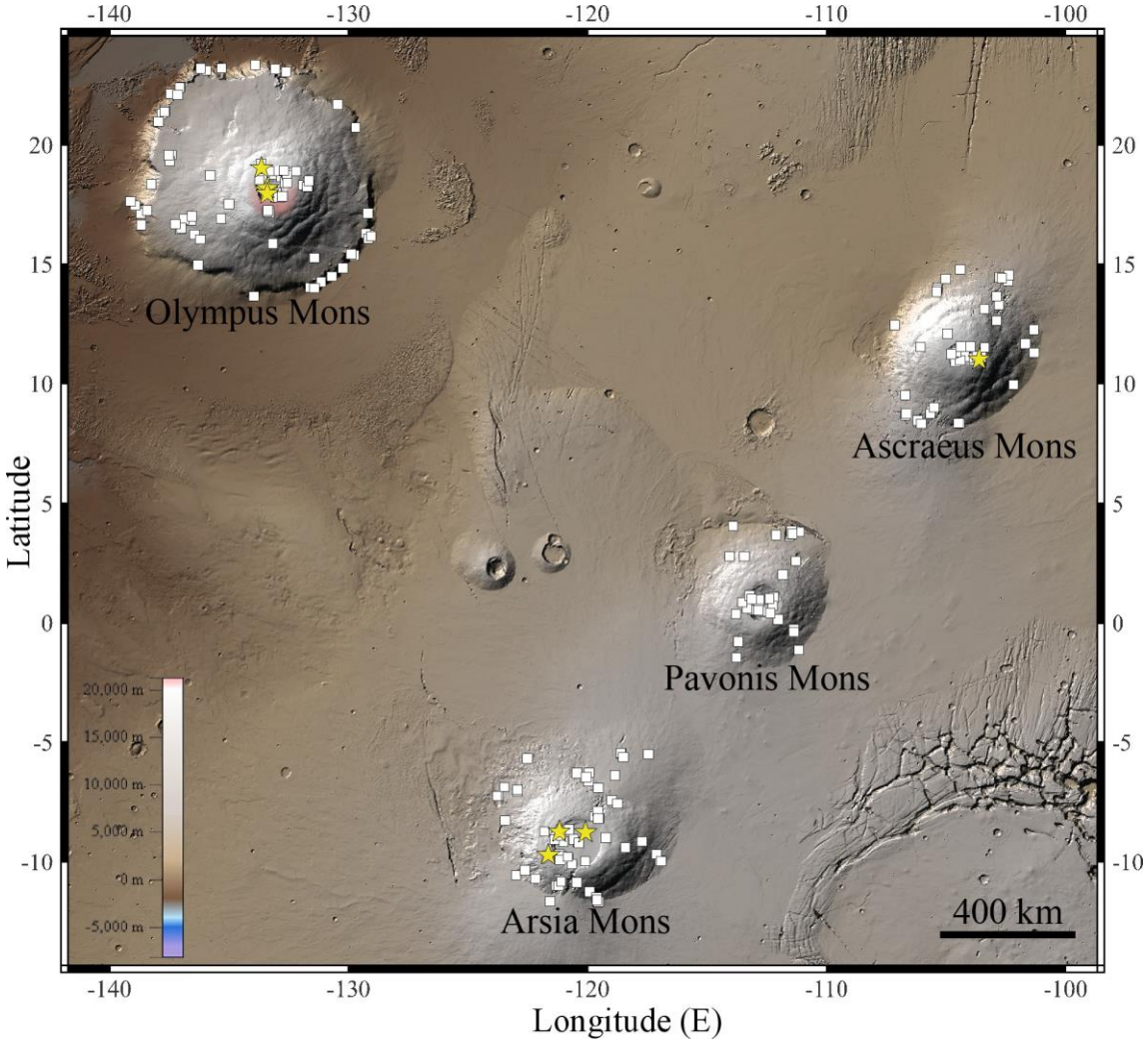

Figure 2. The distribution of CaSSIS frost (yellow stars) and frost-free (white squares) observations in the Tharsis volcanic region. Frost is detected only at the highest elevations (>15 km) on Olympus, Arsia and Ascraeus Mons calderas. Frost is not observed on Pavonis Mons. The basemap is MOLA color hillshade 64 ppd.

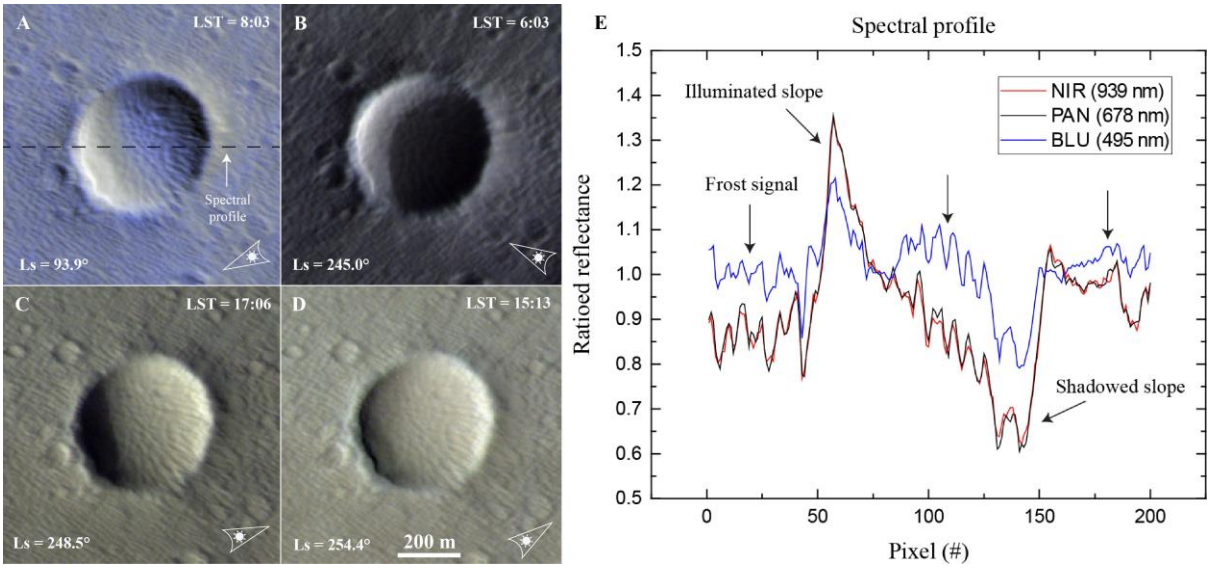

Figure 3. Crater in the frosty plains of Arsia Mons caldera. Early morning observation showing frost in and around the crater in the winter of MY 35 (A). Early morning (B) and afternoon (C-D) observations indicating no frost in the late spring of MY36. The spectral profile in (A) is plotted in (E) and shows a strong increase in reflectance in the BLU filter where frost is present. Each image was given the same linear stretch. Illumination direction is given in the bottom right corner of each image. CaSSIS image IDs shown here are MY35_008465_192_0_NPB, MY36_020297_350_3_NPB, MY36_020366_190_1_NPB and MY36_020478_190_3_NPB.

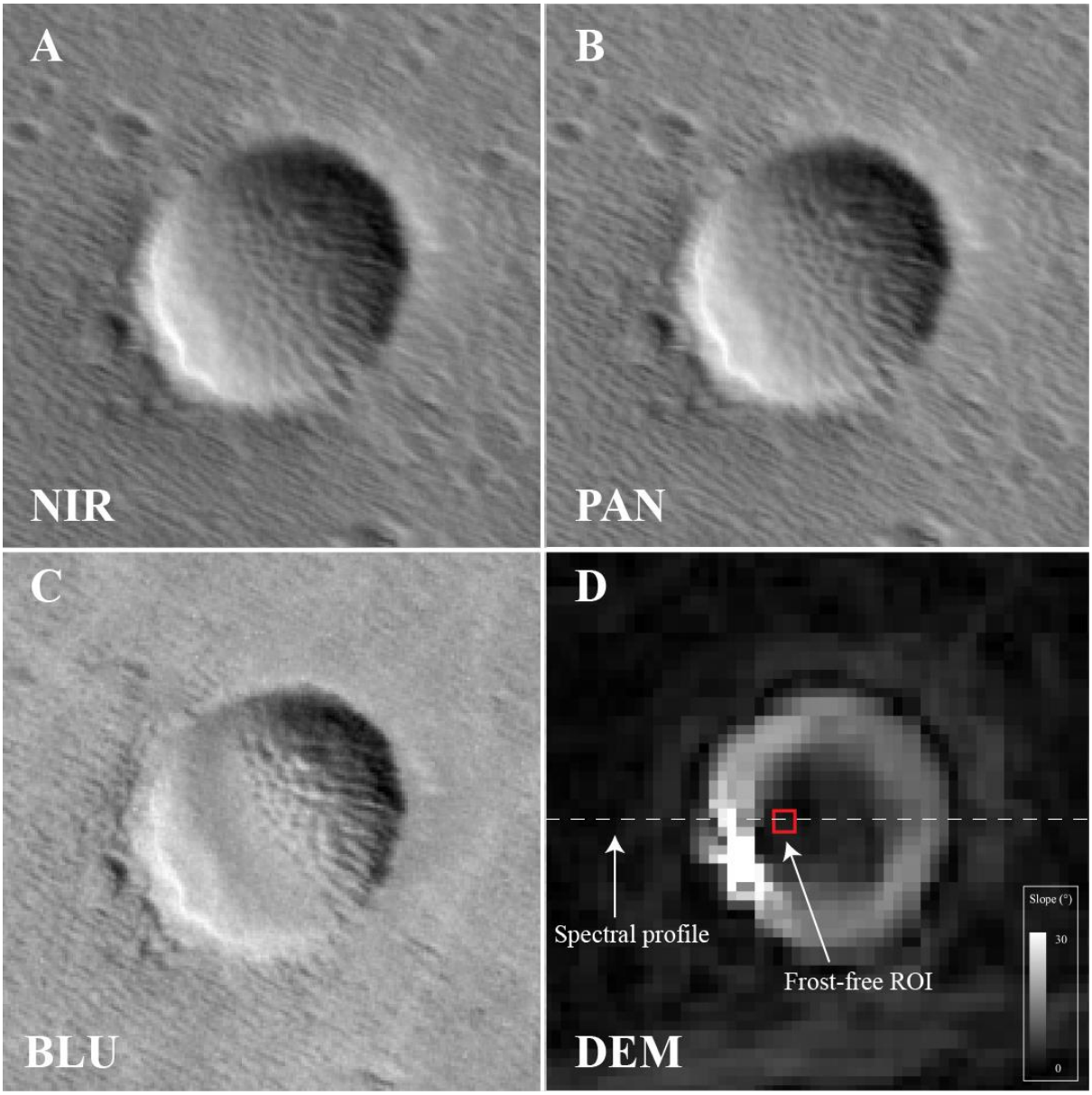

Figure 4. CaSSIS observation of a small frosty crater (from Fig. 3) shown in three individual filters NIR, PAN and BLU (A-C). (D) CaSSIS Digital Elevation Model (DEM) of the same scene with overlain location of the spectral profile and frost-free ROI. The frost deposits can be observed in the CaSSIS BLU filter. CaSSIS DEM ID: CAS-DTM-MY36_020366_190_1-OPD-03-01.

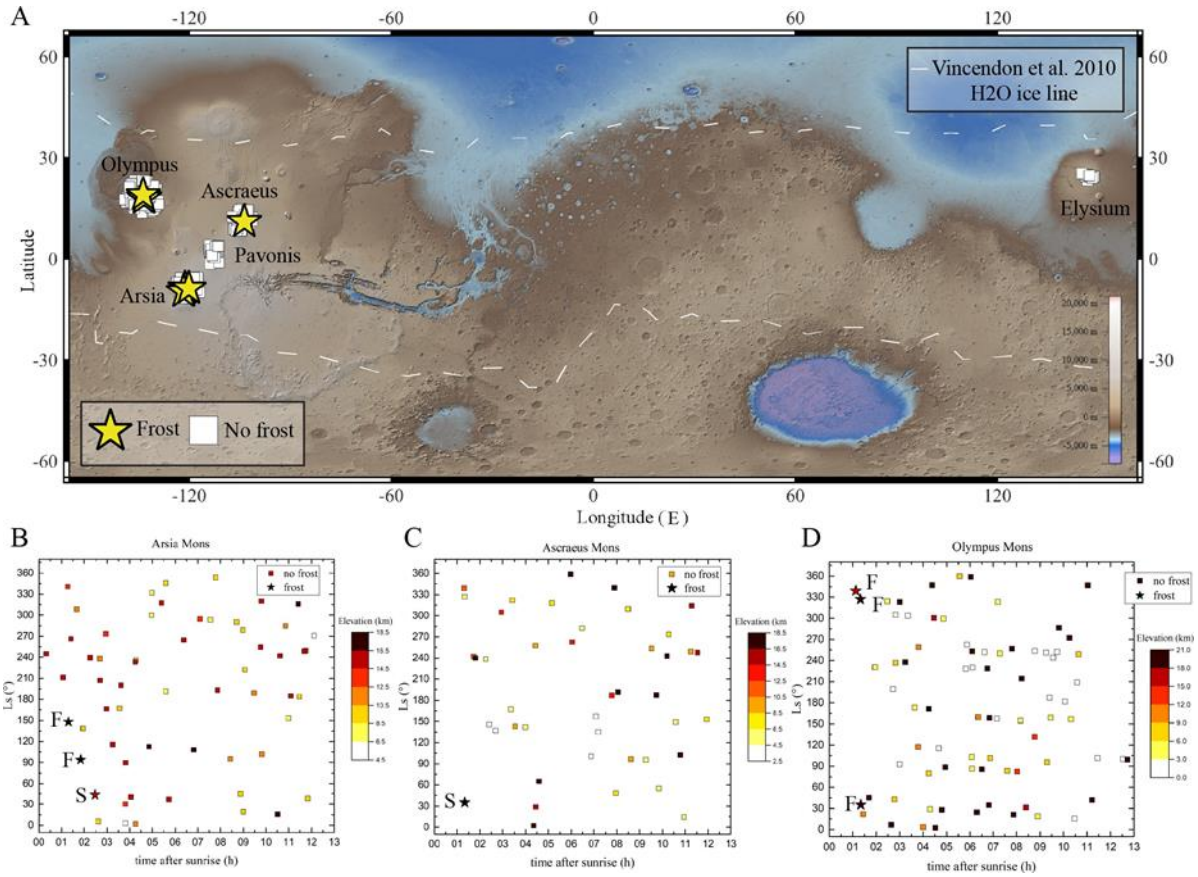

Figure 5. (A) Global distribution of observations used in this study. (B-D) Martian season (Ls) vs local time after sunrise plots for each positive detection site (Arsia, Ascraeus and Olympus Mons). The elevation of each observation site is indicated by a color legend on the right side of each plot. “F” and “S” indicate frost sites that were observed on either flat or sloped surfaces respectively. Frost detections correlate with early LSTs, cold season and extremely high altitudes. The seasonal water ice line in (A) is from (Vincendon, Mustard, et al., 2010). Time after sunrise for each observation was calculated using SPICE.

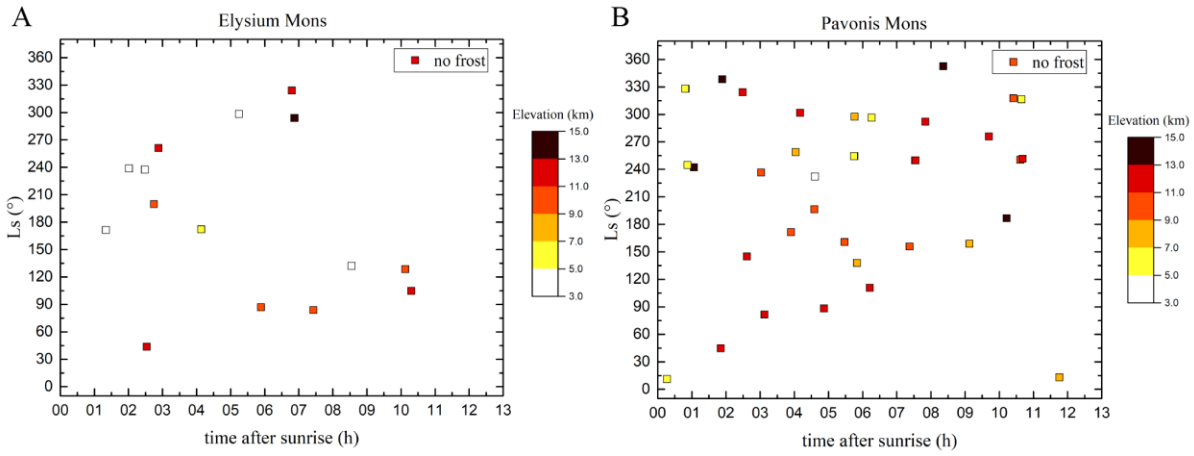

Figure 6. Martian season (Ls) vs local time after sunrise plots for sites where frost was not detected. The non-detections in Elysium (A) might be due to the lack of early morning observations there. In Pavonis (B), there is only one observation above 13 km in altitude in the early morning but perhaps it is too early in the cold season.

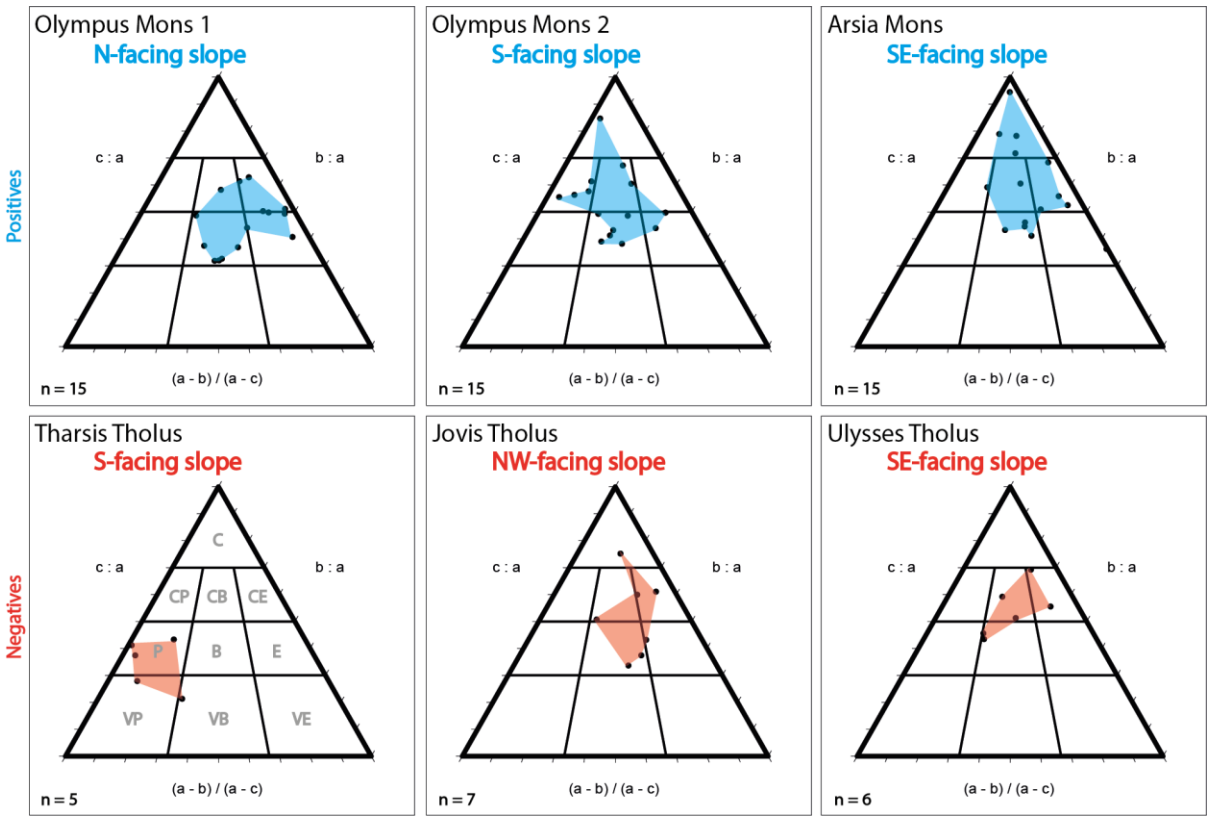

Figure 7. Triangular (ternary) diagrams (Sneed & Folk, 1958) of boulder shape across six sites of interest. The slope aspect of each site is indicated on the respective panel. The Olympus and Arsia Mons sites were found to feature a distinct early morning frost signature (positives, blue), the other three sites not (negatives, red) – yet there is no obvious difference in boulder shape across those sites (the colored polygons underline the distribution of points). C = compact, P = platy, B = bladed, E = elongated, V = very; a = longest boulder dimension, b = intermediate boulder dimension, c = smallest boulder dimension; plots generated with the Tri-Plot software by Graham & Midgley (2000). HiRISE image IDs: ESP_014275_1990_RED, ESP_043272_1980_RED, ESP_047439_1990_RED, PSP_009884_1980_RED, ESP_057843_1715_RED, ESP_012612_1940_RED, ESP_033711_1985_RED, and ESP_045619_1835_RED.

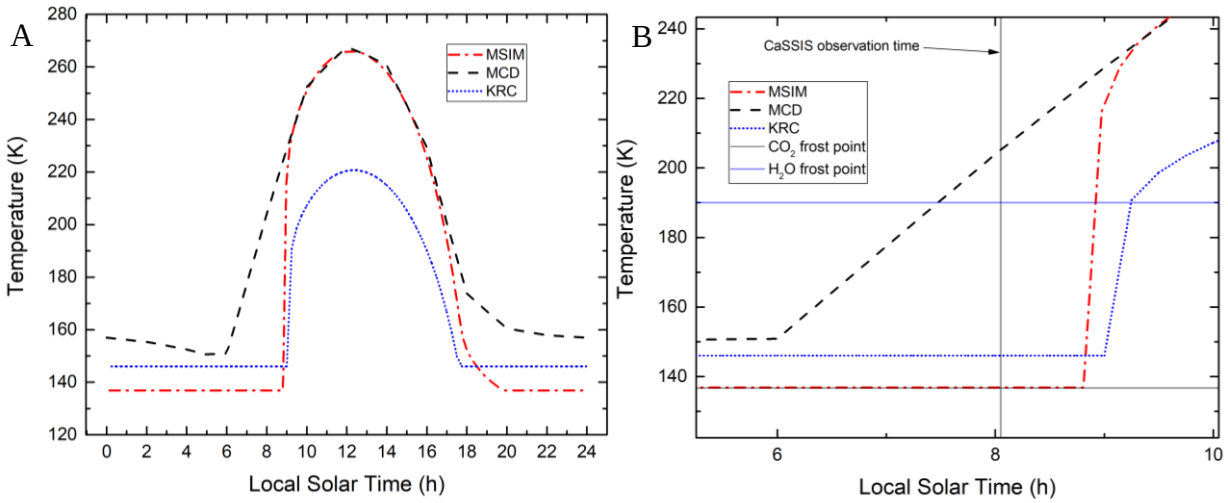

Figure 8. Modeled diurnal temperature profiles for Arsia Mons caldera at Ls = 93.9° (Fig. 2A). Three thermal model results used in this study (A) and a close up of the temperature regime in the early morning hours (B). Night temperatures are within CO_2 frost point only in the MSIM case and extend well into the morning hours indicating that the frost detected by CaSSIS may very well be CO_2.The sharp increase in temperatures predicted by MSIM and KRC at ~9AM indicate that frost has fully sublimed. Although KRC predicts warmer night temperatures by ~10 K. MCD does not predict CO_2 frost, since the temperatures are well above the CO_2 frost point. The CO_2 frost point calculated using Clapeyron's law from James et al. (1992) and assuming 30% lower atmospheric pressure due to seasonal decrease in the southern winter. H_2O frost point calculated using water partial pressure and scale height relation and the water phase diagram (e.g. Schorghofer, 2020). KRC is one-dimensional multilayered thermal-diffusion model (Kieffer, 2013); while MCD is based on atmospheric general circulation models (Forget et al., 1999).

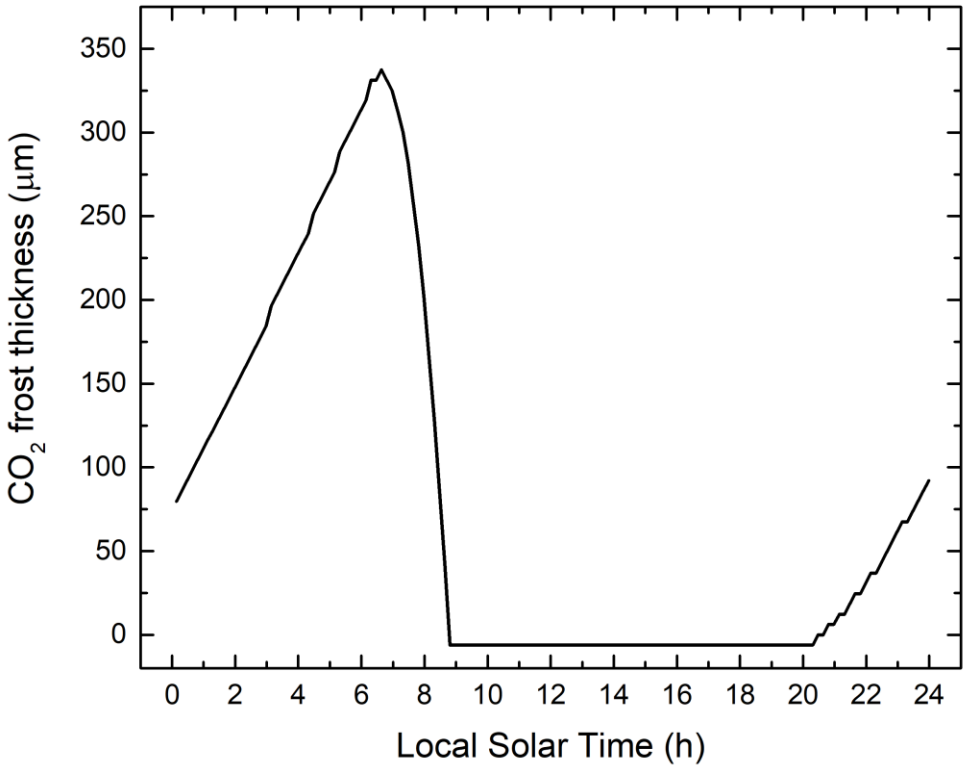

Figure 9. CO_2 frost thickness as a function of time at Arsia Mons (Fig. 2A). At the time of CaSSIS acquisition (~8 AM) it is about 185 μm thick and fully sublimates around 9 AM. Modeled using MSIM. CO_2 frost density taken as ~1.63 g/cm^3 at 140 K (Mangan et al., 2017)

Chapter 4:

ORBITAL EVIDENCE OF FERRIHYDRITE IN THE MARTIAN DUST: IMPLICATIONS FOR THE ANCIENT CLIMATE ON MARS

A. Valantinas[1], V. Chevrier[2], A. Pommerol[1], N. Mangold[3], G. Villanueva[4], M. Patel[5] and N. Thomas[1]

[1]Physikalisches Institut, Universität Bern

[2]Center for Space & Planetary Sciences, University of Arkansas

[3]Laboratoire Planétologie et Géodynamique, Université Nantes

[4]Goddard Space Flight Center, NASA

[5]School of Physical Sciences, Open University

In preparation

Introduction

As discussed in Chapter 1, the composition of Martian dust is still somewhat of an enigma. The dust is probably a chemical alteration product and is hydrated as indicated by the Curiosity rover. Because of its highly X-ray amorphous nature, the iron mineralogy of Martian dust is not fully understood. However, the use of well-calibrated CaSSIS color data provides an opportunity to determine the dominant ferric iron phase in the Martian dust. The determination of such phase can offer fundamental insights into the past Mars' climate. In this chapter, we employ novel CaSSIS color and multi-angular data to study the vast Martian dust deposits in the classical albedo regions of Tharsis, Arabia Terra, Elysium and Isidis Planitia. Then we compare these orbital data with laboratory bidirectional reflectance measurements of several iron oxide powders. The revealed iron oxide phase and its implications for the ancient Mars climate are then discussed.

Methods

1. Orbital observations

We acquired 518 unique CaSSIS observations in dusty areas within the Arabia Terra, Tharsis, Elysium Planitia and Isidis Planitia regions (Fig. 1). The goal was to conduct spectral comparisons between high and intermediate albedo regions where dust might be abundant and uniformly spread (Ruff & Christensen, 2002). In laboratory and orbital investigations of phase angle dependent phenomena, usually the same target surface is used to keep textural/composition parameters constant. However, we were not able to fulfill this latter requirement because, in the CaSSIS database, there are rarely more than five observations of the same given point in dusty regions. Based on the work of Ruff & Christensen (2002), we hypothesized that perhaps Martian

dust can be considered as a single unit over bright regions of similar albedo. This assumption lead to interesting results as will be shown in the Results section.

The reflectance measured in this work is expressed as reflectance factor (REFF) and can be written as:

$$REFF = \frac{I}{F} \cdot \frac{1}{\cos i} \quad (1)$$

where the *I/F* is the calibrated radiance observed at the detector divided by the solar irradiance at the heliocentric distance of the observation and *i* is the incidence angle of the observation. In the literature, the right side of the equation sometimes includes a multiplicative factor π, but in the CaSSIS calibration pipeline the solar flux *F* is defined as πF. This cancels out the π term and results in what is commonly referred to as "I over F" in planetary photometry. These orbital reflectance measurements when plotted versus phase angle result in phase curve plots, which are dependent on surface and particle physical properties and composition (Hapke, 2012). To investigate the compositional variability of Martian dust we employed spectral slope measurements, which can be defined as a change in reflectance over a given wavelength interval (Murchie et al., 2000):

$$S(\lambda_1, \lambda_2) = \frac{REFF_{\lambda_2} - REFF_{\lambda_1}}{\lambda_2 - \lambda_1} \quad (2)$$

where λ is the central bandpass wavelength of a given CaSSIS filter in nm. In this work we compute *S* per 100 nm. Note that, in the literature, several definitions of the spectral slope exist (sometimes also termed as the spectral gradient). Fornasier et al. (2015), for example, divided the right side of the Eq. 2 by reflectance in a reference filter (at 535 nm in their case). This results in spectral slope in units of %/nm. Here we decided not to follow this approach because the visible spectrum of Mars is non-linear with a steeper rise in reflectance at ~600 nm. Our definition of

spectral slope can be understood as simply spectral difference in an analyzed wavelength range. For the sake of consistency and clarity we use the term “spectral slope” as given by Murchie et al. (2000).

Spectral slopes were calculated for these filter pairs: NIR to RED (termed NR), RED to PAN (RP) and NIR to BLU (NB). The spectral slope values can be either negative or positive, depending on the shape of the spectrum. Because some ferric iron oxides contain an absorption band at ~860 nm, the NR slope should provide a means of distinguishing between different mineral phases. Additionally, we investigate reflectance spectral ratios in NIR/BLU, NIR/RED and RED/PAN filter combinations. This serves as complimentary information and is sensitive to relative changes in reflectance.

To collect the individual dust spectra from each CaSSIS cube, we used the Environment for Visualizing Images (ENVI) software to draw regions of interest (ROIs) over relatively flat, spectrally homogenous and stable surfaces (Fig. 2). Each spectrum was the result of averaging 100-1000 pixels in size (at 4.5 m/px scale). Images obviously contaminated by clouds or other atmospheric phenomena were discarded. Following Vincendon (2013), we also excluded observations above 70° phase because of increasingly dominant aerosol effects. Additionally, for each CaSSIS observation we modeled optical depth (τ) values, using the climatological assimilation of dust opacities derived from the MCS experiment (McCleese et al., 2007). This serves as a proxy for the atmospheric conditions during the time of image acquisition and provides confidence when interpreting surface reflectance trends.

2. Laboratory measurements

Over twenty ferric iron oxide/hydroxide samples (many of which are subsamples) were provided by Vincent Chevrier from the Arkansas Center for Space and Planetary Sciences and

investigated using the PHIRE-2 spectrogoniometer (see Fig. 3). In this chapter, we analyze only those phases of oxides that have been rigorously discussed in the literature (Chevrier & Mathé, 2007): ferrihydrite ($5Fe^{3+}{}_2O_3 \cdot 9H_2O$), goethite ($\alpha$-$Fe^{3+}O(OH)$), lepidocrocite ($\gamma$-$Fe^{3+}O(OH)$), hematite ($\alpha$-$Fe^{3+}{}_2O_3$), akaganeite ($\beta$-$Fe^{3+}O(OH)$), maghemite ($\gamma$- $Fe^{3+}{}_2O_3$), schwertmannite ($Fe^{3+}{}_8O_8(OH)_6(SO_4) \cdot n\ H_2O$) and feroxyhyte ($\delta'$-$Fe^{3+}O(OH)$). For each of these ferric iron mineralogies we measured the bidirectional reflectance, derived phase curves and computed spectral slopes/ratios in order to compare these data to the orbital observations of CaSSIS.

In order to mimic CaSSIS observations, PHIRE-2 was set to observe only in the principal plane and in the phase angle range of 5 to 70° (when i = 0°, phase = emission). PHIRE-2 was also equipped with the flight spare CaSSIS filters, which allows direct spectral comparisons between the lab and orbital data. A second set of measurements was conducted with i = 60°, which corresponds to a wider phase angle range of 5 to 130°. We present these measurements in Appendix B. PHIRE-2 reflectance data was radiometrically calibrated using a standard diffuse reflector (Spectralon™) and outputted in units of REFF.

Before each measurement, the samples were flattened using a smooth metal spatula (Gunderson et al., 2006; Pommerol et al., 2013). After flattening, each surface was sprinkled with the remaining sample material using very fine nylon sieves of various mesh sizes (SEFAR NITEX®). Sprinkling effectively served as a dry-sieving procedure and fulfilled the assumption that airfall dust deposits on Mars are loose and not indurated. However, it was noticed that cohesion and particle size properties varied between the samples in this study. Therefore, we used slightly different mesh sizes for the samples (see Table 1).

Results

1. Phase curves for Mars bright regions

The assumption that dust can be treated as a homogeneous material across Mars independent of region seems to be correct within the measurement accuracy. Reflectance vs phase angle plots (Figs. 4-7) show the non-linear reflectance behavior of Martian dust. Dust reflectance properties in Arabia and Elysium are remarkably similar in terms of the shape of the phase curve. The surge in reflectance at low phase angles (also known as the backscattering peak) is caused by the opposition surge phenomenon (e.g. Hapke, 2021). The lowest REFF values are observed at ~40° and there is an indication of increasing reflectance at intermediate phase angles. Many ferric oxide samples measured in the lab in this study show similar behavior (see Appendix B). This is indicative of small and relatively transparent particles (Schröder et al., 2014). The reflectance values of phase curves in the NIR and RED filters are almost identical, which suggests that the ratio of NIR to RED is close to 1. The phase curve for the Tharsis region is similar in shape if compared to the other regions but exhibits slightly elevated REFF values. For example, the REFF value for Tharsis dust is 0.50 at 5° phase, while for Elysium and Arabia it is ~0.48 at the same phase angle. The data for Isidis, on the other hand, show an overall less reflective or darker material. This is not particularly surprising because regional differences in albedo are well-known based on TES (Ruff & Christensen, 2002) and OMEGA (Ody et al., 2012) results and has been attributed to variations in particle size. The modelled optical depth (τ) values shown on each figure indicate that most observations were acquired under relatively clear atmosphere and that the reflectance trends observed here are not correlated with variations in τ.

2. Color comparison of Martian dust and laboratory ferric iron samples

The computed spectral slopes for CaSSIS observations and laboratory data are shown in Fig. 8 & 9. The orbital observations are clustered around the RP spectral slope value of 0.07 but exhibit a nearly flat slope (~0) in the NR range (Fig. 8). The uncertainty in these values resulting from the spectral slope calculation is much smaller than the ~3% relative uncertainty in the absolute calibration of the instrument (Fig. 8; Thomas et al., 2022).

The absorption resulting from Fe^{3+} iron at ~0.86 μm (Bell et al., 1990; Murchie et al., 1993) should be visible in the CaSSIS NR range (0.84-0.93 μm). However, the OMEGA spectrum of Mars bright regions also indicates a nearly flat spectrum in the 0.80-0.95 μm range (Ody et al., 2012), which suggests that with increasing spectral and spatial resolution there is less spectral averaging of spectrally diverse materials.

Ferrihydrite is the closest match of the minerals studied to the Martian dust with ~0.01 NR and ~0.06 RP values (Fig. 8). In the case of the NB spectral slopes, ferrihydrite again is a good match to the orbital data (Fig. 9). The color slopes also suggest that Arabia and Elysium dust are very similar in composition. The Tharsis data points exhibit a larger spread along the x-axis suggesting of greater color variability within the region. Isidis dust on the other hand has the lowest RP and NB values (i.e. slightly "bluer" dust) from the four investigated regions.

The general result of the NIR/RED vs RED/PAN color ratio (Fig. 10) is similar to that of Fig. 8, which is that ferrihydrite provides the best match to the orbital data. However, in the color ratio space one can observe strong phase angle dependency, especially for hematite (i.e. "arch"-like data points). This is also evident in Fig. 11, where the NIR/BLU ratios exhibit the largest spread for hematite, feroxyhyte, ferrihydrite and maghemite. In the case of the last three minerals in this list, the NIR/BLU values are highly dependent on phase angle and in the case of hematite; both the NIR/RED and the NIR/BLU ratios are phase angle dependent. Note that, the large

NIR/BLU ratios of lab oxides result from very low reflectance values in the blue wavelengths (e.g. ferrihydrite's BLU REFF is ~0.05, Fig. 12). Because the REFF values of Arabia dust are higher across all wavelengths (relative to ferrihydrite, Fig. 12), it suggests that Martian dust is probably not pure ferrihydrite and includes a spectrally neutral phase that is relatively bright across all visible wavelengths. The spectrum of silica is nearly flat in the visible (Rice et al., 2013) and, in a mixture with ferrihydrite, would probably not affect the resultant spectral slope but would lower NIR/BLU ratio values. Reflectance studies of Earth dust determined that only Fe^{3+} controls the absorption of light at visible wavelengths (Lafon et al., 2006)**.** Furthermore, Go et al. (2022) showed that the imaginary index of refraction of goethite and hematite (0.1-1 respectively) at wavelengths of <1 μm is 100 times of other soil mineral components found in Earth's dust. Therefore, even minor amounts of ferrihydrite in mixtures with silica would result in a steep red slope.

3. Phase reddening

The dependence of color ratio on phase angle is a known phenomenon from Viking (Guinness, 1981) and Mars Exploration Rover (MER) (Johnson et al., 2021) photometry studies of Martian soils. In a more general planetary context, it is referred to as phase reddening (Gehrels et al., 1964; Taylor et al., 1971), but on Mars, phase bluing is also observed (Guinness, 1981; Schröder et al., 2014; Johnson et al., 2021). This corresponds to an arch-like curve when color ratios are plotted vs phase angle. In Fig. 13, we show these curves for Arabia Terra dust and lab ferrihydrite. To investigate if this phenomenon is dependent on particle size we sieved the ferrihydrite sample with 11- and 1-μm sieves. The shape of color ratio curves for Arabia and 1-μm size ferrihydrite particles are remarkably similar. The roll over point of both curves is at ~40°

phase. This suggests that indeed the shape of the arch depends on particle size. Schröder et al. (2014) showed that smooth, semi-transparent and forward scattering particles exhibit an arch-like color ratio, while rough particles and structures that they form (e.g. 'fairy castle', Hapke & van Hoen, 1963) produce a more monotonic reddening. It is likely that our sieving procedure isolated the individual particles from their larger agglomerates leading to bluing at intermediate phase angles. Our laboratory measurements also show that the shape of the arch depends on incidence angle. Under i = 60° illumination geometry, the arch is wider and peaks at larger phase angles (see Appendix B). Because the Opportunity rover cameras can observe at a wide illumination geometry, it might explain why the color ratio curves computed for dust deposits in Turkey Haven region peaked at ~70° phase (Johnson et al., 2021). Dependence on incidence angle also provides an explanation for the spread of points in the y-axis of the color ratio curves. For example, the CaSSIS observations used for Arabia color ratios (Fig. 13a) were acquired under illumination conditions in which the incidence and phase angles are not always equal. An offset by more than 10° is possible and depends on the TGO's spacecraft attitude during image acquisition. Finally, the phase curves shown in Figures 4-7 can be investigated more deeply using Hapke (1993, 2012) or Shkuratov et al. (1999) radiative transfer models in future work.

Discussion

1. Widespread ferrihydrite in the Martian bright regions

The color evidence presented here points to ferrihydrite as a spectrally dominant mineral phase in the Martian dust. However, dust is not pure ferrihydrite and, as revealed by color ratios (Fig. 11), must contain spectrally neutral (non-absorbing) phases if our interpretation is sound. The CheMin and APXS instruments onboard of Mars Science Laboratory (MSL) showed that the

main components of X-ray amorphous materials in both soils and rocks in Gale Crater are enriched in SiO_2 and FeO_T[1] (Blake et al., 2013; Dehouck et al., 2014; Vaniman et al., 2014). Volatiles such as H_2O, SO_2, CO_2 & O_2 were also detected by the Sample Analysis at Mars (SAM) instrument (Leshin et al., 2013). The spectrally neutral phase (at visible wavelengths) that makes up the bulk volume of the Martian dust particles may therefore be silica. Silica (or opal) has been detected on Mars in various deposits by both orbital- and rover-based studies (e.g. Milliken et al., 2008; Squyres et al., 2008; Tarnas et al., 2019). Opal-A is a highly disordered (amorphous) and hydrated phase of opal (Goryniuk et al., 2004), which may be an adequate candidate to explain the VIS and XRD data. Interestingly, the co-existence of ferrihydrite and silica was one of the possible solutions of mass balance calculations applied to the CheMin data (Dehouck et al., 2014). Recent investigation of sedimentary rock samples in Gale Crater found a mixing relationship between silica-rich and FeO_T-rich X-ray amorphous endmembers, which suggested formation through aqueous processes (Smith et al., 2021).

Both ferrihydrite ($5Fe^{3+}{}_2O_3 \cdot 9H_2O$) and opal-A ($SiO_2 \cdot x\ H_2O$) are hydrated phases. Ferrihydrite's SWIR spectrum contains a weak H_2O overtone near 1.42 μm, a moderate H_2O combination band near 1.93 μm, and a strong H_2O stretching vibration centered at 3 μm (Bishop & Murad, 2002; Bishop, 2019). Opal-A has small absorption features at 1.39, 1.91 and 2.21 μm, and a large band at 3 μm (Bishop, 2019). Therefore one may ask, why does the SWIR spectrum of Mars dust contains only one strong absorption band at 3 μm (Jouglet et al., 2007; Milliken et al., 2007; Audouard et al., 2014)? The answer to this question may be related to the extremely fine nature of Martian dust. From laboratory studies it is known that as the particle size begins to approach the observed wavelength of light, the spectral contrast of a spectrum will change

[1]APXS cannot distinguish between different oxidation states.

(Mustard & Hays, 1997). Studies of fine palagonitic soil in the SWIR range showed that the absorption band strengths of a <5 μm fraction diminishes by 50% at 1.4, 1.9 and 2.2 μm relative to the 45- and 75-μm size fractions (Cooper & Mustard, 1999). Therefore, perhaps the smallest absorption features of very fine particle powders (~1 μm) of opal-A and ferrihydrite are below the detection limits of CRISM/OMEGA. Additionally, because present day Martian conditions are dry, ferrihydrite and opal-A phases on Mars might be in their dehydrated form. For example, the laboratory spectrum of ferrihydrite acquired under ambient conditions contains a water absorption band at 1.93 μm (Bishop & Murad, 2002), which is known to be strongly diminished after heating at ~200 °C for several hours (Pommerol et al., 2009). In general, ferrihydrite is chemically stable and does not break down even under higher temperatures (Stanjek & Weidler, 1992), therefore dehydration experiments are effective at removing adsorbed water. Dehydrated particles also become more easily disaggregated and can then be easily dispersed, and fragmented by surface winds on Mars.

Studies of Saharan dust on Earth have shown that the composition of dust particles varies with particle size (Kandler et al., 2007). Particles above 1 μm in size consist of mainly clays (e.g. kaolinite, illite, muscovite), quartz and carbonates, while particles below 1 micron are relatively more enriched in iron oxides (e.g. hematite), sulfates and carbonaceous materials (e.g. soot). Although the composition of Martian dust is very different, the aforementioned distinction suggests that small compositional differences could exist on Mars as well. For example, the CaSSIS observations show that dust in Isidis is not only brighter but also less red than dust in Arabia or Tharsis (e.g. Fig. 9). Therefore the difference between the highly and moderately bright regions may not only be explained by particle size (Ruff & Christensen, 2002) but also by slight differences in iron content. Variations in the distribution of iron-rich material at a particle

size scales have also been documented in Saharan dust (Kandler et al., 2009). In some dust particles, ferric iron materials are found as coatings while in others, they are distributed within their volumes. In comparison, Morris et al. (1989, 1993) proposed that Martian dust particles are composed of nanophase crystalline hematite ($Fe^{3+}_2O_3$) dispersed in an aluminosilicate matrix. Although such a composite particle model is viable and likely exists on Mars (just as it does on Earth), there is a lack of observational evidence for the individual compositional components proposed by those authors. MSL instruments showed that the Martian dust contains structurally bound H_2O (Leshin et al., 2013; Meslin et al., 2013) and soils in Gale Crater contain relatively low aluminum abundances but are enriched in silica (Rampe, Blake, et al., 2020). Furthermore, observations in our study suggest that lab hematite is not a good match to the orbital data based on: 1) large NR spectral slope values of 11% (vs ferrihydrite ~0.5%), 2) very low RP values of ~0% (vs ferrihydrite 6%) and 3) hematite's strong color ratio dependence on phase angle.

2. Implications for the ancient climate on Mars

One chemical pathway that results in ferrihydrite involves rapid hydrolysis and oxidation of ferrous-bearing materials (Schwertmann & Cornell, 2000). On Earth, ferrihydrite is usually found in relatively young deposits (<10 Ka old) and is a precursor to many other oxides and hydroxides (Torrent & Guzman, 1982; Cornell and Schwertmann, 2003). It is a metastable mineral phase, which favors transformation into hematite with increasing temperatures and pH but evolves into goethite when exposed to decreasing temperatures and pH (Schwertmann et al., 1999). The brownish-orange ferrihydrite is found between anoxic and oxic gradients in cooler soils, which are marked by changing redox conditions (Scheinost, 2005). Laboratory studies showed that silicates, phosphates and/or organic anions may inhibit the crystallization of ferrihydrite into other more stable ferric iron phases (Cornell & Schwertmann, 1979; Cornell et

al., 1987). Additionally, more recent studies have indicated that if amorphous opaline silica is present, ferrihydrite may survive in low-temperature (≤40°C) rock-dominated hydrothermal systems (Dehouck et al., 2017).

Opal-A, an amorphous phase of silica, is found on Earth in relatively young ~145 Ma old rocks (Tosca & Knoll, 2009). It is first converted into opal-CT (a more crystalline silica phase) and then into quartz in sedimentary diagenetic environments (Kastner et al., 1977). For this to occur, moderate temperatures (18–56°C) are needed (Pisciotto, 1981) but there is some evidence for crystallization even under colder conditions (0–4°C) in Antarctic deep-sea environments (Botz & Bohrmann, 1991). On Mars, the presence of amorphous silica in Gale Crater rocks and soils was attributed to cold and icy conditions, in which groundwater activity was intermittent (Rampe et al., 2020). Rampe et al. (2022) concluded that weathering under cold and icy climate is a fundamental mechanism for production of amorphous phases on Mars.

By analogy, the combination of silica and ferrihydrite in Martian dust suggests that liquid water and high temperatures on Mars were unlikely to have been present for an extended period in the past billions of years. Since both are amorphous minerals, in warm and wet conditions they would have been easily altered and crystallized into more stable phases. On the other hand, it raises the question what is the origin of spatially vast and meters-thick deposits of dust observed in Tharsis or Arabia (Keszthelyi et al., 2008; Mangold et al., 2009). It has been suggested that a slow thin-film weathering by either small amounts of liquid water (Yen et al., 2005), frost (Bibring et al., 2006) or acidic volatiles (Banin et al., 1997) are responsible for the production of iron oxides in the Amazonian period. However, Mars is covered by vast seemingly unaltered mafic-rich regions, Noachian and Hesperian in age (Poulet et al., 2009). If thin-film weathering was efficient and global, one can argue that even a thin layer of weathering products in the dark

regions would be visible to reflectance measuring instruments. The thousands of exposures of altered phyllosilicates in the southern highlands likely represent a more ancient period since they are commonly capped by layers of unaltered basalt (Mustard et al., 2008; Murchie et al., 2009; Ehlmann & Edwards, 2014). However, the dark regions are not fully dust-free; some mixing by global storms and local wind events is to be expected. Such processes would redistribute dust from bright to dark regions.

It is likely that some dusty regions are geologic sources of dust. Ojha et al. (2018) reported that the erosion of the sedimentary unit known as the Medusae Fossae Formation (MFF) significantly contributes to the Martian dust reservoir. Bridges & Muhs (2012) suggested that most light-toned deposits such as the ones found in Becquerel Crater and the upper mound of Gale Crater are lithified airfall dust rocks or "duststones". Since these assemblages are not distinct in the VIS and VNIR, their composition was interpreted to be similar to that of dust. Extensive sedimentary layers of light-toned rock that form rhythmic bedding are also found in Arabia Terra (Lewis et al., 2008) and are proposed to have formed by cemented dust as a result of rising groundwater (Grotzinger & Milliken, 2012). However, these are not the only examples of light-toned rock. Similar deposits are pervasive in the whole region of Arabia and are possibly cases of exposed bedrock. In the CaSSIS NPB data, they appear whitish in color and are often observed on crater rims (e.g. Fig. 2), topographic highs where dust is unstable, or anywhere where dust has been removed (Fig. 14). Furthermore, THEMIS night IR data in these areas show elevated temperatures consistent with exposed bedrock. Additional studies are needed to resolve the distribution and thickness of such deposits in Arabia. However, taken together with known occurrences of "duststones" these geologic units may hint at chemical weathering under cold

conditions, which consequently served as a major volatile sink in the Martian past (Huguenin, 1976).

References

Audouard, J., Poulet, F., Vincendon, M., Milliken, R. E., Jouglet, D., Bibring, J.-P., et al. (2014). Water in the Martian regolith from OMEGA/Mars Express. *Journal of Geophysical Research: Planets*, *119*(8), 1969–1989. https://doi.org/https://doi.org/10.1002/2014JE004649

Banin, A., Han, F. X., Kan, I., & Cicelsky, A. (1997). Acidic volatiles and the Mars soil. *Journal of Geophysical Research: Planets*, *102*(E6), 13341–13356. https://doi.org/https://doi.org/10.1029/97JE01160

Bell III, J. F., McCord, T. B., & Owensby, P. D. (1990). Observational evidence of crystalline iron oxides on Mars. *Journal of Geophysical Research: Solid Earth*, *95*(B9), 14447–14461. https://doi.org/https://doi.org/10.1029/JB095iB09p14447

Bibring, J. P., Langevin, Y., Mustard, J. F., Poulet, F., Arvidson, R., Gendrin, A., et al. (2006). Global mineralogical and aqueous Mars history derived from OMEGA/Mars express data. *Science*, *312*(5772), 400–404. https://doi.org/10.1126/science.1122659

Bishop, J. L. (2019). Visible and Near-Infrared Reflectance Spectroscopy. In J. F. Bell III, J. L. Bishop, & J. E. Moersch (Eds.), *Remote Compositional Analysis* (pp. 68–101). Cambridge: Cambridge University Press. https://doi.org/10.1017/9781316888872.006

Bishop, J. L., & Murad, E. (2002, January 1). Spectroscopic and geochemical analyses of

ferrihydrite from springs in Iceland and applications to Mars. (J. L. Smellie & M. G. Chapman, Eds.), *Volcano–Ice Interaction on Earth and Mars*. Geological Society of London. https://doi.org/10.1144/GSL.SP.2002.202.01.18

Blake, D. F., Morris, R. V, Kocurek, G., Morrison, S. M., Downs, R. T., Bish, D., et al. (2013). Curiosity at Gale Crater, Mars: Characterization and Analysis of the Rocknest Sand Shadow. *Science*, *341*(6153). https://doi.org/https://doi.org/10.1126/science.1239505

Botz, R., & Bohrmann, G. (1991). Low-temperature opal-CT precipitation in Antarctic deep-sea sediments: evidence from oxygen isotopes. *Earth and Planetary Science Letters*, *107*(3), 612–617. https://doi.org/https://doi.org/10.1016/0012-821X(91)90105-Q

Bridges, N. T., & Muhs, D. R. (2012). Duststones on Mars: Source, transport, deposition and erosion. *SEPM Special Publication*, *120*, 169–182. https://doi.org/10.2110/pec.12.102.0169

Chevrier, V., & Mathé, P. E. (2007). Mineralogy and evolution of the surface of Mars: A review. *Planetary and Space Science*, *55*(3), 289–314. https://doi.org/https://doi.org/10.1016/j.pss.2006.05.039

Cooper, C. D., & Mustard, J. F. (1999). Effects of Very Fine Particle Size on Reflectance Spectra of Smectite and Palagonitic Soil. *Icarus*, *142*(2), 557–570. https://doi.org/https://doi.org/10.1006/icar.1999.6221

Cornell, R.M. and Schwertmann, U. (2003). Formation. In *The Iron Oxides* (pp. 345–364). John Wiley & Sons, Ltd. https://doi.org/https://doi.org/10.1002/3527602097.ch13

Cornell, R. M., & Schwertmann, U. (1979). Influence of Organic Anions on the Crystallization of Ferrihydrite. *Clays and Clay Minerals*, *27*(6), 402–410.

https://doi.org/10.1346/CCMN.1979.0270602

Cornell, R. M., Giovanoli, R., & Schindler, P. W. (1987). Effect of Silicate Species on the Transformation of Ferrihydrite into Goethite and Hematite in Alkaline Media. *Clays and Clay Minerals*, *35*(1), 21–28. https://doi.org/10.1346/CCMN.1987.0350103

Dehouck, E., McLennan, S. M., Meslin, P.-Y., & Cousin, A. (2014). Constraints on abundance, composition, and nature of X-ray amorphous components of soils and rocks at Gale crater, Mars. *Journal of Geophysical Research: Planets*, *119*(12), 2640–2657. https://doi.org/https://doi.org/10.1002/2014JE004716

Dehouck, E., McLennan, S. M., Sklute, E. C., & Dyar, M. D. (2017). Stability and fate of ferrihydrite during episodes of water/rock interactions on early Mars: An experimental approach. *Journal of Geophysical Research: Planets*, *122*(2), 358–382. https://doi.org/https://doi.org/10.1002/2016JE005222

Ehlmann, B. L., & Edwards, C. S. (2014). Mineralogy of the Martian surface. *Annual Review of Earth and Planetary Sciences*, *42*, 291–315. https://doi.org/10.1146/annurev-earth-060313-055024

Fornasier, S., Hasselmann, P. H., Barucci, M. A., Feller, C., Besse, S., Leyrat, C., et al. (2015). Spectrophotometric properties of the nucleus of comet 67P/Churyumov-Gerasimenko from the OSIRIS instrument onboard the ROSETTA spacecraft. *Astronomy and Astrophysics*, *583*. https://doi.org/10.1051/0004-6361/201525901

Gehrels, T., Coffeen, T., & Owings, D. (1964). Wavelength dependance of polarization. III. The lunar surface. *The Astronomical Journal*, *69*(84 m), 826. https://doi.org/10.1086/109359

Go, S., Lyapustin, A., Schuster, G. L., Choi, M., Ginoux, P., Chin, M., et al. (2022). Inferring iron-oxide species content in atmospheric mineral dust from DSCOVR EPIC observations. *Atmospheric Chemistry and Physics*, *22*(2), 1395–1423. https://doi.org/10.5194/acp-22-1395-2022

Goryniuk, M. C., Rivard, B. A., & Jones, B. (2004). The reflectance spectra of opal-A (0.5–25 μm) from the Taupo Volcanic Zone: Spectra that may identify hydrothermal systems on planetary surfaces. *Geophysical Research Letters*, *31*(24). https://doi.org/https://doi.org/10.1029/2004GL021481

Grotzinger, J. P., & Milliken, R. E. (2012, January 1). The Sedimentary Rock Record of Mars: Distribution, Origins, and Global Stratigraphy. (J. P. Grotzinger & R. E. Milliken, Eds.), *Sedimentary Geology of Mars*. SEPM Society for Sedimentary Geology. https://doi.org/10.2110/pec.12.102.0001

Guinness, E. A. (1981). Spectral Properties Exposed at the Viking 1 Landing Site The reflectance properties of soil exposed at the Viking ing and viewing conditions as telescopic reflectance data of the reflectance spectra including ing the northern summer As part of the photome, *86*, 7983–7992.

Gunderson, K., Thomas, N., & Whitby, J. A. (2006). First measurements with the Physikalisches Institut Radiometric Experiment (PHIRE). Planetary and Space Science, 54(11), 1046–1056. https://doi.org/https://doi.org/10.1016/j.pss.2005.12.020

Hapke, B. (1993). *Theory of Reflectance and Emittance Spectroscopy*. *Topics in Remote Sensing*. Cambridge: Cambridge University Press. https://doi.org/DOI: 10.1017/CBO9780511524998

Hapke, B. (2012). *Theory of Reflectance and Emittance Spectroscopy* (2nd ed.). Cambridge University Press. https://doi.org/https://doi.org/10.1017/CBO9781139025683

Hapke, B. (2021). Bidirectional reflectance spectroscopy 8. The angular width of the opposition effect in regolith-like media. *Icarus*, *354*, 114105. https://doi.org/https://doi.org/10.1016/j.icarus.2020.114105

Hapke, B., & van Hoen, H. (1963). Photometric studies of complex surfaces, with applications to the Moon. *Journal of Geophysical Research (1896-1977)*, *68*(15), 4545–4570. https://doi.org/https://doi.org/10.1029/JZ068i015p04545

Huguenin, R. L. (1976). Mars: Chemical weathering as a massive volatile sink. *Icarus*, *28*(2), 203–212. https://doi.org/https://doi.org/10.1016/0019-1035(76)90033-6

Johnson, J. R., Shepard, M. K., Grundy, W. M., Paige, D. A., & Foote, E. J. (2013). Spectrogoniometry and modeling of martian and lunar analog samples and Apollo soils. *Icarus*, *223*(1), 383–406. https://doi.org/10.1016/j.icarus.2012.12.004

Johnson, J. R., Grundy, W. M., Lemmon, M. T., Liang, W., Bell, J. F., Hayes, A. G., & Deen, R. G. (2021). Spectrophotometric properties of materials observed by Pancam on the Mars Exploration Rovers: 4. Final mission observations. *Icarus*, *357*, 114261. https://doi.org/10.1016/j.icarus.2020.114261

Jouglet, D., Poulet, F., Milliken, R. E., Mustard, J. F., Bibring, J. P., Langevin, Y., et al. (2007). Hydration state of the Martian surface as seen by Mars Express OMEGA: 1. Analysis of the 3 μm hydration feature. *Journal of Geophysical Research: Planets*, *112*(8), 1–20. https://doi.org/10.1029/2006JE002846

Kandler, K., Benker, N., Bundke, U., Cuevas, E., Ebert, M., Knippertz, P., et al. (2007). Chemical composition and complex refractive index of Saharan Mineral Dust at Izaña, Tenerife (Spain) derived by electron microscopy. *Atmospheric Environment*, *41*(37), 8058–8074. https://doi.org/https://doi.org/10.1016/j.atmosenv.2007.06.047

Kandler, K., Schütz, L., Deutscher, C., Ebert, M., Hofmann, H., Jäckel, S., et al. (2009). Size distribution, mass concentration, chemical and mineralogical composition and derived optical parameters of the boundary layer aerosol at Tinfou, Morocco, during SAMUM 2006. *Tellus B*, *61*(1), 32–50. https://doi.org/https://doi.org/10.1111/j.1600-0889.2008.00385.x

Kastner, M., Keene, J. B., & Gieskes, J. M. (1977). Diagenesis of siliceous oozes—I. Chemical controls on the rate of opal-A to opal-CT transformation—an experimental study. *Geochimica et Cosmochimica Acta*, *41*(8), 1041–1059. https://doi.org/https://doi.org/10.1016/0016-7037(77)90099-0

Keszthelyi, L., Jaeger, W., McEwen, A., Tornabene, L., Beyer, R. A., Dundas, C., & Milazzo, M. (2008). High resolution imaging science experiment (HiRISE) images of volcanic terrains from the first 6 months of the Mars reconnaissance orbiter primary science phase. *Journal of Geophysical Research: Planets*, *113*(4), 1–25. https://doi.org/10.1029/2007JE002968

Lafon, S., Sokolik, I. N., Rajot, J. L., Caquineau, S., & Gaudichet, A. (2006). Characterization of iron oxides in mineral dust aerosols: Implications for light absorption. *Journal of Geophysical Research: Atmospheres*, *111*(D21). https://doi.org/https://doi.org/10.1029/2005JD007016

Leshin, L. A., Mahaffy, P. R., Webster, C. R., Cabane, M., Coll, P., Conrad, P. G., et al. (2013). Volatile, Isotope, and Organic Analysis of Martian Fines with the Mars Curiosity Rover. *Science*, *341*(6153), 1238937. https://doi.org/10.1126/science.1238937

Lewis, K. W., Aharonson, O., Grotzinger, J. P., Kirk, R. L., McEwen, A. S., & Suer, T.-A. (2008). Quasi-Periodic Bedding in the Sedimentary Rock Record of Mars. *Science*, *322*(5907), 1532–1535. https://doi.org/10.1126/science.1161870

Mangold, N., Ansan, V., Masson, P., & Vincendon, C. (2009). Estimate of aeolian dust thickness in Arabia Terra, Mars: implications of a thick mantle (> 20 m) for hydrogen detection. *Géomorphologie : Relief, Processus, Environnement*, *15*(1), 23–32. https://doi.org/10.4000/geomorphologie.7472

McCleese, D. J., Schofield, J. T., Taylor, F. W., Calcutt, S. B., Foote, M. C., Kass, D. M., et al. (2007). Mars Climate Sounder: An investigation of thermal and water vapor structure, dust and condensate distributions in the atmosphere, and energy balance of the polar regions. *Journal of Geophysical Research: Planets*, *112*(E5). https://doi.org/https://doi.org/10.1029/2006JE002790

Meslin, P.-Y., Gasnault, O., Forni, O., Schröder, S., Cousin, A., Berger, G., et al. (2013). Soil Diversity and Hydration at Gale Crater , Mars. *Science*, *341*(September), 1–9. Retrieved from http://science.sciencemag.org/content/sci/341/6153/1238670.full.pdf

Milliken, R. E., Mustard, J. F., Poulet, F., Jouglet, D., Bibring, J. P., Gondet, B., & Langevin, Y. (2007). Hydration state of the Martian surface as seen by Mars Express OMEGA: 2. H2O content of the surface. *Journal of Geophysical Research: Planets*, *112*(8), 1–15. https://doi.org/10.1029/2006JE002853

Milliken, R. E., Swayze, G. A., Arvidson, R. E., Bishop, J. L., Clark, R. N., Ehlmann, B. L., et al. (2008). Opaline silica in young deposits on Mars. *Geology*, *36*(11), 847–850. https://doi.org/10.1130/G24967A.1

Morris, R. V., Golden, D. C., Bell, J. F., Lauer, H. V, & Adams, J. B. (1993). Pigmenting agents in martian soils: Inferences from spectral, Mössbauer, and magnetic properties of nanophase and other iron oxides in Hawaiian palagonitic soil PN-9. *Geochimica et Cosmochimica Acta*, *57*(19), 4597–4609. https://doi.org/https://doi.org/10.1016/0016-7037(93)90185-Y

Morris, Richard V, Agresti, D. G., Lauer Jr., H. V, Newcomb, J. A., Shelfer, T. D., & Murali, A. V. (1989). Evidence for pigmentary hematite on Mars based on optical, magnetic, and Mossbauer studies of superparamagnetic (nanocrystalline) hematite. *Journal of Geophysical Research: Solid Earth*, *94*(B3), 2760–2778. https://doi.org/https://doi.org/10.1029/JB094iB03p02760

Murchie, S., Mustard, J., Bishop, J., Head, J., Pieters, C., & Erard, S. (1993). Spatial Variations in the Spectral Properties of Bright Regions on Mars. *Icarus*, *105*(2), 454–468. https://doi.org/https://doi.org/10.1006/icar.1993.1141

Murchie, S., Kirkland, L., Erard, S., Mustard, J., & Robinson, M. (2000). Near-Infrared Spectral Variations of Martian Surface Materials from ISM Imaging Spectrometer Data. *Icarus*, *147*(2), 444–471. https://doi.org/https://doi.org/10.1006/icar.2000.6446

Murchie, S. L., Mustard, J. F., Ehlmann, B. L., Milliken, R. E., Bishop, J. L., McKeown, N. K., et al. (2009). A synthesis of Martian aqueous mineralogy after 1 Mars year of observations from the Mars Reconnaissance Orbiter. *Journal of Geophysical Research: Planets*, *114*(E2). https://doi.org/https://doi.org/10.1029/2009JE003342

Mustard, J. F., & Hays, J. E. (1997). Effects of Hyperfine Particles on Reflectance Spectra from 0.3 to 25 μm. *Icarus*, *125*(1), 145–163. https://doi.org/https://doi.org/10.1006/icar.1996.5583

Mustard, J. F., Murchie, S. L., Pelkey, S. M., Ehlmann, B. L., Milliken, R. E., Grant, J. A., et al. (2008). Hydrated silicate minerals on Mars observed by the Mars Reconnaissance Orbiter CRISM instrument. *Nature*, *454*(7202), 305–309. https://doi.org/10.1038/nature07097

Ody, A., Poulet, F., Langevin, Y., Bibring, J.-P., Bellucci, G., Altieri, F., et al. (2012). Global maps of anhydrous minerals at the surface of Mars from OMEGA/MEx. *Journal of Geophysical Research: Planets*, *117*(E11). https://doi.org/https://doi.org/10.1029/2012JE004117

Ojha, L., Lewis, K., Karunatillake, S., & Schmidt, M. (2018). The Medusae Fossae Formation as the single largest source of dust on Mars. *Nature Communications*, *9*(1), 2867. https://doi.org/10.1038/s41467-018-05291-5

Pisciotto, K. A. (1981). Diagenetic trends in the siliceous facies of the Monterey Shale in the Santa Maria region, California. *Sedimentology*, *28*(4), 547–571. https://doi.org/https://doi.org/10.1111/j.1365-3091.1981.tb01701.x

Pommerol, A., Schmitt, B., Beck, P., & Brissaud, O. (2009). Water sorption on martian regolith analogs: Thermodynamics and near-infrared reflectance spectroscopy. *Icarus*, *204*(1), 114–136. https://doi.org/https://doi.org/10.1016/j.icarus.2009.06.013

Pommerol, A., Thomas, N., Jost, B., Beck, P., Okubo, C., & McEwen, A. S. (2013). Photometric properties of Mars soils analogs. *Journal of Geophysical Research: Planets*, *118*(10), 2045–2072. https://doi.org/10.1002/jgre.20158

Poulet, F., Mangold, N., Platevoet, B., Bardintzeff, J.-M., Sautter, V., Mustard, J. F., et al. (2009). Quantitative compositional analysis of martian mafic regions using the MEx/OMEGA reflectance data: 2. Petrological implications. *Icarus*, *201*(1), 84–101. https://doi.org/https://doi.org/10.1016/j.icarus.2008.12.042

Rampe, E. B., Blake, D. F., Bristow, T. F., Ming, D. W., Vaniman, D. T., Morris, R. V, et al. (2020). Mineralogy and geochemistry of sedimentary rocks and eolian sediments in Gale crater, Mars: A review after six Earth years of exploration with Curiosity. *Geochemistry*, *80*(2), 125605. https://doi.org/https://doi.org/10.1016/j.chemer.2020.125605

Rampe, E. B., Bristow, T. F., Morris, R. V, Morrison, S. M., Achilles, C. N., Ming, D. W., et al. (2020). Mineralogy of Vera Rubin Ridge From the Mars Science Laboratory CheMin Instrument. *Journal of Geophysical Research: Planets*, *125*(9), e2019JE006306. https://doi.org/https://doi.org/10.1029/2019JE006306

Rampe, E. B., Horgan, B. H. N., Smith, R. J., Scudder, N. A., Bamber, E. R., Rutledge, A. M., & Christoffersen, R. (2022). A mineralogical study of glacial flour from Three Sisters, Oregon: An analog for a cold and icy early Mars. *Earth and Planetary Science Letters*, *584*, 117471. https://doi.org/https://doi.org/10.1016/j.epsl.2022.117471

Rice, M. S., Cloutis, E. A., Bell, J. F., Bish, D. L., Horgan, B. H., Mertzman, S. A., et al. (2013). Reflectance spectra diversity of silica-rich materials: Sensitivity to environment and implications for detections on Mars. *Icarus*, *223*(1), 499–533. https://doi.org/https://doi.org/10.1016/j.icarus.2012.09.021

Ruff, S. W., & Christensen, P. R. (2002). Bright and dark regions on Mars: Particle size and mineralogical characteristics based on Thermal Emission Spectrometer data. *Journal of*

Geophysical Research: Planets, *107*(E12). https://doi.org/https://doi.org/10.1029/2001JE001580

Scheinost, A. C. (2005). Metal oxides. In E. Hillel (Ed.), *Encyclopedia of Soils in the Environment* (pp. 428–438). Oxford: Elsevier. https://doi.org/10.1016/B0-12-348530-4/00194-6

Schröder, S. E., Grynko, Y., Pommerol, A., Keller, H. U., Thomas, N., & Roush, T. L. (2014). Laboratory observations and simulations of phase reddening. *Icarus*, *239*, 201–216. https://doi.org/10.1016/j.icarus.2014.06.010

Schwertmann, U., & Cornell, R. M. (2000). Ferrihydrite. In *Iron Oxides in the Laboratory* (pp. 103–112). https://doi.org/https://doi.org/10.1002/9783527613229.ch08

Schwertmann, U., Friedl, J., & Stanjek, H. (1999). From Fe(III) Ions to Ferrihydrite and then to Hematite. *Journal of Colloid and Interface Science*, *209*(1), 215–223. https://doi.org/https://doi.org/10.1006/jcis.1998.5899

Shkuratov, Y., Starukhina, L., Hoffmann, H., & Arnold, G. (1999). A Model of Spectral Albedo of Particulate Surfaces: Implications for Optical Properties of the Moon. *Icarus*, *137*(2), 235–246. https://doi.org/https://doi.org/10.1006/icar.1998.6035

Smith, R. J., McLennan, S. M., Achilles, C. N., Dehouck, E., Horgan, B. H. N., Mangold, N., et al. (2021). X-Ray Amorphous Components in Sedimentary Rocks of Gale Crater, Mars: Evidence for Ancient Formation and Long-Lived Aqueous Activity. *Journal of Geophysical Research: Planets*, *126*(3), e2020JE006782. https://doi.org/https://doi.org/10.1029/2020JE006782

Squyres, S. W., Arvidson, R. E., Ruff, S., Gellert, R., Morris, R. V, Ming, D. W., et al. (2008). Detection of Silica-Rich Deposits on Mars. *Science*, *320*(5879), 1063–1067. https://doi.org/10.1126/science.1155429

Stanjek, H., & Weidler, P. G. (1992). The effect of dry heating on the chemistry, surface area, and oxalate solubility of synthetic 2-line and 6-line ferrihydrites. *Clay Minerals*, *27*(4), 397–411. https://doi.org/DOI: 10.1180/claymin.1992.027.4.01

Tarnas, J. D., Mustard, J. F., Lin, H., Goudge, T. A., Amador, E. S., Bramble, M. S., et al. (2019). Orbital Identification of Hydrated Silica in Jezero Crater, Mars. *Geophysical Research Letters*, *46*(22), 12771–12782. https://doi.org/https://doi.org/10.1029/2019GL085584

Taylor, R. ~C., Gehrels, T., & Silvester, A. ~B. (1971). Minor Planets and Related Objects. VI. Asteroid (110) Lydia. *The Astronomical Journal*, *76*, 141. https://doi.org/10.1086/111097

Torrent, J., & Guzman, R. (1982). Crystallization of Fe(III)-Oxides from ferrihydrite in salt solutions: osmotic and specific ion effects. *Clay Minerals*, *17*(4), 463–469. https://doi.org/DOI: 10.1180/claymin.1982.017.4.09

Tosca, N. J., & Knoll, A. H. (2009). Juvenile chemical sediments and the long term persistence of water at the surface of Mars. *Earth and Planetary Science Letters*, *286*(3), 379–386. https://doi.org/https://doi.org/10.1016/j.epsl.2009.07.004

Vaniman, D. T., Bish, D. L., Ming, D. W., Bristow, T. F., Morris, R. V, Blake, D. F., et al. (2014). Mineralogy of a Mudstone at Yellowknife Bay, Gale Crater, Mars. *Science*, *343*(6169), 1243480. https://doi.org/10.1126/science.1243480

Vincendon, M. (2013). Mars surface phase function constrained by orbital observations. *Planetary and Space Science*, *76*, 87–95. https://doi.org/https://doi.org/10.1016/j.pss.2012.12.005

Yen, A. S., Gellert, R., Schröder, C., Morris, R. V., Bell, J. F., Knudson, A. T., et al. (2005). An integrated view of the chemistry and mineralogy of martian soils. *Nature*, *436*(7047), 49–54. https://doi.org/10.1038/nature03637

Table 1. Mesh sizes used in the sprinkling procedure and cohesion rating for ferrihydrite (FHY), goethite (GOE), lepidocrocite (LEP), hematite (HEM), akaganeite (AKA), maghemite (MGH), schwertmannite (SCH) and feroxyhyte (FOXY).

Sample	FHY	GOE	LEP	HEM	AKA	MGH	SCH	FOXY
Mesh size (µm)	11	11	40	20	30	20	30	40
Cohesion	low	medium	medium	low	medium	low	medium	high

Figures

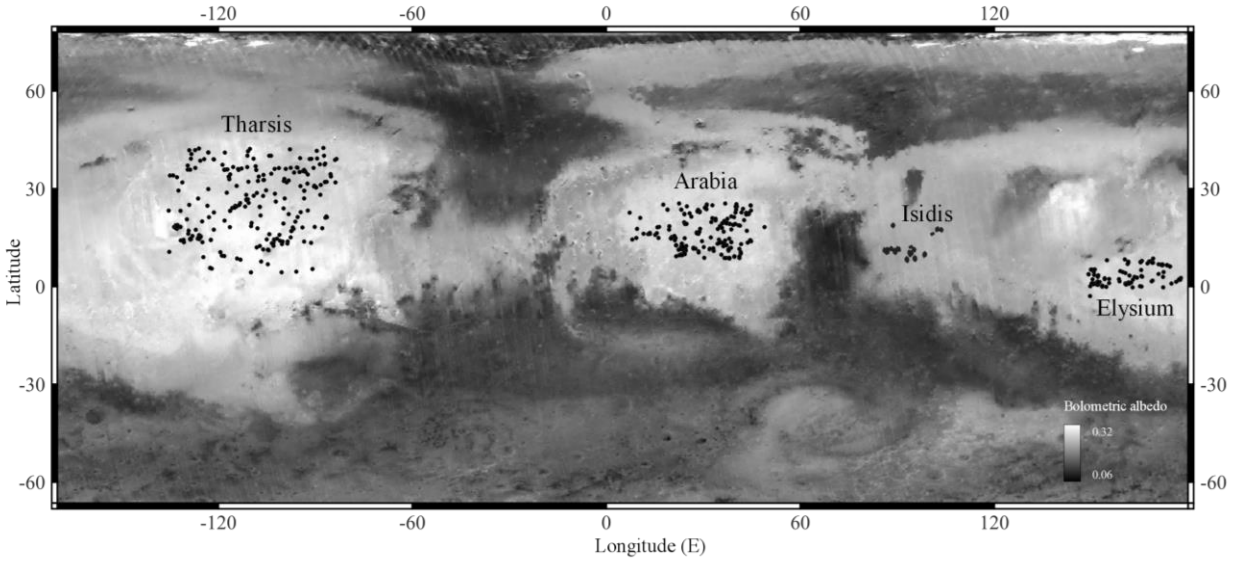

Figure 1. Distribution of CaSSIS observations of dust (black dots) in Tharsis, Arabia, Isidis and Elysium regions. The goal was to target homogenous deposits that are representative of the parent region in terms of similar particle properties (e.g. size, composition). The basemap is the TES bolometric albedo global mosaic (Ruff & Christensen, 2002).

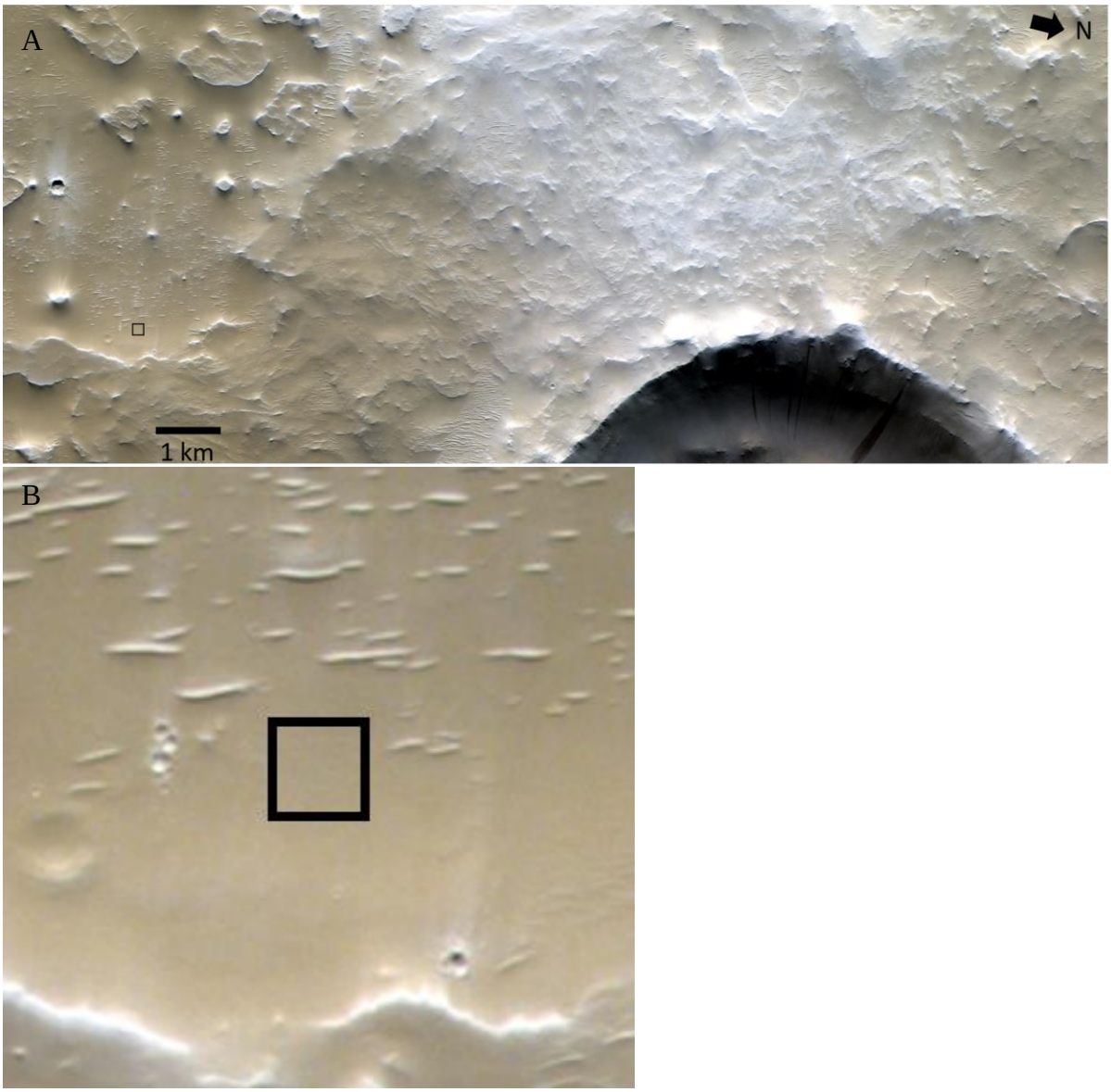

Figure 2. (A) Typical example of a dusty scene in Arabia Terra. Measurement Region of Interest (ROI) used for photometry shown in black. (B) Close up of the same ROI (150 m wide). Homogenous, undisturbed and spectrally pure deposits of dust were investigated in this study. Note the bright and whitish deposits to the south-west of the crater rim. CaSSIS MY35_010772_165_0_NPB image (NIR = 940 nm, PAN = 677 nm, BLU = 497 nm).

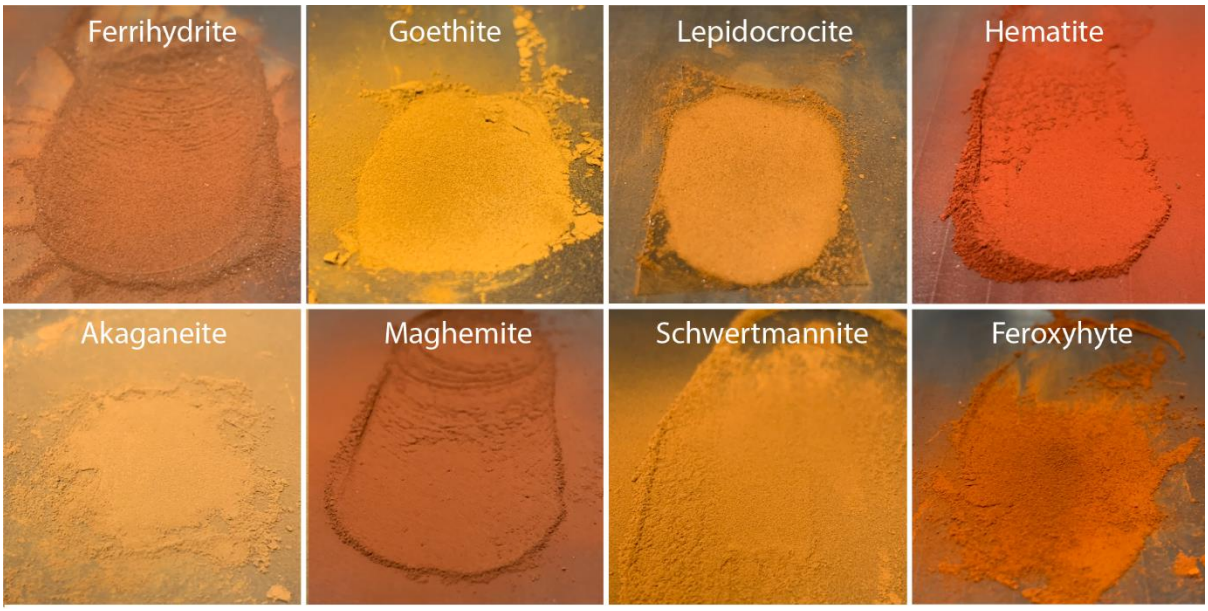

Figure 3. Ferric iron oxide powders investigated in this work using PHIRE-2. Part of each sample was compacted and then sprinkled with the remainder using very fine nylon sieves (see Methods section).

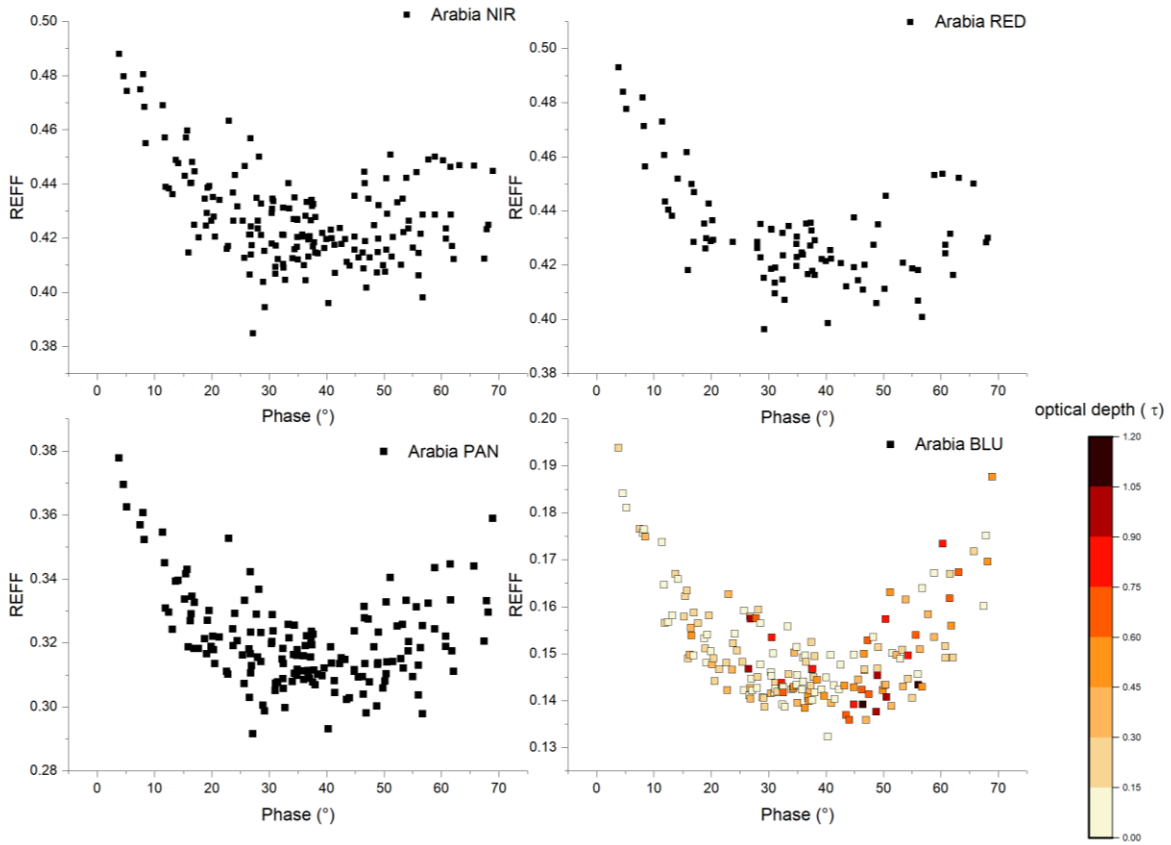

Figure 4. Phase curves of Arabia Terra dust in each CaSSIS filter (NIR, RED, PAN and BLU). Each point is an individual CaSSIS observation. The difference in number of points between each plot results from the fact that CaSSIS images are not always taken in four filters. Reflectance values increase exponentially as phase angle approaches 0° due to the opposition surge effect. Optical depth values given on the right.

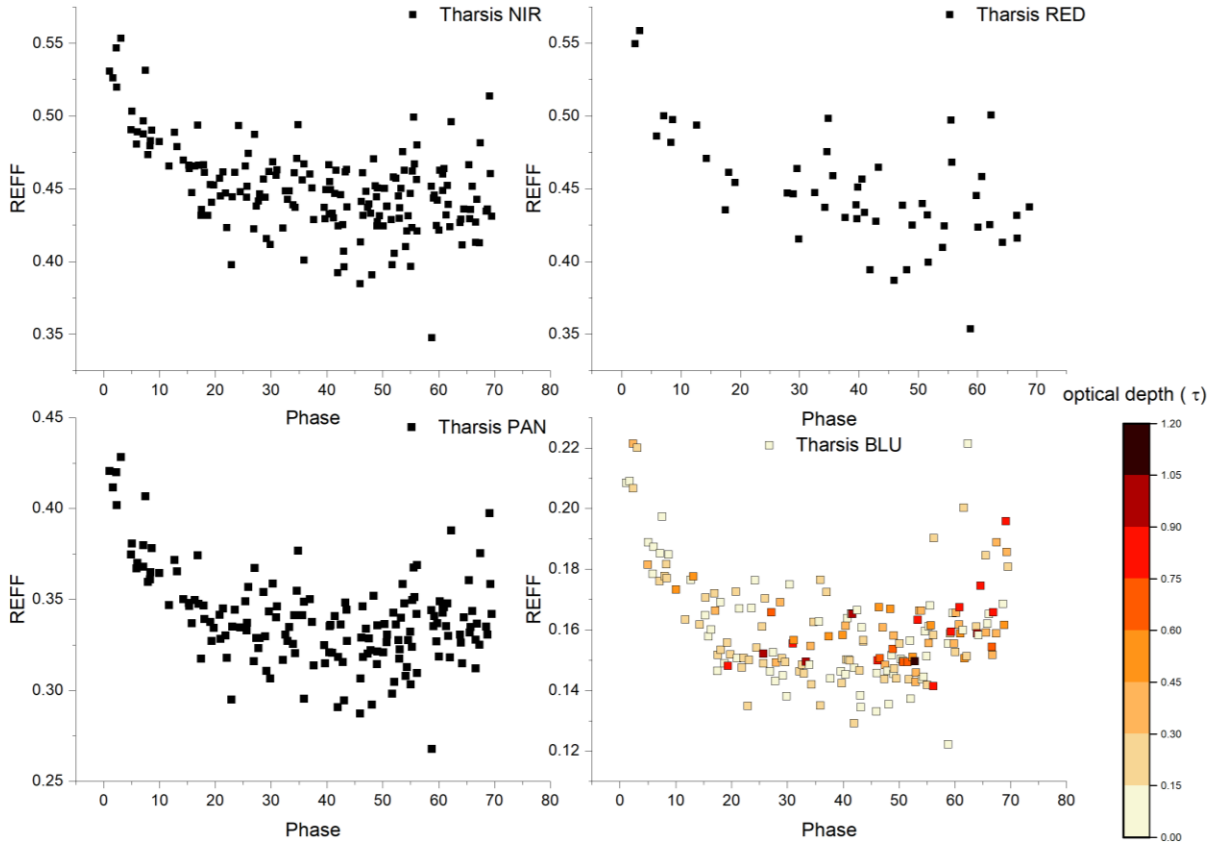

Figure 5. Phase curves of Tharsis dust in each CaSSIS filter. Similar trends can be observed as for Arabia phase curve plots. Optical depth values given on the right.

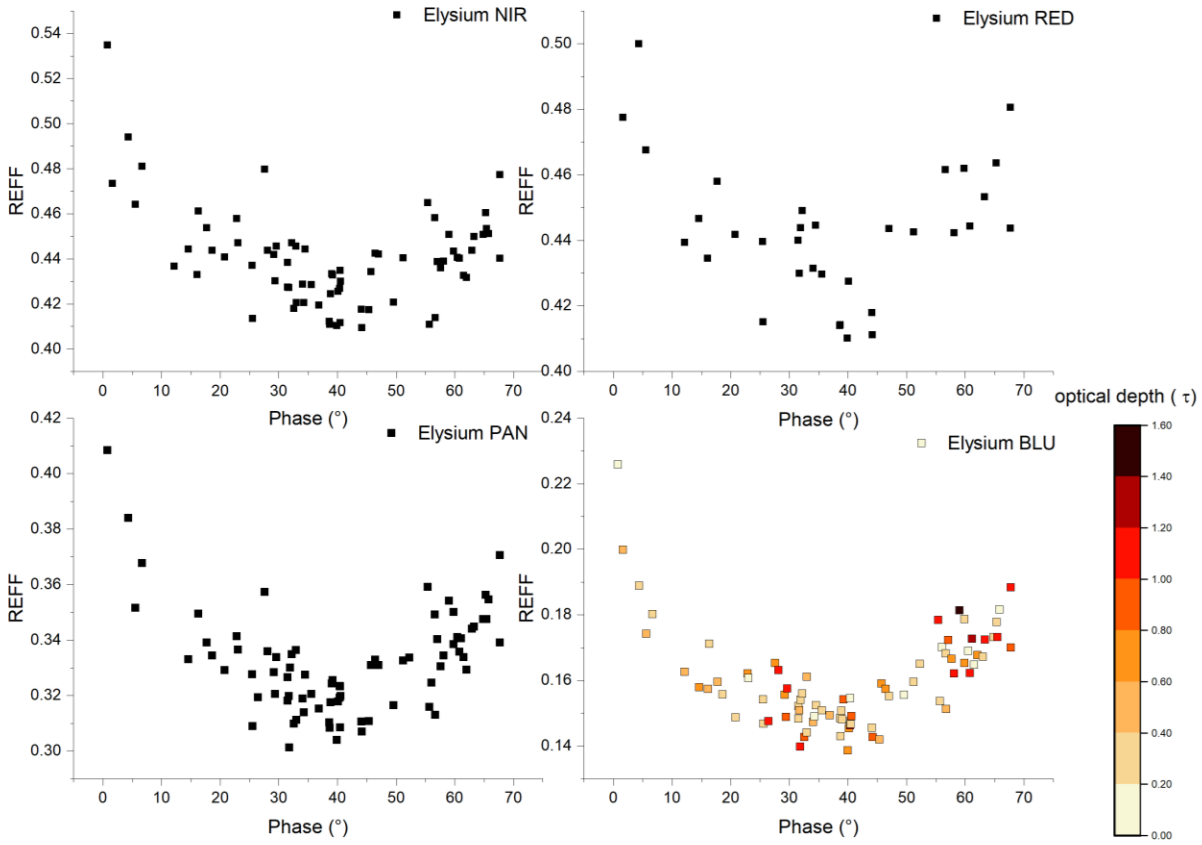

Figure 6. Phase curves of Elysium Planitia dust in each CaSSIS filter. Similar trends can be observed as for Arabia phase curve plots. Note the data point at 0.5° phase (the lowest observed in this study) and its asymptotical behavior. Optical depth values given on the right.

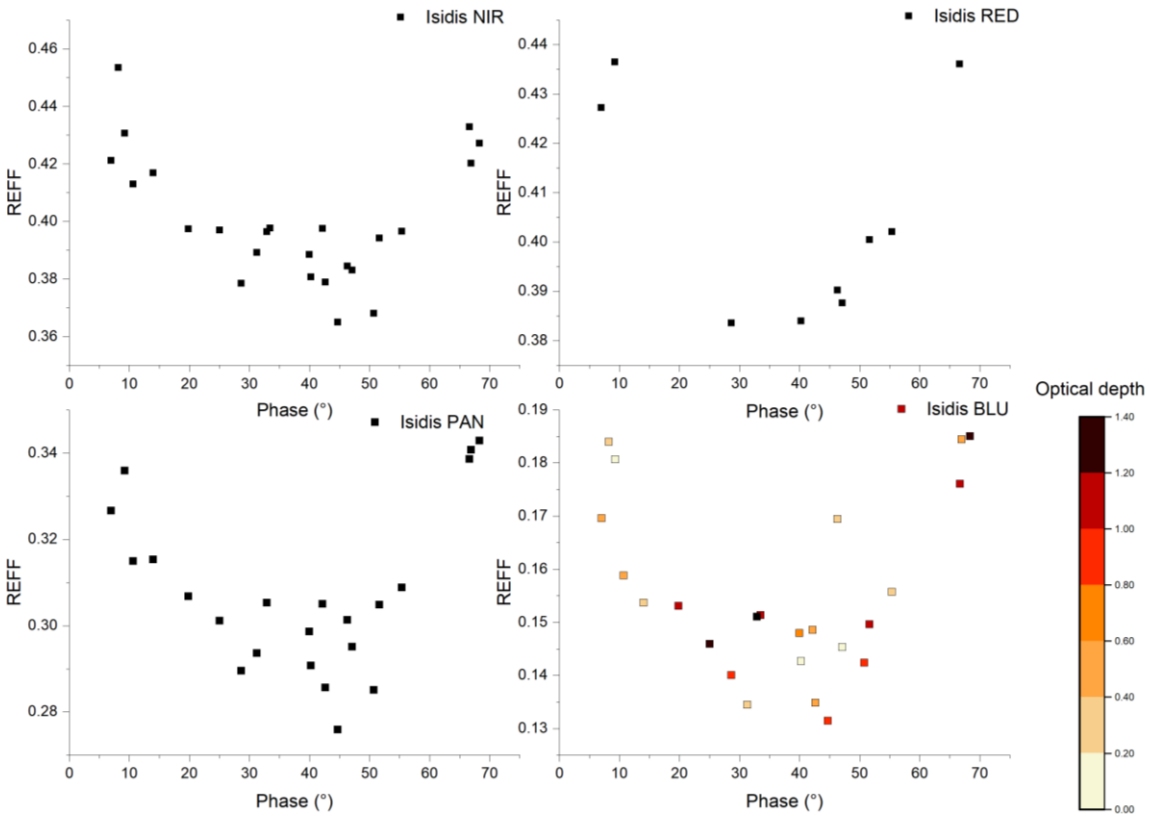

Figure 7. Phase curves of Isidis Planitia dust in each CaSSIS filter. Similar trends can be observed as for Arabia phase curve plots. Optical depth values given on the right.

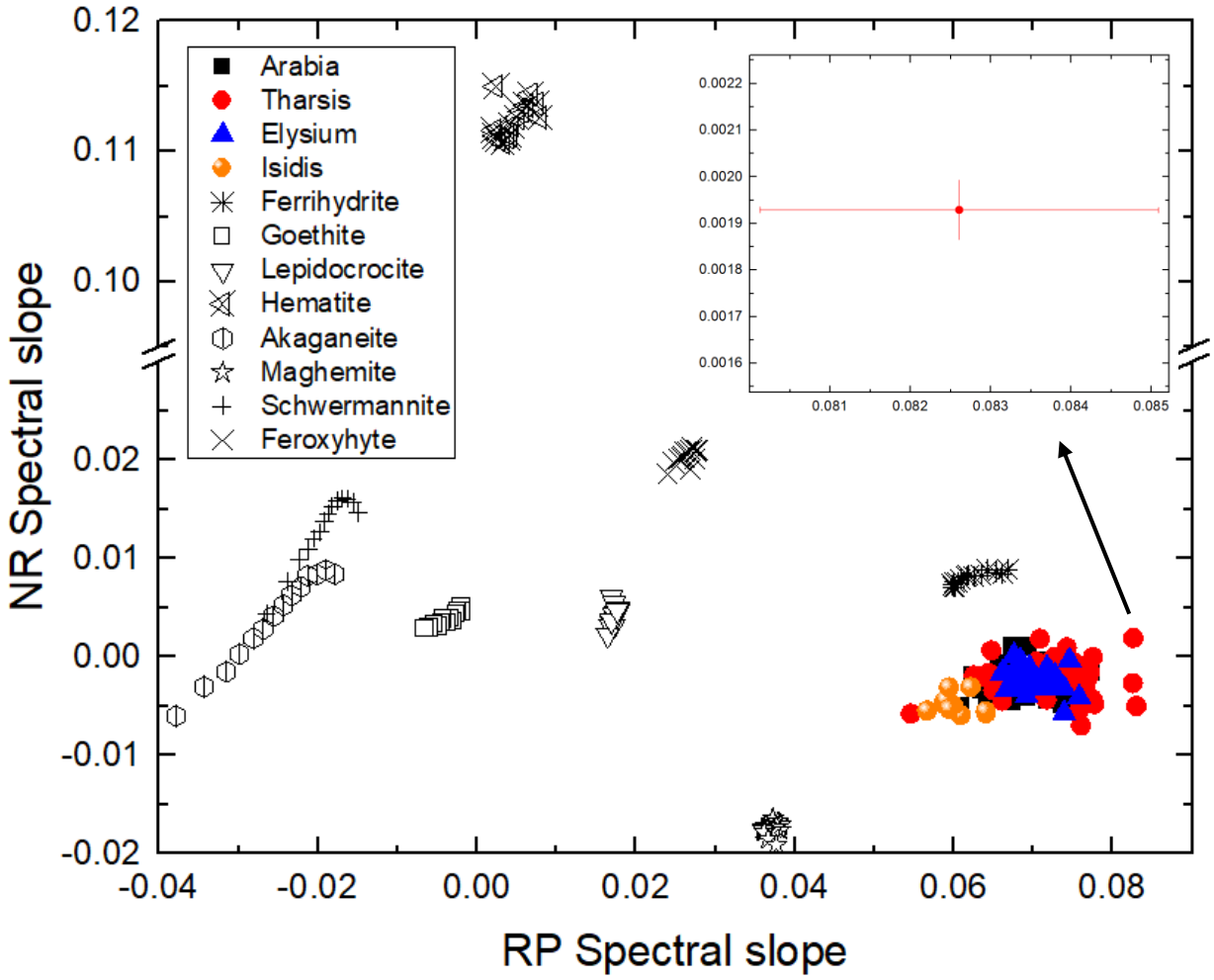

Figure 8. Color spectral slopes NR vs RP of CaSSIS observations and PHIRE-2 laboratory measurements of ferric iron oxides (symbols in black). The plot suggests that spectral slopes are less dependent on phase angle than spectral ratios (i.e. points more closely clustered). Ferrihydrite is remarkably close to the Martian dust in terms of NR and RP spectral slope values. 3% error bars from the uncertainties in the CaSSIS absolute calibration are given in the top right panel. For the sake of clarity they are not shown in this plot.

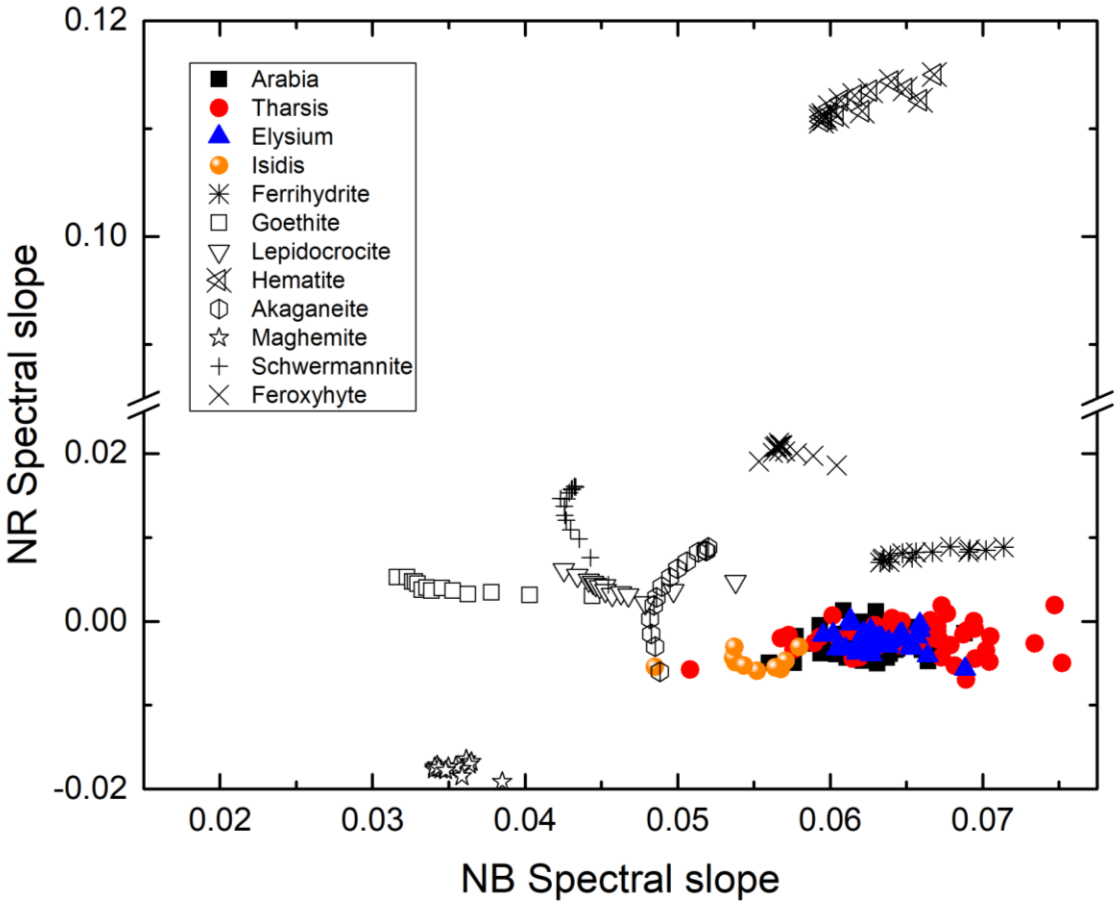

Figure 9. Color spectral slopes NR vs NB of CaSSIS observations and PHIRE-2 laboratory measurements of ferric iron oxides (symbols in black). Although NIR/BLU ratios of Martian dust and ferrihydrite were different, NB spectral slopes are quite similar. This suggests that the Martian dust spectrum is dominated by a mineral similar to ferrihydrite but also contains spectrally neutral impurities.

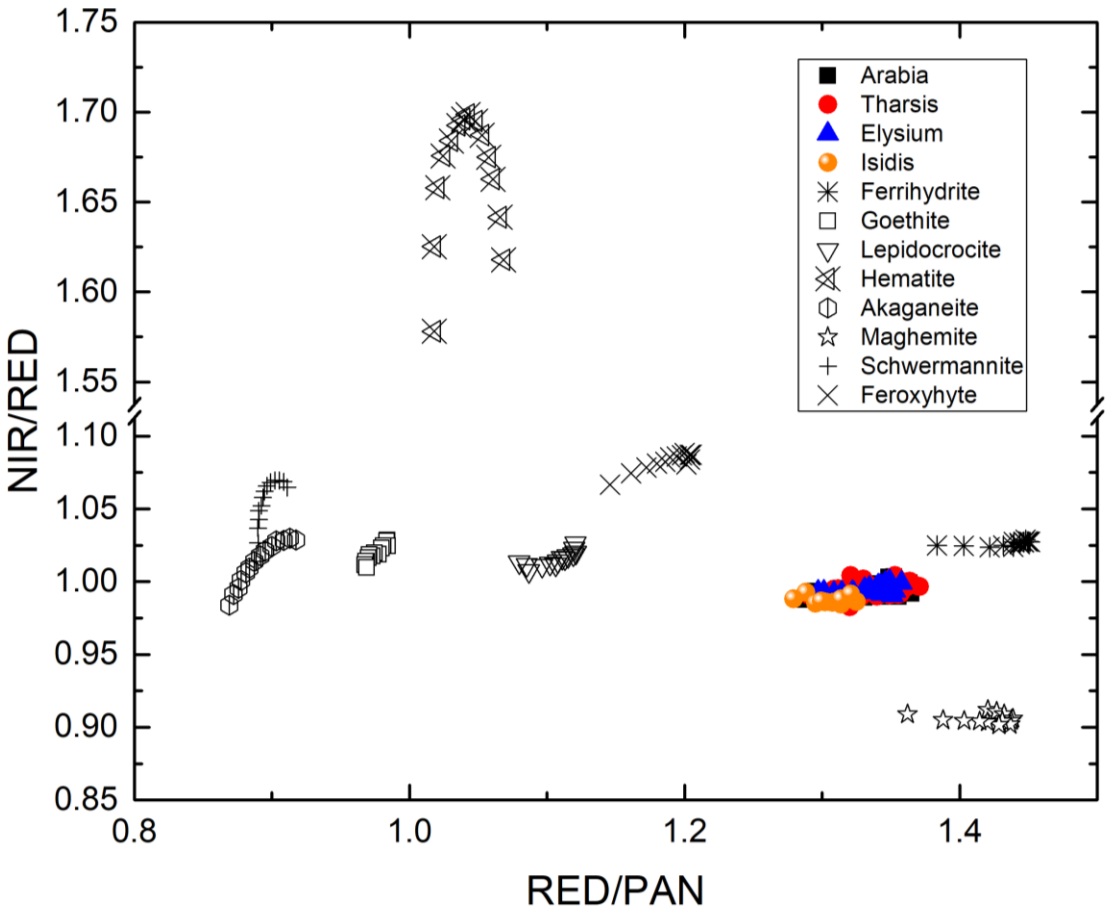

Figure 10. Color spectral ratios NIR/RED vs RED/PAN of all CaSSIS observations of dust and PHIRE-2 laboratory measurements of ferric iron oxides (symbols in black). The shape of the data point distribution of each mineral phase implies a dependency on phase angle (e.g. "arch-like" shape of the hematite ratio). The ratio of NIR to RED is close to 1 and signifies a flat spectrum from 830 nm to 940 nm for lepidocrocite, goethite, akaganeite, ferrihydrite and Martian dust. The similar RED/PAN and NIR/RED values are observed only for Martian dust and ferrihydrite. Each set of laboratory measurements span the entire observation geometry of PHIRE-2 (i.e. 4 – 70° phase).

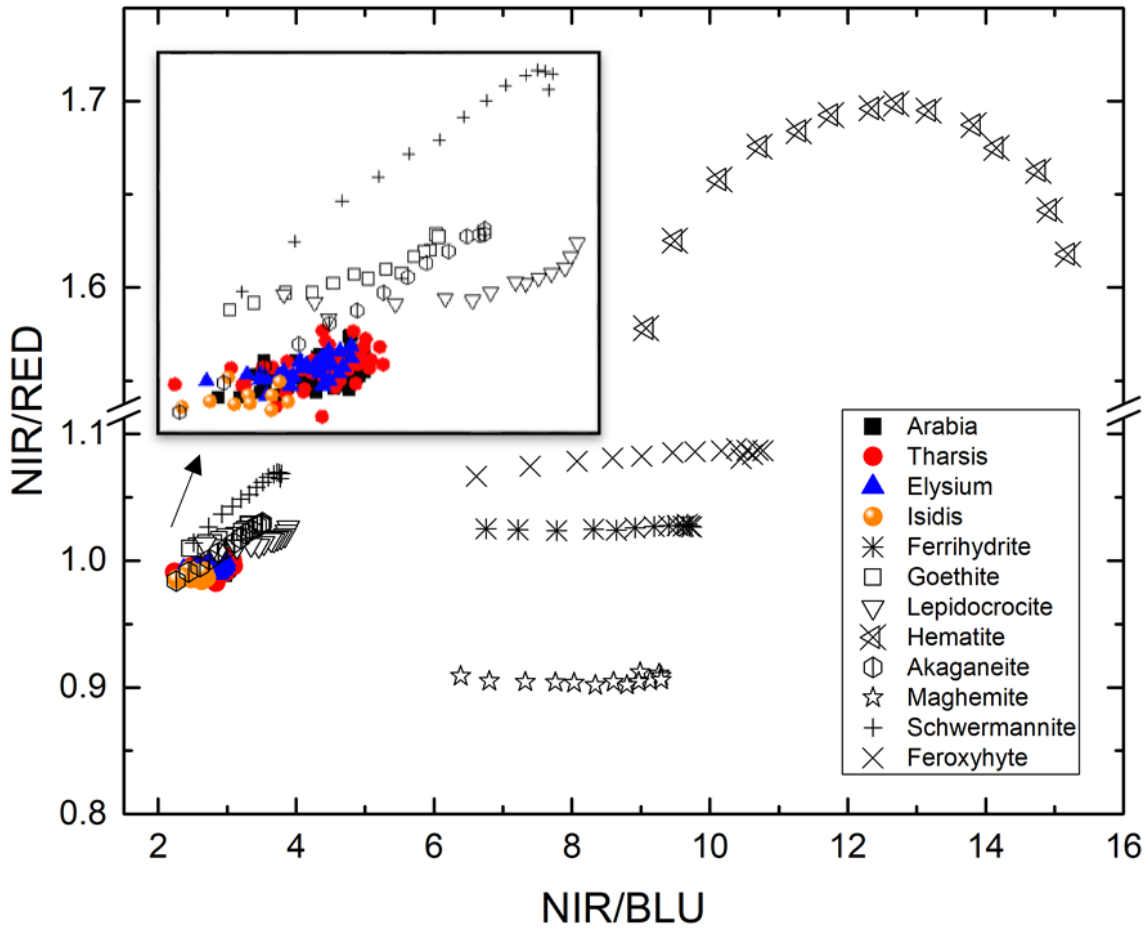

Figure 11. Color spectral ratios NIR/RED vs NIR/BLU of CaSSIS observations and PHIRE-2 laboratory measurements of ferric iron oxides (symbols in black). Similar phase angle effects are observed here as in Fig. 8. The largest NIR/BLU values are observed for hematite, feroxyhyte ferrihydrite and maghemite. The separation of NIR/BLU values between Martian dust and ferrihydrite suggests that Martian dust is relatively bright at blue wavelengths.

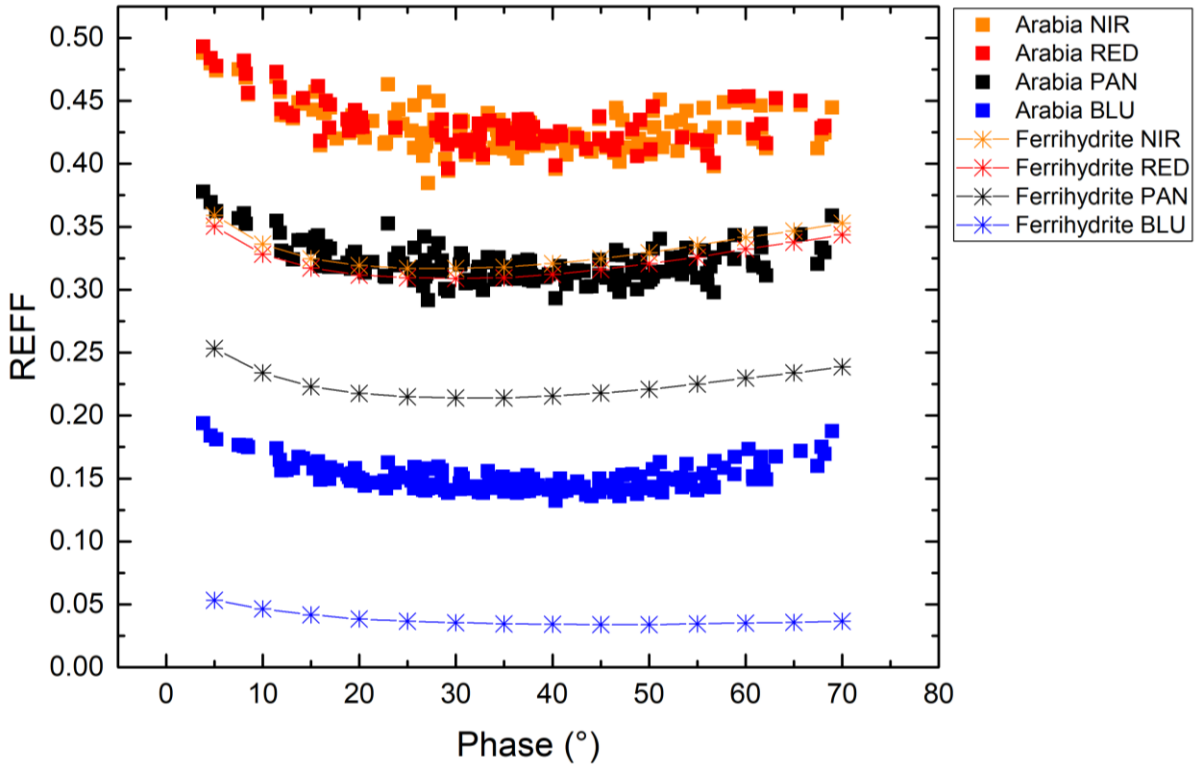

Figure 12. Phase curves of CaSSIS observations of dust in Arabia and lab ferrihydrite (<11 μm size fraction). An "offset" in reflectance can be observed between the orbital and lab phase curves. For example, Arabia NIR and ferrihydrite NIR phase curves are offset by a REFF value of ~0.1. A similar offset is seen for other filter pairs. This suggests that Martian dust is not pure ferrihydrite and includes a spectrally bright and neutral component such as silica.

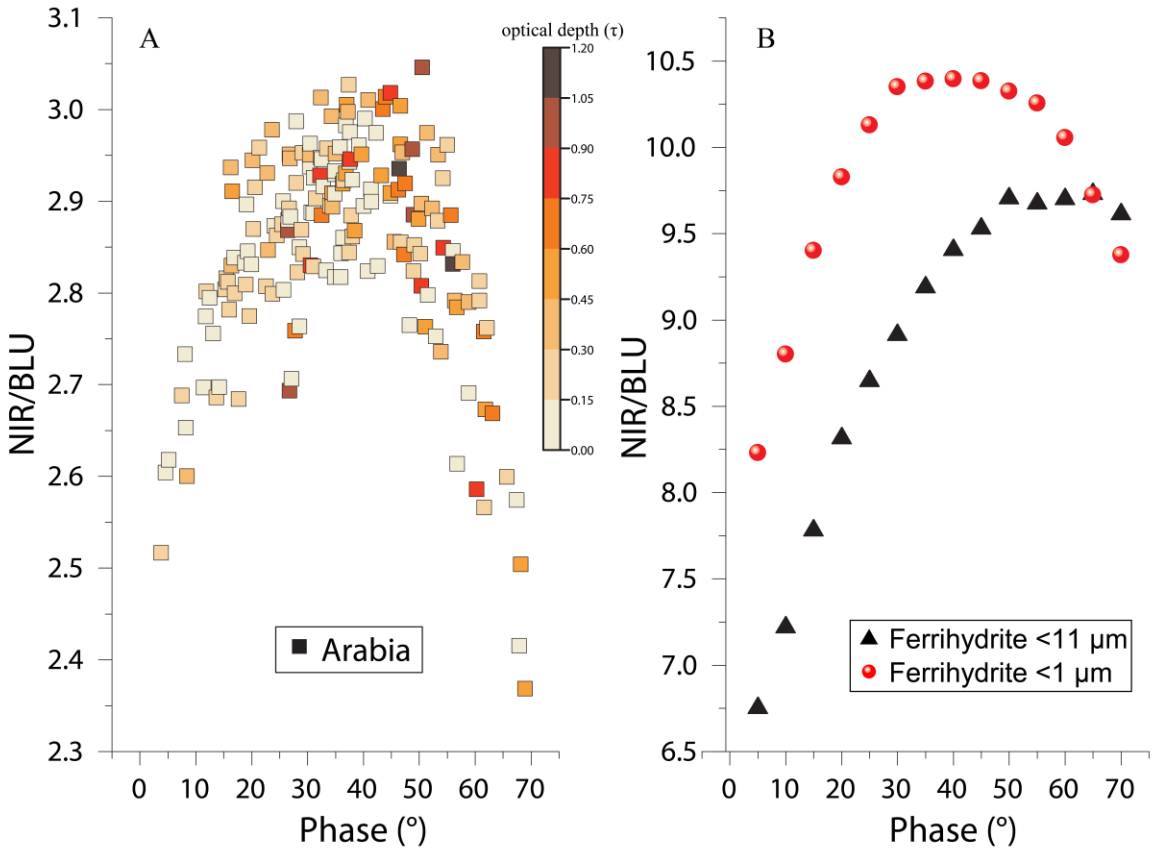

Figure 13. Phase reddening and bluing effect for (A) Arabia orbital observations and (B) laboratory measurements of sieved ferrihydrite size fractions. The <1-μm size fraction exhibits a more defined color ratio arch, which peaks at ~40° phase. The color ratio of dust in Arabia also contain a roll over point at 40°. These observations suggest that particle scale properties contribute to this phenomenon.

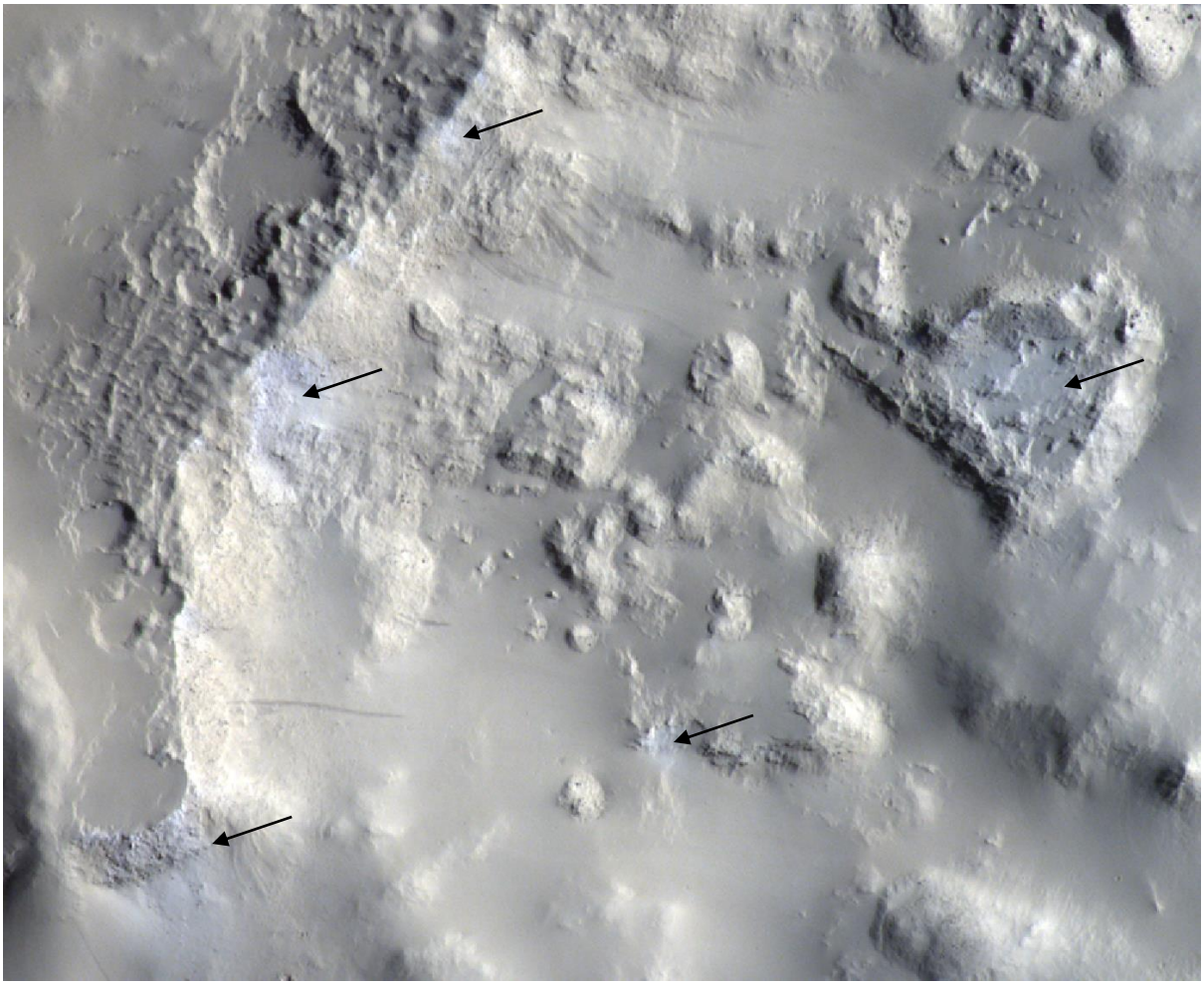

Figure 14. Light-toned bedrock exposures and mantling dust deposits in Arabia Terra. The arrows point to locations where fresh material is being eroded out of the bedrock and/or where dust has been removed. CaSSIS MY35_007117_163_0_NPB image.

Chapter 5:

CONCLUSIONS AND FUTURE WORK

Modern Mars is a cold, arid, and dry planet. These conditions might have persisted for billions of years (Wordsworth, 2016). While early in Mars' history liquid water may have been sustained, the hydrological cycle was significantly inhibited as the atmosphere was lost to space. This dramatic climate change transformed Mars into a desert planet with a surface dominated by aeolian processes. The planet's massive eroding geologic features provided ingredients for global dust storms that circulated and distributed dust all over the Martian surface. Erosion, combined with the transport of dust, produced several meters-thick deposits in the bright and dusty regions (Christensen, 1986). The top meter of dust in these regions is often punctured by dramatic km-scale slope streaks (Schorghofer et al., 2007). Chapter 2 presented evidence that these slope features instead of quickly being erased by airfall dust deposition, remain visible for several decades and even undergo brightness reversal due to the structural changes in their surfaces.

In addition to the dust cycle, Mars undergoes seasonal removal and deposition of CO_2 and H_2O ice within its polar caps (Neugebauer et al., 1971). While the polar caps are the main repositories of Martian volatiles, the midlatitude regions contain buried subsurface water ice (Holt et al., 2008) and are frequently covered by seasonal CO_2 and H_2O frost deposits (Vincendon et al., 2010). As shown in Chapter 3, small amounts of ephemeral CO_2 frost are observed to condense even in the tropical regions on the calderas of Martian volcanoes. Sublimation and condensation of CO_2 frost were predicted to cause the avalanching of slope streaks (Piqueux et al., 2016). Although there is plenty of dust and steep slopes on these volcano calderas, the absence of slope streaks in the regions where CaSSIS observed CO_2 frost precludes a positive correlation between the two processes. In conclusion, although the formation of slope streaks was discovered in the early days of the Viking mission (Morris, 1982), it nonetheless remains an enigmatic phenomenon.

In contrast to Mars' modern climate, the planet's early geologic epochs were dominated by an extensive hydrological cycle. This is marked by hundreds of channels that cross the region of Arabia Terra and empty into the northern lowlands (Davis et al., 2016). Arabia is highly eroded and battered by impacts, making it one of the oldest Martian terrains (Greeley & Guest, 1987). Evidence of sedimentary layers in craters within Arabia indicates that rising groundwater may have been present in the region (Grotzinger & Milliken, 2012). The Noachian age of Arabia (>3.8 Ga), together with the geomorphic evidence of water activity there, might explain the widespread spectrally neutral bedrock exposures shown in Chapter 4. If ferrihydrite-rich Martian dust is indeed derived from these rocks, it could be hypothesized that the bedrock in Arabia Terra was weathered under an oxygenated atmosphere. The cold and icy conditions required to form X-ray amorphous materials such as ferrihydrite (Rampe et al., 2022) may suggest a new class of alteration pathways. This in turn might expand the search for habitable environments - previously constrained only to phyllosilicate deposits - to much larger areas of Mars. Although on Earth amorphous materials are not found in old rocks and soils, such a paradox may be suggestive of unique climatic conditions in the early history of Mars.

Photosynthetic bias

Current and past NASA rover missions (e.g., in Gusev, Gale, and Jezero craters) have focused on the exploration of lacustrine and sedimentary environments partly because they are the most productive settings for investigating life throughout Earth's history (McMahon et al., 2018). However, this terra-centric strategy is predicated on the notion that life had enough time to develop photosynthesis on Mars (Michalski et al., 2018). On Earth, the first undebated evidence for photosynthetic life originates from ~3 Ga old rocks (Fournier et al., 2021). Yet by 3.0 Ga ago, Mars had probably already lost its standing bodies of water and was a cold, toxic, and arid

planet (Wordsworth et al., 2021). The surface was probably subjected to harmful cosmic radiation, resulting in a hostile environment for surface life. In the subsurface, by contrast, liquid water would have been stable, protected from the harsh surface environment. In addition, the abundant sources of chemical energy (Tarnas et al., 2021) would have made the subsurface the longest-lived habitable environment on Mars (Ehlmann et al., 2011; Tarnas, Morgan, et al., 2021). Since anaerobic microbial life in the Earth's subsurface developed earlier, more than 3.5 Ga ago (Wolfe & Fournier, 2018), this might indicate that life also had time to evolve on Mars before the surface conditions became inhospitable to life (Michalski et al., 2018).

On the floors of many craters in Arabia Terra, one can observe hundreds of erosionally resistant raised dykes. Morphologically they resemble polygonal ridges in the Nilosyrtis highlands and Nili Fossae (e.g., Fig. 1). Polygonal ridges have been proposed to be the result of hydrothermal processes and differential erosion (Bramble et al., 2017; Pascuzzo et al., 2019). Hydrothermal environments on Earth are known for their potential to host life (Dodd et al., 2017); therefore, these sites may serve as conduits that bring the deep Mars biosphere to the surface, presenting high astrobiological potential. These different types of hydrothermal environments found in the Noachian terrains could be potentially investigated in future work. Understanding the chemical weathering pathways and the subsurface environments may indicate the types of biosignatures present on Mars.

Since crustal recycling has destroyed most of the early geologic record on Earth, finding clues about the origin of life on Mars, a planet without plate tectonics, would also provide a window into our own history. The NASA-led Mars Sample-Return (MSR) mission will bring several samples back to Earth in the early 2030s (Kminek et al., 2021), which will provide vital clues on the origin of life on Mars. The Perseverance rover, at the time of writing, is sampling

the Jezero Crater delta and preparing an extensive sample cache to be returned by the MSR mission. After the primary campaign in Jezero Crater, Perseverance will head west to the surrounding plains of Nili Planum, informally known as the 'Midway' site (Simon et al., 2021). This region contains ~3.6 Ga old basement rocks predating the Jezero crater forming impact and contains evidence of ancient hydrothermal environments. Therefore, the sample collection of Perseverance will accommodate both the classic sedimentary settings, as well as novel subsurface life opportunities. Further research in this field may aid in one of humanity's key endeavors - the search for life beyond Earth.

References

Bramble, M. S., Mustard, J. F., & Salvatore, M. R. (2017). The geological history of Northeast Syrtis Major, Mars. *Icarus*, *293*, 66–93. https://doi.org/10.1016/j.icarus.2017.03.030

Christensen, P. R. (1986). Regional dust deposits on Mars: Physical properties, age, and history. *Journal of Geophysical Research: Solid Earth*, *91*(B3), 3533–3545. https://doi.org/https://doi.org/10.1029/JB091iB03p03533

Davis, J. M., Balme, M., Grindrod, P. M., Williams, R. M. E., & Gupta, S. (2016). Extensive Noachian fluvial systems in Arabia Terra: Implications for early Martian climate. *Geology*, *44*(10), 847–850. https://doi.org/10.1130/G38247.1

Dodd, M. S., Papineau, D., Grenne, T., Slack, J. F., Rittner, M., Pirajno, F., et al. (2017). Evidence for early life in Earth's oldest hydrothermal vent precipitates. *Nature*, *543*(7643), 60–64. https://doi.org/10.1038/nature21377

Ehlmann, B. L., Mustard, J. F., Murchie, S. L., Bibring, J.-P., Meunier, A., Fraeman, A. A., & Langevin, Y. (2011). Subsurface water and clay mineral formation during the early history of Mars. *Nature*, *479*(7371), 53–60. https://doi.org/10.1038/nature10582

Fournier, G. P., Moore, K. R., Rangel, L. T., Payette, J. G., Momper, L., & Bosak, T. (2021). The Archean origin of oxygenic photosynthesis and extant cyanobacterial lineages. *Proceedings of the Royal Society B: Biological Sciences*, *288*(1959), 1–10. https://doi.org/10.1098/rspb.2021.0675

Greeley, R., & Guest, J. E. (1987). Geologic map of the eastern equatorial region of Mars, Atlas of Mars. *USGS, Denver*.

Grotzinger, J. P., & Milliken, R. E. (2012, January 1). The Sedimentary Rock Record of Mars: Distribution, Origins, and Global Stratigraphy. (J. P. Grotzinger & R. E. Milliken, Eds.), *Sedimentary Geology of Mars*. SEPM Society for Sedimentary Geology. https://doi.org/10.2110/pec.12.102.0001

Holt, J. W., Safaeinili, A., Plaut, J. J., Head, J. W., Phillips, R. J., Seu, R., et al. (2008). Radar Sounding Evidence for Buried Glaciers in the Southern Mid-Latitudes of Mars. *Science*, *322*(5905), 1235–1238. https://doi.org/10.1126/science.1164246

Kminek, G., Meyer, M. A., Beaty, D. W., Carrier, B. L., Haltigin, T., & Hays, L. E. (2021). Mars Sample Return (MSR): Planning for Returned Sample Science. *Astrobiology*, *22*(S1), S-1-S-4. https://doi.org/10.1089/ast.2021.0198

McMahon, S., Bosak, T., Grotzinger, J. P., Milliken, R. E., Summons, R. E., Daye, M., et al. (2018). A Field Guide to Finding Fossils on Mars. *Journal of Geophysical Research: Planets*, *123*(5), 1012–1040. https://doi.org/https://doi.org/10.1029/2017JE005478

Michalski, J. R., Onstott, T. C., Mojzsis, S. J., Mustard, J., Chan, Q. H. S., Niles, P. B., & Johnson, S. S. (2018). The Martian subsurface as a potential window into the origin of life. *Nature Geoscience*, *11*(1), 21–26. https://doi.org/10.1038/s41561-017-0015-2

Morris, E. C. (1982). Aureole deposits of the Martian volcano Olympus Mons. *Journal of Geophysical Research: Solid Earth*, *87*(B2), 1164–1178. https://doi.org/https://doi.org/10.1029/JB087iB02p01164

Neugebauer, G., Münch, G., Kieffer, H., Chase Jr., S. C., & Miner, E. (1971). Mariner 1969 Infrared Radiometer Results: Temperatures and Thermal Properties of the Martian Surface. *The Astronomical Journal*, *76*, 719. https://doi.org/10.1086/111189

Pascuzzo, A. C., Mustard, J. F., Kremer, C. H., & Ebinger, E. (2019). The formation of irregular polygonal ridge networks, Nili Fossae, Mars: Implications for extensive subsurface channelized fluid flow in the Noachian. *Icarus*, *319*(October 2018), 852–868. https://doi.org/10.1016/j.icarus.2018.10.020

Piqueux, S., Kleinböhl, A., Hayne, P. O., Heavens, N. G., Kass, D. M., McCleese, D. J., et al. (2016). Discovery of a widespread low-latitude diurnal CO2 frost cycle on Mars. *Journal of Geophysical Research: Planets*, *121*(7), 1174–1189.

Rampe, E. B., Horgan, B. H. N., Smith, R. J., Scudder, N. A., Bamber, E. R., Rutledge, A. M., & Christoffersen, R. (2022). A mineralogical study of glacial flour from Three Sisters, Oregon: An analog for a cold and icy early Mars. *Earth and Planetary Science Letters*, *584*, 117471. https://doi.org/https://doi.org/10.1016/j.epsl.2022.117471

Schorghofer, N., Aharonson, O., Gerstell, M. F., & Tatsumi, L. (2007). Three decades of slope streak activity on Mars. *Icarus*, *191*(1), 132–140. https://doi.org/https://doi.org/10.1016/j.icarus.2007.04.026

Simon, J. ~I., Scheller, E. ~L., Holm-Alwmark, S., Benison, K. ~C., Bosak, T., Brown, A. ~J., et al. (2021). Characterizing the Stratigraphy of the Nili Planum Region Outside Jezero Crater: Implications for Mars 2020 Strategic Planning. In *52nd Lunar and Planetary Science Conference* (p. 1515).

Tarnas, J. D., Mustard, J. F., Sherwood Lollar, B., Stamenković, V., Cannon, K. M., Lorand, J.-P., et al. (2021). Earth-like Habitable Environments in the Subsurface of Mars. *Astrobiology*, *21*(6), 741–756. https://doi.org/10.1089/ast.2020.2386

Vincendon, M., Forget, F., & Mustard, J. (2010). Water ice at low to midlatitudes on Mars.

Journal of Geophysical Research: Planets, *115*(E10).

Wolfe, J. M., & Fournier, G. P. (2018). Horizontal gene transfer constrains the timing of methanogen evolution. *Nature Ecology & Evolution*, *2*(5), 897–903. https://doi.org/10.1038/s41559-018-0513-7

Wordsworth, R., Knoll, A. H., Hurowitz, J., Baum, M., Ehlmann, B. L., Head, J. W., & Steakley, K. (2021). A coupled model of episodic warming, oxidation and geochemical transitions on early Mars. *Nature Geoscience*, *14*(3), 127–132. https://doi.org/10.1038/s41561-021-00701-8

Wordsworth, R. D. (2016). The Climate of Early Mars. *Annual Review of Earth and Planetary Sciences*, *44*(1), 381–408. https://doi.org/10.1146/annurev-earth-060115-012355

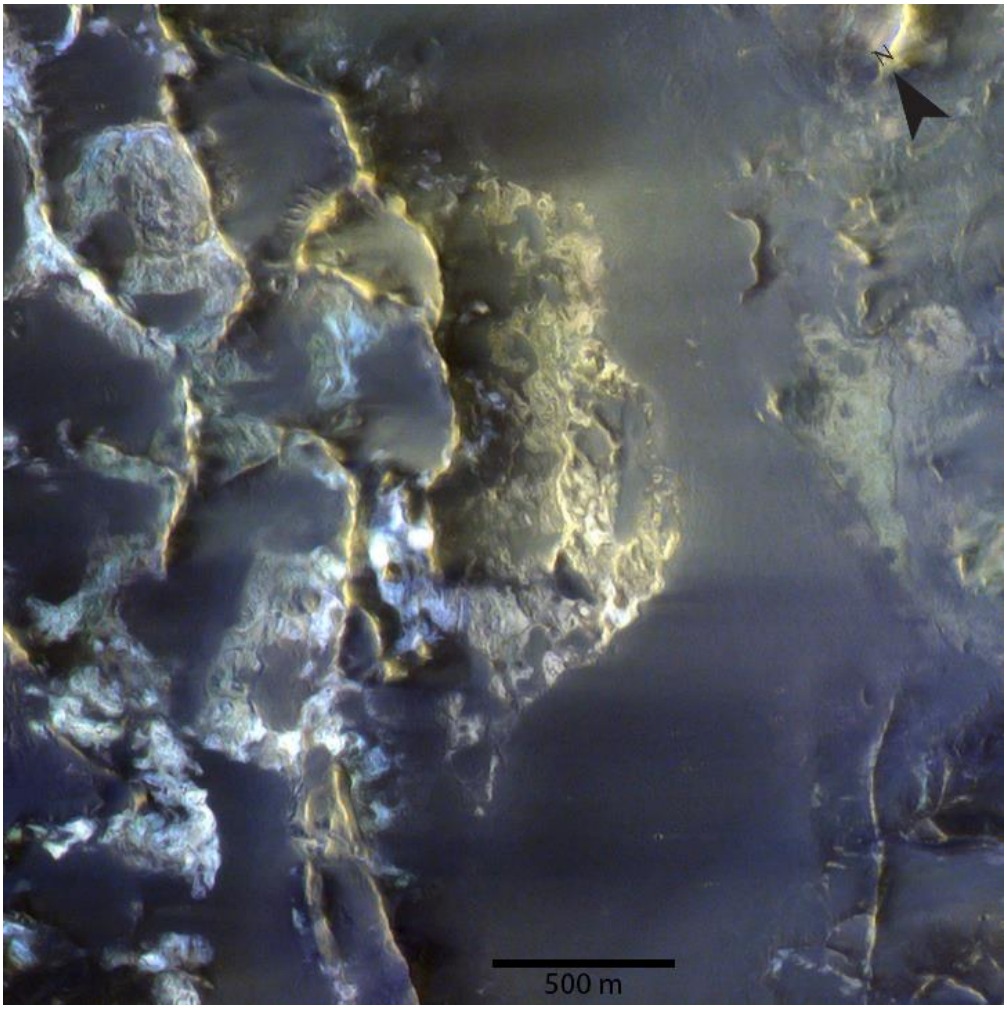

Figure 1. Erosionally exhumed polygonal ridges near Nili Planum. The plethora of colors here implies diverse mineralogy and the abundance of hydrated minerals possibly altered by hydrothermal activity in ancient Mars' past. CaSSIS false-color composite image (R = 940 nm, G = 677 nm, B = 497 nm).

APPENDIX A:

THE ORIGIN OF NEOTECTONICS ON THE LUNAR NEARSIDE

A. Valantinas[1] and P. H. Schultz[2]

[1]Physikalisches Institut, Universität Bern, Sidlerstrasse 5, 3012 Bern, Switzerland.
[2]Brown University, Department of Earth, Environmental, and Planetary Sciences, 324 Brook Street, Providence, Rhode Island 02912, USA.

Published in:

Geology

13 April 2020

Valantinas, A., and Schultz, P.H., 2020, Geology, v. 48, p. 649–653
https://doi.org/10.1130/G47202.1

ABSTRACT

New observations of wrinkle ridges on the nearside maria of the Moon display signs of ongoing ridge modification. In association with the wrinkle ridges we observe an absence of superposed craters, narrow (<30 m) lobate scarps and graben, and thermal anomalies related to exposures of meter-size blocks. Many of these active wrinkle-ridge systems are well beyond the influence of mascon basins and unrelated to any global tectonic pattern. Nevertheless, they spatially correlate with ancient deep-seated dike intrusions on the lunar nearside revealed by gravity data analysis. We propose that this Active Nearside Tectonic System (ANTS) reflects on-going reactivation of an ancient system related to offset antipodal effects from the South-Pole-Aitken Basin.

INTRODUCTION

Tectonic stresses surrounding lunar mare basins have been associated with either extensional graben or contractional wrinkle-ridges. Graben are known to have formed ~3.6 Ga ago (Lucchitta and Watkins, 1978), while wrinkle ridges remained active due to mass loading after the bulk of basaltic lava emplacement within mare-filled impact basins ~3 Ga ago (Solomon and Head, 1979). Other studies, using Lunar Orbiter images documented examples of narrow wrinkle ridges and lobate scarps in the highlands (away from the maria) that cross cut small (<250 m) craters well outside the influence of mass loading (Schultz, 1976; Binder and Gunga, 1985). They concluded that combined with the existence of narrow (<15 m) grabens, much more recent (<~0.1 Ga) contractional and extensional tectonics must be ongoing. The distinction between a narrow lobate scarp and wrinkle ridge is primarily found in the lithology and layering (Howard and Muehlberger, 1973; Schultz, 1976).

High-resolution global coverage by the Lunar Reconnaissance Orbiter Camera (LROC) now establishes that some lobate scarps and wrinkle ridges indicate activity as recently as ~1 Ga ago (Watters et al., 2010; Yue et al., 2017; Williams et al., 2019). Even younger ages have been inferred based on multiple approaches including cross-cutting relations, crater counts and exposed boulders (Schultz, 1976; Clark et al., 2017; van der Bogert et al., 2018; Valantinas et al., 2018, Valantinas and Schultz, 2018; French et al., 2019). Recently, Watters et al. (2019) proposed that the Moon is currently tectonically active, the expression of which lies in young highland thrust faults that would have formed in response to tidal stresses superimposed on global contraction and correlated with seismic activity based on their distribution beyond the maria. Here, we document active tectonic regions of wrinkle ridge assemblages on the lunar nearside maria using LRO (Lunar Reconnaissance Orbiter) global data sets (high-resolution imaging, topography, and thermal infrared) and propose one possible origin for their activity. Most of the wrinkle ridge systems are beyond the influence of mascon loading, and are unrelated to what would be expected solely from global contraction or tidal interactions. Because of their recent formation, we argue that these young ridges are part of an Active Nearside Tectonic System (ANTS).

OBSERVATIONS

The LRO Diviner radiometer data and high-resolution LRO Narrow Angle Camera (NAC) images allow the mapping of over 500 individual wrinkle ridge segments across the lunar nearside (see **Fig. 1a**) with varying degrees of rockiness. The majority of them correlate with deep seated intrusions discovered by the Gravity Recovery and Interior Laboratory (GRAIL) (**Fig. 1b**) (Andrews-Hanna, 2014). The widespread abundance of boulders on wrinkle ridges can be clearly observed in Diviner rock abundance maps (Bandfield et al., 2011). The fractional area covered by

lunar boulders is illustrated in **Fig. 2a** for southern Oceanus Procellarum (for the whole nearside see **Fig. DR2**). These rock abundance maps allow characterization of rocky wrinkle ridges into three qualitative categories: low, medium and high (shown in white, orange and red in **Fig. 1a**). To quantify these categories, we select 12 representative wrinkle ridges (see Table 1) and use high-resolution NAC images to measure their boulder patch areal density (total area of the boulder patches along the wrinkle ridge divided by ridge length). The calculated values are: <0.05 for low, ~0.05 – 0.1 for medium and ~0.1 – 0.26 for high rock abundance. There is a bias against ridges exposing highland materials with fewer boulders as well as unresolved by the Diviner instrument (yet still active) smaller scale systems. Boulder-topped ridges do not only occur along the margins of mascon-loaded impact basins (e.g., Serenitatis, Imbrium, Humorum, Crisium), but also in regions with very thin mare fill and very small gravity anomalies (Procellarum, Frigoris). Conversely, boulder-topped ridges are poorly expressed in the mare-filled Nectaris and Imbrium basins that have large Bouguer gravity anomalies indicative of significant mascon loading.

Individual exposed boulder patches vary from a few meters to several hundreds of meters in size and form continuous regions or break into several segments along the wrinkle ridge (**Fig. 2b**). The boulders that comprise these outcrops range in size from just below the resolution limit of the NAC (~0.5 m/px) to ~10 m in diameter. Some patches are covered with a thin regolith layer, whereas others have little to no regolith cover, which seems to indicate ongoing exhumation at very small scales. In some cases, during exhumation the removed regolith accumulates at the bottom of the wrinkle ridge slopes and in between individual outcrops (**DR1**).

Boulder fields in the lunar maria are rare, except along steep walls of craters or rilles due to ongoing mass wasting. Recent impacts also can excavate competent bedrock from beneath the regolith and distribute boulders across the surface (Ghent et al, 2014). In both cases, the

continuous impact bombardment gradually breaks down the boulders or buries them beneath mobilized regolith (ejecta or talus). This means that the transition from steep blocky crater walls to relatively smooth gradual slopes is a proxy for relative age. Preservation of blocky crater ejecta, whether recognized in high-resolution images or expressed as nighttime thermal anomalies, can also be used to establish a relative age (e.g., Ghent et al., 2014). Similarly, the occurrence of boulders associated with wrinkle ridges, and the boulder field area along a ridge can be related to recent activity.

We observe boulder patches on both high (20° – 30°) and low-slope (<10°) topography close to the ridges (e.g. **Fig. 2b & 2c**). In some cases, boulder fields occur on top of wrinkle ridges with slopes as low as 2° slopes, rather than as a talus along an abrupt break in slope (**Fig. 2d & 3a, b, c, d & DR3**). Because boulder tracks are uncommon on these regolith piles, most boulders along these ridges are immobile or the local slopes are too low for boulders to roll downhill in response to seismic activity. Small graben on top of some wrinkle ridges require a component of extensional flexure during the recent thrust faulting as the fault reaches the surface (**DR4**).

DISCUSSION

High rock abundances on wrinkle ridges, such as those seen in Diviner and NAC images, require recent tectonic activity. Boulder-size distributions in ejecta around young craters of known ages indicate complete rock destruction in 300 Ma (Basilevsky et al., 2013). This result qualitatively agrees with the general Diviner rock abundance dataset (Ghent et al., 2014). However, on many ridges, the cluster of numerous boulders with minimal accumulations of regolith implies an age < 26 Ma (Basilevsky et al., 2013). The absence of small craters on the boulder patches presented in

our study further indicates that these features are geologically young and are forming faster than eroded via meteorite bombardment. Low small crater abundances on select wrinkle ridges with boulder-free ridge areas have been shown to imply surface ages of <10 Ma in Mare Humorum (Valantinas et al., 2018; see also Williams et al., 2019 for ridges in Frigoris).

The origin of boulder-topped ridges requires either that the rate of boulder exposure exceeds the rate of downslope movement and subsequent regolith development or that the regolith be removed by some process. As an example of the former, an elephant-hide texture (Gold, 1972; Schultz, 1976) has been attributed to downslope mass wasting and occurs on numerous ridges (even without exposed boulders). As for regolith removal, the presence of closely packed boulders on flat surfaces implies that the rate of boulder exposure must be high (and ongoing). Otherwise, meteoritic bombardment would have generated a narrow accumulation of debris around each boulder, and boulders would occur in isolation. Boulder fields on flat regions on top of a ridge may represent an exposed bedrock layer. When layered mare basalts buckled during sudden episodes of uplift (or after reaching a critical state), the regolith may have drained into small fractures and voids below. Layered basalts would then be expected since emplacement likely occurred in a succession of thin (~10 m) flows billions of years ago (Schaber et al., 1976). A broken layer from cooling or proto-regolith development likely forms in between basalt flows. The existence of blocky surfaces on low-slope surfaces requires ongoing processes that continuously expose the substrates (French et al., 2019).

Four models have been proposed to account for lunar tectonics: 1) subsidence due to mascon loading within impact basins (Melosh, 1978; Solomon and Head, 1979), 2) orbital recession and despinning (Melosh, 1977; Melosh, 1980), 3) global contraction (Solomon and Chaiken, 1976), and 4) Earth-raised solid body tides (Watters et al., 2015). The first process cannot account for the

distribution of active ridges well beyond impact basins and within relatively thin sequences of mare basalts, e.g., Oceanus Procellarum (**Fig. 1a**). In the second model, orbital recession and despinning of a synchronously rotating planet should create global stresses in the lithosphere. This model predicts a distinct fault pattern: contractional N-S striking thrust faults in an area of 30° latitude and longitude at the sub-Earth point and its antipode; a system of strike-slip faults outside of this area; and extensional E-W oriented normal faults at the polar regions. This pattern is inconsistent with the Procellarum system. While despinning alone might account for the global distribution of small lobate scarps in the lunar highlands (Watters et al., 2015), such a mechanism cannot explain the localization and the NW orientation of active wrinkle ridge systems in the SW Procellarum (e.g. Fig. 2). The third model states that global contraction due to cooling of the interior should result in horizontally isotropic compressional stress that produce uniformly distributed thrust faults with random orientations. This pattern is also inconsistent with the orientations of small lobate scarps (Watters et al., 2015) and the distribution of wrinkle ridges shown here. Finally, diurnal tidal stresses due to Earth-generated during lunar librations are too low (Weber et al., 2009). Watters et al. (2019) recently proposed that a mechanism combining orbital recession and de-spinning with Earth-generated tides could account for the distribution of shallow moonquakes. Nonetheless, this mechanism alone also cannot account for the ridge/graben system of Procellarum.

Active ridge formation beyond the effects of impact basin loading (see **DR5**) requires a mechanism other than mascon-controlled sagging. The Active Nearside Tectonic System, ANTS (**Fig. 1b)** could be the surface expression of ongoing reactivated faults, which spatially correlate with the deep seated ancient intrusions discovered by GRAIL (Andrews-Hanna et al., 2014). That study proposed that these intrusions could have been responsible for PKT volcanism ~3.51 Ga

ago, but were closed off due to load-induced flexure and contraction of the upper lithosphere. According to the model, these intrusions formed long ago and are no longer active therefore it does not explain the origin of recent and ongoing deformation of wrinkle ridges following the ANTS. While those authors also suggested that wrinkle ridges may be surface manifestations of these ancient intrusions, there was no explanation for the disparity in ages. During a period of global extension (in response to increased radiogenic heating around 4 Ga), however, intrusions would have followed pre-existing structural weaknesses and would have controlled the conduits expressed by the source regions of sinuous rilles located on the crests of wrinkle ridges (e.g., Herigonius region in southern Procellarum), unrelated to basin loading by mascons. In fact, the level of ongoing tectonic activity along ridges expressed by blocky exposures within Procellarum and Frigoris, where mascon loading is absent, is comparable to mascon-loaded regions of Serenitatis and Humorum.

Two underlying processes could be controlling current wrinkle ridge activity. First, the nearside lunar lithosphere could still be adjusting to an ancient "Procellarum Basin" that shaped the lunar nearside and resulted in a radial/concentric tectonic pattern and nearside geochemical anomalies (Cadogan, 1974; Whitaker, 1981). However, Andrews-Hanna et al. (2014) argue that the GRAIL geophysical record is inconsistent with such a basin. Alternatively, Schultz and Crawford (2011) proposed that nearside tectonics reflect much later reactivation of faults related to deep transient stresses generated by the South-Pole-Aitken (SPA) basin about 4.3 Ga. In this model, the proposed trajectory of the SPA impactor is oblique, based on the shape of its relict rim massifs, asymmetric exposure of KREEP materials, and expected collapse during a large oblique impact. Both experiments and shock-physics models indicated antipodal failure occurs due to extension conditions deep within a spherical body. Introduction of thermal conditions and self-gravity into

the model revealed that antipodal extensional failure extended nearly to the core/mantle interface, while deep-seated failure occurred within the mantle and crust. Rather than occurring directly opposite the center of the SPA, the predicted damage is expected to be opposite of the region of first contact by the SPA impactor. This region corresponds to a broad, low-relief dome southwest of the Imbrium basin that centers on a system of radial and concentric graben and wrinkle ridges (e.g. **DR6**). Schultz and Crawford (2011) postulate that the nearside concentration of mare basalts, geochemical anomalies and tectonic systems were all controlled by the offset-antipodal effects of SPA.

Boulder capped wrinkle ridge systems observed as thermal anomalies in Diviner data and as morphologic evidence in LROC NAC images (see also French et al., 2019) require a currently active tectonic process to explain their origin in the lunar nearside maria. Orientations and distributions of these active ridges do not match the ones predicted by other mechanisms (e.g. despinning, global contraction and Earth-raised solid body tides), but match with GRAIL intrusions and SPA-induced damage features. Activity could be sustained by continued fault adjustments over these deep-seated intrusions. The Apollo seismometers may have recorded signs of these adjustments within currently occurring moonquakes (Nakamura et al., 1982). While shallow moonquakes may correlate with the combined effects of Earth-generated tides and global contraction (Watters et al., 2019), deep moonquakes require a different origin. Zhao et al. (2012) note that deep nearside moonquakes may reflect mantle heterogeneity, and Frolich and Nakamura (2009) argue that deep moonquakes occur in regions where brittle fracture is not possible. Hence, they may reflect movement of liquid phases or partial melts in the mantle that fill cracks or are tidally pumped into properly oriented shear zones. These deep moonquakes could be related to conditions initiated by the SPA collision.

Wrinkle ridges should thus be a target of interest for future exploration of lunar seismicity and sample collection. Exposed boulders on wrinkle ridges contain the original *in-situ* bedrock material of lunar basalts, which was not available for Apollo astronauts. The identification of young tectonic features indicative of ongoing moonquakes (Kumar et al., 2016; Watters et al., 2019) speak to the need for a global geophysical network (NRC, 2011). This would increase our understanding of the intensity, frequency and risks of the current seismic activity.

REFERENCES CITED

Andrews-Hanna, et al., 2014, Structure and evolution of the lunar Procellarum region as revealed by GRAIL gravity data: Nature, v. 514, p. 68–71, doi:10.1038/nature13697.

Bandfield, J. L., Ghent, R. R., Vasavada, A. R., Paige, D. A., Lawrence, S. J., and Robinson, M. S., 2011, Lunar surface rock abundance and regolith fines temperatures derived from LRO Diviner Radiometer data: Journal of Geophysical Research, v. 116, E00H02, doi:10.1029/2011JE003866.

Basilevsky, A. T., Head, J. W., and Hörz, F., 2013, Survival times of meter-sized boulders on the surface of the Moon: Planetary and Space Science, v. 89, p. 118-126, doi:10.1016/j.pss.2013.07.011.

Binder, A. B., and Gunga, H.-C., 1985, Young thrust-fault scarps in the highlands: Evidence for an initially totally molten Moon: Icarus, v. 63, p. 421-441, doi:10.1016/0019-1035(85)90055-7.

Cadogan, P. H., 1974, Oldest and largest lunar basin?: Nature, v. 250(5464), p. 315-316, doi:10.1038/250315a0.

Clark, J. D., Hurtado, J. M., Hiesinger, H., van der Bogert, C. H., and Bernhardt, H., 2017, Investigation of newly discovered lobate scarps: Implications for the tectonic and thermal evolution of the Moon: Icarus, v. 298, p. 78-88, doi:10.1016/j.icarus.2017.08.017.

French, R. A., Watters, T. R., and Robinson, M. S., 2019, Provenance of Block Fields Along Lunar Wrinkle Ridges: Journal of Geophysical Research: Planets, 124, 2970-2982, doi: 10.1029/2019JE006018.

Frolich, C., and Nakamura, Y., 2009, The physical mechanisms of deep moonquakes and intermediate earthquakes: How similar and how different? Physics of the Earth and Planetary Interiors, v. 173, p. 365-374, doi:10.1016/j.icarus.2017.08.017.

Ghent, R. R., Hayne, P. O., Bandfield, J. L., Campbell, B. A., Allen, C. C., Carter, L. M., and Paige, D. A., 2014, Constraints on the recent rate of lunar ejecta breakdown and implications for crater ages: Geology, v. 42, p. 1059-1062, doi:10.1130/G35926.1.

Gold, T., 1972, Erosion, Transportation and the Nature of the Maria: The Moon, International Astronomical Union, 47, 55-67, doi:10.1017/S0074180900097424.

Howard, K. A., and Muehlberger, W. R., 1973, Lunar thrust faults in the Taurus-Littrow region: In Apollo 17 Preliminary Science Report, NASA SP-330, 31-22.

Kumar, P. S., et al., Recent shallow moonquake and impact triggered-boulder falls on the Moon: new insights from the Schrodinger basin: JGR: Planets, v. 121, p. 147-179, doi:10.1002/ 2015JE004850.

Lucchitta, B. K., and Watkins, J. A., 1978, Age of graben systems on the moon, in Proceedings, Ninth Lunar Science Conference, Houston, Texas, 13–17 March: New York, Pergamon Pres, p. 3459-3472.

Melosh, H. J., 1977, Global Tectonics of a Despun Planet: Icarus, v. 31, p. 221-243, doi:10.1016/0019-1035(77)90035-5.

Melosh, H. J., 1978, The tectonics of mascon loading, in: Proceedings, Ninth Lunar Science Conference, Houston, Texas, 13–17 March: New York, Pergamon Pres, p. 3513-3525.

Melosh, H. J., 1980, Tectonic patterns on a tidally distorted planet: Icarus, v. 43, p. 334–337, doi: 10.1016 /0019-1035(80)90178-5.

Nakamura, Y., Latham, G. V., and Dorman, H. J., 1982, Apollo Lunar Seismic Experiment—Final summary: Journal of Geophysical Research, v. 87, p. A117-A123, doi:10.1029/JB087iS01p0A117.

National Research Council, 2011, Vision and Voyages for Planetary Science in the Decade 2013–2022: National Academies Press, Washington DC.

Schaber, G. G., Boyce, J. M., and Moore, H. J., 1976, The scarcity of mappable flow lobes on the lunar maria: Unique morphology of the Imbrium flows, in: Proceedings, Seventh Lunar Science Conference, Houston, Texas, 15–19 March: New York, Pergamon Press, p. 2783-2800.

Schultz, P. H., 1976, Moon Morphology: Austin, University of Texas Press, Austin.

Schultz, P. H., and Crawford, D. A., 2011, Origin of nearside structural and geochemical anomalies on the Moon, in Ambrose, W.A., and Williams, D.A., eds., Recent Advances and Current Research Issues in Lunar Stratigraphy: Geological Society of America Special Paper 477, p. 141–159, doi:10.1130/2011.2477(07).

Solomon, S. C., and Chaiken, J., 1976, Thermal expansion and the thermal stress in the Moon and terrestrial planets: Clues to early thermal history, in: Proceedings, Seventh Lunar Science Conference, Houston, Texas, 15–19 March: New York, Pergamon Press, p. 3229-3243.

Solomon, S. C., and Head, J. W., 1979, Vertical movement in mare basins: Relation to mare emplacement, basin tectonics, and lunar thermal history: Journal of Geophysical Research, v. 84, p. 1667–1682, doi:10.1029/JB084iB04p01667.

Valantinas, A., Kinch, K. M., and Bridžius, A., 2018, Low crater frequencies and low model ages in lunar maria: Recent endogenic activity or degradation effects? Meteorit. Planet. Sci, 53: 826-838. doi:10.1111/maps.13033.

Valantinas, A., and Schultz, P. H., 2018, Neotectonics on the Lunar Nearside: 49th Lunar and Planetary Science Conference, Houston, Texas, Abstract #2385.

van der Bogert, C. H., Clark, J. D., Hiesinger, H., Banks, M. E., Watters, T. R., and Robinson, M. S., 2018, How old are lunar lobate scarps? 1. Seismic resetting of crater size-frequency distributions: Icarus, v. 306, p. 225-242, doi:10.1016/j.icarus.2018.01.019.

Watters, T. R., et al., 2010, Evidence of recent thrust faulting on the Moon revealed by the Lunar Reconnaissance Orbiter Camera: Science, v. 329, p. 936–940, doi:10.1126 /science.1189590.

Watters, T. R., Robinson, M. S., Collins, G. C., Banks, M. E., Daud, K., Williams, N. R., and Selvans, M. M., 2015, Global thrust faulting on the Moon and the influence of tidal stresses: Geology, v. 43, p. 851-854, doi:10.1130/G37120.1.

Watters, T. R., Weber, R. C., Collins, G. C., Howley, I. J., Schmerr, N. C., and Johnson, C. L., 2019, Shallow seismic activity and young thrust faults on the Moon: Nature Geoscience, v. 12, p. 411-417, doi:10.1038/s41561-019-0362-2

Weber, R. C., Bills, B.G., and Johnson, C. L., 2009, Constraints on deep moonquake focal mechanisms through analyses of tidal stress: Journal of Geophysical Research, v. 114, E05001, doi:10.1029/2008JE003286.

Whitaker, E. A., 1981, The lunar Procellarum basin, in Schultz, P. H., and Merrill, R. B., eds., Multi-Ring Basins: Formation and Evolution, in: Proceedings of the Lunar and Planetary Science Conference: New York and Oxford, Pergamon Press, p. 105–111.

Wilhelms, D.E., 1987, Geologic History of the Moon: U.S. Geological Survey Professional Paper 1348, p. 302.

Williams, N. R., Bell, J. F. III, Watters, T. R., Banks, M. E., Daud, K., and French, R. A., 2019, Evidence for recent and ancient faulting at Mare Frigoris and implications for lunar tectonic evolution: Icarus, 326, p. 151-161, doi:10.1016/j.icarus.2019.03.002

Yue, Z., Michael, G. G., Di, K., and Liu, J., 2017, Global survey of lunar wrinkle ridge formation times: Earth and Planetary Science Letters, v. 477, p. 14-20, doi:10.1016/j.epsl.2017.07.048.

Zhao, D., Arai, T., Liu, L., and Ohtani, E., 2012, Seismic tomography and geochemical evidence for lunar mantle heterogeneity: Comparing with the Earth, Global and Planetary Change v. 90-91, 29-36, doi:10.1016/j.gloplacha.2012.01.004.

ACKNOWLEDGEMENTS

This work was funded by Universität Bern and used the support of the Northeast Planetary Data Center (Brown University).

Table 1. Representative cases of the three rockiness categories of wrinkle ridges observed in this study.

ID	Location/ Coordinates (lat, lon)	Category	Length of the ridge segment (km)	Area of boulder patches (km^2)	Area density (boulder patch area / ridge length)	NAC IDs
H1	N. Mare Humorum (-19.78, -39.59)	High	13.49	2.00	0.1483	M183781901LC M183781901RC M1206265050LC
H2	E. Mare Humorum (-23.58, -33.52)	Medium	11.72	0.76	0.0649	M1106146286LC
H3	E. Mare Humorum (-26.01, -35.46)	Low	11.81	0.23	0.0192	M127164712RC M1096730387LC
P1	Oceanus Procellarum (-11.25, -37.96)	High	16.88	4.34	0.2568	M1152107657RC M1152107657LC M1206258182RC
P2	Oceanus Procellarum (12.39, -56.08)	Medium	14.78	0.98	0.0660	M104884367LC
P3	Oceanus Procellarum (-13.76, -36.32)	Medium	15.75	1.05	0.0667	M1215661122RC M1215661122LC
P4	Oceanus Procellarum (-10.72, -38.75)	Low	16.48	0.41	0.0251	M190851652RC M1139165661RC M1154470943LC
P5	Oceanus Procellarum (-6.20, -45.34)	High	20.19	2.74	0.1358	M1123888973LC M1139208249LC
P6	Oceanus Procellarum (-2.28, -34.8)	Low	8.04	0.20	0.0247	M1190941117LC
S1	E. Mare Serenitatis (25.09, 28.97)	High	16.30	1.98	0.1214	M1197569085RC M1197583152RC
S2	E. Mare Serenitatis (26.63, 29.30)	Low	12.74	0.40	0.0316	M1129289908LC
S3	E. Mare Serenitatis (20.31, 23.84)	Medium	19.00	1.79	0.0942	M1175254780RC M1175254780LC

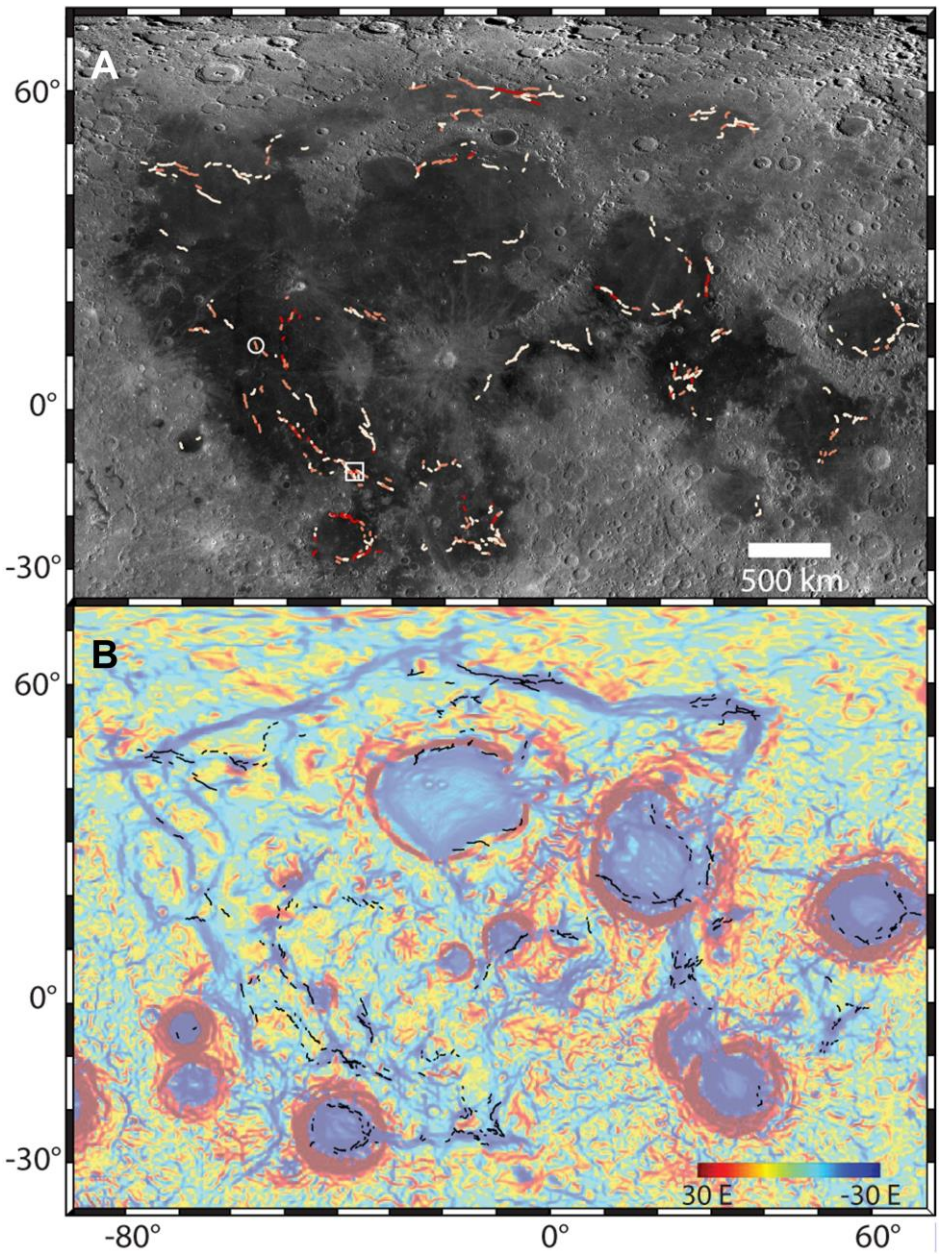

Figure 1. A global map of lunar wrinkle ridge segments exhibiting boulder abundance distributions, which make up the Active Nearside Tectonic System (ANTS). (a) LRO Wide Angle Camera (WAC) mosaic. Circle denotes the location of Fig 2 and the square the location of Fig 3. Abundances are marked from red to white in decreasing concentration. (b) GRAIL gravity gradients (Andrews-Hanna et al., 2014) in units of Eötvös (1 E= $10^{-9}s^{-2}$) with wrinkle ridges from this study overlain as black lines.

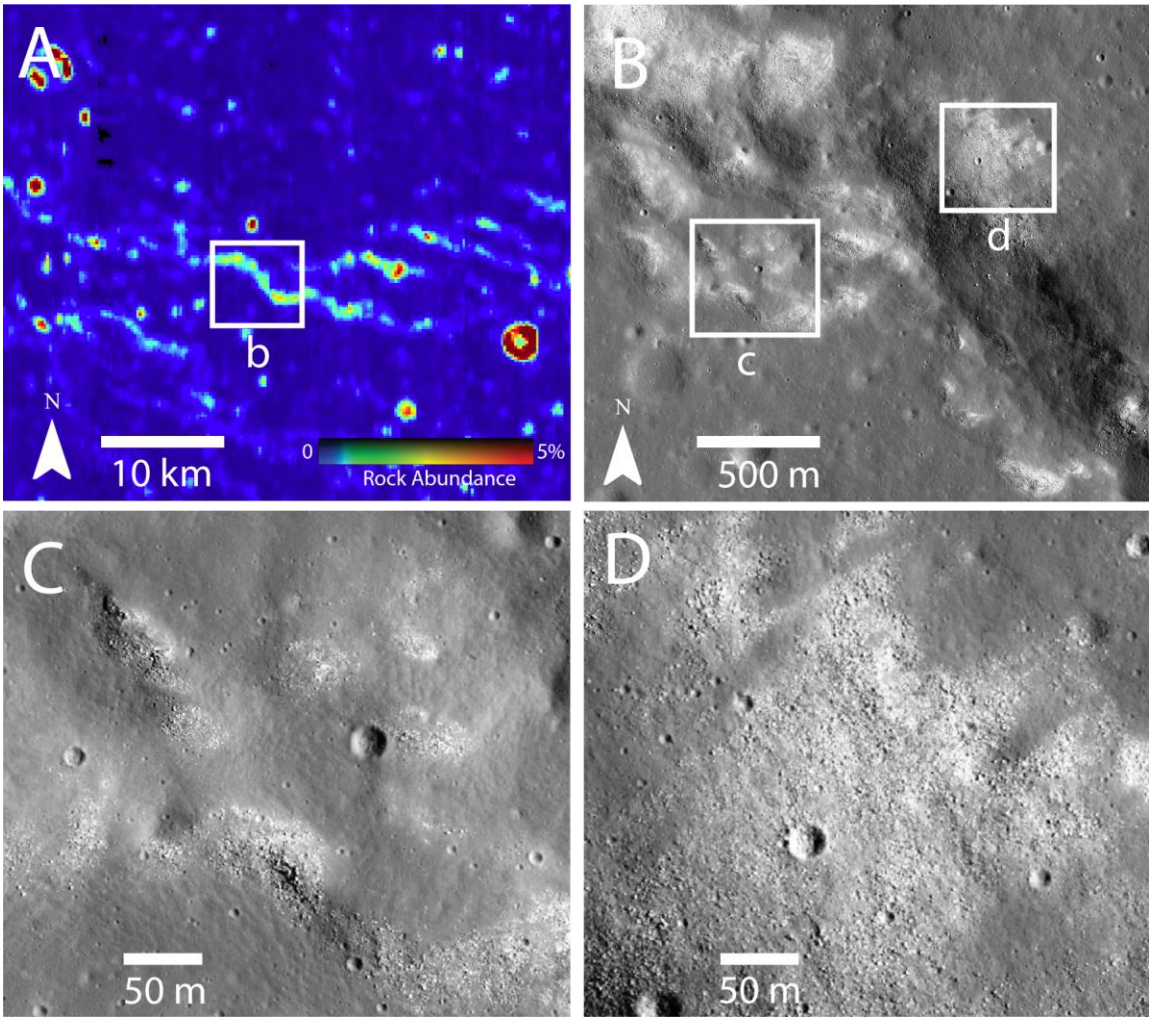

Figure 2. (a) Wrinkle ridge with very high rock abundances in southern Oceanus Procellarum. (b) Close up of the same ridge. (c) Rocky area on top of the ridge. (d) Small boulder patches outside of the ridge (Coords: -11.27, -37.92). NAC frame M160200185RC.

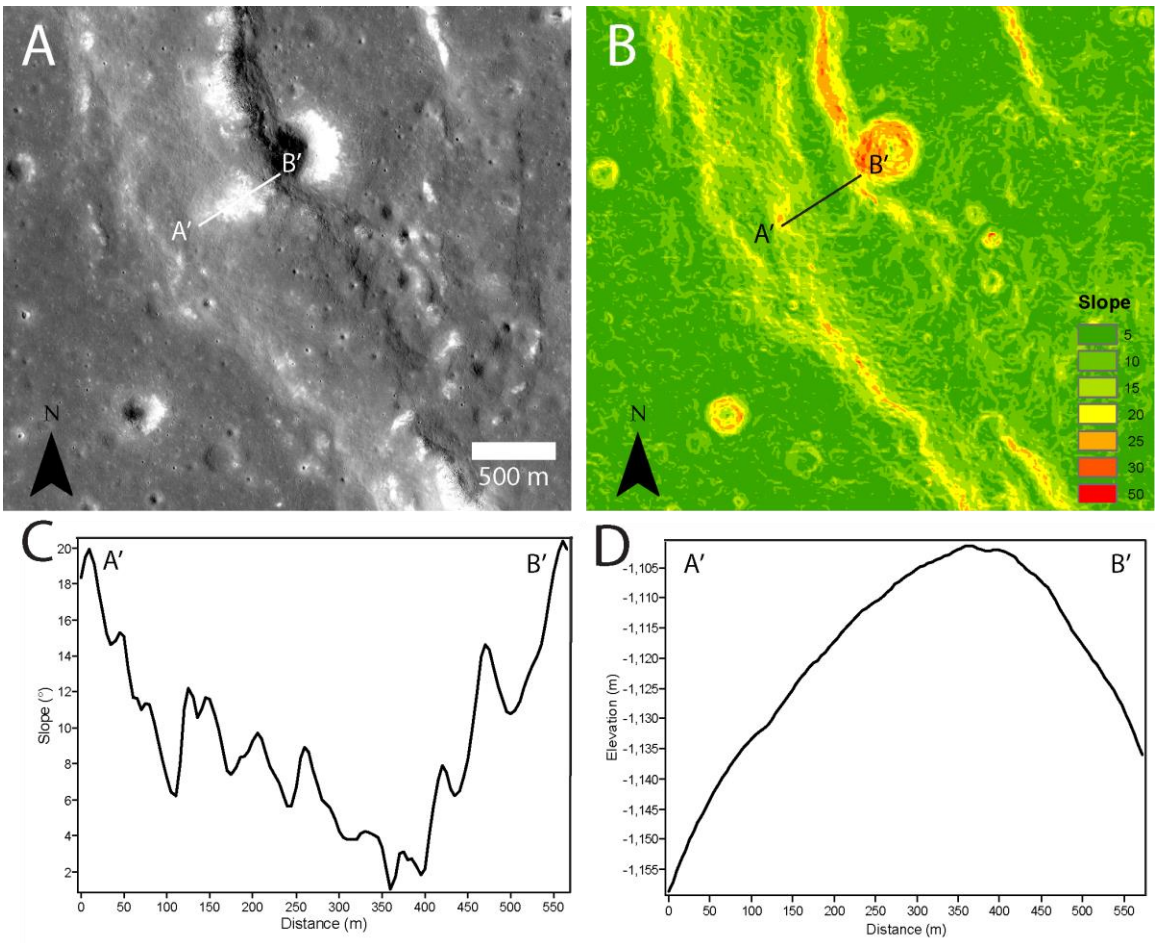

Figure 3. (a) LRO NAC image showing a wrinkle ridge segment in Oceanus Procellarum. (b) LROC NAC Digital Terrain Model (DTM) of the same area. (c) Slope profile of a boulder field, denoted by the A' to B' transect in (a) and (b). (d) Elevation profile of a boulder field, denoted by the A' to B' transect in (a) and (b). Boulder fields are commonly observed on slopes of wrinkle ridges but also can form on relatively flat terrains (slopes <10 degrees). Note small boulder patches on the southeastern part of the image, which appear to be on very gentle slopes.

Supplemental Information (DR1-DR5)

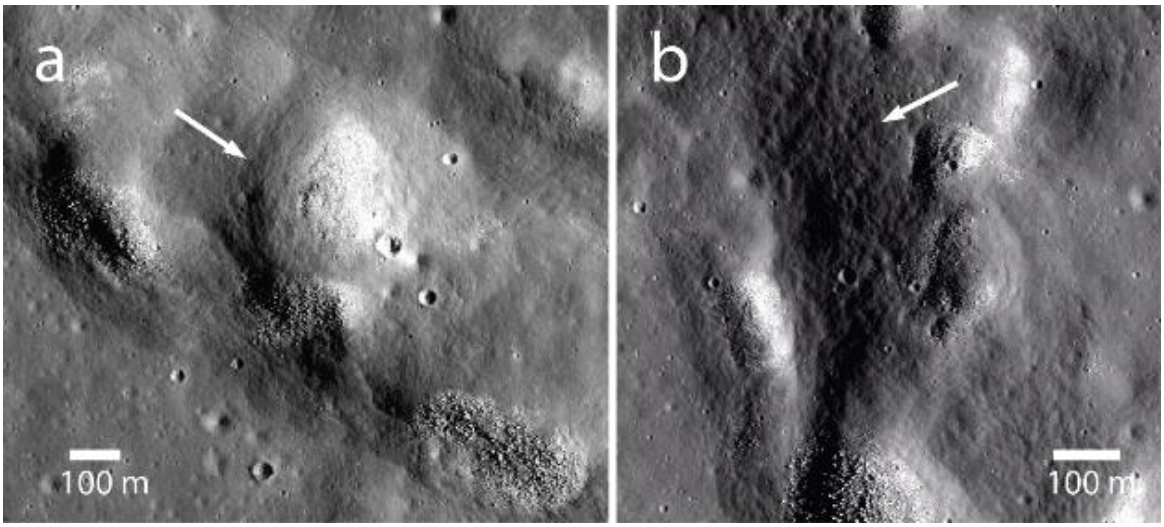

Figure DR1. Boulder patches on wrinkle ridges in Oceanus Procellarum (a, b) (Coordinates respectively: -6.53, -45.17; -6.34, -45.28). Regolith piles expressed as an "elephant hide" pattern occurs around the boulder patches (white arrows), consistent with ongoing mass movement (Gold, 1972; Schultz, 1976).

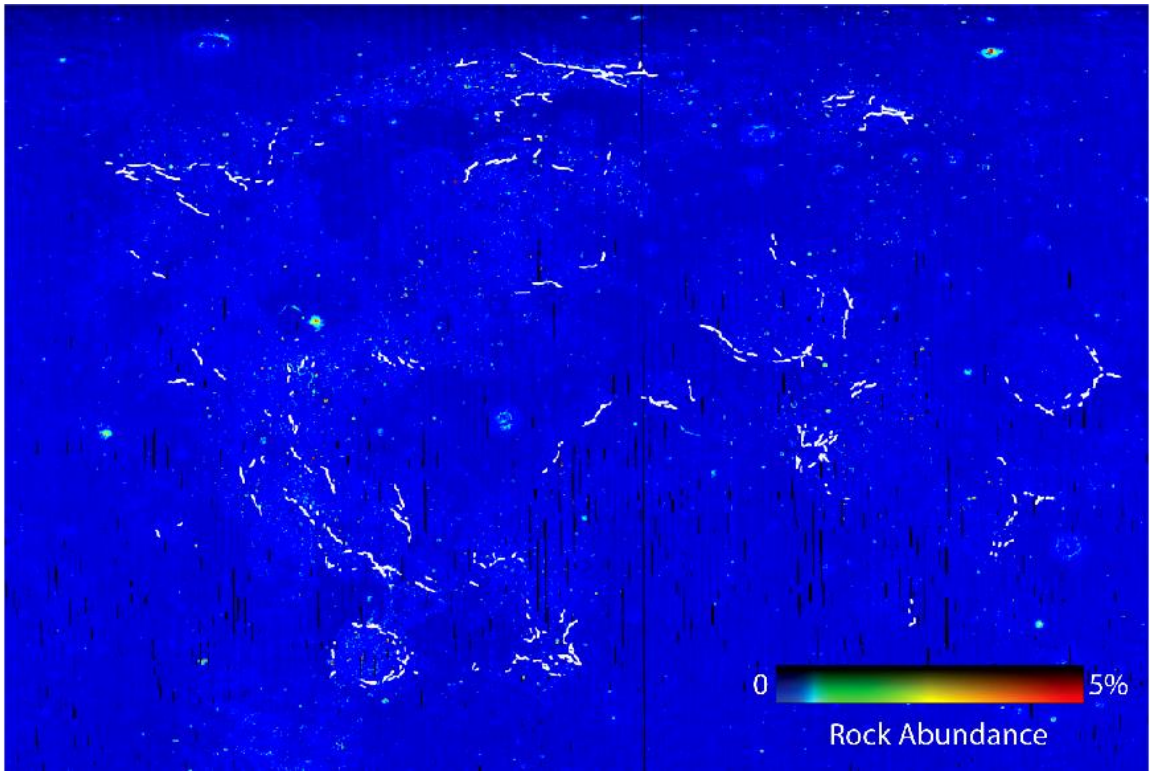

Figure DR2. Rock abundance map (Bandfield et al., 2011) with wrinkle ridges from this study overlain as white lines. Rock abundance map can be viewed with: https://quickmap.lroc.asu.edu/.

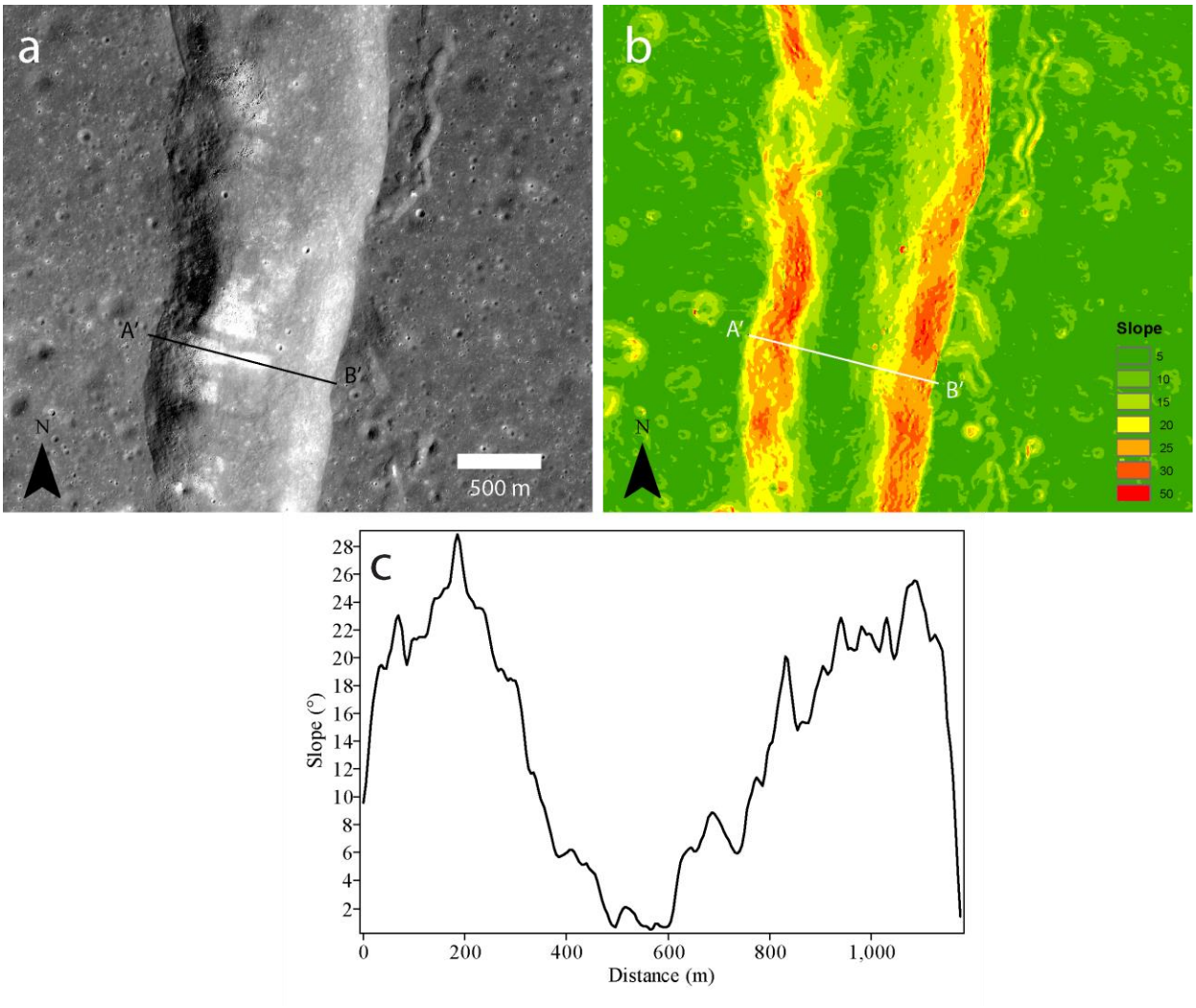

Figure DR3. A) LRO NAC image showing a wrinkle ridge segment in Eastern Mare Serenitatis and b) a Digital Terrain Model (DTM) of the same area. A' to B' denotes the slope profile of a boulder field shown in c). Bright patches of boulders occur on top of surfaces with high and low slopes.

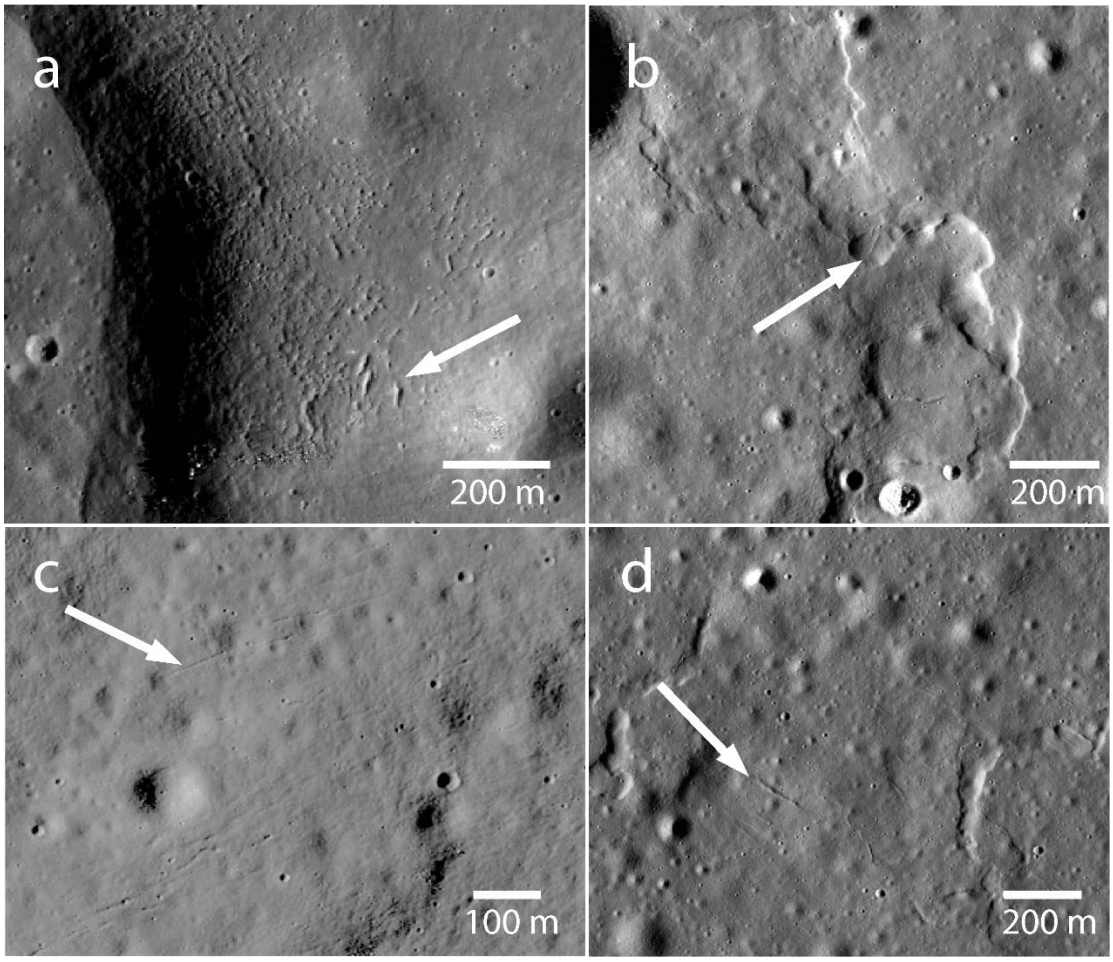

Figure DR4. Small fractures and graben (white arrows) observed on top (a,b) and on the sides (c,d) of wrinkle ridges in Mare Serenitatis and Oceanus Procellarum respectively (coordinates in order: 24.71, 28.99; -25.64, -35.12; -27.06, -37.18; -25.52, -35.16).

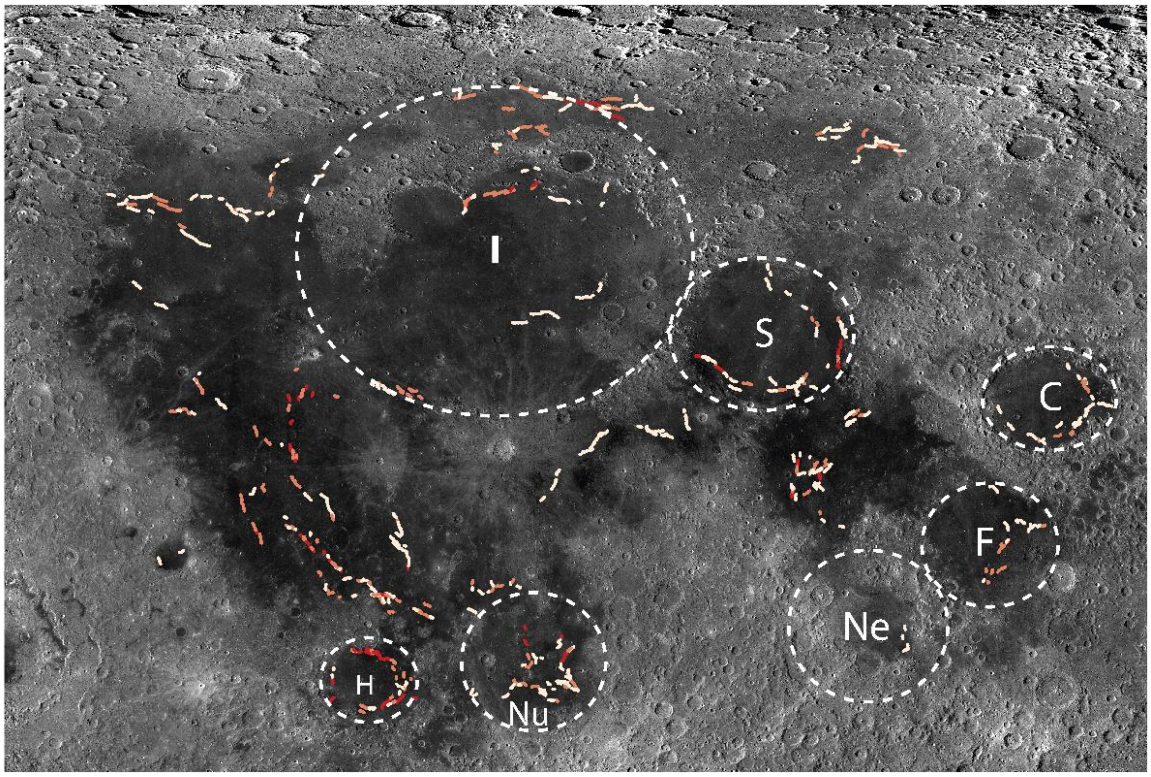

Figure DR5. Active Nearside Tectonic System (ANTS) shown on LROC WAC mosaic and overlain with known basin boundaries. Majority of active wrinkle ridges appear to be outside of mascon basins, especially those associated with Oceanus Procellarum.

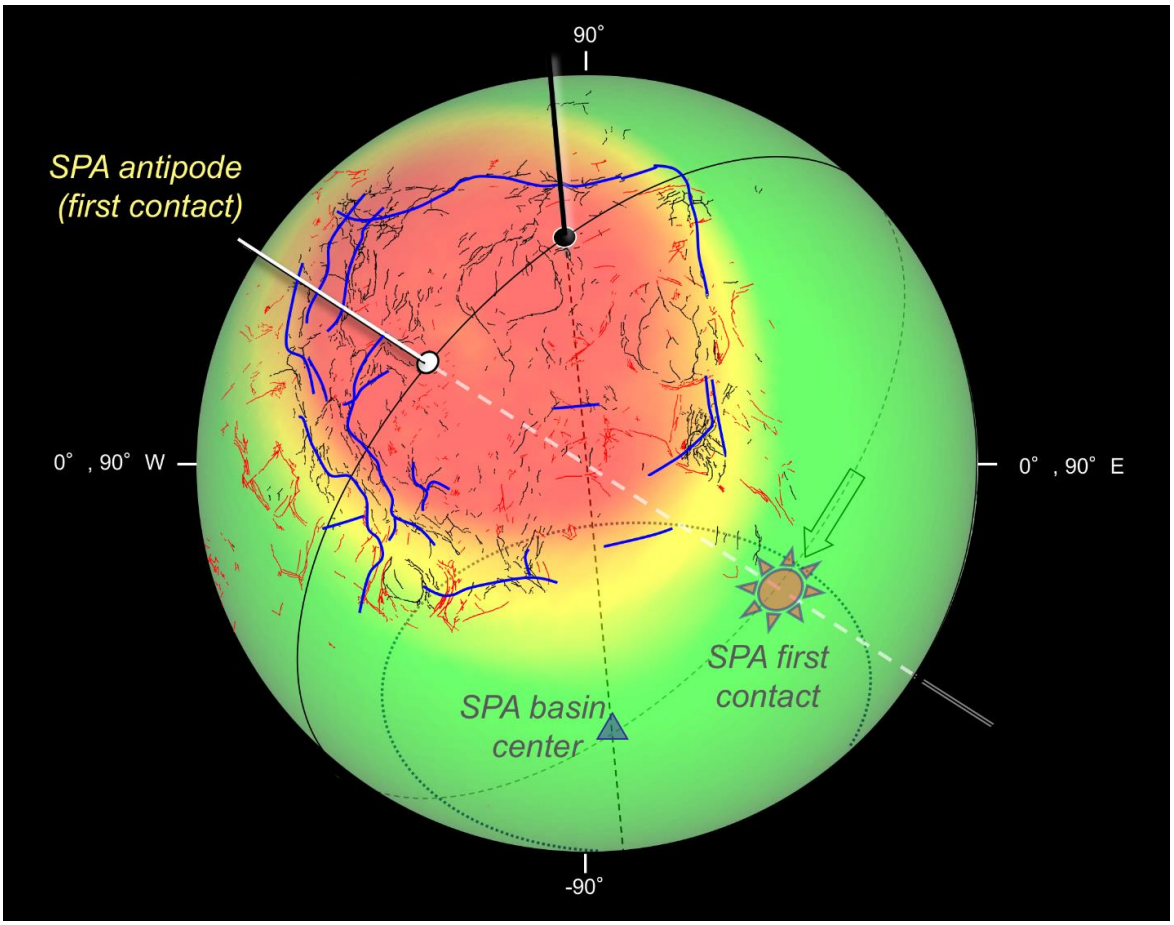

Figure DR6. Long-lasting damage on the lunar nearside due to the oblique impact that formed the South Pole–Aitken (SPA) (Schultz and Crawford, 2011). This figure depicts a "transparent Moon" with the nearside tectonic system as well as the farside SPA Basin center and first-contact by the SPA impactor. GRAIL deep seated intrusions (Andrews-Hanna et al., 2014) are mapped as blue lines. Red lines indicate extensional graben, whereas black lines indicate mapped wrinkle ridges (Wilhelms, 1987; Schultz and Crawford, 2011).

APPENDIX B:

BIDIRECTIONAL REFLECTANCE MEASUREMENTS OF IRON OXIDES

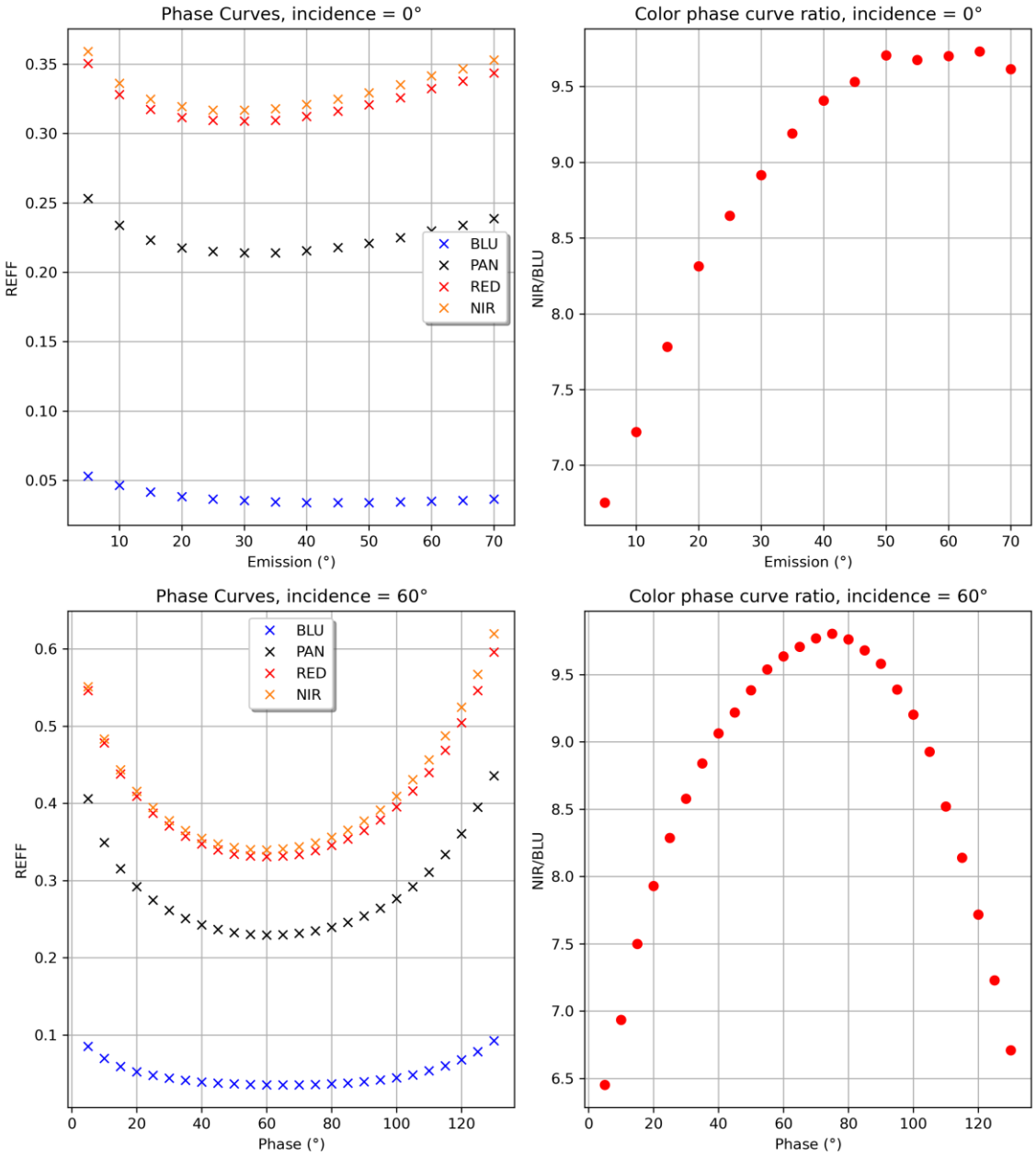

Figure 1. Phase curves and color ratios of ferrihydrite <11-µm size fraction.

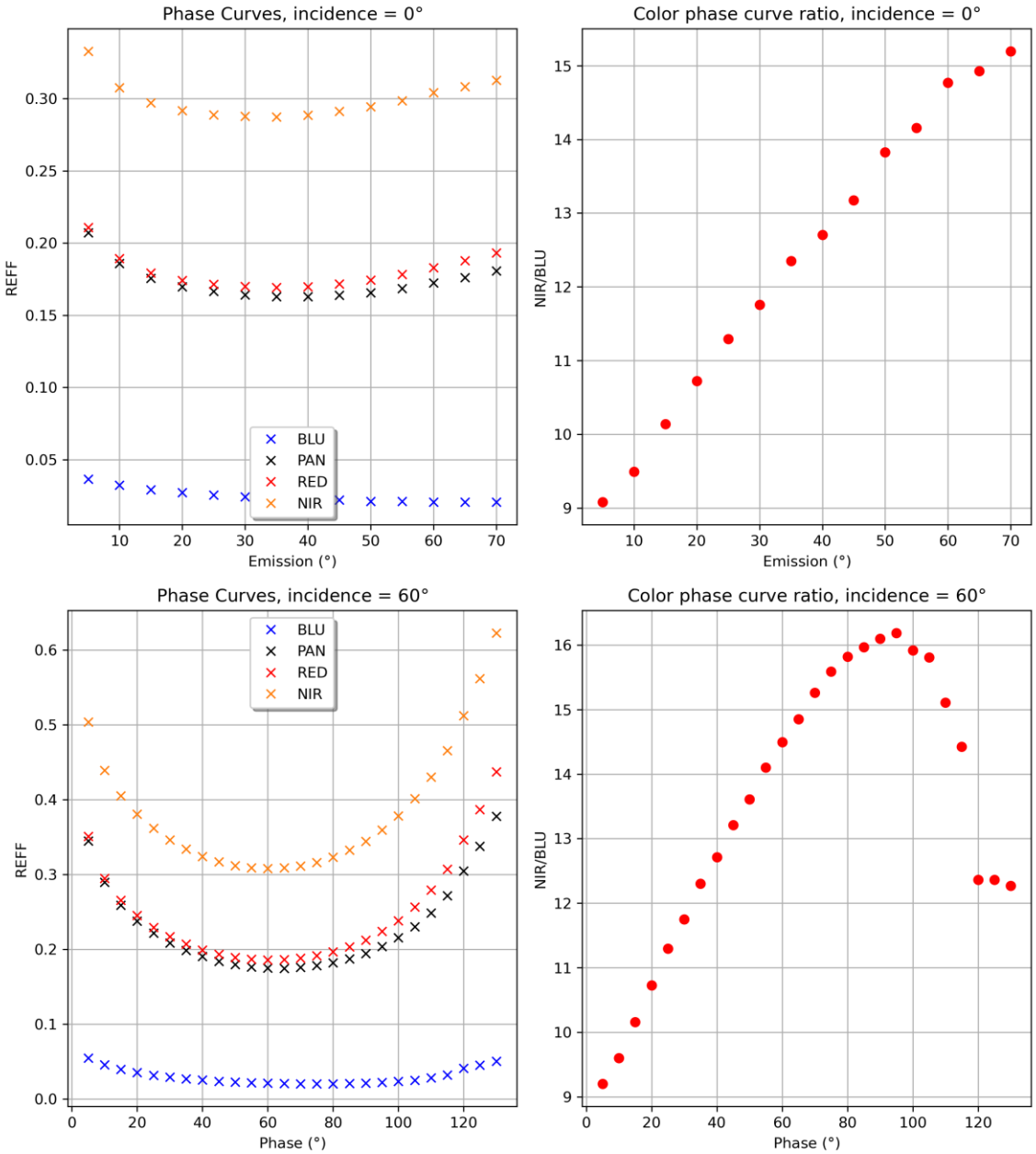

Figure 2. Phase curves and color ratios of hematite <20-µm size fraction.

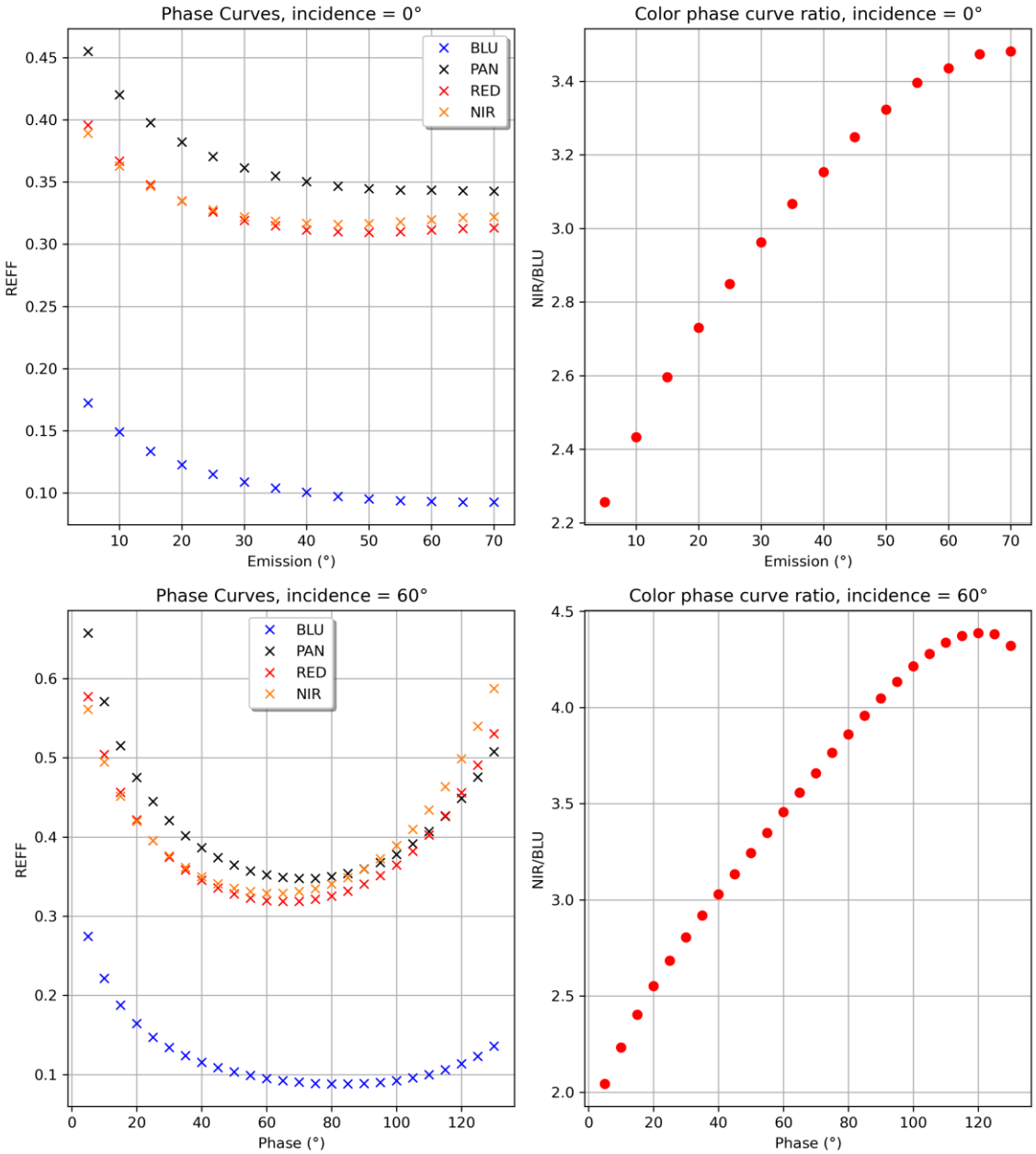

Figure 3. Phase curves and color ratios of akaganeite <30-µm size fraction.

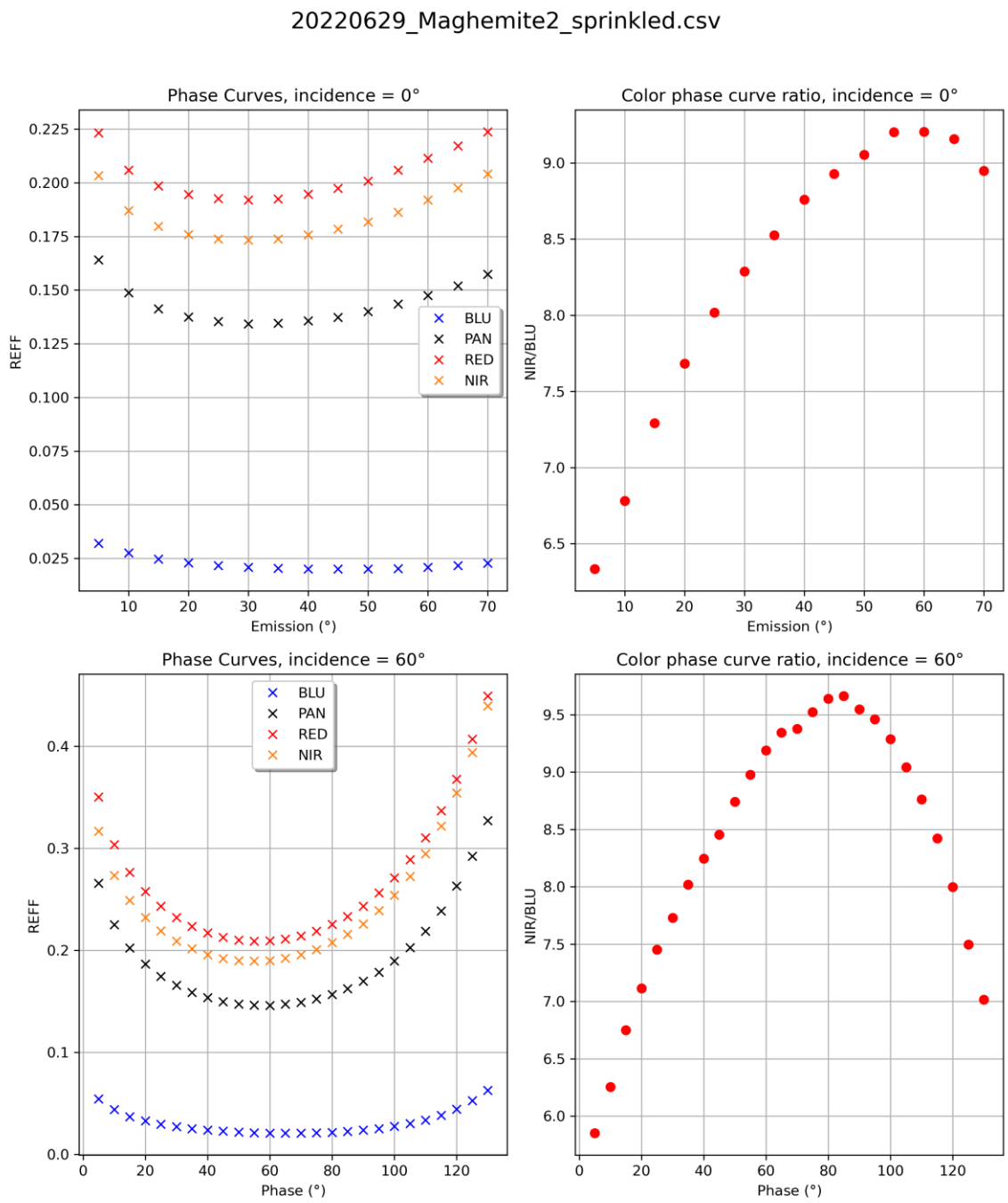

Figure 4. Phase curves and color ratios of maghemite <20-µm size fraction.

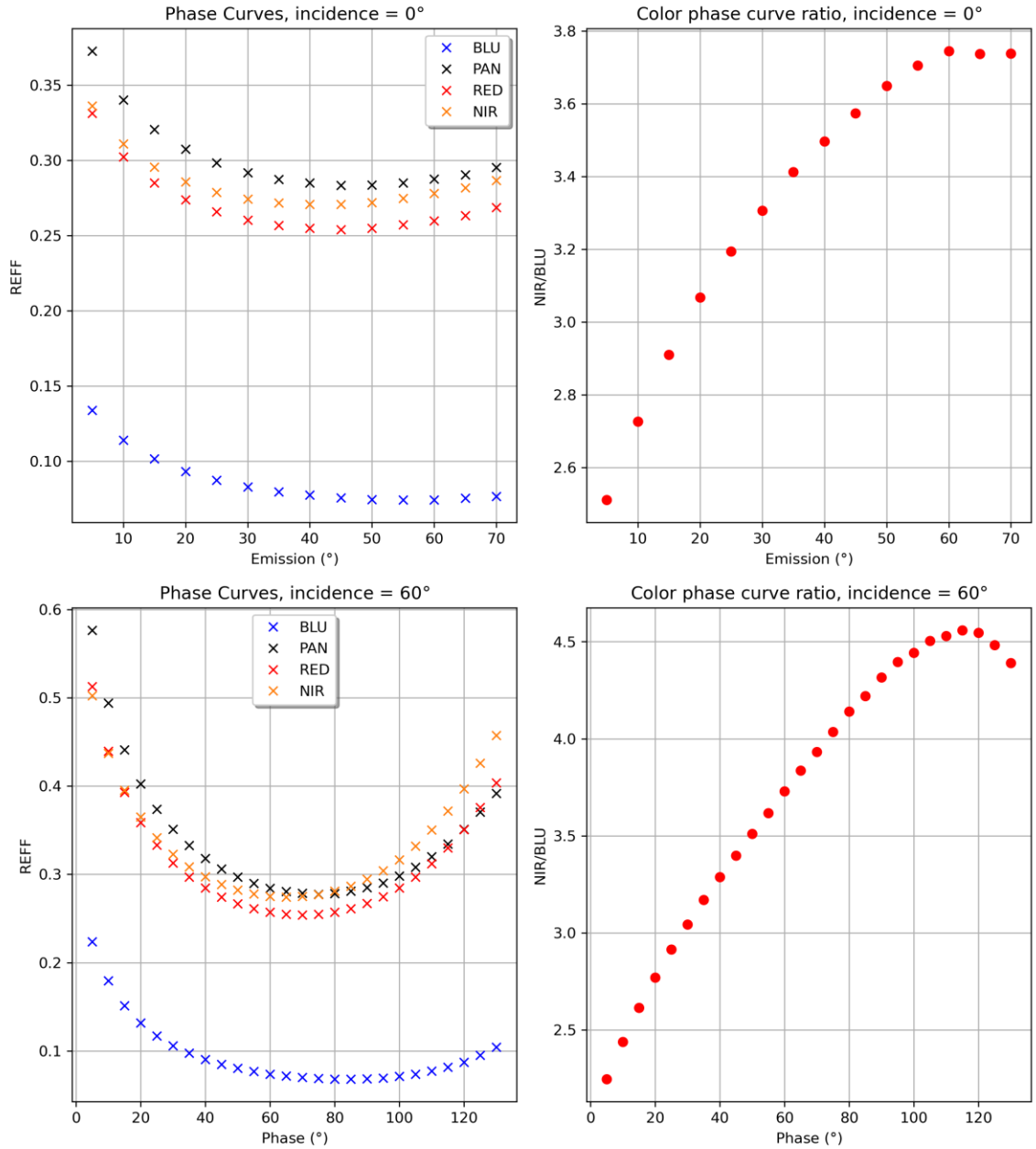

Figure 5. Phase curves and color ratios of schwertmannite <30-µm size fraction.

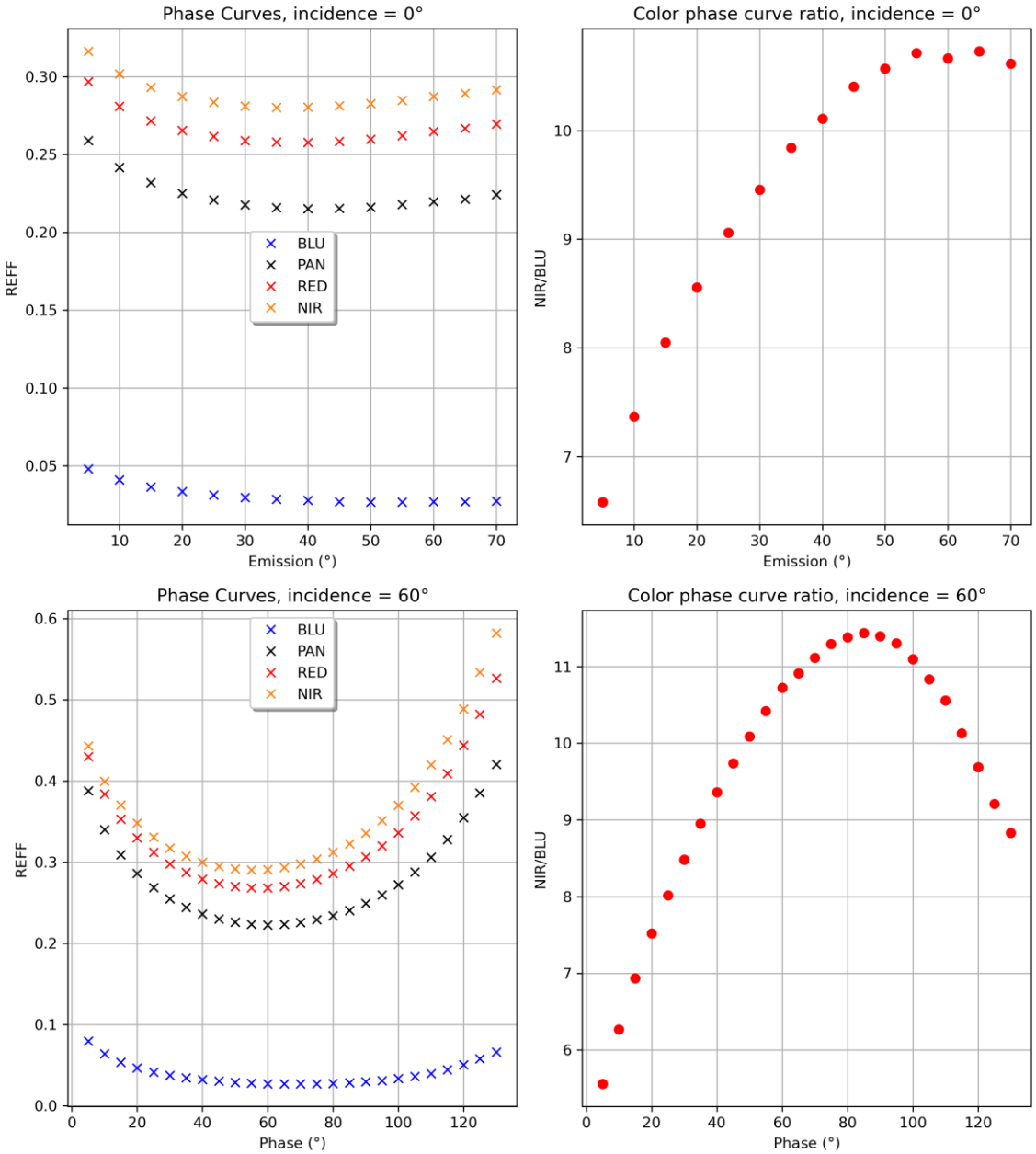

Figure 6. Phase curves and color ratios of feroxyhyte <40-µm size fraction.

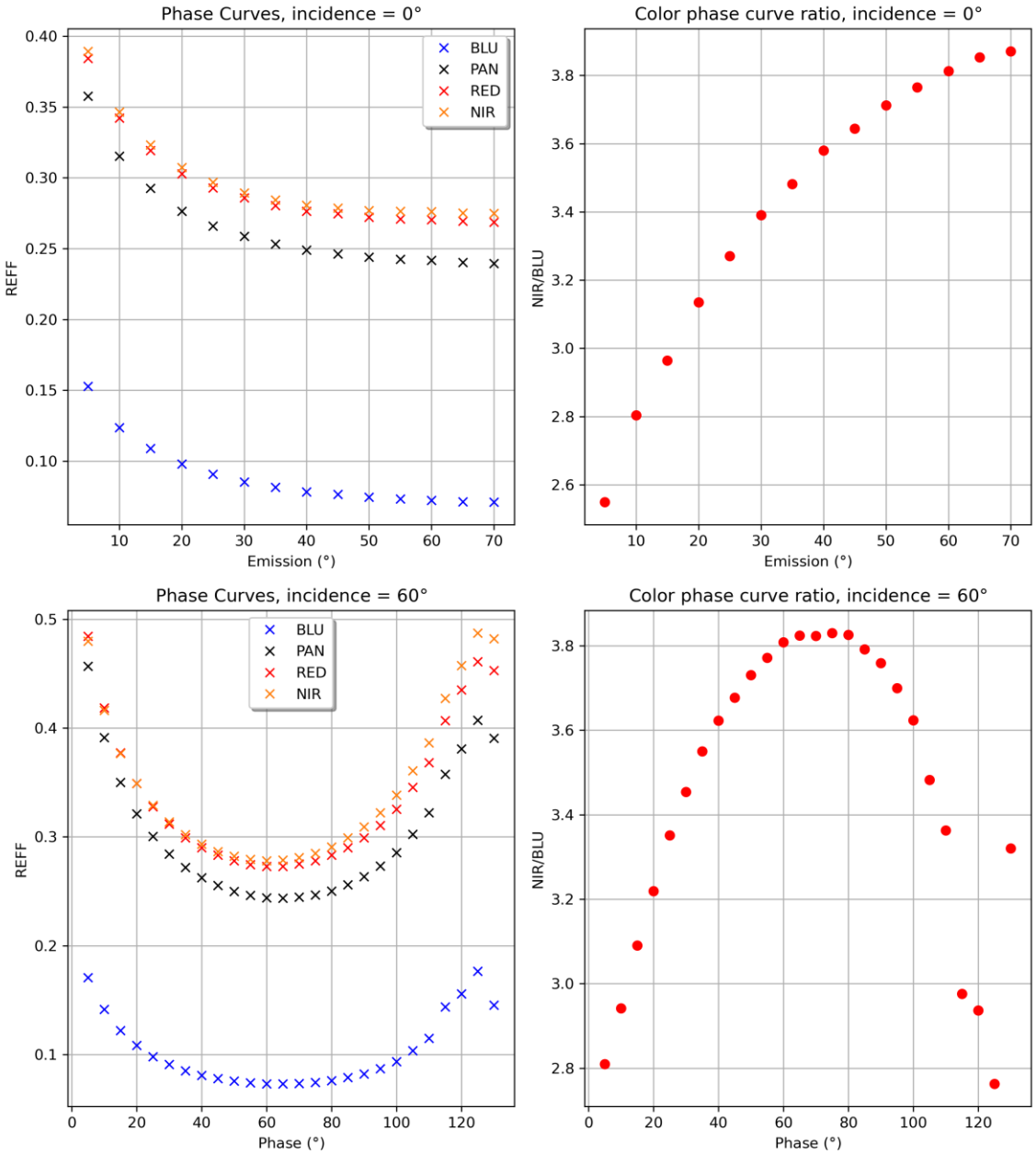

Figure 7. Phase curves and color ratios of lepidocrocite <40-µm size fraction.

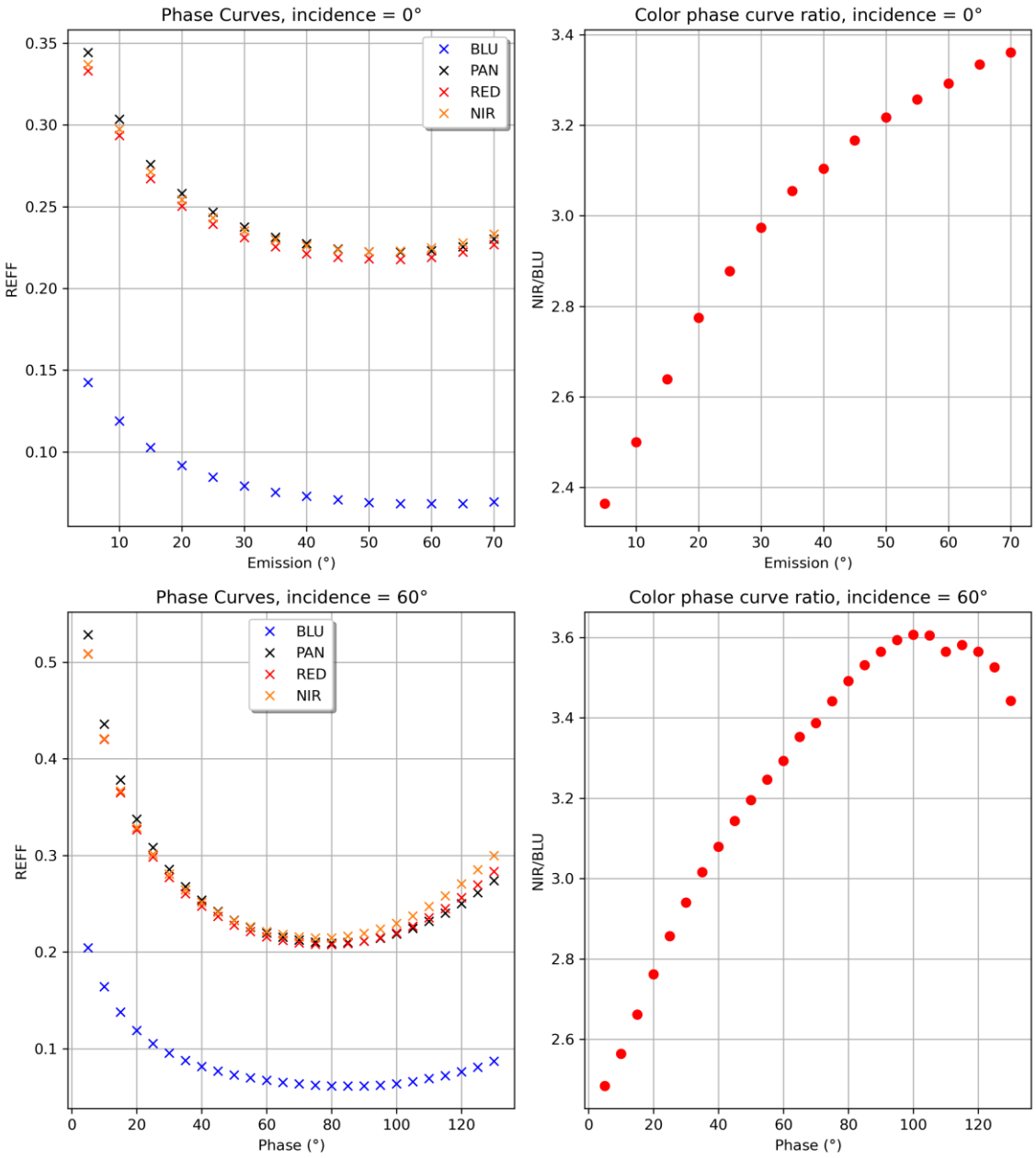

Figure 8. Phase curves and color ratios of goethite <11-µm size fraction.

Declaration

"I declare herewith that this thesis is my own work and that I have not used any sources other than those stated. I have indicated the adoption of quotations as well as thoughts taken from other authors as such in the thesis. I am aware that the Senate pursuant to Article 36 paragraph 1 litera r of the University Act of September 5th, 1996 and Article 69 of the University Statute of June 7th, 2011 is authorized to revoke the doctoral degree awarded on the basis of this thesis. For the purposes of evaluation and verification of compliance with the declaration of originality and the regulations governing plagiarism, I hereby grant the University of Bern the right to process my personal data and to perform the acts of use this requires, in particular, to reproduce the written thesis and to store it permanently in a database, and to use said database, or to make said database available, to enable comparison with theses submitted by others."

Signature  Date: 2022-11-28